REPORT DOCUMENTATION PAGE

Public reporting burden for this collection of information is estimated to average 1 hour per response, including the time for reviewing instructions, searching existing data sources, gathering and maintaining the data needed, and completing and reviewing the collection of information. Send comments regarding this burden estimate or any other aspect of this collection of information, including suggestions for reducing this burden, to Washington Headquarters Services, Directorate for Information Operations and Reports, 1215 Jefferson Davis Highway, Suite 1204, Arlington, VA 22202-4302, and to the Office of Management and Budget, Paperwork Reduction Project (0704-0188), Washington, DC 20503.

1. AGENCY USE ONLY (Leave Blank)	2. REPORT DATE Nov. 30, 1995	3. REPORT TYPE AND DATES COVERED Final Report - Nov. 1, 1991 - Oct. 31, 1995

4. TITLE AND SUBTITLE

Effect of Particle Shape on the Mechanical Behavior of Granular Materials: A Discrete Element Study

5. FUNDING NUMBERS

F49620-92-J-0017

6. AUTHOR(S)

John M. Ting, Larry R. Meachum, Mahmood Khwaja, Jeffrey D. Rowell, Wai-Lim Chin & Gregory Mischel

7. PERFORMING ORGANIZATION NAME(S) AND ADDRESS(ES)

Dept. of Civil & Environmental Engineering
University of Massachusetts Lowell
One University Avenue
Lowell, MA 01854

8. PERFORMING ORGANIZATION REPORT NUMBER

UML-CEE-95-T2

AFOSR-TR-96 0031

9. SPONSORING/MONITORING AGENCY NAME(S) AND ADDRESS(ES)

Directorate of Aerospace & Engineering Sciences
Air Force Office of Scientific Research
110 Duncan Ave. Suite B115
Bolling AFB, DC 20332-2001

NA

10. SPONSORING/MONITORING AGENCY REPORT NUMBER

F49620-92-J-0017

11. SUPPLEMENTARY NOTES

12a. DISTRIBUTION/AVAILABILITY STATEMENT

Unlimited; Approved for public release

12b. DISTRIBUTION CODE

19960201 107

13. ABSTRACT (Maximum 200 words)

An existing two dimensional Discrete Element numerical model which incorporates elliptical particles is used to simulate the biaxial shear of particulate systems. Comparisons are made with physical tests on circular and oval shaped rod systems. Good quantitative agreement was found with the circular rod data, but significantly weaker and softer response was found compared with the oval rod data. This discrepancy is attributed to differences in particle shape in the physical and numerical tests. Additional simulations were conducted using bedded, strongly anistropic systems at varying degrees of particle flatness. These exhibit distinctly different stress-strain and strength behavior, as well as different controlling mechanisms, as function of particle flatness and bedding plane orientation. Shear bands were observed in some flatness and bedding combinations. Interparticle interlocking, dilatancy and inhibition of particle rolling were all observed. Samples with bedding normal to the principal stress direction exhibited the highest shear resistance, as well as largest dilatancy. In systems composed of flat particles with bedding parallel to one of the planes of maximumum obliquity, shear bands sometimes formed in the maximum obliquity plane opposite to the bedding plane.

14. SUBJECT TERMS

soil mechanics, numerical model, instability, shear bands, discrete elements, failure, anistropy, simulation, stress-dilatancy

15. NUMBER OF PAGES

163

16. PRICE CODE

17. SECURITY CLASSIFICATION OF REPORT Unclassified	18. SECURITY CLASSIFICATION OF THIS PAGE Unclassified	19. SECURITY CLASSIFICATION OF ABSTRACT Unclassified	20. LIMITATION OF ABSTRACT Unlimited

DTIC QUALITY INSPECTED 1

Effect of Particle Shape on the Mechanical Behavior of Granular Materials: A Discrete Element Study

John Ting, Pricipal Investigator
University of Massachusetts Lowell

EXECUTIVE SUMMARY

This Report presents the results of an Air Force Office of Scientific Research-funded study on the effect of particle shape on the overall material behavior of granular materials through a Discrete Element numerical study using ellipse-shaped particles. The Discrete Element Method (DEM) possesses unique capabilities for studying the behavior of particulate materials. Because it is a numerical simulation, internal contact forces, particle orientations and average stresses and strains may be monitored inobstrusively. Because the DEM models each particle explicitly, contacts may be broken and renewed, allowing for large local deformations. However, past attempts at using DEM with circular particles have resulted in simulated mechanical behavior which is considerably weaker than expected for natural granular materials. The first portion of this study involved calibrating a recently developed two-dimensional ellipse-based computational model (Ting and Corkum, 1993) with physical test data by Konishi, Oda and Nemat-Nasser (1983) on oval cross-section rods and by Chapuis (1976) on circular rods.

The ellipse-based DEM model yields behavior results that are quantitatively closer to real soil than those yielded by DEM models using round particles. Average angles of internal friction ranged from 26 to greater than 50° degrees, depending on particle aspect ratio and nature of the anisotropy. Good quantitative agreement was found with the circular rod biaxial shear data of Chapuis (1976). Good qualitative, but not quantitative, agreement was found with the oval rod biaxial shear data of Konishi *et al* (1983), despite considerable effort in varying contact paramenters in the DEM model. The ellipse-based DEM yielded consistently softer and weaker response compared to the physical oval rod data. These differences are attributed to the subtle but significant differences in the shape of the particles used in each case. It is recommended that validation of the ellipse-based DEM should continue by comparing with additional physical test results. Such a study is currently underway using the results of interfacial shear tests between a rough interface an assemblage of carefully machined circular and elliptical rods.

In the second portion of this study, additional numerical simulations of biaxial shear tests were conducted to determine the relative importance of particle aspect ratio, anisotropy, and contact friction. Numerical samples were formed similar to the Konish *et al* rod tests, consisting of multiple sized particles of varying particle aspect ratio with their major axes aligned along preferred bedding planes. Individual particle aspect ratio (major axis:minor axis) ranged from 1:1 to 3:1. The samples were initially compressed to isotropic conditions, then sheared in biaxial shear.

Results from these tests exhibit distinctly different stress-strain-strength behavior, as well as different controlling deformational mechanisms, as a function of both bedding plane angle and particle flatness. Interparticle interlocking, dilatancy and inhibition of particle rolling were all observed and significantly affect the overall mechanical behavior. Overall, the samples with bedding orientation normal to the principal stress direction exhibited the highest shear resistance, as well as the largest dilatancy. Increasing particle flatness usually increases overall shear strength, except when the bedding plane coincides with the planes of maximum obliquity. Systems with randomly oriented particles exhibit lower strength than systems with bedding unfavorable to shear, but exhibit greater strength than systems with bedding favorable for shear.

Shear band formation was observed in some bedding and particle flatness combinations. In systems composed of flat particles with bedding parallel to one of the planes of maximum obliquity, the shear band sometimes formed in the maximum obliquity plane opposite to the bedding plane. When shear band formation was observed, the deformation of the assemblage more closely resembles rigid body motion of two opposing particulate wedges with the shear band forming the slip plane.

Based on analysis of the contact statistics during shearing, this study confirms that particle rolling is a dominant deformational mechanism for systems with rounded particles. For systems with flatter particles, interparticle slidng becomes more prominent, with the relative importance of particle motion due to translation and rotation becoming virtually equal for flatter particles. For assemblages with low interparticle friction, particle sliding is the dominant deformation mechanism, while particle rolling is the dominant deformation mechanism in assemblages with high interparticle friction.

The DEM simulations show that assemblages with preferred bedding possess more anisotropic distribution of contact normals. As particle angularity increases, interlocking increases producing a more anisotropic fabric. During the course of deformation, the distribution of contact normal orientations tend to rotate toward the direction of the major principal stress.

The ellipse-based DEM model used for the current study has been shown to be an effective tool for realistically modeling the microstructure and overall mechanical behavior of granular materials. Additional research is planned or underway in several areas: validation with systems composed of carefully machined circular and elliptical rods subjected to shear; modifying the code to allow for fluid-solid interaction; modifying the code to model multiphase materials such as frozen soil systems; validating the method for large scale problems such as shallow plate bearing capacity; and application of the technique to specific problems in granular flow and failure such as pressures during silo filling and vehicle-soil interaction.

Personnel who have worked on this Research project, either in a funded or unfunded capacity include: John M. Ting (Principal Investigator), Larry R. Meachum, Jeffrey D. Rowell, Wai-Lim Chin, Mahmood Khwaja, John Sanchez and Gregory Mischel.

TABLE OF CONTENTS

1. INTRODUCTION

Particle shape is one of the major factors determining the overall mechanical behavior of cohesionless particulate materials. In materials possessing more rounded particles, the mechanism of rolling between particles dominates compared with other deformational mechanisms such as interparticle sliding, resulting in a greatly decreased overall shear resistance and a lower strain at peak resistance. As well, systems composed of more rounded particles exhibit fabric differences such as a decreased range of void ratios between the densest and loosest conditions, lower average void ratios, and less variation in void ratio throughout a sample.

Micromechanically-based constitutive models based on disks and spheres which explicitly account for particle rotation have recently been developed. Disk-based and sphere-based Discrete Element Method (DEM) computational models are common in micromechanical and geotechnical modeling. Since these models may exhibit considerably more rolling behavior than is found in real (*ie* more angular) soils, it is particularly important to quantify the effect of particle shape and the rolling mechanism on granular material behavior at this point in time.

This Report presents the results of an Air Force Office of Scientific Research-funded study on the effect of particle shape on the overall material behavior of granular materials through a Discrete Element numerical study using ellipse-shaped particles. The Discrete Element Method possesses unique capabilities for studying the behavior of particulate materials. Because it is a numerical simulation, internal contact forces, particle orientations and average stresses and strains may be monitored inobstrusively, and reproducible "samples" can be guaranteed from test to test. Because the DEM models each particle explicitly, particle-to-particle contacts may be broken and renewed, allowing for large local deformations. This study involved calibrating a previously developed two-dimensional ellipse-based computational model (Ting and Corkum, 1993) with physical test data by Oda *et al* (1983) on oval cross-section rods and by Chapuis (1976) on circular rods.

Additional numerical simulations were then conducted to determine the relative importance of angularity, contact friction, form and magnitude of contact stiffness, particle gradation and degree of densification. Numerical samples consisting of multiple sized particles of varying particle aspect ratio were formed by packing particles with their major axes along preferred bedding orientations ranging from horizontal to vertical bedding. Individual particle aspect ratio (major axis:minor axis) ranged from 1:1 to 3:1. The samples were initially compressed to isotropic conditions, then sheared in biaxial shear. This Report presents the results from these tests along with the conclusions which were drawn based on these data.

2. BACKGROUND

One of the most important factors governing the behavior of cohesionless granular materials is particle shape. This Section details the effects of particle shape on strength, densification, pore pressure buildup and mechanisms of deformation.

The mechanical behavior of soils is a function of soil structure and applied stress system. Soil structure is composed of two components fabric (spatial arrangement of particles) and nature and magnitude of interparticle forces. For cohesionless soils, the interparticle forces are largely governed by the fabric (Ladd *et al* 1977). The four factors which are generally accepted as having the most influence on the fabric (and hence the behavior) of a cohesionless particulate material are: particle shape, relative density D_r, gradation and mineralogy.

Of these factors, particle shape and relative density are particularly important. Terzaghi and Peck (1967) report an increase in ϕ of 5 to 11° for sands with increasing angularity, while Lambe and Whitman (1968) report a 5 to 6° increase. Holubec and D'Appolonia (1973) reported an increase in ϕ of 10° by increasing angularity (see Figure 1) and 5° by increasing D_r. It is often difficult to separate the effects of these two factors, as the particle shape affects the range of void ratios e_{min} and e_{max} possible for a given gradation, and hence influences the actual density range over which a particular relative density is computed. Koerner (1970) found that mineralogy was important to the observed internal friction angle ϕ through its influence on the physical properties of the particles, *ie* shape and interparticle friction ϕ_μ. Several researchers report increases in ϕ as the material becomes less uniform in particle size (*ie* becomes well-graded). Lambe and Whitman (1968) report increases of 2 to 4° between uniform and well-graded materials.

Particle shape is often quantified by the terms sphericity and roundness (Feda 1982), where sphericity refers to how close the overall particle shape is to a sphere and roundness refers to how rounded the corners are. The coefficient of angularity E used in Figure 1 is a function of the reciprocal of the sphericity, with a value of unity for spheres and increasing with increasing particle angularity.

2.1 Effect of Particle Shape on Strength

The results in Table 1 indicate that increasing particle angularity can increase measured material angle of internal friction ϕ by about 5°. Terzaghi and Peck (1967) report increases in ϕ of up to 11°. Koerner (1970) reported increases in ϕ of 6 to 8° with increasing angularity. Holubec and D'Appolonia (1973) ran tests on materials with similar coefficients of uniformity and coefficient of curvature . Figure 1 plots ϕ as a function of angularity, and shows that ϕ varies up to 10° over the range of angularities tested, where the "angularity" was computed from specific surface areas determined indirectly from permeability tests. In addition, Holubec and D'Appolonia report that the axial strain at peak strength ϵ_{peak} increased with increasing angularity. For glass beads, almost no change was observed in ϵ_{peak} while the angular sands show considerable variation in ϵ_{peak} with D_r.

2.2 Effect of Particle Shape on Densification

According to Youd (1973), the primary factors controlling the maximum and minimum void ratio limits of sands are particle shape, particle size range and the shape of the gradation curve. His data indicate that increasing roundness leads to increasing densities (lower void ratios) as well as a decreased range of density $e_{max} - e_{min}$. These trends were confirmed by Holubec and D'Appolonia (1973) and Dickin (1973). Bhatia and Soliman (1990) analyzed the distribution of void ratios from sections of samples and found that the range in the local void ratios increased (*ie* greater local density variation) as the particle shape became more angular and the relative density increased.
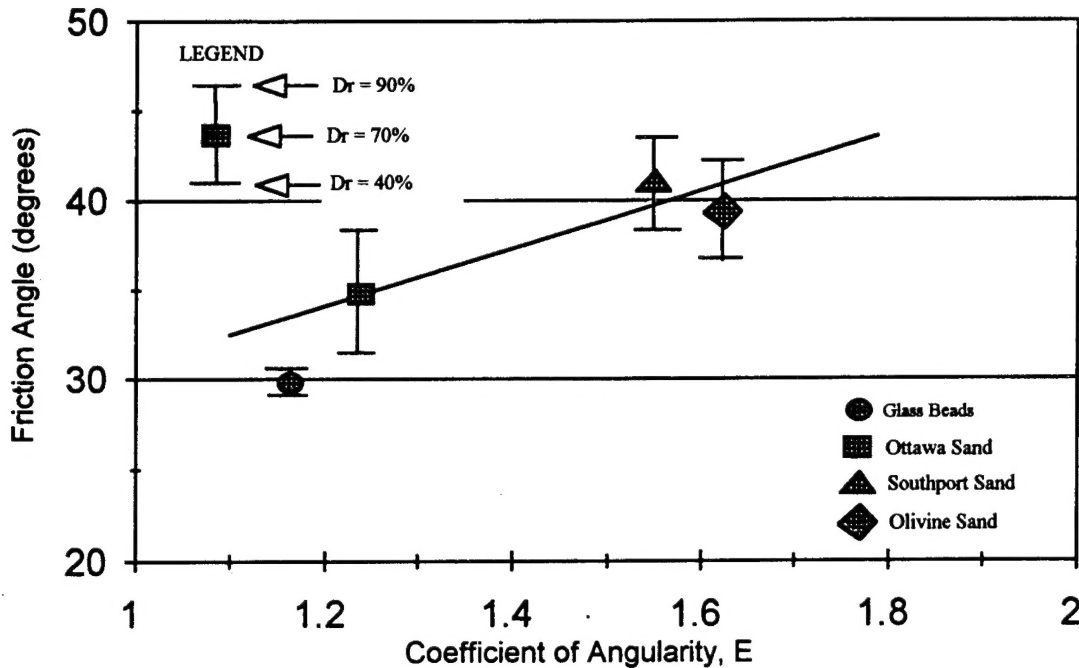
Figure 1. Effect of particle angularity on peak angle of internal friction (from Holubec & d'Appolonia 1973).

2.3 Effect of Particle Shape on Pore-pressure Buildup

According to Ishibashi *et al* (1982), the soil properties having the greatest influence on liquefaction are: (1) grain-size distribution, (2) soil uniformity, (3) grain shape, and (4) void ratio. According to them, properties (1) and (2) may be represented by the mean particle diameter D_{50} and coefficient of uniformity C_u, (3) by the sphericity and (4) by the natural void ratio e and e_{min}. Their data indicate that the applied shear stress ratio τ/σ_c' to cause liquefaction at the 30th cycle:

- increased with increasing angularity
- increased with increasing C_u up to C_u=5
- increased with decreasing volume change potential $e - e_{min}$.

In other words, increasing angularity, decreasing sample uniformity and decreasing the potential volume change all tend to increase the resistance of the material to potential liquefaction.

These results were confirmed by Vaid *et al* (1985), who also found that at high confining stresses, samples made of angular particles can still be made to liquefy, while samples made of rounded particles tended to stabilize above a relative density of 85%. They attributed this to contact crushing and breakage of the angular particles at the high confining stresses.

2.4 Effect of Particle Shape on Mechanisms of Strength and Deformation

Based on the deformational behavior of regularly packed rigid spheres, Rowe (1962) proposed his stress-dilatancy theory wherein he decomposed the shear resistance of cohesionless granular materials into three

3

components:
- frictional resistance, due to interparticle sliding,
- interference resistance, where particles rearrange and reorient at constant volume, and
- dilatant resistance, due to the effect of dilation against a confining stress.

Rowe's stress-dilatancy theory, and Horne's (1965, 1969) revisions did not consider the possibility of rolling between particles. Skinner (1969) showed that for an assemblage of uniform spheres, the rolling phenomenon is very important. By direct shear tests on dry and wet glass ballotini, steel balls and lead shot, Skinner measured peak ϕ_{max} values varying from 30 to 40°, depending on initial porosity. However, the constant volume angle ϕ_{cv} was observed at about 25° regardless of ϕ_μ, even though ϕ_μ varied from 4° to 40°. Skinner concluded that as the sliding friction angle increased, the sliding mechanism became less prominent, and rolling predominates.

This conclusion is confirmed by tests on two dimensional photoelastic oval rods (Oda *et al* 1983, 1985, Konishi *et al* 1983, Mehrabadi *et al* 1988). These were biaxial compression loading tests which included two different particle aspect ratios (1.1 and 1.4), two interparticle friction angles ϕ_μ (26° and 52°) and a variety of bedding angles (0°, 30°, 60° and 90°). By considering the statistics of the contacts where pure rolling, pure sliding and both rolling and sliding were occurring, as well as the contacts where the frictional resistance was fully mobilized, they concluded that the rolling mechanism dominates when the interparticle friction angle is large.

In particular, note the samples of nearly round particles (aspect ratio 1.1, Oval I) exhibit relatively small dependence on ϕ_μ or bedding plane. For the more angular particles (aspect ratio 1.4, Oval II), there is a pronounced drop in shear strength at the bedding angle of 60°, as expected when the plane of maximum τ/σ closely aligns with the bedding plane. However, since the material with the higher ϕ_μ exhibits a much higher strength, this suggests that sliding is more important for the more angular particles. Conversely, this also suggests that rotation is inhibited for the more angular particles. Direct comparison of the strengths for Oval I and Oval II at the same friction angle ϕ_μ at the 0° bedding angle indicates that the more angular particles exhibit more than double the strength of the more rounded particles.

The conclusion that particle rolling is an important deformational mechanism is further supported by various experimental and numerical data on two dimensional circular and oval rod systems. Chapuis (1976) tested samples of circular rods and found ϕ_{cv} of 15° and ϕ_{max} of 25° for a dense sample. They measured the rod-surface friction angle ϕ_μ as 15 to 16° (greater than their ϕ_{cv}) based on shearing parallel to the axis of the rods (*ie* sliding only) and 10 to 11° when shearing occurred perpendicular to the direction of the rods (*ie* rolling and sliding).

Ting *et al* (1987) simulated the shearing of two dimensional disk systems using the Discrete Element Method (**DEM**). The **DEM** is a numerical method which treats each particle distinctly, allowing interparticle slip and rolling, and will be described in greater detail later in this Proposal. They reported the results of shearing disks in direct simple shear. For an interparticle friction ϕ_μ of 0°, the observed ϕ_{max} was 5°, while for $\phi_\mu = 25°$, ϕ_{max} was 19°. In simulations of "triaxial" tests with rigid and flexible side boundaries, ϕ_{max} was 20° for $\phi_\mu = 25°$, correlating well with the results from the simple shear simulations. The individual particle rotations could be inhibited by artificially increasing the individual particle moments of inertia I_o. When *no* rotation is permitted (*ie* pure translation), the peak observed friction angle could be increased up to 40° for $\phi_\mu = 25°$.

All the data cited in the previous section suggest that rolling can be an important deformational mechanism in granular materials, especially when the particles are round. However, real soils are far from the nearly perfect spheres or disks considered in most of these tests. As a result, real soils may actually exhibit much less rolling that might be suggested from the above data. In the study by Oda *et al*, the aspect ratio of the ovals was varied only from 1.1 to 1.4 (equivalent to roundness values of 0.91 to 0.71 and sphericity values of 0.998 to 0.97, respectively). Nevertheless, they observed a twofold increase in peak resistance with decreasing roundness.

4

3. RESEARCH PROGRAM

The data cited in the preceding Section has shown that particle shape critically influences the stress-strain-strength behavior of drained and undrained cohesionless particulate materials. It is hypothesized that the much of the observed behavior differences between rounded and angular materials is due to a different packing and densification behavior, and altered controlling deformational mechanisms. In particular, samples composed of rounded particles more readily permit interparticle rolling, with a resultant weaker observed shear resistance.

In the research areas relating to particulate mechanics, various analytical and numerical models based on disks and spheres have emerged and become fairly popular. Recently, Chang and Liao (1990) developed an analytical micromechanically-based constitutive relationship for disks and spheres accounting for particle rotation. These continuum formulations may be incorporated into finite element code to incrementally solve full boundary value problems. This very promising development must be tempered by the knowledge that "real" soils possess heterogenous strain fields (Chang and Misra 1990) and also may actually roll a great deal less than that predicted by any round particle model.

Numerically, the Discrete Element Method (**DEM**) models particulates as a collection of individual particles, and was originally developed by Cundall (1974) to model rock masses composed of angular blocks. This has spawned various two-dimensional disk-based programs such as *BALL* (Cundall and Strack 1979), *DISC* (Corkum and Ting 1986), *DISC* (Bathurst and Rothenburg 1988), *SKRUBAL*, *CONBAL-2* (Dobry and Ng 1989) and three-dimensional sphere-based programs *TRUBAL* (Cundall 1988), *3DSHEAR* (Walton *et al* 1988), *DMC* (Taylor and Preece 1989), and *SPHERE* (Hassan 1990). Other disk-based algorithms have also been developed (Kishino 1988, Bazant *et al* 1990). These numerical simulations appear to quantitatively approximate the behavior of disks and spheres appropriately (Ishibashi *et al* 1989, Chen 1989). However, approximation of realistic *soil* behavior using disk-based models (especially at fairly large strains) requires inhibition of individual particle rotation (Ting *et al* 1989).

Because of the promise exhibited by the analytical as well as numerical developments in particle modeling, it was considered to be especially important to investigate the effect that using a circular particle form factor would have on the overall response of a particulate system. In particular, to what degree does out-of-roundness affect material behavior? To gain insight to these and other questions, a previously-developed ellipse-based implementation of the Discrete Element Method was used. The **DEM** possesses unique capabilities for studying the behavior of particulates, from its ability to model the fine detail of mechanisms of deformation to generating the force and orientation distributions during numerical testing. The computer model was first used to simulate the physical experiments of Oda, Konishi and Nemat-Nasser on oval rods and Chapuis (1976) on circular rods by varying the contact parameters and contact stiffness.

For the second stage of the research, numerical samples of approximately 700 ellipse-shaped rods were formed with the particles aligned along preferred bedding planes, then isotropically compressed, and sheared in biaxial compression. Samples were tested with bedding planes varying from 0, 30, 60 and 90° normal to the major principal stress direction, as well as "random" orientation (no preferred bedding). Different samples were formed at varying particle aspect ratio, with the ratio of the major:minor axes of the individual particles varying from 1:1 to 3:1, with the aspect ratio held constant in each sample. As well, interparticle angle of sliding friction ϕ_μ, sample size (number of particles), and contact properties were varied in some instances. This Report presents the results of this study.

5

4. DISCRETE ELEMENT METHOD

The Discrete (or Distinct) Element Method (DEM) has been used for over a decade for numerically modeling the mechanical behavior of granular materials. Instead of a continuum, the DEM treats granular material as an assemblage of distinct particles, each governed by physical laws. Each particle interacts with its neighbors through particle-to-particle contacts which can be formed or broken at each time step, as shown in Figure 2. Because no restrictions exist regarding mode of deformation or amount of displacement of each particle, the DEM is uniquely suited for modeling large deformation processes and bifurcation-type behavior in granular materials.

This numerical technique was first adapted by Cundall (1974) to geomechanics for studying the dynamic behavior of rock masses. As this technique has evolved, it has been used in a wide variety of research applications in engineering mechanics and geotechnical engineering. These applications include statistical micromechanics (Cundall and Strack 1979, Cundall 1988, Bathurst and Rothenburg 1988), constitutive behavior of granular soils (Zhang and Cundall 1986, Ting and Corkum 1988, Dobry and Ng 1989, Issa and Nelson 1989), creep of soils (Kuhn and Mitchell 1989), flow of granular materials (Walton *et al* 1988, Campbell and Bronwen 1983, Ghaboussi and Barbosa 1988, Hakuno *et al* 1980), analysis of rock-support interaction (Lorig and Brady 1984), blast loading of ground (Butkovich *et al* 1988, Taylor and Preece 1989) and large deformation geotechnical modeling (Barbosa and Ghaboussi 1987, Ting *et al* 1989).

The largest problems tackled to date with the DEM involve up to a few tens of thousands of two- or three-dimensional particles simulated with a few tens of thousands of time steps. The particles are usually of simple geometric shape, either two-dimensional discs, polygons, three dimensional spheres or polygonal blocks. While circular particles have the great advantage of computational simplicity, they also possess the inherent tendency to roll. In particular, computed normal contact forces never contribute to the moment acting on a particle as each normal contact force always acts through the particle centroid. As a result, it is difficult to simulate "real" material behavior when the basic particle is even slightly angular (Ting and Corkum 1988).
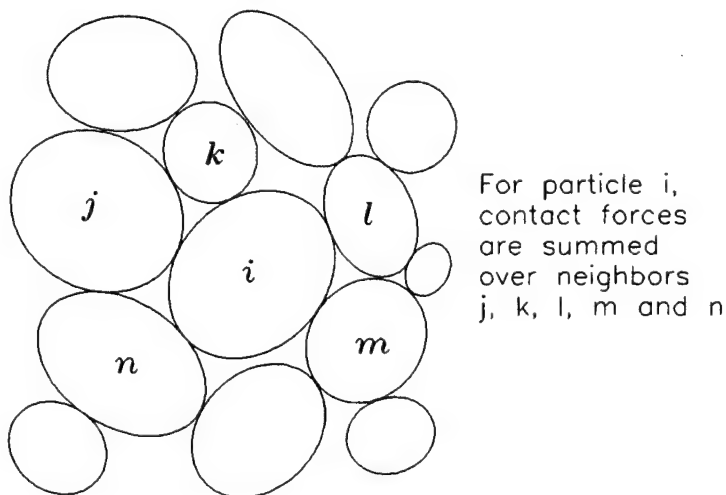

For particle i, contact forces are summed over neighbors j, k, l, m and n

Figure 2. Local equilibrium scheme in Discrete Element Method

An alternative is to use polygonal particles, which can present difficulties at the vertices. For instance, one must distinguish between edge-edge, edge-corner and corner-corner contacts, and also maintain a smooth transition in behavior from one contact type to another. In addition, polygons have no unique outward normal

6

at each vertex, and are complex to extend to three dimensional blocks. In particular, approximating the shape of rounded or subangular granular materials such as cohesionless soil or powders using polygonal particles may require using a large number of sides, hence increasing the number of corners and sides in a particle.

Because of these difficulties, it was decided to implement the **DEM** using two-dimensional ellipse-shaped particles. The ellipse shape has the advantage of having a unique outward normal and no singularities at every point along its surface. Extension to three dimensions should be relatively simple. The ellipse falls into a general class of functions known as superquadrics which have been proposed for modeling solids (Williams and Pentland 1989). However, because the ellipse has a maximum degree of only two, roundoff errors are minimized in comparison with some of the higher degree superquadric functions. Because of these properties, and the inherent limitations of using circular particles for modeling "real" granular materials, it has recently become popular to use the ellipse shape for Discrete Element modeling (Ting 1991, Wei *et al* 1991, Rothenberg and Bathurst 1991, Ng 1992).

This Section presents the detailed development of the numerical algorithm for the Discrete Element Method using two-dimensional ellipse-shaped particles. This Section derives the equations for determining particle-particle and particle-wall contact locations and incremental velocities and integrates them into the conventional **DEM** algorithm. Initial validation tests on rod assemblies of varying aspect ratio are presented.
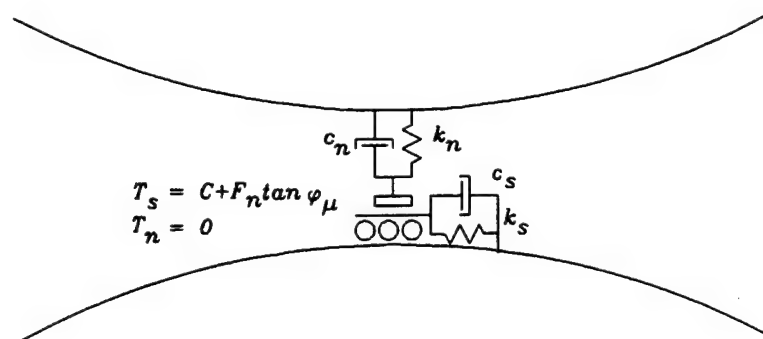

$$T_s = C + F_n \tan \varphi_\mu$$
$$T_n = 0$$

Figure 3. Nature of particle-particle contact in Discrete Element Method.

4.1 Derivation of Ellipse-based Discrete Element Method Algorithm

In the **DEM**, every particle in the soil mass is identified separately, with its own mass, moment of inertia and contact properties, as shown in Figure 2. Each particle (or discrete element) is considered to be geometrically inviolate, with deformable contacts. Normal and tangential springs and dashpots exist at each contact to represent contact compliance and energy absorption, with a limit placed on the maximum tangential shear strength, as seen in Figure 3. The contact springs may be linear or nonlinear, and in some cases have been based on Mindlin's solutions for Hertzian contact (Cundall 1988, Dobry and Ng 1989). The amount and rate of overlap between neighboring elements are used to determine the contact forces at each instant in time. The total unbalanced forces and moment acting on each particle are computed based on local equilibrium of direct neighbors and are used to estimate each particle's accelerations. The accelerations are then integrated for velocities and displacements using a second order leapfrog scheme (Cundall and Strack 1979).

```
for all time do
    |         store data to files, if necessary
    |         compute flexible wall stresses, if necessary
    |         for all particles do
    |             |         for all items in contact with current particle do
    |             |             |         compute contact location and veloc-
ities
    |             |             |         compute contact forces
    |             |             |         update particle and wall forces
    |             |         compute accelerations for current particle
    |         update rigid wall velocities
    |         for all particles do
    |             |         integrate for velocities and displacements
    |             |         form list of particles to check for new contacts
    |         for all walls do
    |             |         update wall locations
```

TABLE 1. Pseudocode for Discrete Element simulation.

The flow diagram for the general **DEM** algorithm is shown in pseudocode in Table 1. The following Sections present the derivation of the ellipse-based **DEM** algorithm based on computations of ellipse-ellipse and ellipse-wall intersection, and associated incremental contact velocities (Ting 1991).

4.1.1   Ellipse-ellipse Intersection

Since the **DEM** considers particles to be quasi-rigid with deformable contacts, one can arbitrarily define the "point" of contact (x_c, y_c) between two ellipses as the midpoint of the line connecting the two ellipse-ellipse intersection points. To solve for these intersections, note that the equation of a two-dimensional ellipse located at the origin of its local coordinate system is simply:

$$\left(\frac{x}{a}\right)^2 + \left(\frac{y}{b}\right)^2 - 1 = 0 \tag{1}$$

where a and b are the major and minor axes aligned along the x and y coordinate axes, respectively. Transformation between local and world coordinates can be performed using the following:

$$\begin{Bmatrix} x \\ y \\ 1 \end{Bmatrix}_{world} = \begin{bmatrix} \cos\theta & -\sin\theta & dx \\ \sin\theta & \cos\theta & dy \\ 0 & 0 & 1 \end{bmatrix} \begin{Bmatrix} x \\ y \\ 1 \end{Bmatrix}_{local} \tag{2}$$

where θ is the orientation of the local system with respect to the world, measured counterclockwise positive. For an ellipse with center at (dx, dy) in world coordinates and major axis rotated at angle θ to the x axis, measured counterclockwise, the general equation in world coordinates is:

$$f(x,y) = A(x-dx)^2 + B(y-dy)^2 + 2C(x-dx)(y-dy) - 1 = 0 \tag{3}$$

where coefficients A, B and C are functions of dx, dy, a, b and θ only:

8

$$A = \left(\frac{\cos\theta}{a}\right)^2 + \left(\frac{\sin\theta}{b}\right)^2$$

$$B = \left(\frac{\sin\theta}{a}\right)^2 + \left(\frac{\cos\theta}{b}\right)^2 \qquad (4)$$

$$C = \cos\theta \sin\theta \left(\frac{1}{a^2} - \frac{1}{b^2}\right)$$

For two ellipses I and j with axes a_i, b_i and a_j, b_j, centers (x_{ci}, y_{ci}) and (x_{cj}, y_{cj}) with rotations θ_i and θ_j, the equation for ellipse j expressed in the local coordinate system of ellipse I is simply equation (3), except that a_j, b_j replace a and b in equation (4), and the new θ, dx and dy are given by:

$$\theta = \theta_j - \theta_i$$

$$dx = (x_{cj} - x_{ci}) \cos\theta_i + (y_{cj} - y_{ci}) \sin\theta_i \qquad (5)$$

$$dy = -(x_{cj} - x_{ci}) \sin\theta_i + (y_{cj} - y_{ci}) \cos\theta_i$$

Since particles in a **DEM** simulation are usually only *marginally* in contact, it is important to minimize the effect of any roundoff error in computing ellipse-to-ellipse intersections. As well, the intersection equation should maintain the same accuracy regardless of the units used, and should allow for a wide range in the magnitude of the aspect ratio a/b. To address these issues, first transform the ellipses to the local coordinate system of ellipse I using equations (3), (4) and (5), then further transform the system by scaling both local x and y axes to homogeneous form:

$$X = \frac{x}{a_i} \ ; \ Y = \frac{y}{b_i} \qquad (6)$$
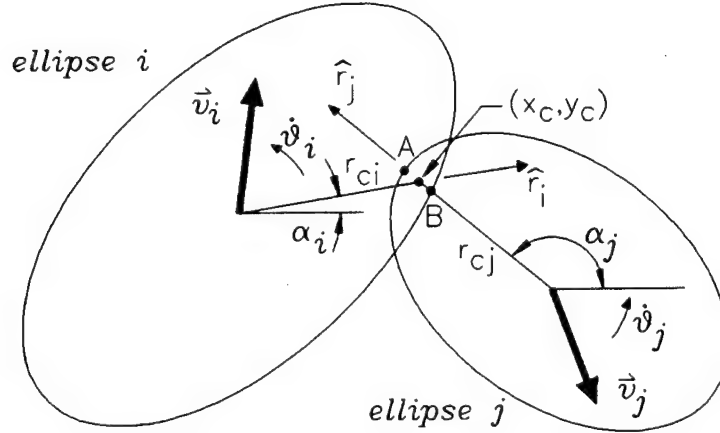
Figure 4.   Nomenclature for contact between two ellipses.

Ellipse I then reduces to a unit circle:

$$X^2 + Y^2 - 1 = 0 \qquad (7)$$

The equation for ellipse j in the new homogeneous local coordinates X and Y becomes:

9

$$\overline{A}\ (X - \overline{dx})^2\ +\ \overline{B}\ (Y - \overline{dy})^2\ +\ 2\ \overline{C}\ (X - \overline{dx})\ (Y - \overline{dy}) \tag{8}$$

where

$$\overline{A} = a_i^2 A,\ \overline{B} = b_i^2 B,\ \overline{C} = a_i b_i C,\ \overline{dx} = \frac{dx}{a_i},\ \overline{dy} = \frac{dy}{b_i} \tag{9}$$

To solve for the intersection, Y is eliminated from equations (7) and (8), resulting in a quartic equation in terms of X. This equation has been presented elsewhere (Ting 1991, Rothenberg and Bathurst 1991). However, it turns out that this equation can be quite ill-conditioned. Since the particles being simulated are usually fairly "hard", the amount of overlap is usually quite small. As a result, the location of contact often approaches a single point. If both particles are fairly flat near the contact location, considerable error may result in computing the contact location. Also, in some situations where both particles have major axes aligned with each other (*ie* $\theta \rightarrow$ 0), the quartic equation nearly reduces to a quadratic, that is, the coefficients of X^4 and X^3 approach zero. This can also lead to problems, as the solution process requires normalizing the quartic so that the leading coefficient of X^4 is unity. If this leading coefficient is nearly zero, then the other coefficients become very large after the normalization, resulting in considerable roundoff error.

Alternatively, it is better to solve for a "contact" location for the two ellipses using a better-conditioned, quartic polynomial (Ting 1992). As seen in Figure 5, the function $g(x,y) = c$ is a family of ellipses sharing origin, orientation and aspect ratio with varying axis magnitudes a,b depending on the value of the constant c. It is possible to locate a function $g(x,y) = c$ which *just* touches the ellipse $f(x,y) = 0$ (at point **A'**). At the common point between these ellipses $f(x,y) = 0$ and $g(x,y) = c$, the slope of each ellipse is the same. Similarly, one can locate a function $f(x,y) = c'$ which just touches ellipse $g(x,y) = 0$ (at point **B'**). It is possible to define a new function $h(x,y) = 0$ which is the locus of all points where $f(x,y) = c$ and $g(x,y) = c'$ share the same slope. This function $h(x,y) = 0$, shown in Figure 5, intersects both $f(x,y) = 0$ and $g(x,y) = 0$ nearly at right angles. The solution of the $h(x,y) = 0$ with $g(x,y) = 0$ and $h(x,y) = 0$ with $f(x,y) = 0$ results in two quartic equations which are better conditioned than the quartic resulting from merely intersecting two ellipses. The resulting intersections can then be combined to locate a "point" of contact, just as with ellipse-ellipse intersections, only now the presumed contact location (x_c, y_c) is midway between points **A'** and **B'**.
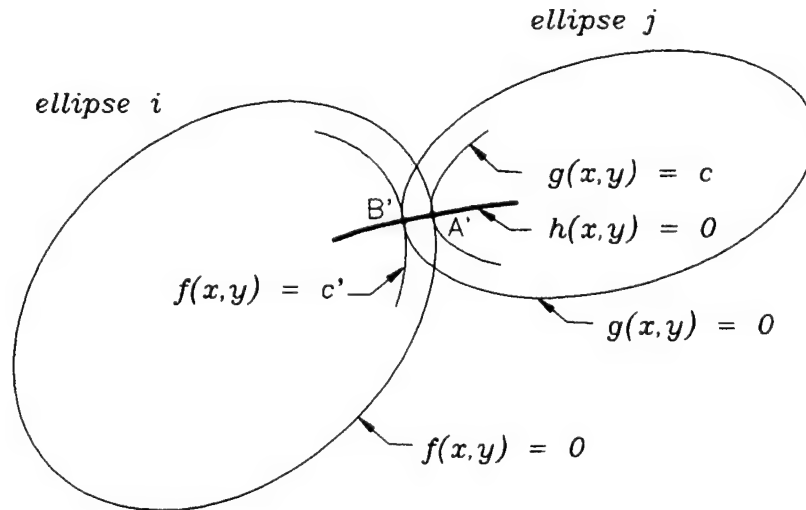

Figure 5. Robust scheme for contact location.

Locating the intersection of $h(x,y) = 0$ with $(x,y) = 0$ (point $\mathbf{A'}$ in Figure 5) requires the solution of the following quartic in terms of X (derived in Ting 1992):

$$(4\bar{P}^2 + \bar{Q}^2)X^4 + (4\bar{P}\bar{R} + 2\bar{S}\bar{Q})X^3 + (\bar{R}^2 - 4\bar{P}^2 - \bar{Q}^2$$
$$(-2\bar{P}\bar{R} - 2\bar{S}\bar{Q})X + (\bar{P}^2 - \bar{S}^2) = 0 \tag{10}$$

where

$$\bar{P} = \bar{C}; \quad \bar{Q} = \bar{B} - \bar{A}; \quad \bar{R} = -\bar{B}\bar{dy} - \bar{C}\bar{dx}; \quad \bar{S} = \bar{A}\bar{dx} + \bar{C}d \tag{11}$$

Solving equation (10) results in up to four roots where $(x,y) = 0$ and $h(x,y) = 0$. The roots are tested to see which has the smallest magnitude $|g(x,y)|$ to see which lies closest to the intersection point. The local coordinates of the intersection are then converted to world coordinates. The entire system is the solved for ellipse j in terms of ellipse I to yield a second intersection which would correspond to the intersection of $g(x,y) = 0$ and $h(x,y) = 0$ (point $\mathbf{B'}$). The presumed location of the contact is then taken as the *average* of the two "intersection" points $\mathbf{A'}$ and $\mathbf{B'}$, that is, the midpoint of the line joining points $\mathbf{A'}$ and $\mathbf{B'}$. The normal at the contact is also taken as the average of the outward normals to each ellipse at each point $\mathbf{A'}$ and $\mathbf{B'}$.

This technique results in a much more reliable and accurate algorithm for computing ellipse-ellipse intersection (Ting 1992). In addition, it should be possible to extend the method to three dimensions more easily than computing the actual surface of intersection between two ellipsoids.

4.1.2   Ellipse-Ellipse Incremental Contact Velocities

To compute the incremental contact force between particles I and j, one needs to estimate the relative velocity of the contact point (x_c, y_c) on particle I with respect to the same point on particle j. Figure 6 shows the sign convention used for the normal and tangential vectors at the contact, where

$$\hat{e} = e_1 \hat{i} + e_2 \hat{j}$$
$$\hat{t} = e_2 \hat{i} - e_1 \hat{j} \tag{12}$$
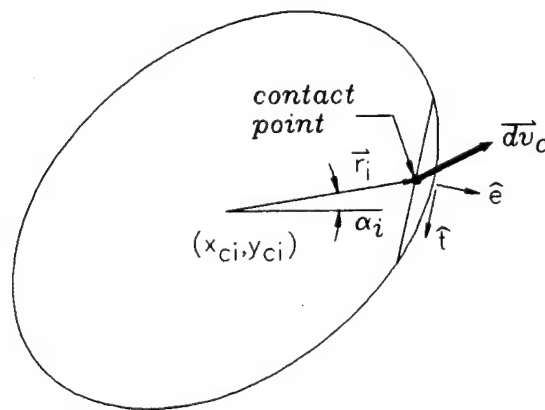
Figure 6. Sign convention for vectors at a contact.

For particle I, the magnitude of the moment arm r_{ci} from the centroid to the contact is:

11

$$r_{ci} = \sqrt{(x_c - x_{ci})^2 + (y_c - y_{ci})^2} \tag{13}$$

in local *or* global coordinates, while the radius vector in the direction of the contact is:

$$\vec{r}_i = (x_c - x_{ci})\hat{i} + (y_c - y_{ci})\hat{j} = r_{ci}\cos\alpha_i\hat{i} + r_{ci}\sin\alpha_i\hat{i} \tag{14}$$

The relative velocity of the contact point on I relative to j is simply:

$$\vec{dv}_c = \vec{v}_{ci} - \vec{v}_{cj} \tag{15}$$

where the velocity of the contact on particle I is:

$$\begin{aligned} \vec{v}_{ci} &= (v_{xi}\hat{i} + v_{yi}\hat{j}) + \dot{\theta}_i\hat{k} \times \vec{r}_i \\ &= (v_{xi} - \dot{\theta}_i r_{ci}\sin\alpha_i)\hat{i} + (v_{yi} + \dot{\theta}_i r_{ci}\cos\alpha_i)\hat{j} \end{aligned} \tag{16}$$

Then, the relative velocity of the contact between I and j is:

$$\begin{aligned} \vec{dv}_c &= dvc_x\hat{i} + dvc_y\hat{j} \\ &= [(v_{xi} - \dot{\theta}_i r_{ci}\sin\alpha_i) - (v_{xj} - \dot{\theta}_j r_{cj}\sin\alpha_j)]\hat{i} + \\ &\quad [(v_{yi} + \dot{\theta}_i r_{ci}\cos\alpha_i) - (v_{yj} + \dot{\theta}_j r_{cj}\cos\alpha_j)]\hat{j} \end{aligned} \tag{17}$$

This relative velocity is then resolved parallel and perpendicular to the contact normal to yield the incremental normal and tangential contact velocities:

$$\begin{aligned} \vec{dv}_{cn} &= dv_n\hat{e} = \hat{e}(\vec{dv}_c \cdot \hat{e}) = (dvc_x e_1 + dvc_y e_2)\hat{e} \\ \vec{dv}_{cs} &= dv_s\hat{t} = \hat{t}(\vec{dv}_c \cdot \hat{t}) = (dvc_x e_2 - dvc_y e_1)\hat{t} \end{aligned} \tag{18}$$

Note that the relative contact velocity from j to I has identical magnitudes dv_n and dv_s as equation (18), but the outward normal and tangential vectors differ.

The incremental contact forces during a given time step may then be computed based on the contact spring stiffness k_n and k_s, contact dashpot values c_n and c_s and time step of integration Δt:

$$\begin{aligned} \Delta F_n &= k_n dv_n \Delta t + c_n dv_n \\ \Delta F_s &= k_s dv_s \Delta t + c_s dv_s \end{aligned} \tag{19}$$

The total contact force may be computed at time t using the known total contact force at time $t-\Delta t$ using:

$$\begin{aligned} F_{n_t} &= F_{n_{t-\Delta t}} + \Delta F_n \\ F_{s_t} &= F_{s_{t-\Delta t}} + \Delta F_s \end{aligned} \tag{20}$$

To represent nonlinear contact behavior, tangent stiffnesses which are history-dependent could be used for the normal and shear spring values. The maximum tangential shear force at the contact is usually limited by a function which is dependent upon the normal contact force.

It turns out that summing incremental contact forces at each time step can lead to significant accumulated error. This was noted by Ting *et al* (1989) in their work with disk-shaped particles. Instead, they computed total normal overlap at each instant, then used this total overlap to obtain the total contact normal force. Tangential forces were still obtained using incremental forces, as in Cundall and Strack's original algorithm. For ellipse-

ellipse intersection using the modified intersection routine described above, it is possible to estimate the total normal overlap as the distance between points A' and B' in Figure 5. These points are merely the intersection of $g(x,y) = 0$ with $h(x,y) = 0$ and $f(x,y) = 0$ with $h(x,y) = 0$, respectively.

This procedure is carried out for all contacts between all particles. Then the contact forces are summed for all contacts k for each particle I to yield net particle accelerations at time t:

$$
\begin{aligned}
m_i \ddot{x}_i &= \sum F_{xi} = \sum (-F_n e_1 - F_s e_2) \\
m_i \ddot{y}_i &= \sum F_{yi} = \sum (-F_n e_2 + F_s e_1) \\
I_i \ddot{\theta}_i &= \sum M_{oi} = \sum \vec{r}_i \times (\vec{F}_n + \vec{F}_s) \\
&= \sum [(x_c - x_{ci})(-e_1 F_{ni} - e_2 F_{si}) + (y_c - y_{ci})(-e_2 F
\end{aligned}
\tag{21}
$$

where m_i and I_i are the mass and polar moment of inertia for particle I, respectively. Body forces such as gravitational effects may be added in the force sum for F_y in equation (21).

Using the leapfrog integration scheme proposed by Cundall and Strack [2], velocities of each particle I are computed at the next half time step $t+\frac{1}{2}\Delta t$:

$$
\begin{aligned}
\dot{x}_{t+\frac{1}{2}\Delta t} &= \dot{x}_{t-\frac{1}{2}\Delta t} + \ddot{x}_t \Delta t \\
\dot{y}_{t+\frac{1}{2}\Delta t} &= \dot{y}_{t-\frac{1}{2}\Delta t} + \ddot{y}_t \Delta t \\
\dot{\theta}_{t+\frac{1}{2}\Delta t} &= \dot{\theta}_{t-\frac{1}{2}\Delta t} + \ddot{\theta}_t \Delta t
\end{aligned}
$$

The displacements and rotation of each particle I are then obtained by:

$$
\begin{aligned}
x_{t+\Delta t} &= x_{t-\Delta t} + \dot{x}_{t+\frac{1}{2}\Delta t} \Delta t \\
y_{t+\Delta t} &= y_{t-\Delta t} + \dot{y}_{t+\frac{1}{2}\Delta t} \Delta t \\
\theta_{t+\Delta t} &= \theta_{t-\Delta t} + \dot{\theta}_{t+\frac{1}{2}\Delta t} \Delta t
\end{aligned}
$$

Overall, this explicit integration scheme is second-order accurate, and is generally regarded as the best overall for accuracy, stability and efficiency for many-body simulation (Hockney and Eastwood 1981). Global viscous or acceleration-proportional damping may also be incorporated using the techniques outlined by Cundall and Strack (1979) and Zhang and Cundall (1986).

4.1.3 Ellipse-line Intersection and contact velocities

The calculation of ellipse-line intersection is required when computing the interaction between an ellipse particle and a wall. To compute the intersection points, first transform the equation of the line into the local coordinates of the ellipse. Then, one may solve a quadratic equation based on the intersection of an ellipse I and wall j in local coordinates.

Figure 7 shows the detailed nomenclature for an ellipse I and wall j intersection. For a wall j with endpoints in local coordinates of ellipse I equal to (x_1, y_1) and (x_2, y_2), the equation of the wall in the homogeneous local coordinates of ellipse I is:

$$Y = m_l X + b_l \ , \ m_l = \left(\frac{a}{b}\right) \left(\frac{y_2 - y_1}{x_2 - x_1}\right) \ , \ b_l = \frac{y_1}{b} - m_l \left(\frac{x_1}{a}\right) \tag{24}$$

while the equation of the ellipse is the same as in equation (7). Eliminating Y from equations (7) and (24) results in the following quadratic:

$$(m_l^2 + 1) X^2 + 2 m_l b_l X + (b_l^2 - 1) = 0 \tag{25}$$

The roots of this quadratic are substituted back into the local ellipse equation (7) to obtain the full coordinate pairs. For a pair of intersection points, the contact location may be taken to be the average location, which is the midpoint on the wall between the intersections. This contact location is then transformed back into world coordinates (x_c, y_c) using equations (7) and (2).

Once the intersection location is determined, the incremental contact velocities need to be calculated. The wall is specified by a center of rotation (x_{cj}, y_{cj}) and endpoints (x_1, y_1) and (x_2, y_2). In addition, the wall possesses a "sense" which is considered positive when the solid side of the wall is found clockwise with respect to the tangential vector $\hat{w}$. Derived quantities include the angle of orientation α_j with respect the horizontal, and the *inward* normal vector $\hat{e}$ and tangential vector $\hat{w}$ from endpoint 1 to endpoint 2. The distance from the wall center of rotation to the contact is r_w.
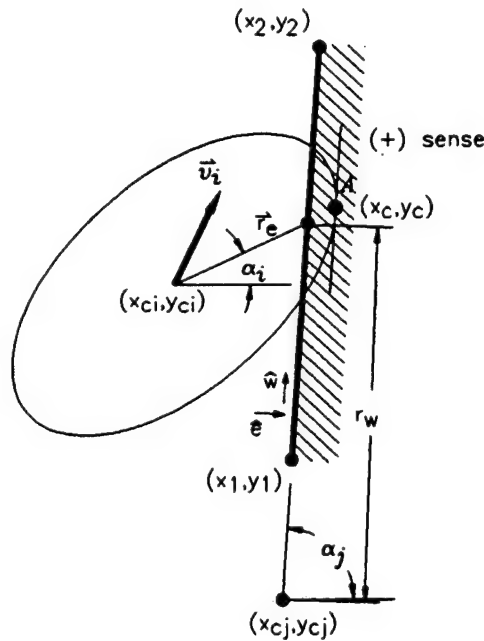
Figure 7. Nomenclature for ellipse-wall intersection.

The wall vectors are simply:

$$\begin{aligned} \hat{w} &= w_1 \hat{i} + w_2 \hat{j} \\ \hat{e} &= e_1 \hat{i} + e_2 \hat{j} = sense \cdot (w_2 \hat{i} - w_1 \hat{j}) \end{aligned} \tag{26}$$

14

The velocity of the contact on ellipse I is the same as equation (16), while the velocity of the contact on the wall is:

$$\vec{v}_{cj} = (v_{xj}\hat{i} + v_{yj}\hat{j}) + \theta_j\hat{k} \times r_w\hat{w}$$
$$= [v_{xj} - \theta_j(y_c - y_{cj})]\hat{i} + [v_{yj} + \theta_j(x_c - x_{cj})]\hat{j} \tag{27}$$

where v_{xj} and v_{yj} are the components of the velocity vector of the center of rotation of the wall.

The relative velocity of the contact from ellipse I to wall j is then:

$$\vec{dv}_c = dvc_x\hat{i} + dvc_y\hat{j}$$
$$= [(v_{xi} - v_{xj}) - \theta_i(y_c - y_{ci}) + \theta_j(y_c - y_{cj})]\hat{i} + \tag{28}$$
$$[(v_{yi} - v_{yj}) + \theta_i(x_c - x_{ci}) - \theta_j(x_c - x_{cj})]\hat{j}$$

This relative velocity is then resolved parallel and perpendicular to the wall in the same manner as before, with the same results as equation (18).

Resolving the normal and tangential contact forces into their x and y components leaves the following contributions to the force and moment sums for wall j:

$$F_x = +F_n e_1 + F_s e_2$$
$$F_y = +F_n e_2 - F_s e_1 \tag{29}$$
$$M_o = F_n[(x_c - x_o)e_2 - (y_c - y_o)e_1]$$

where the moment is taken about an arbitrary point (x_o, y_o). These are summed for all particles adjacent to the wall to obtain the total wall forces and moment.

Use of the incremental equations (18) for wall-ellipse contact in computing the total contact forces can also lead to significant accumulated error, as with ellipse-ellipse contact. Alternatively, the total overlap may be approximated as the normal distance between the wall and the point on the ellipse with slope parallel to the wall (point A in Figure 7). Using equation (24) as the equation of the wall in local homogeneous coordinates of ellipse I (for m_I not $\rightarrow \infty$), the point on the ellipse of common slope may be obtained from:

$$\frac{dy}{dx} = -\frac{f_x}{f_y} = -\frac{2X}{2Y} = -\frac{X}{Y} = m \tag{30}$$

Substituting (30) into the equation of the ellipse (7) and eliminating X leads to:

$$Y = \pm\frac{1}{\sqrt{1 + m^2}} \quad ; \quad X = -mY \tag{31}$$

After converting X, Y to world coordinates, the total normal overlap Δn may be computed by:

$$\Delta n = \hat{e} \bullet \vec{r}_w \tag{32}$$

where $\hat{e}$ and r_w are defined in Figure 8. This total normal overlap is then used directly in computing total normal contact force.

4.2 Derivation of Associated Properties

4.2.1 Contact properties

The typical spring, dashpot and slider arrangement at each contact for most implementations of the DEM is shown in Figure 3. In the current formulation, this has been modified somewhat in that it is presumed that *each* particle possesses a set of springs and dashpots at each contact, which combine in a series or average manner. At present, normal and tangential springs and viscous dashpots are considered to act in series, while the slider for limiting the maximum shear strength uses an average set of strength parameters. This allows simulation of variable particle-particle and particle-wall properties.

The spring stiffnesses recommended for use can be inferred from Hertzian contact theory for elastic spheres or cylinders in contact (Cundall 1988, Ting *et al* 1989). Alternatively, one may use empirical modifications to the Hertz values to account for local yield (Chang *et al.* 1989). The spring stiffnesses recommended for use can be inferred from Hertzian contact theory for elastic spheres or cylinders in contact. For two cylindrical disks in contact with partial slip, Chang, Misra and Xue (1989) quote the following nonlinear relationship for normal spring stiffness k_n:

$$k_n = \frac{2\pi G}{(1-v) \ [2 \ ln(2r/A) - 1]}$$ (33)

where

$$\frac{1}{r} = \frac{1}{2} \left(\frac{1}{r_1} + \frac{1}{r_2} \right) \ ; \ A = \left[\frac{2r(1-v)F_n}{\pi G} \right]^{1/2}$$ (34)

G, v are the shear modulus and Poisson's ratio, respectively, of the *individual* particles. r is a combined radius formed from the individual radii r_1 and r_2 and F is the normal contact force. In the current computer implementation, only constant spring stiffnesses are used.

The normal dashpots at each contact may be used to represent the energy absorption capability of the particle. In particular, the dashpot value may be directly related to the coefficient of restitution e for the individual particle (Corkum and Ting 1986).. The combined dashpot value c_n based on collision of two particles with masses m_1 and m_2, with combined normal spring k_n is:

$$c_n = \frac{-2\ln e \sqrt{k_n m^*}}{\sqrt{(\ln e)^2 + (\pi)^2}} \ , \ \ where \ m^* = \frac{m_1 m_2}{m_1 + m_2}$$ (35)

The maximum shear strength at the contact is related to the current normal spring force using a Coulomb-type friction, as indicated in Figure 3. Tensile strength normal to the contact is currently set to zero, although efforts have recently been made to allow for tensile strength in an effort to model ice interaction.

4.2.2 Stress Tensor

Average macroscopic stresses within the particle assembly may be estimated using the external wall forces or contact forces within a subregion of the system. Using only the boundary contact forces, the average stress tensor in a volume V may be computed as follows (Cundall and Strack 1979):

16

$$\sigma_{ij} = \frac{1}{V} \sum_{c \in S} x_i^c T_j^c \tag{36}$$

where I, j are direction indices, the summation occurs for all contacts c on the boundary S, x_i is the location coordinate and T_j is the boundary traction at contact c. Alternatively, the average internal stress tensor σ_{ij} may be computed using *all* the contact forces within the specified region V (Bathurst and Rothenburg 1988):

$$\sigma_{ij} = \frac{1}{V} \sum_{c \in V} f_i^c l_j^c \tag{37}$$

where the summation occurs for all contacts c within the region V, f^c is the contact force vector, and l^c is the contact vector (centroid-contact) for contact c. Note that for circular particles, equation (37) degenerates to equation (36) as all contributions to the summation from interior contacts cancel out and only contributions from the surface S remain. This is not true for noncircular particles, however.

4.2.3 Strain Tensor

Several methods have been used for computing an average strain tensor from a deformed assemblage of granular materials. These methods usually rely on analyzing the deformation of an external membrane, rather than internal displacements of the particles. Alternatively, one may approximate the deformation pattern within a region with a constant strain finite element (Ting and Corkum 1992). A linear displacement field may be specified by:

$$\begin{aligned}
u &= \alpha_1 + \alpha_2 x_i + \alpha_3 y_i \\
v &= \beta_1 + \beta_2 x_i + \beta_3 y_i
\end{aligned} \tag{38}$$

where u, v are the displacements in the x and y directions, respectively, and $\alpha_1, \alpha_2, \alpha_3, \beta_1, \beta_2$ and β_3 are constants to be determined. The "best" strain field may be computed from particulate data by using the best least-squares fit of the particulate displacement data. The sum of the squares of the error for each particle is:

$$\begin{aligned}
S_x &= \sum_{i=1}^{N} [u(x_i, y_i) - u_i]^2 = \sum_{i=1}^{N} [\alpha_1 + \alpha_2 x_i + \alpha_3 y_i - u_i]^2 \\
S_y &= \sum_{i=1}^{N} [v(x_i, y_i) - v_i]^2 = \sum_{i=1}^{N} [\beta_1 + \beta_2 x_i + \beta_3 y_i - v_i]^2
\end{aligned} \tag{39}$$

where (x_i, y_i) are the initial coordinates of particle I, u_i and v_i are the x and y displacements for the ith particle, respectively, and the summation is over all N particles in the region of interest. Then, taking partial derivatives of equation (39) with respect to each unknown and equating to zero, the following two systems of 3x3 equations result:

$$\begin{bmatrix} N & \sum x_i & \sum y_i \\ \sum x_i & \sum x_i^2 & \sum x_i y_i \\ \sum y_i & \sum x_i y_i & \sum y_i^2 \end{bmatrix} \begin{bmatrix} \alpha_1 & \beta_1 \\ \alpha_2 & \beta_2 \\ \alpha_3 & \beta_3 \end{bmatrix} = \begin{bmatrix} \sum u_i & \sum v_i \\ \sum u_i x_i & \sum v_i x_i \\ \sum u_i y_i & \sum v_i y_i \end{bmatrix} \tag{40}$$

Solution of equation (40) for the variables $\alpha_1 \dots \beta_3$ results in the following for the average strain tensor ϵ_{ij}:

17

$$\epsilon_{ij} = \begin{bmatrix} \alpha_2 & \dfrac{(\alpha_3 + \beta_2)}{2} \\ \dfrac{(\alpha_3 + \beta_2)}{2} & \beta_3 \end{bmatrix} \tag{41}$$

4.3 Implementation of Ellipse-based DEM

The ellipse-based Discrete Element Method algorithm described above has been implemented as part of a menu-driven interactive simulation program using ANSI-standard C as the programming language. Many of the advanced concepts from Cundall and Strack's (1979) *BALL* program are implemented. Single-linked lists were used extensively for keeping track of particles in contact and particles in close proximity to one another. "Grid boxes" or "microcells" are used to assist in tracking neighbors.

At every instant in time, contact intersection is computed between every particle I and the items in that particle's "contact list", that is, those balls or walls which are in contact and nearly in contact. A search for new contacts is initiated any time particle I displaces past a specified threshold value. This search consists of checking for contact between the current particle and the current contact list, as well as the particles residing in the grid box(es) in which particle I resides. This contact check consists of successively testing for overlap of the rectangular boxes circumscribing each ellipse, then overlap of the circles circumscribing each ellipse, then finally overlap between two ellipses. The ellipse-ellipse overlap computation is performed only after testing positive on the simple contact checks. Note that use of the contact and grid box lists reduces the order of the problem from an "*n-squared*" problem, where the number of computations is proportional to the number of particles n squared.

As an example, Figure 8 plots a typical system of particles together with its grid box scheme. Particle 4 (shown in dots) resides in grid boxes 6 and 7 and is drawn together with a bounding ellipse approximately *dn* larger. The box list for box 6 contains ellipses 1, 4, 5, 6 and 7, while box 7 contains 2, 3, 4 and 7. While particle 4 is actually in contact with balls 1, 2, 5 and 6, ball 7 also exists in the contact list for particle 4 since it lies within *dn* of ball 4, even though these particles are actually not in contact. At every time step, the contact between ball 4 and balls 1, 2, 5, 6 as well as 7 are recomputed and updated. When any part of particle 4 moves by a "significant" fraction of *dn*, then a contact check is initiated for all the particles (and walls) lying in grid boxes 6 and 7, *ie* particles 1, 2, 3, 5, 6 and 7. Note that wall identification numbers can also be included in the grid box list, and are stored as negatives to distinguish them from particles, which are stored positive.
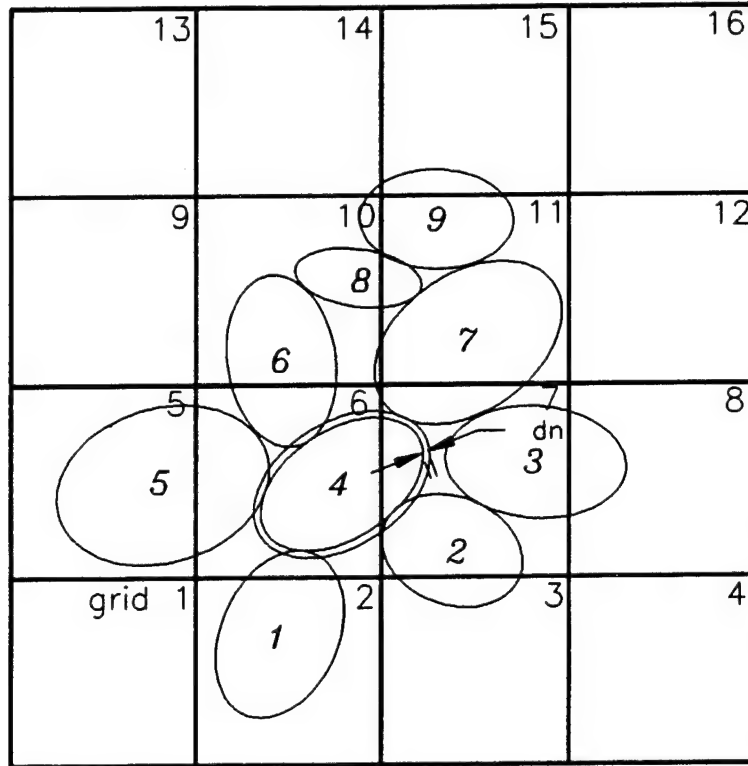
Figure 8. Contact list and grid box list schemes.

Dynamic memory allocation and deallocation occur at runtime as contacts are made and broken. A variety of boundaries are supported, including rigid stress- and force-controlled walls and linked displacement-controlled balls. Periodic boundaries are being implemented. The simulation program is text-based, with no system-specific graphics, and has been ported to numerous different computers such as IBM-compatible personal computers, UNIX workstations and minisupercomputers.

4.4 Code Validation

The model was initially validated using several simple particulate systems to ensure compliance with physical laws based on static and dynamic equilibrium conditions (Ting and Corkum 1991). These simple test simulations included particle-to-particle and particle-to-wall collisions as well as systems of stacked particles. The computed forces and energy relationships for the simple test simulations compared well to analytical solutions.

As an example, Figure 9 plots a simple close-packed array of 5 frictionless disks each with radius 1 m and specific gravity 2.67. The numbers shown on the left half of the Figure are theoretical normal contact forces in kN, while the italicized numbers on the right half are computed values from the DEM simulation. The normal damping was taken as the value which would result in a coefficient of restitution of 0.5, with disk-disk and disk-wall normal spring stiffnesses 105 kN/m^2 and 106 kN/m^2, respectively. Timestep of integration was 0.00025 sec. The simulation was allowed to run for 2 sec (8000 timesteps), and dynamic forces were observed to dissipate after about 1 sec.
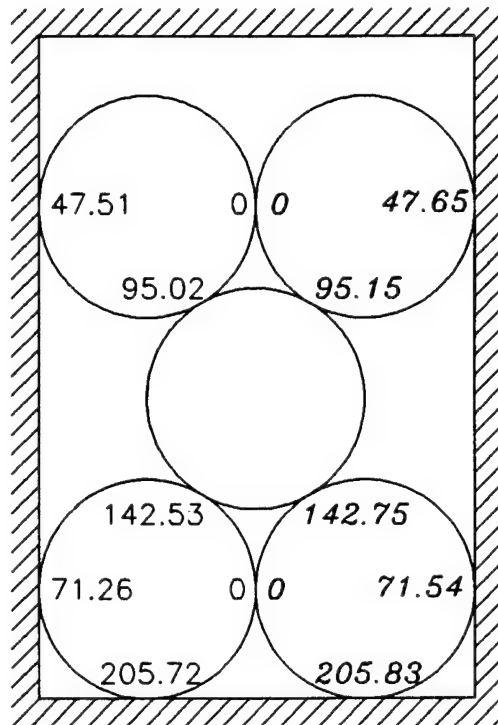
Figure 9.. Comparison of theoretical and computed (italicized) normal contact forces for a symmetric frictionless, close-packed five disk system subjected to gravity loading. Values in kN.

4.5 Interface Programs

Also implemented are separate graphical preprocessing and postprocessing modules incorporating a CAD-style interface. The graphical interface programs allow the setup of granular systems for simulation and allow the viewing of output files written by the simulation. These personal computer-based programs plot force chains, time sequences, animations, contact statistics and distributions, and also compute the average stress and strain according to the algorithms described above. These are described in greater detail in Ting and Corkum (1992).

It was decided to maintain separate programs for the simulation and the interface. This allows the flexibility of porting the main compute-intensive portion, the simulation, to the fastest computer available to the user. The interface programs are all based on the personal computer-based CAD drawing and interface package FEINT developed by Corkum (1990). This paradigm of separating the graphical user interface (GUI) from the main solver has some very real advantages not only in its current application with the DEM, but also with any existing program written in any computer language. A GUI program based on the FEINT package may be tailored to write a data file for the specific solver program. Similarly, a tailored post-processor GUI program accepts the output file from the solver program for graphical interpretation of the results. This removes the need for rewriting existing batch-style programs while making available the easy-to-use graphical environment and mouse support currently employed in modern computer programs. At present, the FEINT graphical interface package is written in ANSI-standard C using BorlandC++ and also Watcom C++. The FEINT package consists of drawing functions such as expected of a two-dimensional CAD package, such as zoom, clip, copy, etc. All drawing entities are stored through calls to the FEINT library in a drawing database maintained using a double-linked list. This package can support most of the popular IBM PC-based graphical adapters, with automatic hardware detection available at runtime.

One shortcoming of most C-language packages is the lack of a plotting capability for a general ellipse oriented at any angle to the horizontal. Since each ellipse particle is stored in the drawing database using the center coordinates and angle of rotation, and since the FEINT drawing package allows zooming into parts of the drawing database, it was necessary to implement a pixel-based plotting routine for general ellipses. This was done by modifying Bresenham's circle algorithm, where decisions on plotting are made on a pixel-by-pixel basis (Foley and Van Dam 1982).

The front-end generation program FEGEN allows the user to specify a set of particle properties such as shape, size, contact stiffnesses, dampings and strengths, as well as a gradation in terms of the relative fraction of each property type. FEGEN provides assistance with choosing the contact properties based on the desired elastic modulus, Poisson's ratio and coefficient of restitution of each particle type. Orientations of the particles may be specified at any angle with respect to the horizontal, and may be uniform or normally distributed with a specified standard deviation about the required orientation. After the region bounds and the desired area ratio are specified, the particles are generated randomly according to the gradation and orientation information. The particles are plotted as they are being generated. Particles may be added or deleted graphically using the drawing editor. An ASCII data file is written which may be used as a starting input file to the simulation program PARSE.

As with PARSE, both FEGEN and FEPARSE were written and debugged with BorlandC++ under MicroSoft Windows. The two interface modules together total over 10,000 lines of C. Because the interface routines link with FEINT which makes calls to BorlandC-specific graphics routines, a separate translation library was made for Watcom C++. When the interface programs are compiled with the WatcomC++ package, the resulting interface routines are no longer confined to the artifical lower 640 KB of memory limitation.

5. VALIDATION

Proper validation of any numerical method should include comparison of numerical results with analytical and physical results. For particulate systems, few, if any, analytical solutions are available where the system is properly treated as a particulate system. Continuum-based analyses are possible based on linear elasticity and elasto-plasticity, for example, but these would not offer proper validation of the DEM method and code (although such comparisons would nevertheless be useful in their own right). Exceptions include the 5-disk systems subject to static equilibrium under gravity loading (Ting and Corkum 1991), or multiple rock blocks on an inclined plane (Grabinsky 1989). In this latter case, a polygonal two-dimensional DEM code (*ADEM*) was used successfully to determine the mode of failure of a collection of rock blocks, with the analytical solution of the onset of failure from Goodman and Bray (1976). Since analytical solutions for particulate are rare, the importance of proper code validation with physical test results is particularly important.

For the current study, two datasets were used for comparison - the two dimensional photoelastic rod data of Konishi, Oda and Nemat-Nasser (1983), and the circular rod data of Chapuis (1976). Konishi *et al* sheared assemblies of approximately 700 photoelastic rods of varying particle angularity (aspect ratio) in order to study the effects of particle shape on mechanical behavior. The detailed physical test setup and numerical simulations and comparisons are described later in this section. In addition, a variety of particle-particle contact relations were investigated. These ranged from contact springs-dashpot combinations as shown in Figure 3 where the springs are linear (constant stiffness) to linear hysteretic springs (with no dashpot). In addition, the nonlinear contact model proposed by Chang and Misra (1990) was investigated. However, the range of contact forces in the current simulations were found to be in a nearly linearly range, and hence this nonlinear contact relation was not explicitly implemented in the *PARSE* simulation code.

The next few sections describe the linear hysteretic and nonlinear contact laws which were investigated.

5.1 The Hysteretic Force-Deflection Algorithm

Figure 10 shows a linear force-deflection algorithm that includes position dependent hysteresis (Walton and Braun 1986).
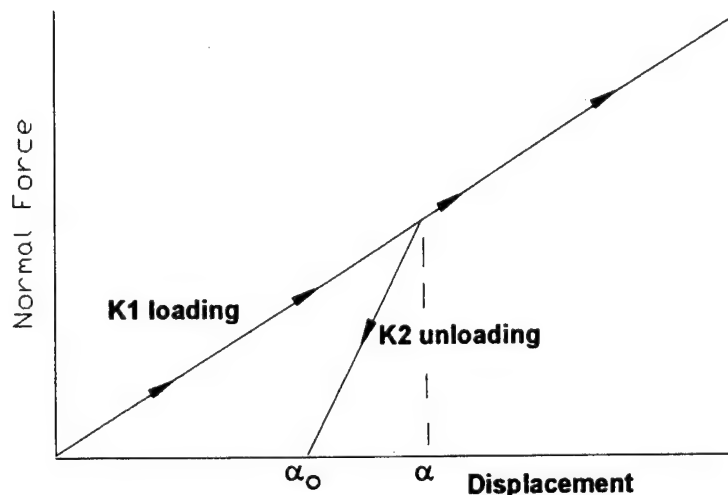
Figure 10. Linear hysteretic force-deflection relationship (Walton and Braun, 1986)

22

The normal force, F_n, is calculated as,

$$F_n = K_1 \alpha, \, loading \tag{42}$$

$$F_n = K_2(\alpha - \alpha_0), \, unloading \tag{43}$$

Walton, Brandeis and Cooper (1984) performed numerical experiments using an elastic-perfectly-plastic two dimensional finite element model, NIKE2D. The experiments consisted of moving a hemisphere into a rigid wall, withdrawing the hemisphere, and then moving the hemisphere into the wall again. Walton and Braun (1986) modeled the resulting force-deflection behavior using a linear loading curve of slope K_1, and a linear unloading curve of steeper slope K_2. Upon reloading, the normal force and deformation will increase linearly with slope K_2 until the original loading curve is reached, at which point, continued loading will follow the original loading curve with slope K_1. In this model, the area between the loading and unloading curves, represents the energy lost to plastic deformation. The loading and unloading slopes, K_1 and K_2, were related based on the coefficient of restitution, e, as follows.

$$e = \sqrt{K_1/K_2} \tag{44}$$

The programs FEGEN and PARSE were altered to allow for hysteretic contacts. The hysteretic version of FEGEN recommends values for K_1, loading stiffness, based on the relationships previously discussed. For given values of K_1 and coefficient of restitution, e, K_2 is calculated and stored.

5.2 Nonlinear Force-Deflection Relationship

The nonlinear force deflection relationship of Chang, Misra and Xue (1989) was also investigated. This relationship is a modification of Hertzian contact theory for cylindrical disks in contact which allows for contact slip. The normal stiffness k_n is:

$$k_n = \frac{2\pi G}{(1-\nu)[2\ln(\frac{2r}{A})-1]} \tag{45}$$

where

$$\frac{1}{r} = \frac{1}{2}(\frac{1}{r_1} + \frac{1}{r_2}) \tag{46}$$

$$A = [\frac{2r(1-\nu)f_n}{\pi G}]^{\frac{1}{2}} \tag{47}$$

In the preceding equations, G is the shear modulus of a particle, ν is Poisson's ratio of a particle, r is the average radius of the two particles of radii r_1 and r_2, A is the half-width of the contact, and f_n is the normal contact force. For two ellipses in contact (instead of disks), modifications were made to these equations. The average radius r used in the solution for ellipses in contact was obtained by first averaging the major and minor axes of each ellipse, and then taking the average for the two ellipses.

In this nonlinear contact model, the normal force increases nonlinearly as the deformation at the contact increases. Similarly, the normal contact stiffness varies, and is defined as the instantaneous slope for any two values of normal force, f_n, and deformation, delta, as illustrated in Figure 11.

23
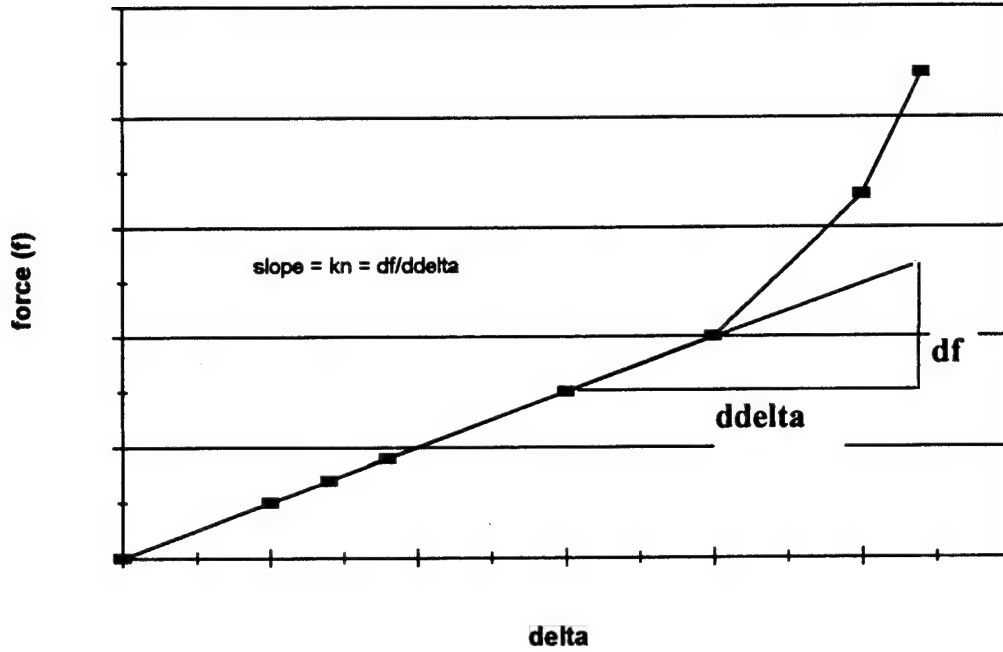
Figure 11. Nonlinear force-deflection relationship (Chang *et al* 1989).

In the DEM algorithm, overlap and contact deformation information is available at each timestep. Therefore, to implement the nonlinear force-deformation contact law, it is necessary to solve Chang's equations to arrive at the appropriate stiffness and normal force values for a given particle deformation. As illustrated in Figure 11, the normal spring stiffness, k_n, is related to the normal force and the deformation as follows, stiffness = instantaneous slope =

$$k_n = \frac{dF_n}{d\Delta} \tag{48}$$

which yields the following:

$$\int d\Delta = \int \frac{1}{k_n} dF_n \tag{49}$$

Substituting the value for normal contact stiffness,

$$\Delta = \int \frac{(1-v)[2\ln(\frac{2r}{A})-1]}{2\pi G} dF_n \tag{50}$$

and from the relationship between half-width, A, and normal force, F_n,

$$dF_n = \frac{2A\pi G}{2r(1-v)} dA = \frac{A\pi G}{r(1-v)} dA \tag{51}$$

Substituting this equation in the preceding equation yields:

24

$$\Delta = \int \frac{(1-v)[2\ln(\frac{2r}{A})-1]}{2\pi G}(\frac{A\pi G}{r(1-v)})dA \tag{52}$$

which simplifies to:

$$\Delta = (\frac{\ln 2r}{r} - \frac{1}{2r})\int A dA - \frac{1}{r}\int A\ln A dA \tag{53}$$

Integrating this equation yields:

$$\Delta = (\frac{\ln 2r}{r} - \frac{1}{2r})\frac{1}{2}A^2 - \frac{1}{2r}[A^2(\ln A) - \frac{1}{2}A^2] \tag{54}$$

Using equation (54) to calculate the half-width, A, and the deformation, Δ, for input values of normal force, Fn, with appropriate values of Young's modulus and Poisson's ratio for rubber results in the nonlinear contact relation plotted in Figure 12 below.
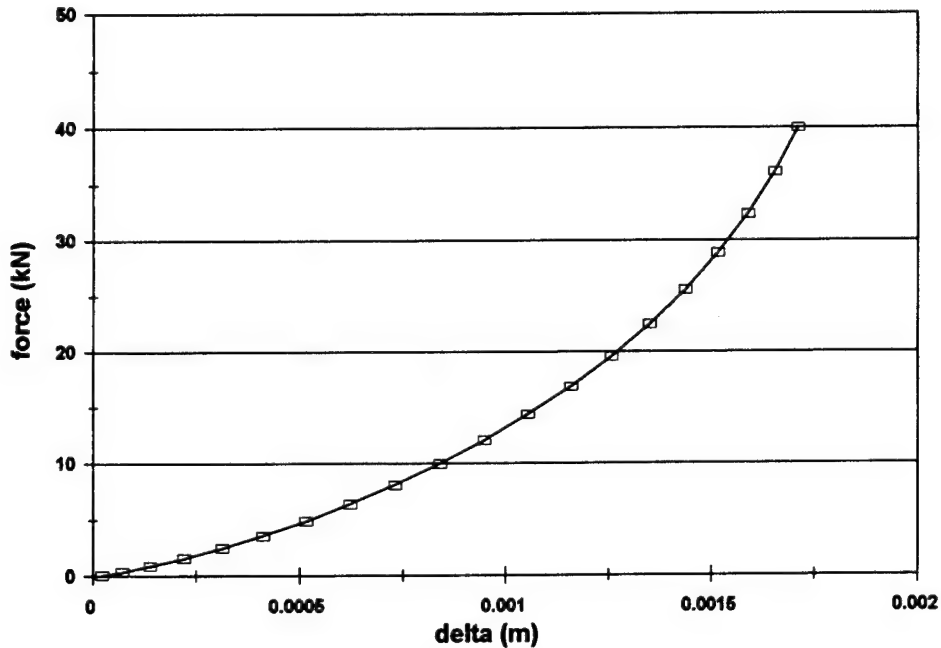
Figure 12. Nonlinear force-deflection relationship from Chang *et al* (1989).

To implement the nonlinear force-deflection relationship, it was necessary to obtain a simple equation that would relate the particle overlap at a contact to the normal force. A least squares curve fit of the data generated in Figure 12 was carried out using a power function. This resulted in the following equation for normal force as a function of normal contact overlap delta:

$$F_n = a_1\Delta + a_2\Delta^2 + a_3\Delta^3 \tag{55}$$

where:

$a_1 = 4786.786;$ $a_2 = 12330798;$ $a_3 = -6.8e9$

25

Since the overlap at contacts in the DEM simulations is small compared to the radii of the particles, a linear regression analysis of the portion of the curve below a normalized deformation of 0.02 was deemed appropriate. The purpose of this analysis was to determine how close the data was to being linear in this region of interest. The result of the linear regression analysis are plotted together with the modified Chang force deflection relation in Figure 13. The linear regression analysis of these values yielded a slope, k_n, of 5783 kN/m, and an R^2 value of 0.985. In this small contact deformation range, the normal force-deflection relation is nearly linear.
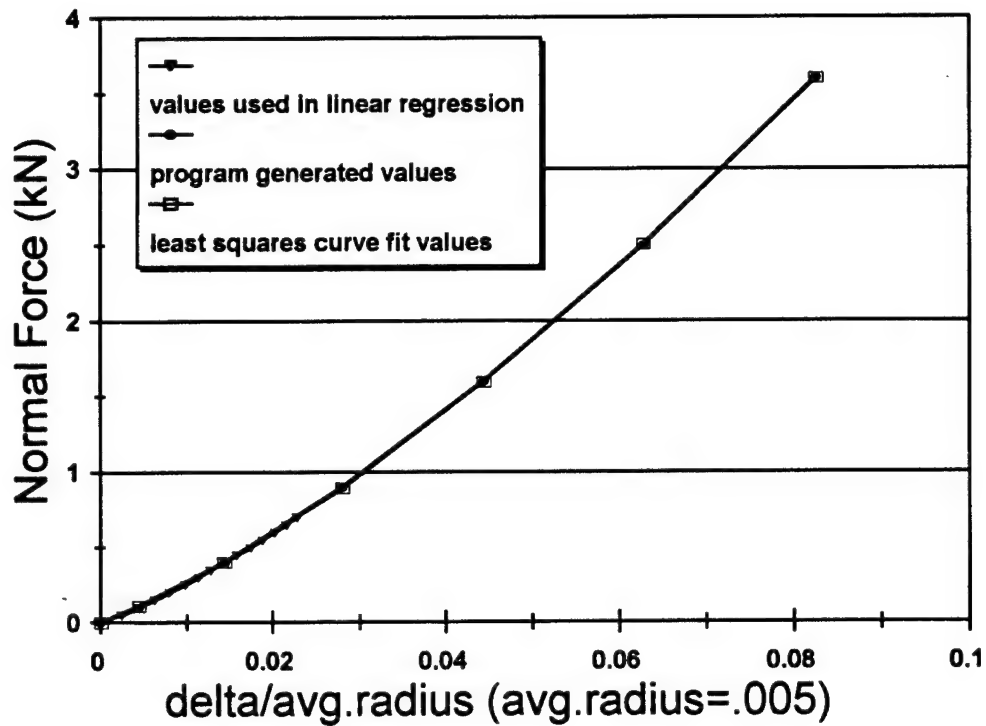
Figure 13. Best least squares linear force contact relation compared with modified Chang relation.

5.3 Chapuis (1976) Test Data

Chapuis (1976) performed biaxial compression tests on assemblies of 400 to 600 rubber cylinders, each 10 mm in length. The cylinders were of four different sizes, with diameters of 19.05 mm, 22.38 mm, 25.65 mm, and 38.76 mm, with gradation proportions of 4:3:2:1 respectively. The two largest cylinders were nearly circular in cross section, while the smaller diameter particles were reported to be between 2 to 5 percent out of round. The resulting aspect ratio of the smaller particles was approximately 1.03.

Chapuis performed several tests, including a simple shear test of a dense assembly, biaxial tests on both a dense and a loose assembly, and a biaxial unloading test. As part of DEM model validation, only the dense and loose biaxial tests and the unloading test were attempted. These results were reported in detail in Rowell (1994), and are summarized in this Report.

From the reported data, the initial isotropic confining stress prior to shear was approximately 3.6 lb/in cm, or 63 kN/m². The biaxial compression testing apparatus used to shear the assemblies is shown in Figure 14. The size of the apparatus in Figure 14 was measured to arrive at the initial height to width ratio of the sample. This information was then combined with gradation and void ratio information to arrive at an approximate total sample area of 0.3267 m² and an initial sample size of 0.484 m width by 0.675 m height.

The front-end graphical interface program, FEGEN, was used to create dense and loose samples with the same gradation and number of particles as the Chapuis tests. Figure 15 represents one sample that was compressed to form a dense assembly of particles.

Table 2 contains the particle size information, gradation information, and model input parameters for the first attempt to simulate the Chapuis tests. One of the difficulties encountered in modeling these tests was that the type and properties of the material being tested were not reported. (It has since been determined by direct communication that the rods were made from hard rubber). Since the confining stress applied for these tests was several orders of magnitude greater than that applied for the Konishi *et al* tests, this suggested that a much stiffer material was used in the Chapuis tests. The stiffness values used in Table 2 resulted in large particle overlapping and an overall material response that was much too soft. Subsequent simulations included (higher) stiffness values which would more accurately model the physical test results. For example, the interface program FEGEN recommended a value of k_n= 70,000,000 kN/m for disks made from granite. Simulations using higher normal contact produced excellent agreement with the physical results. The stiffness value used in these successful simulations was k_n= 2,400,000 kN/m. Also, the physical interparticle sliding friction reported for the ovals was 16°, not the 10° used in the simulation. According to Chapuis, the reported 10° friction angle includes particle rolling, while the reported 16° friction angle was for pure sliding.

Figure 16 presents the results from attempts to model the Chapuis tests. Two different samples were created and tested. Both samples were tested with the same model parameters. These simulations were conducted with k_n= 2,400,000 kN/m. The maximum friction angle obtained during the physical testing of the dense sample was 25°. The DEM simulations yielded a maximum friction angle of 24 , which is in excellent agreement. The volume change behavior of the DEM simulated test also compared favorably with the Chapuis tests. This data is presented in Figure 17.
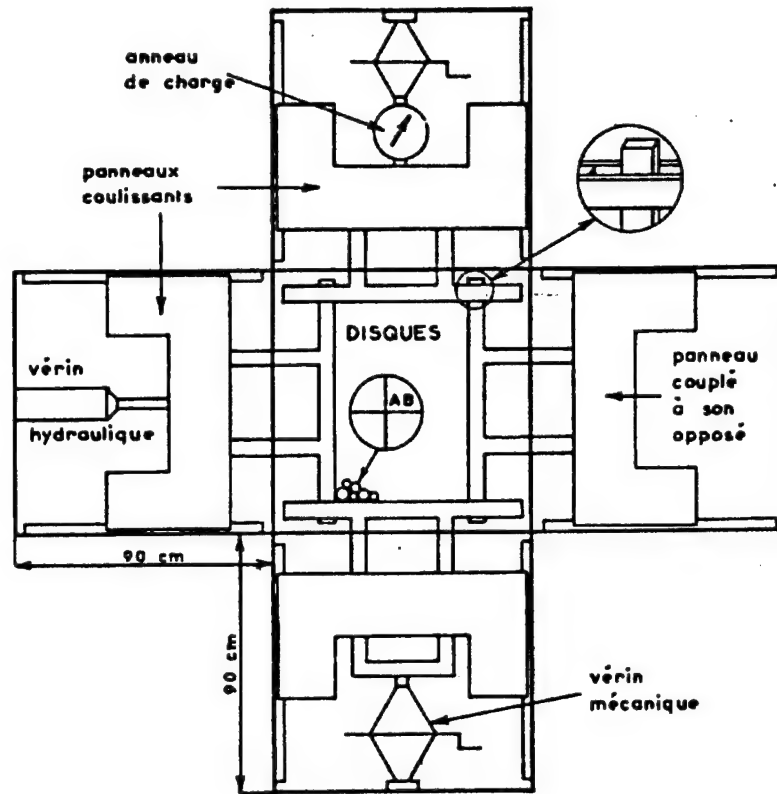
Figure 14. Testing apparatus used in Chapuis (1976) tests.
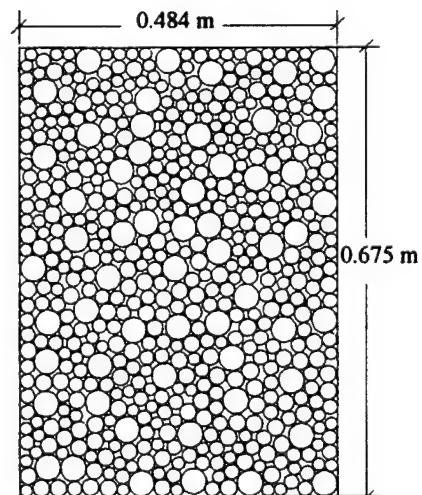
Figure 15. DEM sample for dense Chapuis test.

gradation information					simulation parameters	
type	ball1	ball2	ball3	ball4	timestep (s)	4×10^8
a (mm)	9.525	11.190	12.825	19.380	gravity (m/s²)	0
b (mm)	9.240	10.965	12.825	19.380	dntol⁺(mm)	.80
# particles	232	174	116	58	dutol⁺⁺(mm)	.080
φ (g/cm³)	1.5	1.5	1.5	1.5	dthtol⁺⁺(rad)	.01
contact properties	ball1	ball2	ball3	ball4	wall	
k_n (kN/m³)	12,000	12,000	12,000	12,000	120,000	
k_t kN/m³)	8,000	8,000	8,000	8,000	80,000	
c_n (kN/m³s)	.960	1.14	1.32	1.98	19.68	
c_t (kN/m³s)	0	0	0	0		
ϕ_u (degrees)	10°	10°	10°	10°		
cohesion	0	0	0	0		
e⁺⁺⁺	0.5	0.5	0.5	0.5		
⁺	tolerance before contact list broken					
⁺⁺	accumulator tolerances for deflection and rotation					
⁺⁺⁺	coefficient of restitution					

TABLE 2. Simulation parameters for an initial simulation of Chapuis' tests.
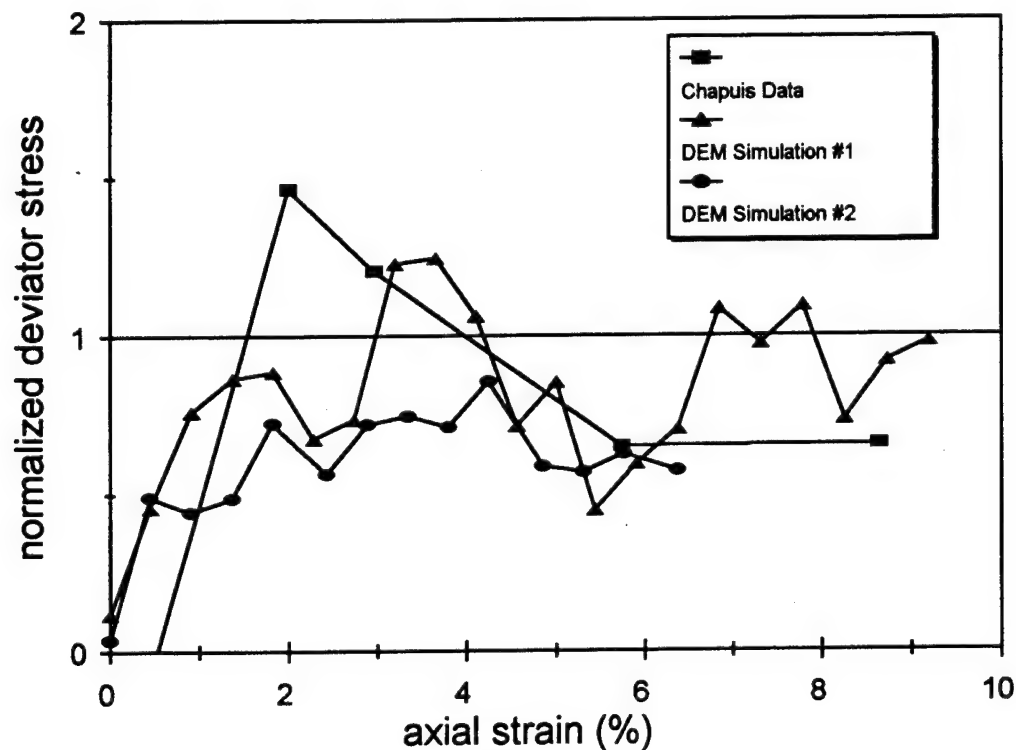
Figure 16. Validation results for dense Chapuis (1976) disk tests: normalized deviator stress vs. axial strain.
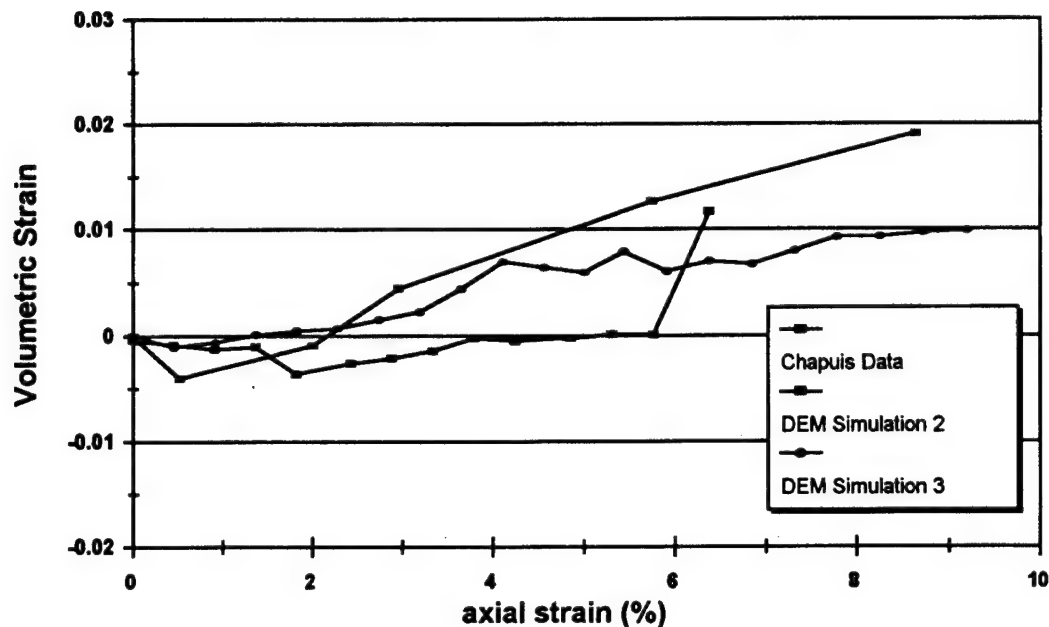
Figure 17. DEM validation results of for dense Chapuis test: volumetric strain vs. axial strain.

Efforts were also made to simulate a loose biaxial shear test, and an unloading test performed by Chapuis. The attempts to simulate the loose test were unsuccessful, due to difficulties associated with obtaining a sample at the same void ratio and initial stress as the Chapuis loose sample. The same problems were encountered in modeling the Chapuis unloading test. However an unloading test was performed at an initial void ratio different than the value reported by Chapuis, and the results are shown in Figure 18 for a qualitative comparison. As this Figure suggests, the behavior of the sample is qualitatively comparable to the unloading test performed by Chapuis, with the sample rebounding to a denser state. It is believed that better agreement is possible if a numerical sample could be created with the same initial density as the Chapuis unloading test.

Overall, the DEM results were similar, both qualitatively and quantitatively, to the physical tests performed by Chapuis on elliptical particles. The measured peak friction angle, ϕ_{max}, from the DEM simulation of a dense sample was 24°, compared to 25° achieved during the physical tests. Volumetric strain data also compared favorably. Although the Chapuis tests were conducted without complete information available regarding the material being tested, it is conjectured that modeling of the Chapuis tests was successful because the particle shape and gradation matched in the physical and numerical tests. Additionally, the stiffness value used in the simulation was large enough to guarantee small particle deformations, which is the key to achieving proper mechanical behavior in these numerical simulations.
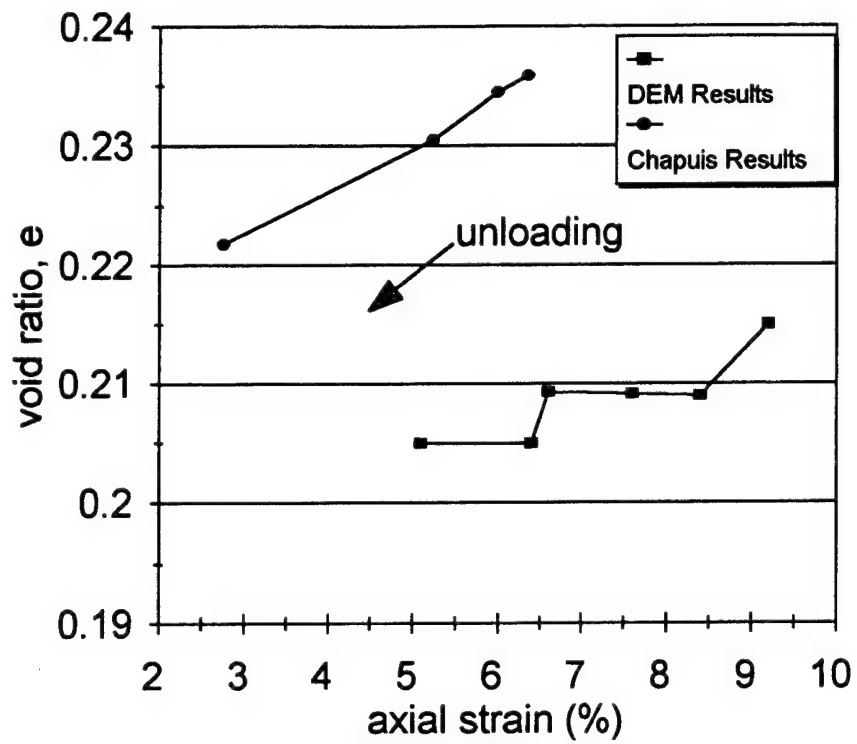
Figure 18. Results of attempted simulation of Chapuis(1976) unloading test.

5.4 Konishi, Oda and Nemat-Nasser (1983) Tests

Konishi *et al.* (1983) performed physical tests on assemblages of approximately 700 photoelastic oval rods of varying aspect ratio, subjected to biaxial shear. This chapter describes the physical test setup and results of these tests. Detailed photographic prints of one of the physical tests were obtained and digitized for use in one of the simulations. Model input parameters were varied extensively to assess the effect on the simulation results.

The oval photoelastic rods had common length of 19 mm. Two different cross sectional shapes were used: "Oval I" and "Oval II", with 1.1:1 and 1.4:1 particle aspect ratios. Samples were formed from three different sized particles for each oval cross sectional shape. Table 3 summarizes the particle dimensions used. Two sets of experiments were performed. In one set, the particles were lubricated with talcum powder that reportedly produced an estimated interparticle friction angle of 26°. The other set consisted of unlubricated particles with an estimated interparticle friction angle of 52°. The rods were cast from polyurethane rubber with a reported 100% modulus of 80 kgf/cm². Particle cohesion was reportedly zero for all tests. Figure 19 illustrates the biaxial testing apparatus used to test the samples. Initial dimensions of the loading frame were 330 mm height and 207 mm width. The particles were stacked by hand in the loading frame, which could be tilted to create samples with varying bedding angle. Samples with bedding angles of 0°, 30°, 60°, and 90° were tested.

Designation	a/b	Diameters a/b (mm)
Oval I	1.1	Large 14.8/13.4
		Medium 9.9/8.9
		Small 6.3/5.7
Oval II	1.4	Large 16.0/11.3
		Medium 10.7/7.4
		Small 7.1/4.9

Table 3. Description of particle sizes and shapes used by Konishi *et al* (1983).

A constant force of 0.45 kgf (0.70 kPa), was applied laterally to the samples, and vertical compression was applied incrementally by lowering the upper part of the loading frame. Displacements were monitored by dial gauges, and load transducers monitored applied loads. The side platens of the loading frame were coated with Teflon to reduce wall friction, and the applied horizontal and vertical stresses were assumed to be principal stresses. Throughout the loading, photoelastic photographs were taken to record force chain formation. Table 4 presents the results from the tests conducted by Konishi *et al.* (1983).

Samples that matched the general gradation, aspect ratio, number of particles, and bedding angles of Konishi's tests were generated using the front-end graphical interface program FEGEN. The results of these initial validation tests have been reported by Ting *et al* (1993), and exhibited qualitatively similar behavior to Konishi's tests. However, the peak stress ratios reported by Konishi et al were 4.9 for Oval I samples of 26° internal friction, 0° bedding angle, and 11.8 for Oval II samples of 26° internal friction, 0° bedding angle. These values of peak stress ratio, and consequently peak friction angle, were consistently higher than the resulting values of DEM simulations. Figure 20 presents the results of the initial DEM validation tests, plotted as peak friction angle versus aspect ratio. Additional tests are presented later in this Report, as well as Meachum (1994).

Figure 19. Schematic of biaxial testing apparatus from Konishi, Oda and Nemat-Nasser (1983).
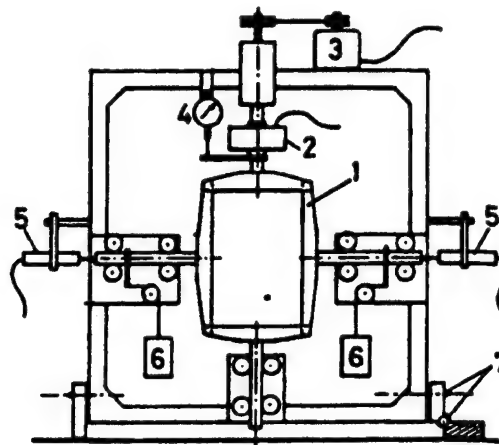
1 loading frame
2 load transducer
3 motor for vertical loading
4 dial gauge
5 LVDT's
6 weights for lateral loading
7 tilting axes
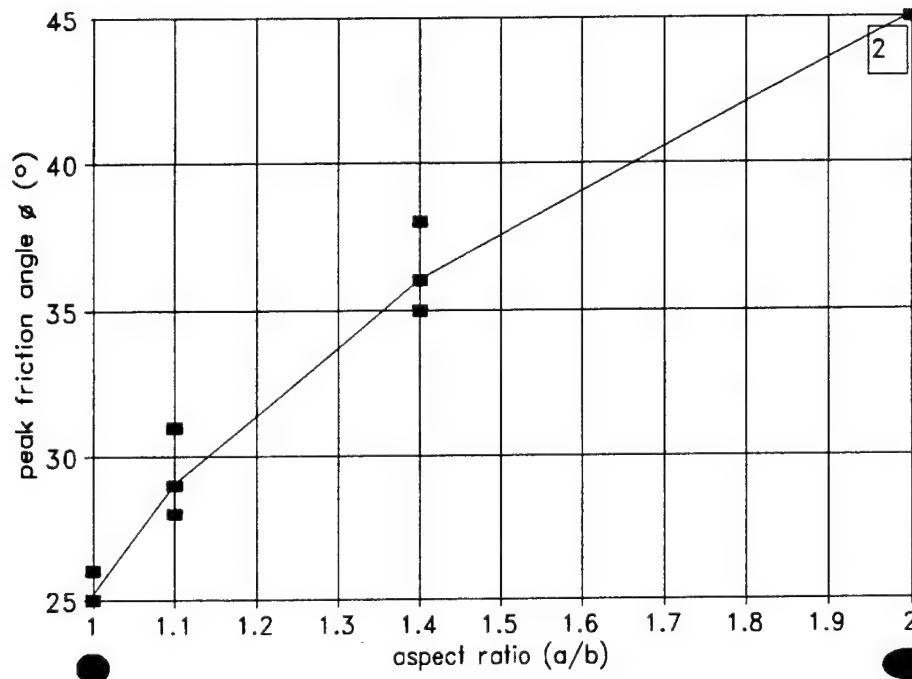
Figure 20. Peak angle of internal friction measured in initial DEM simulations of biaxial shear tests as a function of aspect ratio (Ting *et al* 1993).

Cross Section	Friction Angle ϕ_u	Bedding Angle θ	Void Ratio e	Peak Stress Ratio ($\sigma 1/\sigma 2$)	Internal Friction Angle ϕ_{max}
OVAL I	52°	0°	0.190	7.0	49°
		30°	0.183	4.7	40°
		60°	0.185	4.1	37°
		90°	0.192	5.9	45°
OVAL II	52°	0°	0.177	14.4	60°
		30°	0.154	11.4	57°
		60°	0.159	8.3	52°
		90°	0.155	10.4	55°
OVAL I	26°	0°	---	4.9	42°
		30°	0.169	6.0	46°
		60°	0.174	5.4	43°
		90°	0.168	4.8	41°
OVAL II	26°	0°	0.158	11.8	58°
		30°	0.160	7.5	50°
		60°	0.155	4.3	39°
		90°	---	5.5	44°

Table 4. Results of physical tests on oval rods performed by Konishi *et al* (1983).

For the samples described above, Konishi et al report peak friction angles of 42° for Oval I, and 58° for Oval II for the 0° bedding angle samples. The initial sequence of DEM simulations reported by Ting *et al* (1993), yielded peak friction angle values of 31° for Oval I, and 37° for Oval II. It was therefore necessary to investigate the reasons for the discrepancy in the macroscopic strength behavior of the DEM samples.

To better model the system of particles tested by Konishi *et al*, photoelastic photos of the Oval II sample with 0° bedding angle, were obtained from the authors and digitized. The Oval II sample that was obtained and digitized is depicted in Figure 21. The digitized data was used to create a numerical sample that would accurately represent the exact particle locations and orientations of Konishi's Oval II sample. The sample was created with the program FEGEN, and is represented in Figure 22.
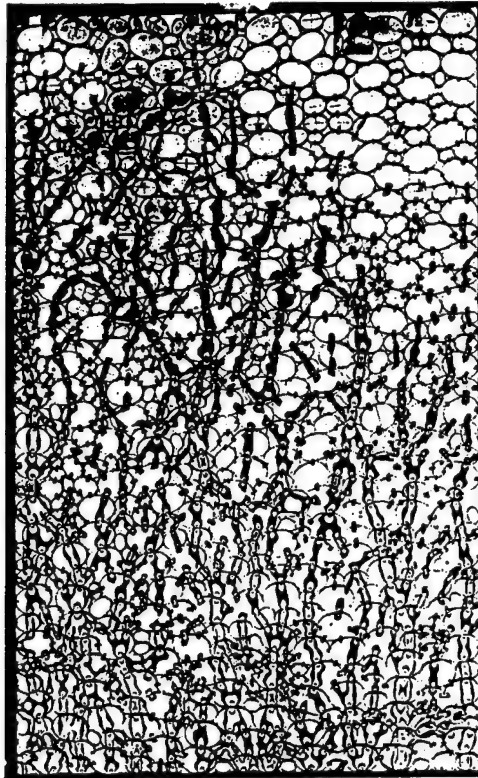
Figure 21. Photo of Konishi *et al*'s Oval II sample prior to shear.
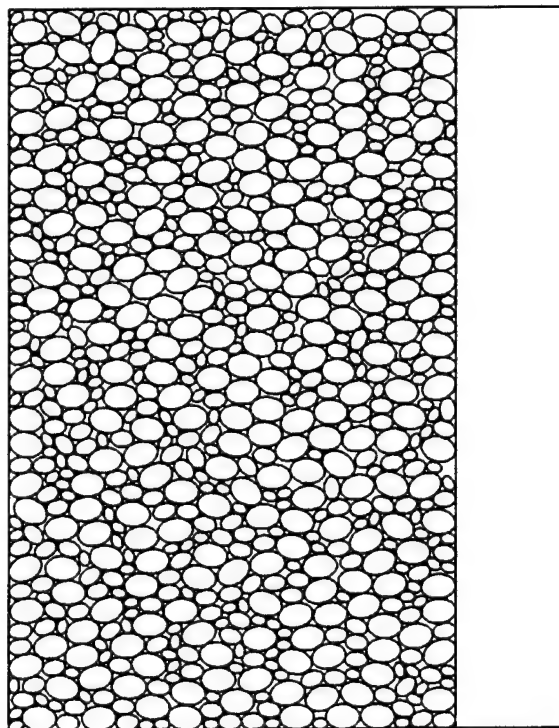
Figure 22. Digitized version of Konishi *et al's* Oval II sample.

Following the digitized Oval II sample generation, simulations were carried out for comparison with the reported Konishi *et al* data. The input parameters for the initial DEM simulation of Konishi's tests are presented in Table 5. The DEM results from this digitized sample of Konishi's tests yielded a friction angle, ϕ, of 40° compared to the value of 37° from earlier DEM simulations. However, large dissimilarities still existed in the stress-strain behavior of the samples, and this friction angle value was still low compared to the value reported by Konishi of 58°. The results of this simulation are presented in Figure 23.

gradation information					simulation parameters	
type	ball1	ball2	ball3		timestep (s)	2×10^{6}
a (mm)	8.00	5.35	3.55		gravity (m/s^2)	0
b (mm)	5.65	3.70	2.45		dntol $^+$(mm)	.80
# particles	239	241	249		dutol $^{++}$(mm)	.080
φ (g/cm^3)	1.5	1.5	1.5		dthtol $^{++}$(rad)	.01
contact properties	ball1	ball2	ball3	wall	global	
k_n (kN/m^3)	3,000	3,000	3,000	30,000		
k_s kN/m^3)	2,000	2,000	2,000	20,000		
c_n (kN/m^{3}s)	.48	.33	.216	1.08		
c_s (kN/m^{3}s)	0	0	0	0		
ϕ_μ (degrees)	26°	26°	26°	0		
cohesion	.10	.10	.10	0		
e $^{+++}$	0.5	0.5	0.5	0.5		
+		tolerance before contact list broken				
++		accumulator tolerances for deflection and rotation				
+++		coefficient of restitution				

TABLE 5. Simulation parameters for oda2.dat
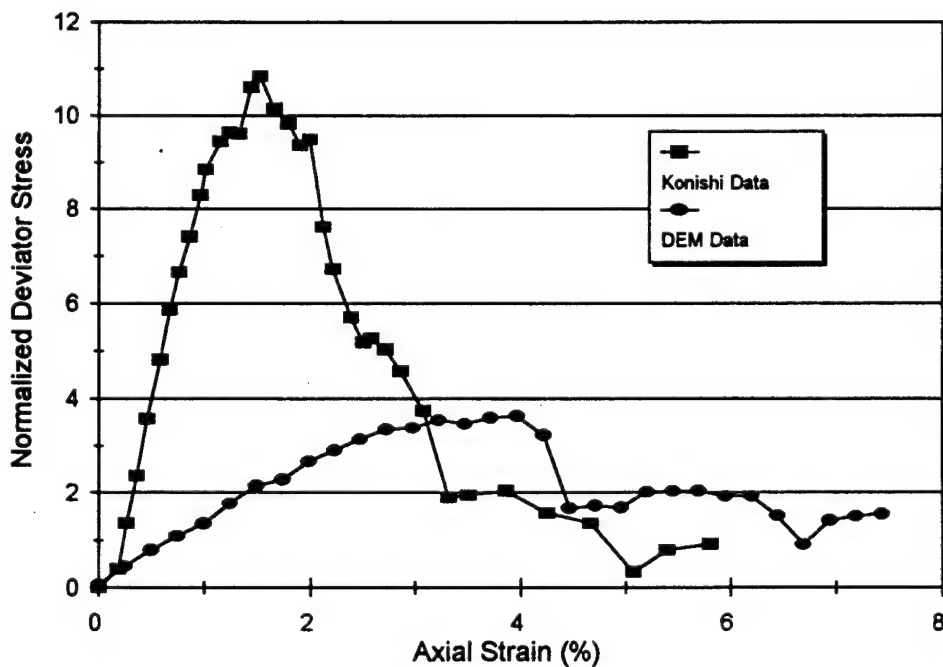
Figure 23. Comparison of initial DEM simulation of biaxial shear using digitized Oval II sample.

36

5.5 Variation of Contact Properties

Although careful consideration was given to the properties and simulation parameters used in the initial DEM tests, additional simulations with varying contact properties were conducted on the digitized Oval II sample. These tests were conducted to assess the effect of variation of simulation parameters, and to determine if the DEM simulations would more closely model the Konishi tests. Extensive testing was performed as part of this validation procedure, consisting of contact stiffness variation, the addition of contact cohesion, variation of contact friction, variation of contact damping, the addition of wall friction, testing with gravitational effects implemented, and simulations with various combinations of these parameters invoked. The effect of changing the timestep of integration was studied, as well as the effect of shearing the samples at different rates. These test results are described in full in Rowell (1994), and only the major findings are reported here.

5.5.1 Variation of Linear Contact Spring Stiffness

To determine the effect of contact stiffness variation on the DEM simulation results, the linear contact stiffness k_n was varied from 300 kN/m^2 to 10,000 kN/m^2 while all model parameters not affected by contact stiffness remained constant. Candle and Strack showed that when the ratio of tangential stiffness to normal stiffness, k_s/k_n, was varied from 2/3 to 1, there was little change in mechanical behavior. Of the nine simulations that were performed as part of this testing sequence, eight simulations used k_s equal to 2/3 k_n. The remaining test was run with k_n equal to k_s. Figure 24 illustrates the effect of contact stiffness variation on the DEM results.
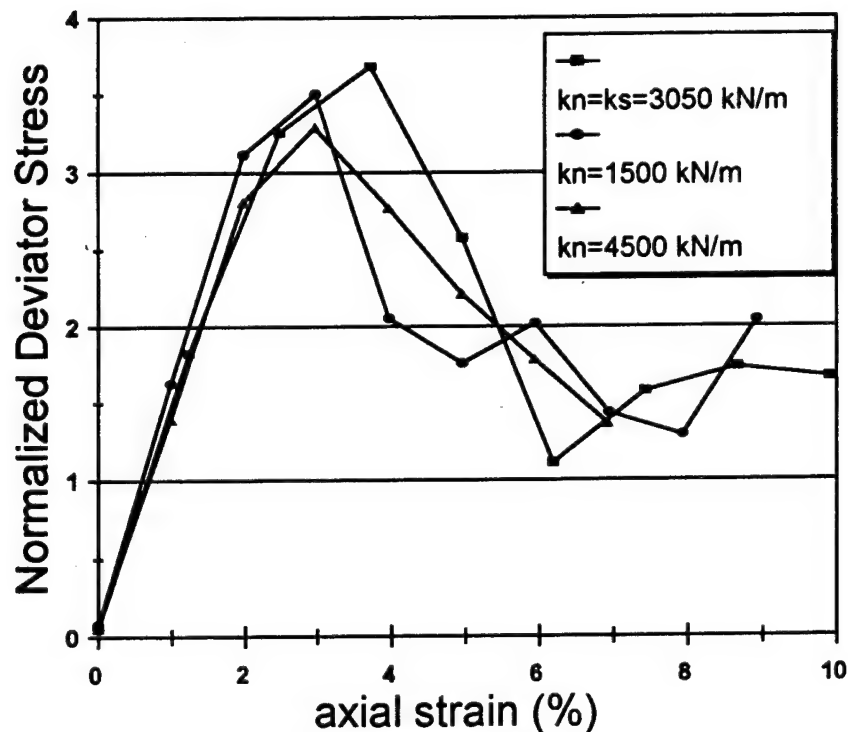
Figure 24. Effect of varying linear normal contact stiffness k_n on DEM simulation results.

5.5.2   Alternate Contact Stiffness Model

DEM simulations were also conducted using the linear hysteretic contact model proposed by Walton and Braun (1986). For a specified coefficient of restitution of 0.5 and a loading stiffness of $K_1 = 4500$ kN/m^2, the unloading stiffness, K_2 was calculated as 18,000 kN/m^2. All other simulation parameters and contact properties remained unchanged from the linear contact parameters except for the contact damping, which is zero in the hysteretic model. Figure 25 plots the normalized deviator stress versus axial strain for the linear spring-dashpot and linear hysteretic spring tests, and shows that these two contact models exhibit similar behavior.
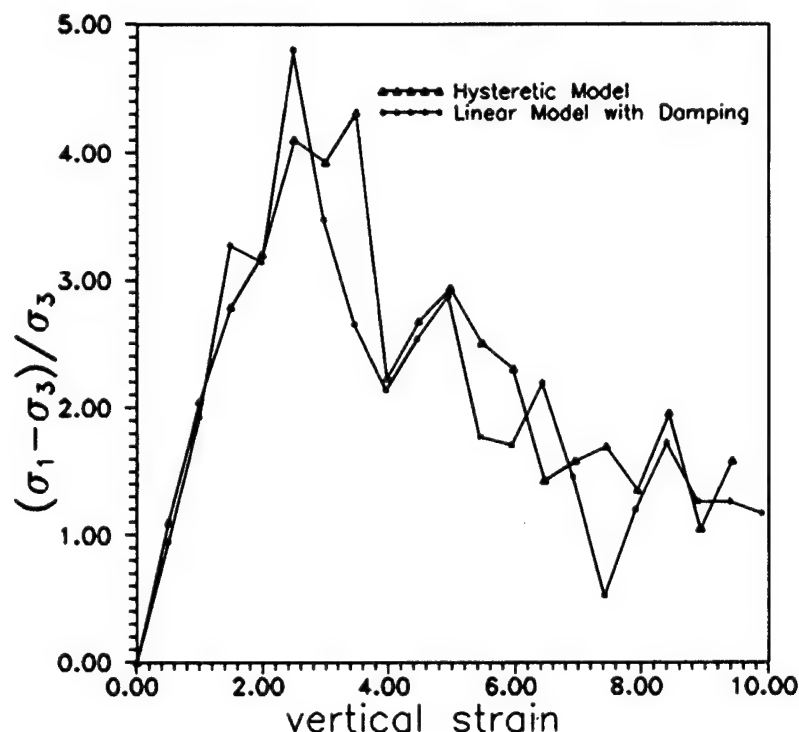
Figure 25. Comparison of linear spring-dashpot and linear hysteretic spring contact models for biaxial shear of digitized Oval II sample.

5.5.3   Variation of Contact Cohesion

Although Konishi *et al* reported that the photoelastic material used in the physical tests possessed no contact cohesion, it is possible that a small amount of cohesion existed at the particle contacts. To assess the effect of this cohesion, DEM simulations were carried out where a small cohesion was introduced. The shear force, T, at a contact is related to the normal force, N, at a contact by the relationship,

$$T = c_a + N\tan\phi_u$$

where c_a is the contact cohesion, and ϕ_u is the interparticle friction angle. This relationship was used with the results from previous DEM tests to arrive at realistic cohesion values for input into the model. The DEM results from this series of tests are represented in Figure 26, and showed no appreciable difference over the range of cohesion values tested.
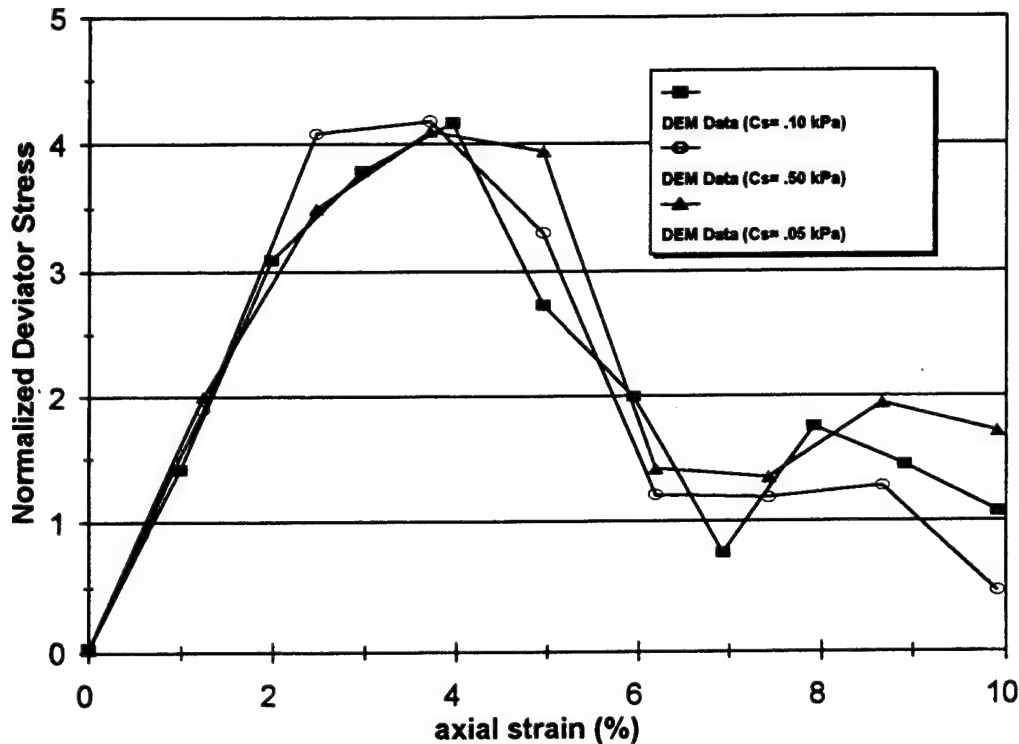
Figure 26. Effect of varying contact cohesion on DEM simulation results for digitized Oval II sample..

5.5.4 Variation of Interparticle Friction Angle, ϕ_μ

The average interparticle friction angle reported by Konishi *et al.* (1983) for their particles lubricated with talcum powder is 26°. How this friction angle was measured was not described in the available literature. In addition, one can envisage how this friction angle value could change during testing as a result of particles sliding past each other, resulting in an uneven distribution of talcum powder. Since this friction angle value is an average value, and because there is some uncertainty related to this value, DEM simulations were performed on samples with varying interparticle friction angle while all other parameters remained constant. The results of these tests are plotted in Figure 27.

5.5.5 Effect of Contact Damping, c_n

The normal contact damping value, c_n , can be related explicitly to the contact stiffness, masses of the particles in contact, and the coefficient of restitution of the particles, according to equation [35] (Corkum and Ting 1986). Since the value of the coefficient of restitution of the photoelastic material used in the physical tests is not reported in the available literature, a value had to be selected arbitrarily. For rubber, a realistic value for the coefficient of restitution was selected as $e = 0.5$, based on typical known values. All of the simulations in this study used values of e equal to 0.5. To learn if higher damping would significantly influence simulation results, a test with $e = 0.25$ was conducted. The resulting data was plotted in Figure 28.
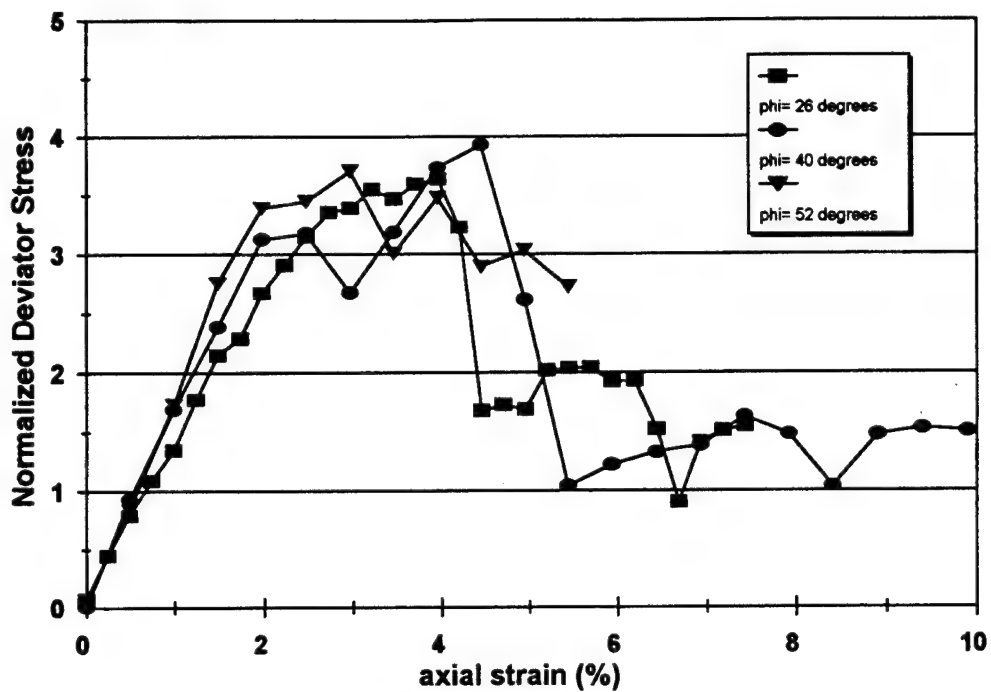
Figure 27. Effect of varying interparticle friction angle on DEM simulation results for digitized Oval II sample.
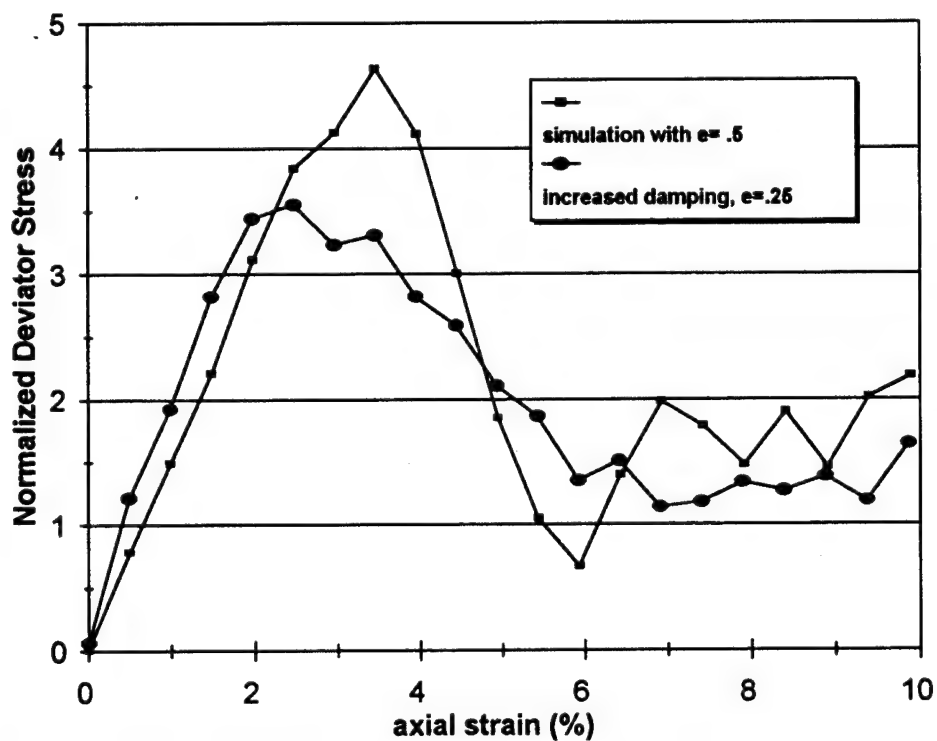
Figure 28. Effect of varying contact damping on DEM simulation results.

5.6 Discussion of Validation Testing and Konishi *et al* Data

The value of 47° obtained in the DEM simulation is still much lower than the reported value of 58° obtained in the physical tests. Konishi reported a maximum normalized deviator stress of 11.8, which was achieved at approximately 1.5% axial strain, for the Oval II sample with an interparticle friction of 26° and 0° bedding angle. The DEM results for this test yielded a maximum normalized deviator stress of approximately 5.5 at 4% strain.

Several possibilities exist that would explain the differences between the numerical and physical test results. One possibility is that the linear contacts used in the DEM model does not adequately reflect the physical contact behavior. This possibility has been investigated through the study of a hysteretic contact relationship, and through the analysis of a nonlinear contact relationship. Comparisons between simulation results incorporating Walton's hysteretic contact model and the simple linear contact model currently used in the simulation program PARSE, reveal little difference in the observed macroscopic mechanical behavior of the samples tested. Figure 25 suggests that both the linear hysteretic spring and the linear spring-dashpot contact models yield results consistent with each other and with typical soil behavior. This research finding suggests that although these two contact models are modeling the force-deflection behavior and energy dissipation at particle to particle and particle to wall contacts differently, the overall mechanical response yielded by both contact models is comparable.

Analysis of the nonlinear Hertzian contact model derived by Chang and Misra (1990) suggests that for small contact deformations, the relationship between normal contact force and normal deformation very nearly linear. Since it is necessary to use stiffness values in the DEM model that will result in small deformation or overlap of particles relative to particle size, analysis of the nonlinear contact model focused on contact deformations in the range of up to 2% of the average particle radius. It was found that in this range of small contact deformation, the resulting force-deformation relationship is nearly linear, with a resultant R^2 value of 0.985. Although Hertzian contact theory suggests that the force-deformation relationship of solids in contact is nonlinear in nature, it is unnecessary to model this relationship exactly in the DEM model for the current low stress level simulations.

Based on these findings, and the findings concerning comparisons with the hysteretic contact model, it appears that the DEM model with the simple linear contact relationship is sufficient to properly model the overall mechanical behavior of particulate systems. The key to the proper selection of normal contact stiffness for the simple linear DEM model is that deformation at particle contacts must be kept small relative to the size of the particle. It is unlikely that the force-deflection relationship is responsible for the differences between the numerical and physical test results.

The extensive validation effort consisting of variation of DEM model input parameters also failed to provide a better approximation of Konishi *et al*'s physical test results. Only small changes in the macroscopic behavior were observed through this effort. Therefore, it is highly unlikely that the reason for the discrepancy between physical and numerical test results lies in the improper selection of model input parameters.

It is conjectured that the reason for the discrepancy in test results lies in the fact that the photoelastic rods sheared in the Konishi *et al* tests are **oval** and **not elliptical** in shape. Figure 29 presents an enlarged view of the lower left corner of the Oval II photoelastic photo taken at stage 1, provided by Prof. Oda. A close inspection of the particle shape reveals that the Oval II rods have a significantly large flat surface parallel to the major axis. In addition, for the 0° bedding sample, these flat surfaces are aligned horizontally, which creates a situation where many particles are in contact over these large flat regions. When the sample is loaded vertically, the load can be transferred directly through chains of these stacked flat rods, which are very stable.

41
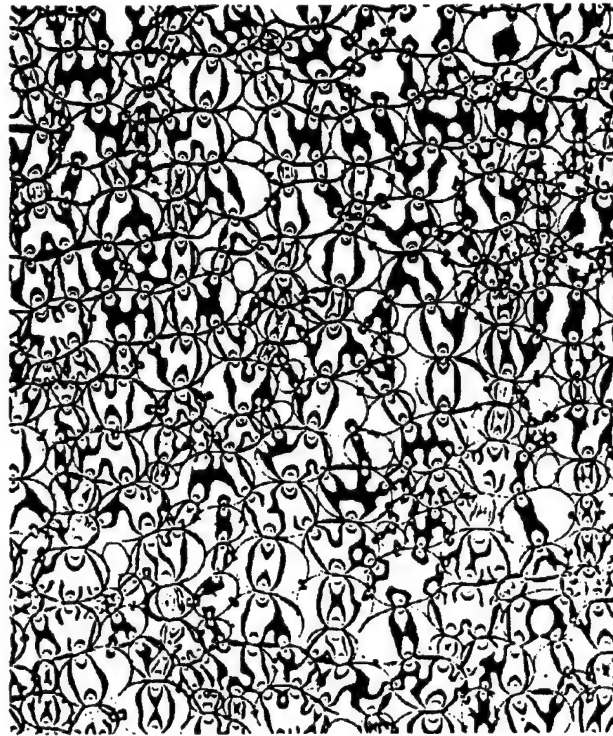
Figure 29. Enlarged view of lower left corner of
Konishi *et al* (1983) Oval II sample at stage 1.

As further support of this theory, simulations at bedding angles greater than 0°, specifically the 60° bedding samples, yielded friction angles much closer to the Konishi test results. Konishi reports a friction angle, ϕ_{max}, of 39°, for the Oval II, 26 interparticle friction, 60 bedding test sequence. A DEM simulation of this test sequence yielded a friction angle, ϕ_{max} of 37°(Meachum 1994) For these samples, the effect of the flat surfaces is less pronounced, as these flats are not aligned with the loading platen, resulting in a less stable sample fabric.

To quantify the particle shape differences that exist between the photoelastic oval rods and the ellipses used to model the ovals, it is useful to look at the contact normal distributions of each system of particles. Figure 30 plots the distribution of contact normals for the Oval II, 26° interparticle friction, 0° bedding angle Konishi *et al* test at the initial condition prior to shear. Figure 31 plots the contact normal distribution at the peak stress state.

For comparison, the contact normal distributions for the initial and peak stress states of the DEM simulation are presented in Figures 32 and 33. As expected, the contact normals in the initial state are generally directed perpendicular to the bedding plane (*ie* vertically). However, for the DEM simulation, the contact normals are more widely distributed about the 90° direction. Since the particle locations and orientations are identical at the initial condition for both the numerical and physical tests, the difference in the contact normal distribution must be due to the particle shape differences.

To help further explain the effect of the flatter oval particles in the physical tests, the physical and DEM samples are shown at peak stress state in Figures 34 and 35. Inspection of these Figures shows that the contact normals are aligned nearly vertically in the physical tests. In addition, it is clear that a very stable soil fabric has been formed with the stacked oval rods. Figure 35 shows that the DEM ellipse-based sample possesses contact normals which are more widely distributed and in all likelihood a soil fabric that is less stable than the system of ovals.

42
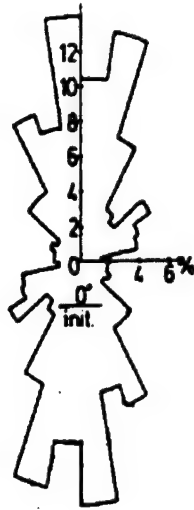
Figure 30. Distribution of contact normals from Konishi *et al* (1983) Oval II test prior to shear.
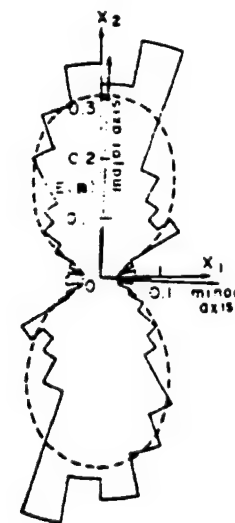
(a) oval II (θ=0.4)

Figure 31. Distribution of contact normals for Konishi *et al* Oval II test at peak stress state.

Further comparison with physical, two dimensional test data are required to fully validate the numerical code. Additional data are presently being collected on the interfacial shear of photoelastic rods and a variety of smooth and rough surfaces (Paikowsky and Xi 1995). As part of this research program, contact normal and tangential forces are being computed based on photoelastic fringe patterns. Rods which are carefully machined to be circular, and also ellipse-shaped are being tested in these shear tests. These physical disk and eventually ellipse-based physical test results will be used to help validate the PARSE numerical code (Paikowsky, Ting, Xi and Mischel, in press 1996).

43
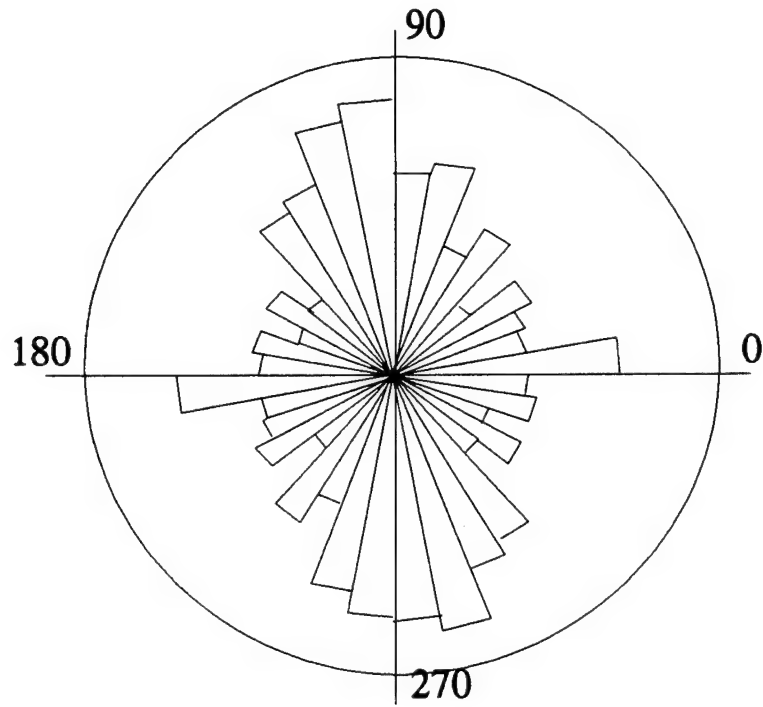
Figure 32. Contact normal distribution of 1.4:1 aspect ratio DEM sample prior to shear.
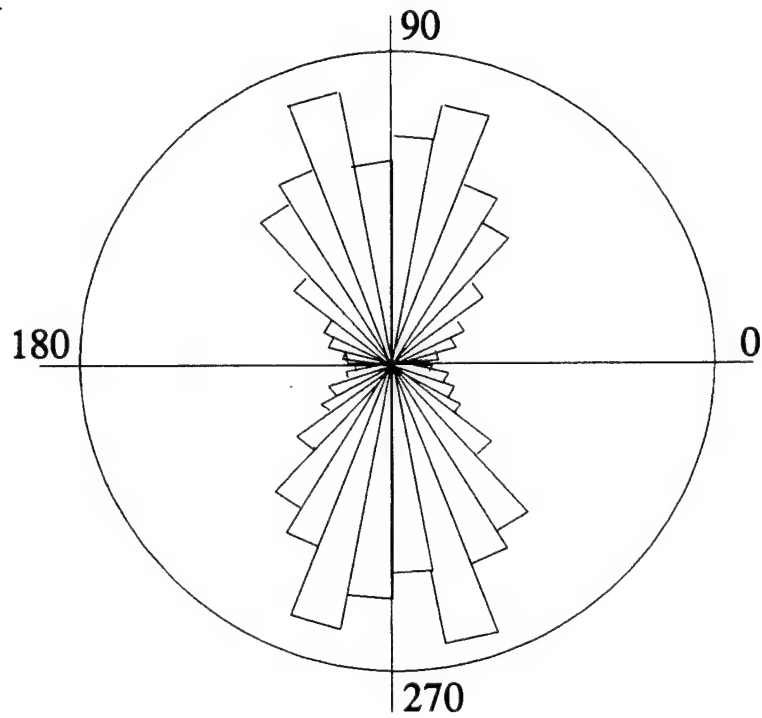
Figure 33. Contact normals distribution of 1.4:1 aspect ratio DEM Simulation at peak stress.
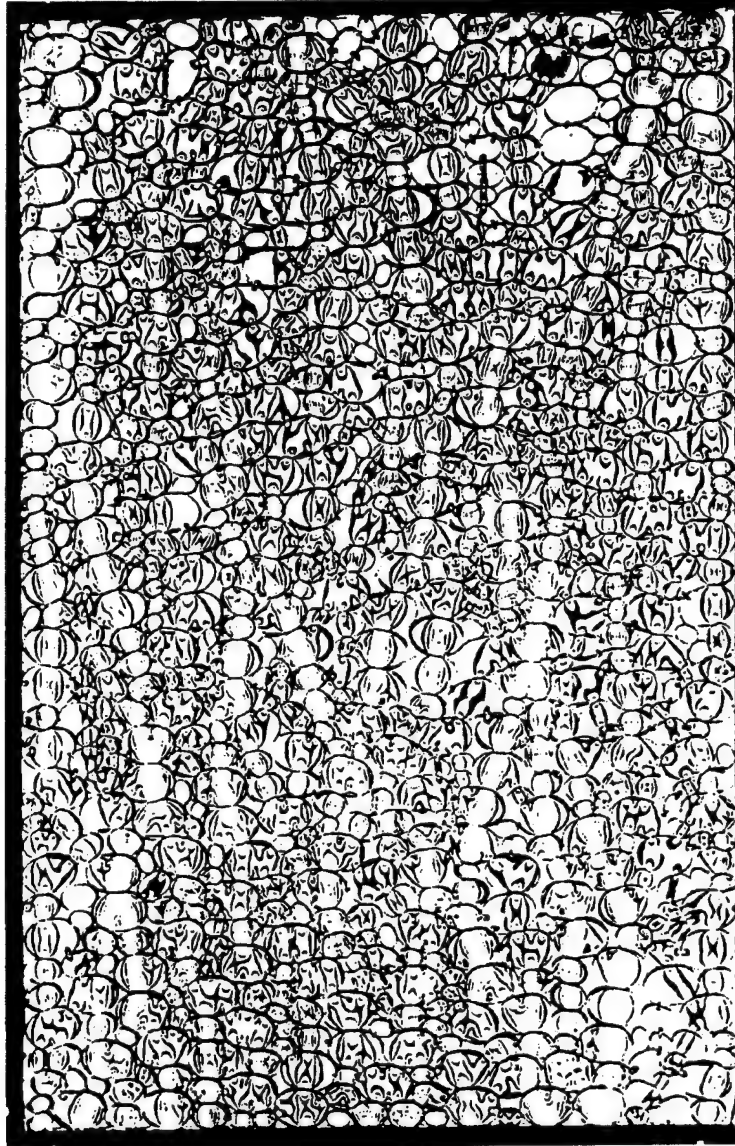
Figure 34. Photo of Konishi *et al.*'s Oval II horizontally bedded sample at peak stress state.
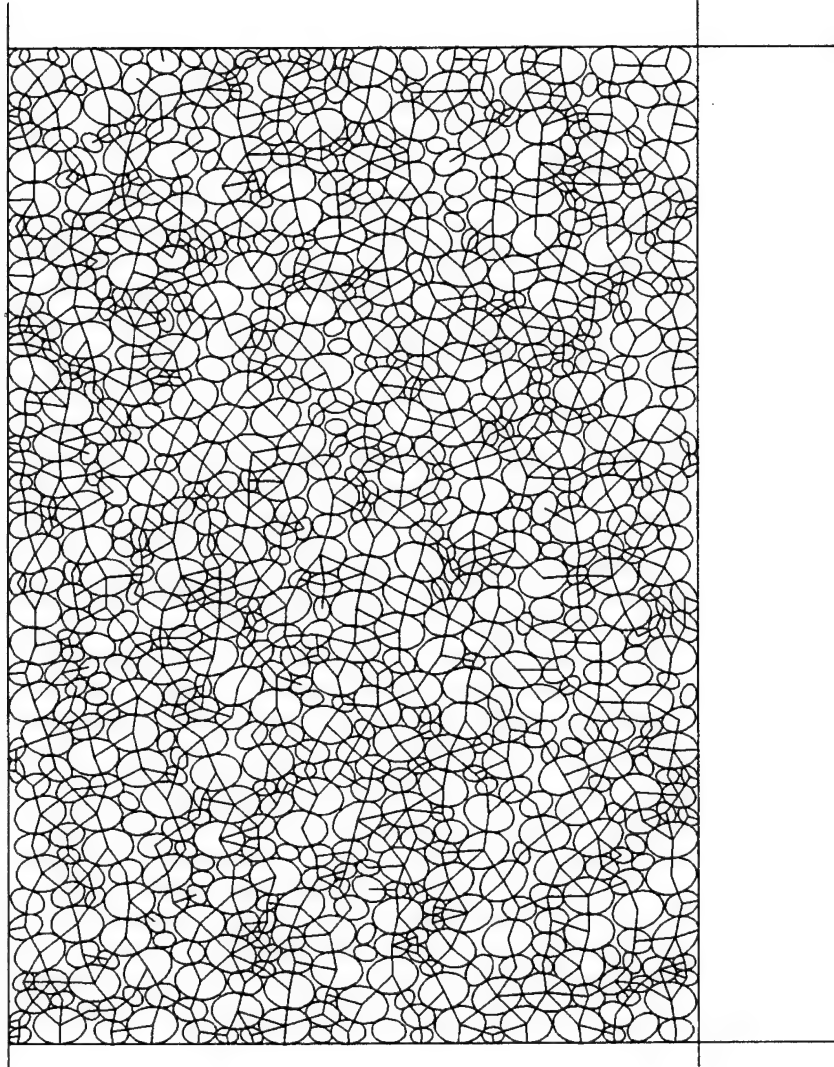
Figure 35. Horizontally bedded 1.4:1 :1 aspect ratio sample at peak stress state based on DEM simulation of initial digitized Oval II sample..

5.7 Comparison with Other DEM Results

5.7.1 Numerical Results from Rothenburg and Bathurst (1991)

Several researchers have used ellipse-based DEM models to study particle shape effects on the mechanical behavior of particulate systems. Rothenburg and Bathurst (1991, 1992) performed biaxial compression tests on assemblies of 1000 elliptical shaped particles of varying density and eccentricity. Samples were formed by growing the particles from the same initial assembly. This was accomplished by selecting a target eccentricity, which was increased incrementally while maintaining hydrostatic boundary conditions. The assemblies created in this manner were dense, with no preferred bedding angle. Since no particle size is specified in this generation scheme, particle sizes vary. A simple linear contact model, similar to that used by Cundall and Strack and in this study, was used to govern contact behavior. For all tests conducted, the interparticle friction angle was 26.6°.

Rothenburg and Bathurst express the angularity of the ellipses in their study as particle eccentricity, e, which is defined as,

$$e = \frac{a-b}{a+b} \tag{56}$$

where a and b are the values of the major and minor axis lengths respectively. A plot of the peak friction angle vs. eccentricity obtained in the tests performed by Rothenburg and Bathurst (1991) is presented in Figure 36.

Figure 36 shows that the maximum friction angle obtained by Rothenburg and Bathurst was 42° at an eccentricity of approximately 0.15, which is equivalent to an aspect ratio of 1.35. As particle eccentricity increases beyond a value of 0.15, the shear strength decreases.
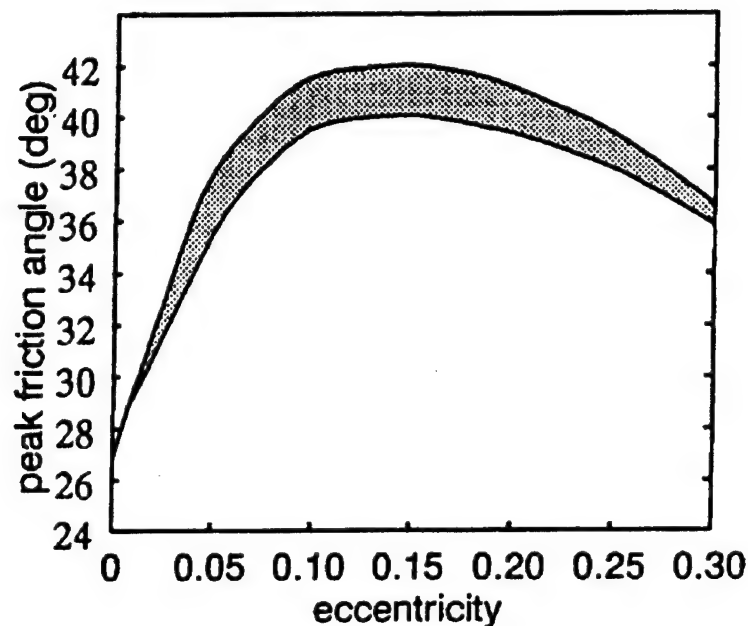
Figure 36. Peak friction angle vs. eccentricity from Rothenburg and Bathurst (1991)

5.7.2 Numerical Results from Ng (1992)

Ng (1992) performed numerical simulations on assemblies of elliptical particles, using a DEM program ELLIPSE2. As with the current study, simulations were performed on assemblies of varying particle aspect ratio to assess the effect of particle angularity on the mechanical behavior of the specimens.

The simulations were conducted using input parameters for quartz particles with a shear modulus G of 2.9 x 10^4 MPa, Poisson's ratio 0.15, and a particle to particle sliding friction angle of 26.6°. The specimens consisted of particles of one size only for each sample. Samples were generated with particle aspect ratios of 1.00, 1.25, 1.51 and 1.67. Sample generation was accomplished with a depositional particle generation scheme, which randomly generated samples by introducing a gravity field while particles were being rained from the top of the sample. The specimens were consolidated isotropically, following sample generation, in increments of 40 kPa, up to approximately 160 kPa total consolidation pressure. Prior to the shearing of the samples, Ng reports void ratios varying between 0.254 for the sample with circular elements, to approximately 0.23 for the samples of aspect ratio 1.51 and 1.67.

Biaxial compression tests were conducted on three of the samples. The sample with particles of aspect ratio 1.67 was sheared to 12% axial strain. The samples of aspect ratio 1.00 and 1.25 were sheared to only 2.5% axial strain, due to computational time constraints. Ng found that the particles with larger aspect ratios produced larger friction angles, a result that is consistent with the results produced by the PARSE program. The friction angles yielded by the ELLIPSE2 program were low, however, compared to typical friction angles for medium dense natural sands. Figure 37 illustrates the results obtained by Ng (1992) for the three biaxial tests performed. Note that in Figures 37 and 38, the deviator stress is quantified using the mobilized friction angle, which is just:

$$\text{mobilized } \phi = \sin^{-1}(\frac{q}{p}) \tag{56}$$

where p and q are the mean and maximum deviator stress, respectively.

Figure 39 plots the simulation results on ellipse assemblages of Rothenburg and Bathurst (1991), Ng 1991) and DEM program PARSE. The fact that the assemblies created by Rothenburg and Bathurst were dense, with no preferred bedding angle accounts for the increased strength evident in this comparison. The assemblies tested with the PARSE program were horizontally bedded, medium dense, and consisted of three different particle sizes. The comparison of data is quite good in light of these differences.

The assemblies created by Ng were loose compared to the samples tested with the PARSE program and those tested by Rothenburg and Bathurst. As expected, the resulting shear strength of the Ng samples is less than that yielded by the other two programs. Additionally, Ng tested samples consisting of one particle size as opposed to the graded samples of the other two researchers. In general, the PARSE results compare favorably with the other DEM model results.
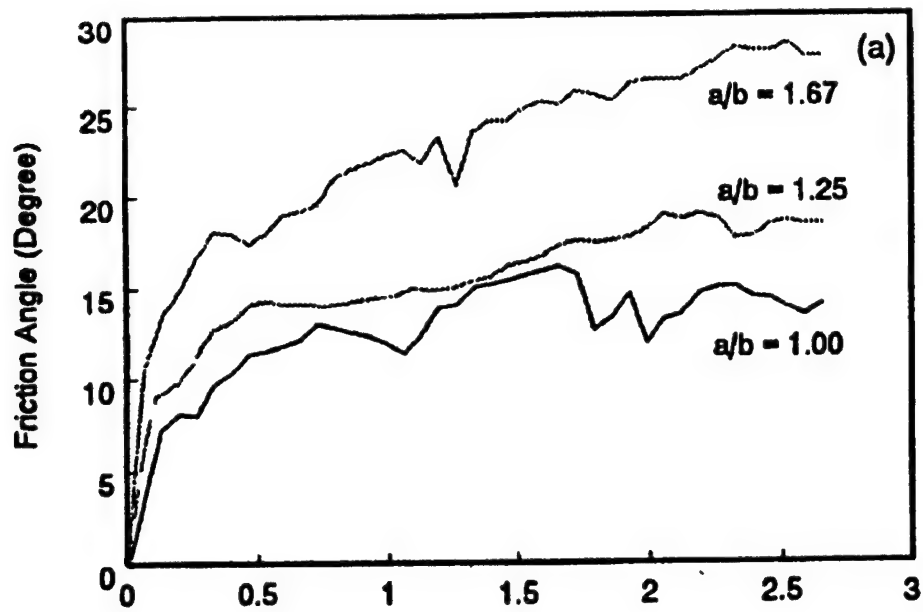
Figure 37. Mobilized angle of internal friction vs. axial strain from Ng (1991).
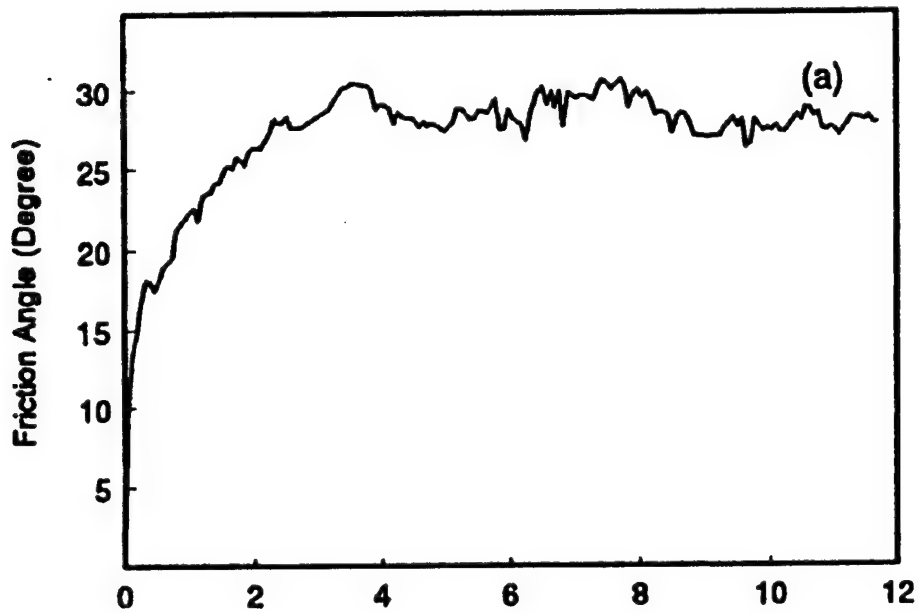
Figure 38. Mobilized friction angle vs. axial strain for 1.67:1 aspect ratio sample from Ng (1991).

49
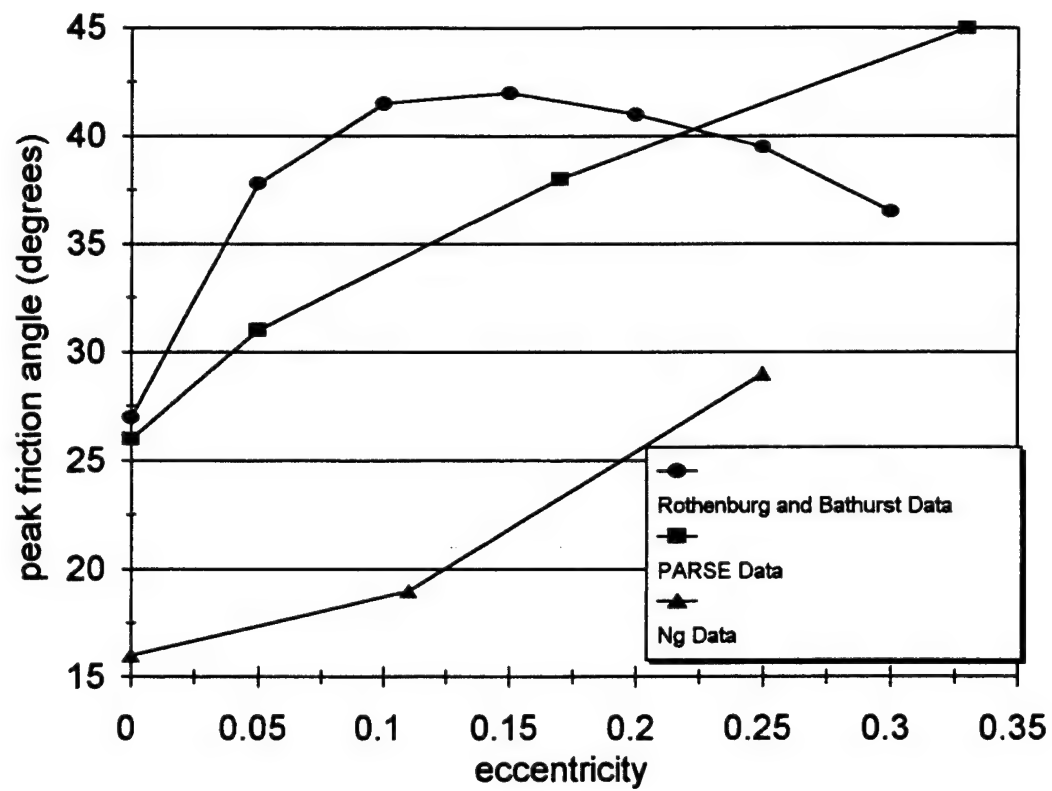
Figure 39. Plot of maximum angle of internal friction vs. particle eccentricity e for three DEM models.

6. SAMPLE FORMATION AND TEST SIMULATIONS

The next few Sections deal with the use of the ellipse-based DEM for investigating the influence of fabric anistropy on the mechanical behavior of granular systems. Numerous particulate assemblages were generated with variations in particle angularity (aspect ratio), preferred bedding orientation and initial void ratios. The samples were isotropically compressed and then biaxially sheared to approximately 10% axial strain. This Section describes the system generation, formation and test simulation procedures used in the current DEM study. The numerical samples were generated using the preprocessor program FEGEN. Geometry parameters and material properties were selected to obtain particulate assemblages similar to those used by Konishi *et al* (1983). Details of the sample preparation and test results are also found in Meachum (1994).

6.1 Sample Generation

Numerous samples were generated consisting of approximately 700 particles having aspect ratios a/b (major semi-axis to minor semi-axis) of 1.0, 1.1, 1.4, 1.7, 2.0, 2.5 and 3.0:1 and preferred orientations θ (measured from the horizontal) of 0, 30, 60 and 90°. To maintain a preferred bedding plane during the sample's formation, particle bedding angles θ were assigned a standard deviation of ±15° within which the orientations could vary slightly while maintaining overall particle alignment. At least two samples were generated for each combination of a/b and θ. Larger samples consisting of approximately 2000 and 5000 particles were also generated. Some samples were generated without preferred particle alignment producing geometric fabrics with more random distributions of particle orientations. The gradation for all of the numerical assemblages consisted of an equal number of three different-sized particles, the largest approximately two times as large as the smallest particle. Table 6 presents the particle dimensions of the three different particle sizes for each aspect ratio group.

The geometry of the two-dimensional numerical assemblages consisting of approximately 700 particles was similar to that used by Konishi *et al.*, measuring approximately 0.21 m wide and 0.33 m high. The larger 2000- and 5000-particle samples were scaled proportionally so that the sample height was approximately 1.5 times the width.

Several packing schemes were used to form numerical samples with variations in the initial void ratio. Forming samples with loose packing proved very difficult as the curvature of the ellipses tended to cause the sample to be unstable, collapsing into a dense packing even under the application of low confining stresses.

- *O* **Sample Series** - Particles were individually placed by hand to obtain densely packed samples yielding void ratios similar to those reported by Konishi. The larger samples consisting of 2004 and 5115 particles were formed as composites of the smaller 700-particle samples.

- *R* **Sample Series** - Some samples were formed by generating the particles in a much larger "box" and simply moving the top and right-side rigid boundaries (or walls) in using confining stresses of 0.7 kPa. Control of the preferred particle bedding to within a standard deviation of ±15° was lost, however, due to particle rolling. The resulting orientation fabrics were more isotropic than the extremely anisotropic bedding planes of the hand-packed *O* sample series. Looser packing was obtained using this packing scheme as more edge-to-face particle contacts existed, particularly in samples containing the flatter particles.

- *L* **Sample Series** - To form loosely packed numerical samples while maintaining preferred horizontal particle bedding ($\theta = 0°$), the particles were individually and loosely placed into a sample box of fixed width of 0.21 m and varied height. A uniaxial stress of 0.7 kPa was then applied vertically to the assemblage producing a rather stable sample confined laterally by the left and right rigid walls. After simulating for 1 second, the assemblages were isotropically compressed at a mean stress p of 0.7 kPa.

51

- *FL* and *FD* Sample Series - Another technique used to form loose samples while maintaining preferred particle bedding was to vary the interparticle sliding friction angle ϕ_μ during consolidation. Previously hand-packed Oval 3 and Oval 5 (a/b = 2.0) samples were given a value for ϕ_μ of 5° or 52° during the isotropic compression simulation. When the samples reached static equilibrium, ϕ_μ was returned to 26° and the samples were then isotropically compressed further at p = 0.7. The *FL* sample series are looser samples using ϕ_μ = 52° during formation, while the *FD* sample series are denser samples using ϕ = 5° during formation.

Cross-section Group	Aspect Ratio (a/b)	Particle Size	Particle Diameters (mm) Max/Min
Oval 0	1.0	large medium small	14.0/14.0 10.0/10.0 6.0/6.0
Oval 1	1.1	large medium small	14.8/13.4 9.9/8.9 6.3/5.7
Oval 2	1.4	large medium small	16.0/11.3 10.7/7.4 7.1/4.9
Oval 3	2.0	large medium small	19.52/9.76 13.04/6.52 8.7/4.34
Oval 4	1.7	large medium small	17.0/10.0 12.0/7.0 8.0/4.8
Oval 5	2.0	large medium small	18.4/9.2 12.8/6.4 8.8/4.4
Oval 6	2.5	large medium small	20.4/8.2 14.4/5.8 10.0/4.0
Oval 7	3.0	large medium small	22.8/7.6 15.6/5.2 10.8/3.6

Table 6.   Dimensions of DEM particles

Material Properties for DEM Particles	
Mass Density ρ (g/cm^3)	1.50
Poisson Ratio v	0.25
Coefficient of Restitution e	0.50
Cohesion C (kN/m^2)	0
Normal Spring Stiffness k_n (kN/m^2)	3000
Tangential Spring Stiffness k_t (kN/m^2)	2000
Sliding Friction Angle ϕ_μ (°)	26 or 52

Material Properties for DEM Boundaries (Walls)	
Coefficient of Restitution e	0.50
Cohesion C (kN/m^2)	0
Normal Spring Stiffness k_n (kN/m^2)	30000
Tangential Spring Stiffness k_t (kN/m^2)	20000
Sliding Friction Angle ϕ_μ (°)	0

Table 7. Material properties used for the DEM simulations.

All of the numerical samples were generated having the same material and system properties and gradation while the particle shapes and orientations and the sample packing varied. Table 7 presents the material property values used to define the numerical systems in the preprocessor program FEGEN. To eliminate unbalanced forces due to the sample's self-weight, the simulations were performed without gravity.

6.2 Isotropic Compression Simulation

After the samples were formed, they were isotropically compressed to a mean stress p of 0.7 kPa using the simulation program PARSE. Higher isotropic confining stresses of 1.4 kPa and 2.1 kPa were also applied to Oval 2 (a/b = 1.4) and Oval 5 (a/b = 2.0) samples with preferred horizontal bedding (θ = 0°). Figure 40 illustrates a typical numerical sample isotropically compressed at a mean confining stress p of 0.7 kPa. The resulting normal contact force chains, shown in Figure 41, are plotted from particle center to particle center with the relative thickness of the force chains proportional to the magnitudes of the normal forces.

The isotropic compression tests were simulated for 1 second until the samples achieved static equilibrium at the desired mean confining stress p of 0.7 kPa. The simulation time necessary to reach equilibrium conditions can vary depending on the number of particles in the samples. The smaller 700-particle sample achieved equilibrium faster than the larger 5115-particle sample. For the 700-particle samples, a 1-second simulation translated to approximately 30 hours of dedicated computer time on the a DEC 5000/120 UNIX workstation.

O2111
a/b = 1.4
θ = 0°
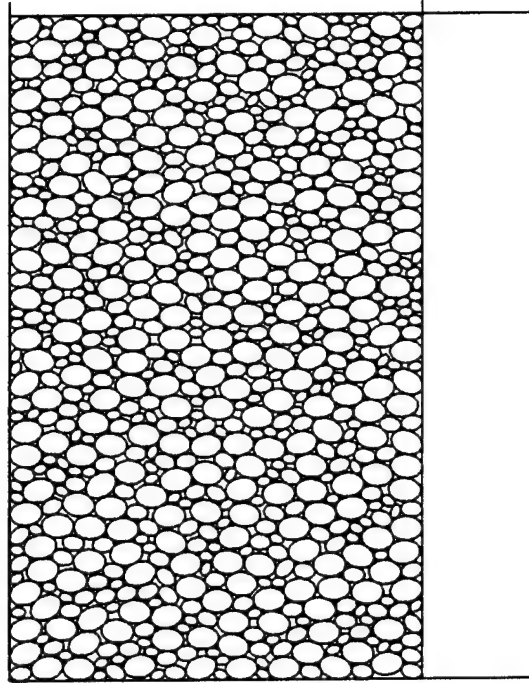
Figure 40. Typical isotropically compressed DEM sample with a/b = 1.4 and θ = 0° prior to shear.

·O2111
a/b = 1.4
θ = 0°
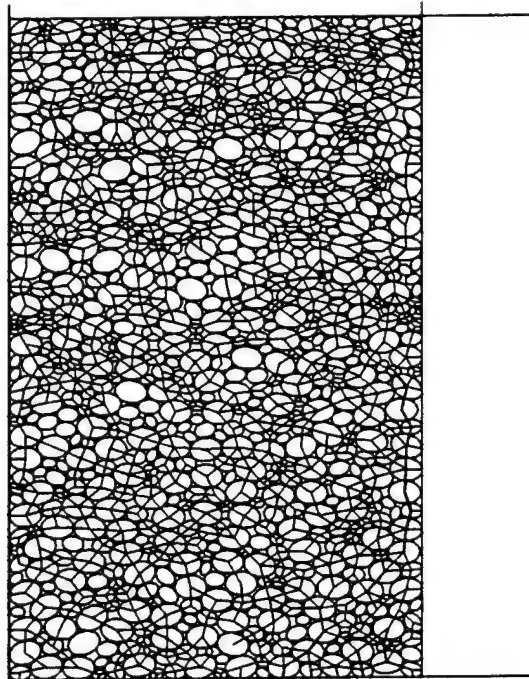
Figure 41. Force chains of a typical isotropically compressed DEM sample with a/b = 1.4 and θ = 0° prior to shear

54

6.3 Biaxial Compression Test Simulation

The isotropically compressed samples were sheared beyond failure under biaxial compression to approximately 10% axial strain using the simulation program PARSE. The compression tests were simulated by moving the top and bottom walls toward each other at a constant velocity while the right side wall maintained a confining stress of 0.7 kPa. Figures 42 and 43 show the test sample from Figures 40 and 41 at approximately 10% axial strain.

Owing to a need to conserve computational effort, it was necessary to minimize the number of timesteps needed to complete the shearing of the sample. This entailed shearing the samples at the fastest possible strain rate, with the largest possible time step of integration. If the walls are moved too fast (too high a strain rate), excessive dynamic and possibly abnormal numerical effects may occur, such as excessive overlapping between neighboring particles. It is desirable to move the walls as fast as possible without significantly compromising the model's accuracy.

To determine how fast the biaxial shear could be conducted without compromising accuracy, four biaxial compression tests were performed on the same sample with different wall velocities. To achieve 10% axial strain for each test simulation, top (-) and bottom (+) wall velocities of ±0.0192, ±0.0096, ±0.0064 and ±0.0048 m/s were used to compress the samples for 1, 2, 3 and 4 seconds, respectively. Figures 44 and 45 plot the deviator stress-axial strain and volumetric strain-axial strain data for these tests, which indicate little difference in the observed overall strength and deformation behavior. Based on these results, the numerical assemblages were biaxially compressed using the faster simulation time of 1 second with wall velocities of ±0.016 m/s, which represents an axial strain rate of about 0.1 s^{-1}. Note that in Figures 44, the deviator stress is quantified using the mobilized friction angle which was previously defined in equation (56). Also, note that in Figure 45 and in all subsequent plots, volumetric strain is plotted positive for contraction and negative for dilation (even though this is opposite to the compression positive sign convention).

To determine how large a timestep can be used, several considerations need to be made. The ellipse-based DEM model suggests a timestep Δt based on several considerations including the natural vibration of a single spring-mass system, multiple spring-single mass system, and ensuring that colliding particles remain in contact for at least three timesteps. These tests are described in detain in Corkum and Ting (1986). For the given particle geometry and contact properties used in the current study, a timestep of 2×10^{-5} s was suggested by FEGEN and PARSE. To test whether the suggested timestep was adequate to produce reasonably accurate results, a numerical sample was biaxially sheared under the same simulation conditions except with variations in the timestep. The results for the mobilized internal friction angle ϕ and the volumetric strain of these simulations are shown in Figures 46 and 47. The minor behavioral differences using the different timesteps suggests that use of $\Delta t = 2 \times 10^{-5}$ s is appropriate.

O2111
a/b = 1.4
θ = 0°
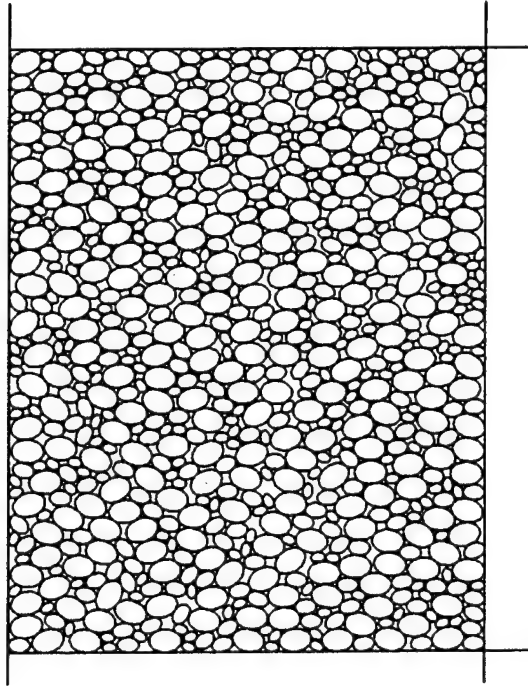
Figure 42. Biaxially compressed DEM sample with a/b = 1.4 and θ = 0° at approximately 10% axial strain

O2111
a/b = 1.4
θ = 0°
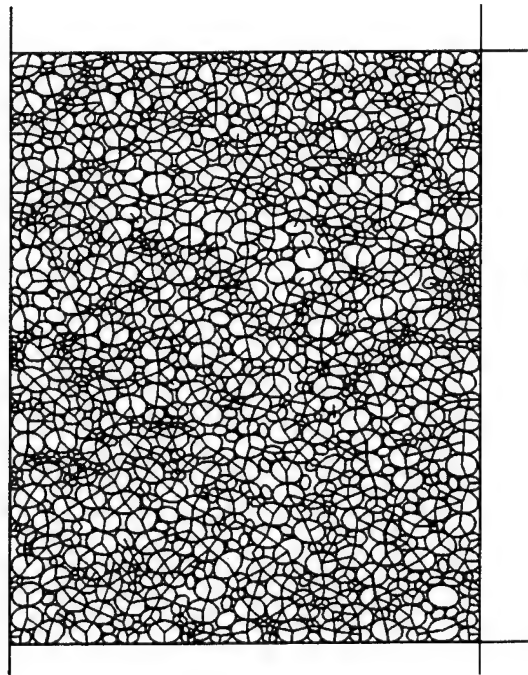
Figure 43. Force chains for biaxially compressed DEM sample with a/b = 1.4 and θ = 0° at approximately 10% axial strain
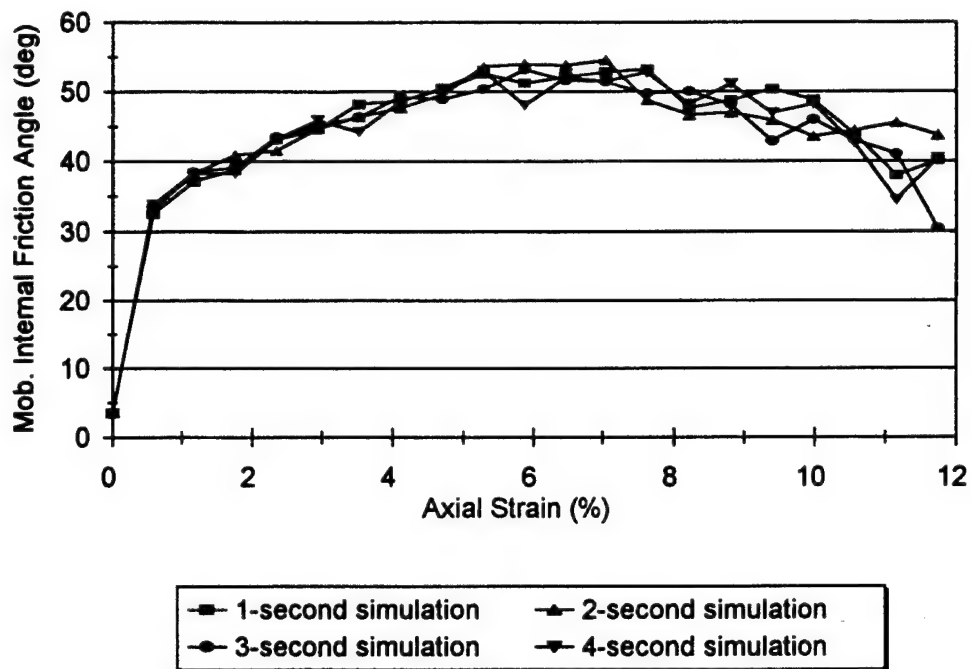
Figure 44. Mobilized internal friction angle for a/b = 3.0 and θ = 0° sample biaxially sheared using different wall velocities
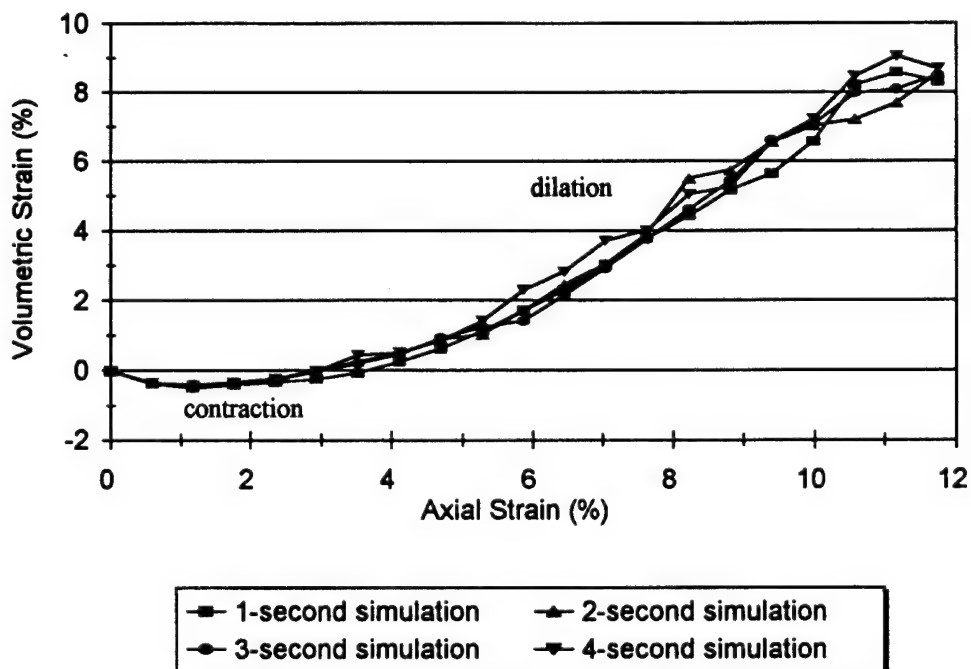
Figure 45. Volumetric strain behavior for a/b = 3.0 and θ = 0° sample biaxially sheared using different wall velocities

57
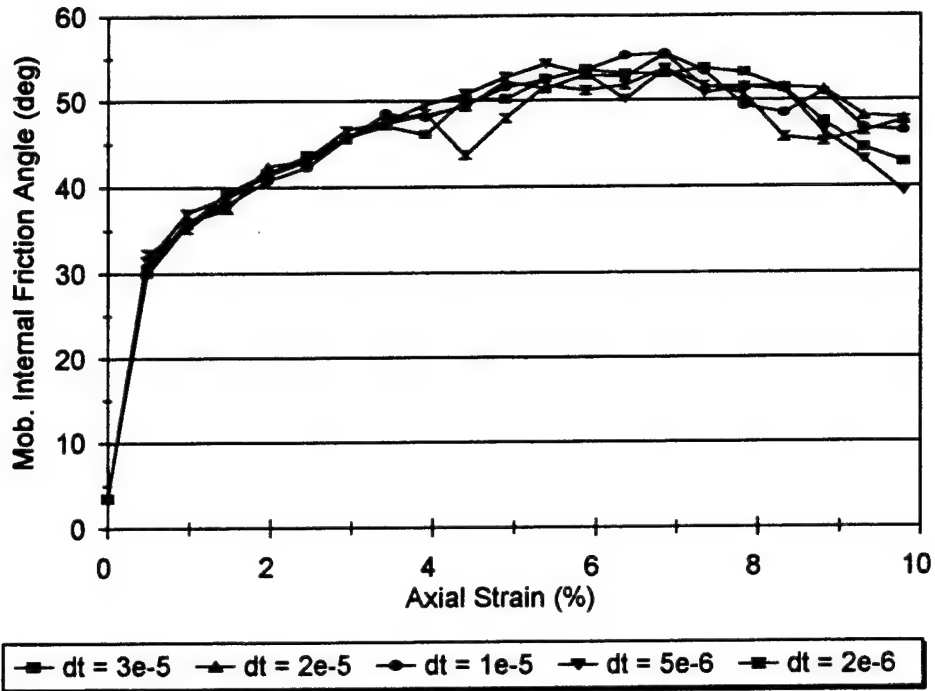
Figure 46. Mobilized internal angle of friction for a/b = 3.0 and θ = 0° sample biaxially sheared using different timesteps *dt*.
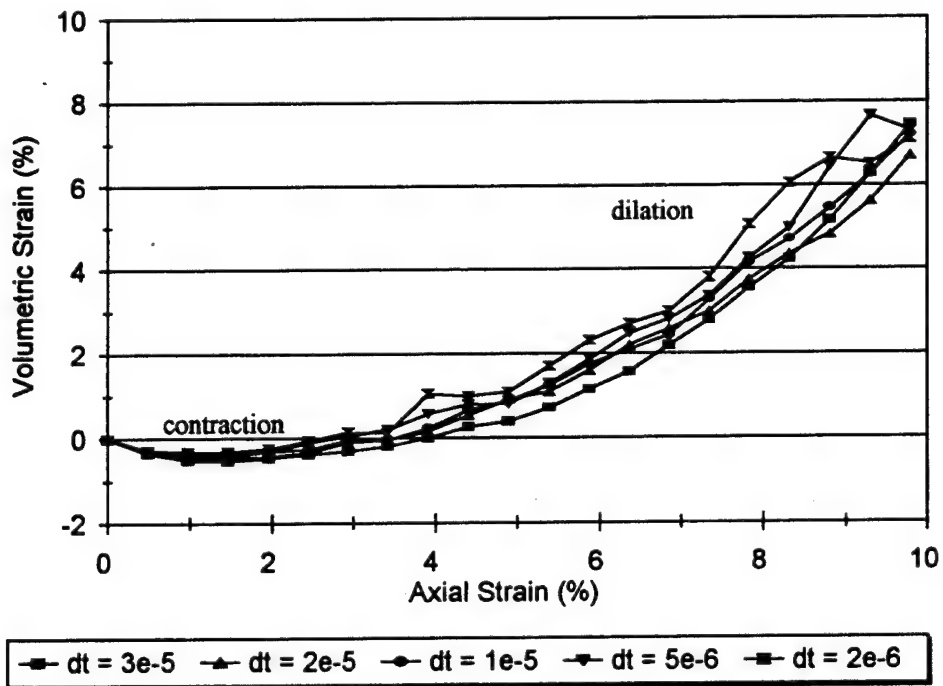
Figure 47. Volumetric strain behavior for a/b = 3.0 and θ = 0° sample biaxially sheared using different timesteps *dt*.

58

7. COMPARISON WITH KONISHI, ODA AND NEMAT-NASSER RESULTS

As previously described in Section 5.4, Konishi, Oda and Nemat-Nasser (1983, 1982) investigated the influence of particle shape on the overall mechanical behavior of granular materials using photoelastic polyurethane rubber rods. In that Section, a series of detailed photographic plates supplied by Prof. Oda was digitized and used as input to the DEM simulation. This single physical test was then used in the validation phase of this study. In the current Section, the other experimental results from the Konishi *et al* tests are compared with DEM results. The numerical tests in this Section have the same overall general geometry and particle gradation as the physical tests, but not the exact initial locations. As before, the DEM particles have slightly different shapes (ellipse *vs* oval) but the same overall dimensions. Results obtained from the ellipse-based DEM test simulations are similar qualitatively to the physical test data reported by Konishi *et al*. The numerical results, however, yield consistently lower stresses than the physical test results. As previously described for the single test comparison in Section 5.6, it is conjectured that these differences are due to differences in the particle shapes.

7.1 Data Comparison for Samples with $\phi_\mu = 26°$

Figure 48 shows the influence of particle angularity and preferred (or aligned) particle bedding on the peak internal friction angle ϕ_{max} for the physical and DEM samples with interparticle sliding friction angle ϕ_μ of 26°. Qualitatively, the results are similar. In general, higher values for ϕ_{max} are achieved by samples with preferred horizontal bedding ($\theta = 0°$), while for samples with 60 and 90° bedding, the values are lower. Samples consisting of angular particles (a/b = 1.4) yield higher internal friction angles than those consisting of more rounded particles (a/b = 1.1). The results of the physical tests performed by Konishi *et al*, however, are significantly higher than the results obtained from the DEM test simulations.
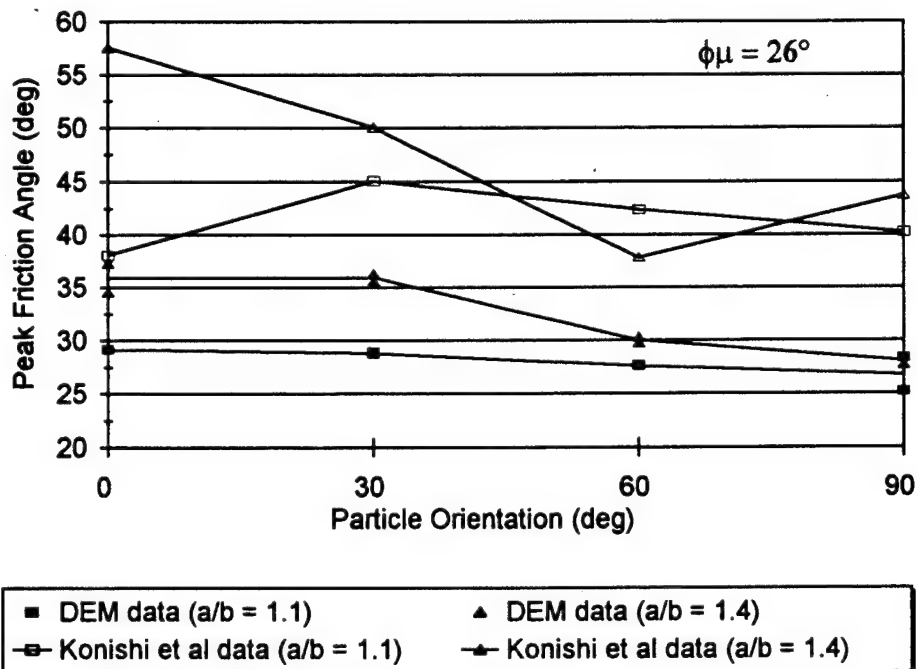
Figure 48. Comparison of DEM results and Konishi *et al* (1983) physical results for samples with an interparticle sliding friction angle ϕ_μ of 26°

The peak friction angles ϕ_{max} and initial void ratios (e_o) for the physical and numerical samples are presented in Table 8. The DEM results are average values for numerical samples having the same particle aspect ratio a/b, bedding plane θ and confining stress ($\sigma_2 = 0.7$ kPa). In general, ϕ_{max} increases with particle angularity, the exception being the physical sample with 60° bedding. The slightly looser numerical samples yield significantly lower values for ϕ_{max} than the physical samples used by Konishi.

Cross-Section Group	Interparticle Friction Angle ϕ_μ (°)	Bedding Angle θ (°)	Initial Void Ratio e_o		Peak Internal Friction Angle ϕ_{max} (°)	
			DEM data*	Konishi et al data	DEM data*	Konishi et al data
Oval 1	26	0	0.186	----	29	42
		30	0.184	0.169	29	46
		60	0.181	0.174	28	43
		90	0.182	0.168	27	41
Oval 2	26	0	0.174	0.158	36	58
		30	0.163	0.160	36	50
		60	0.165	0.155	30	39
		90	0.166	----	28	44

* Average values for numerical samples with similar geometries

Table 8.   Results of biaxial compression tests performed by Konishi et al and DEM test simulations

Figures 49 to 52 show the progression of the principal stress ratio σ_1/σ_2 during the course of deformation for the physical and numerical samples with bedding planes of 0, 30, 60 and 90°, respectively. The data yielded by both the physical and numerical samples show that σ_1/σ_2 achieves higher peak values for samples with angular particles ($a/b = 1.4$). The peak principal stress ratio achieved by the physical samples is significantly higher than the DEM samples and is achieved at much lower failure strains. The differences in the residual stress ratios, however, are rather insignificant. The differences in peak stress ratio between the Konishi data and the DEM data are worst in samples with horizontal bedding ($\theta = 0°$).
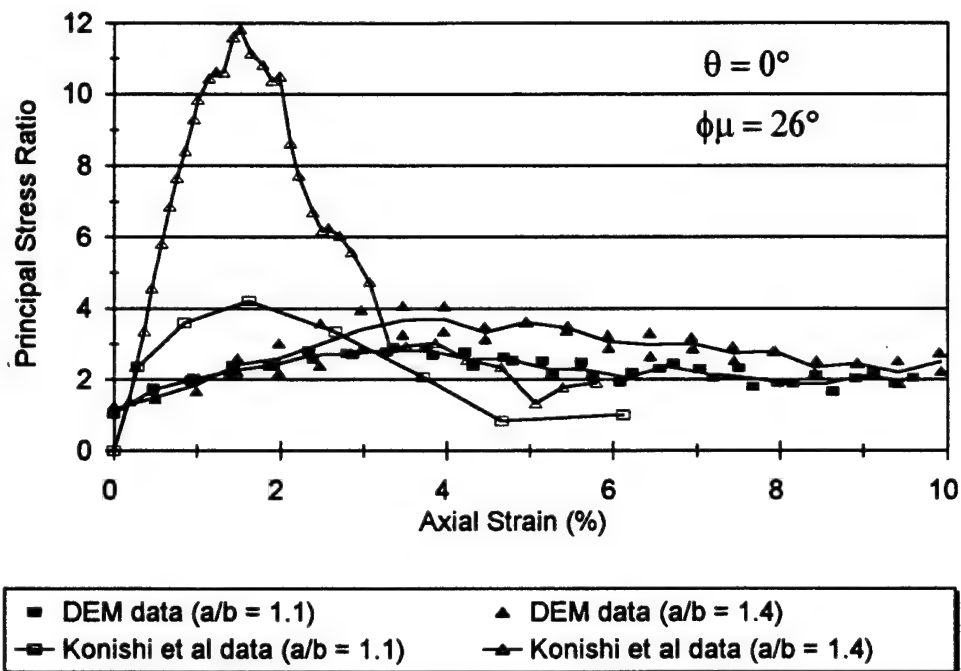
Figure 49. Comparison of DEM and Konishi *et al* physical results for samples with 0° bedding and interparticle sliding friction angle ϕ_μ of 26°.
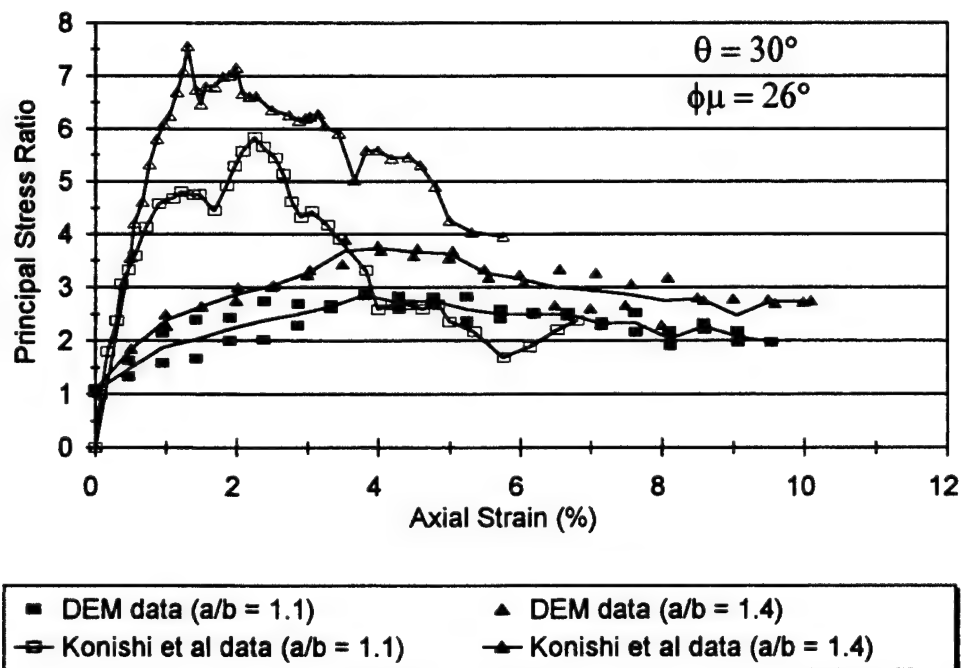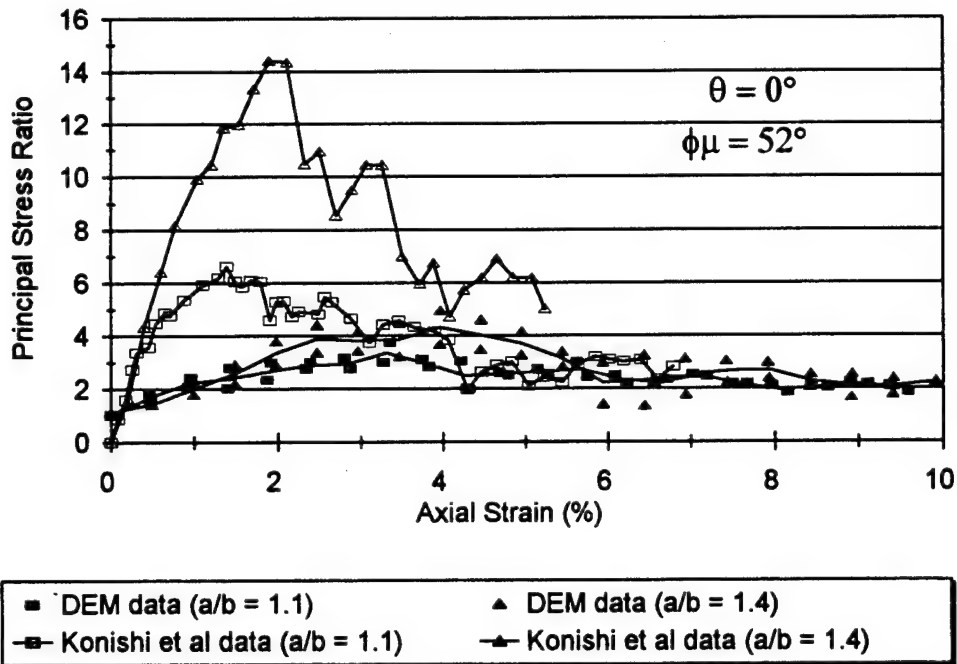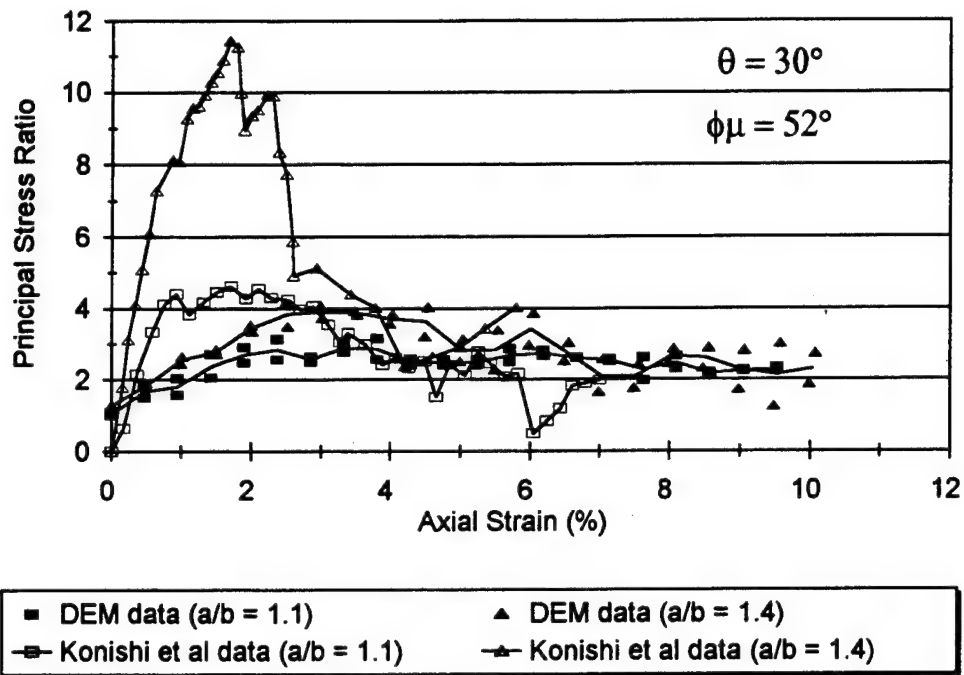

Figure 50. Comparison of DEM and Konishi *et al* physical results for samples with 30° bedding and interparticle sliding friction angle ϕ_μ of 26°.
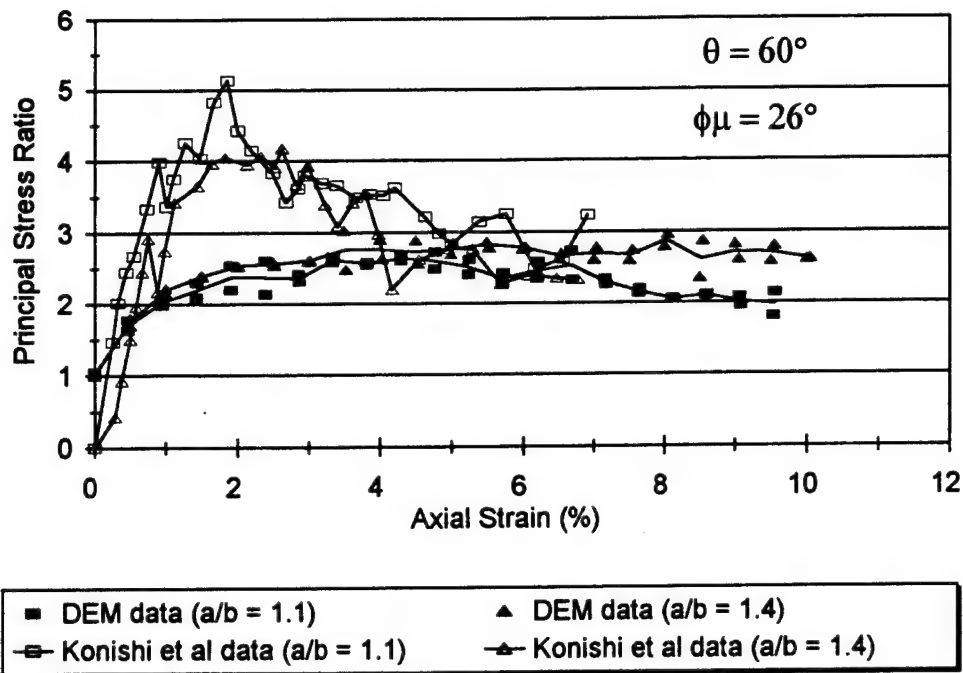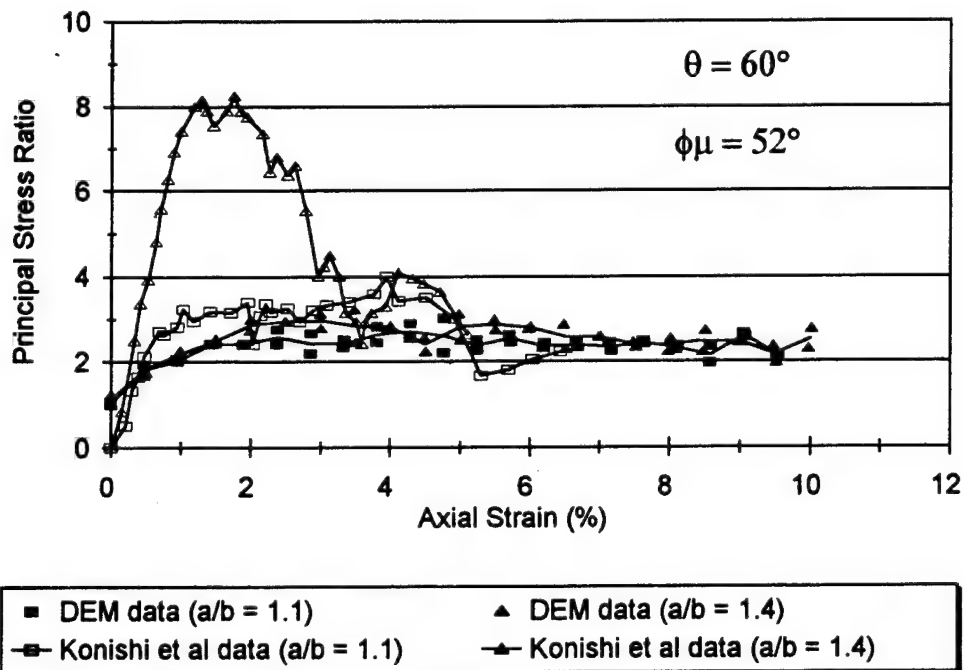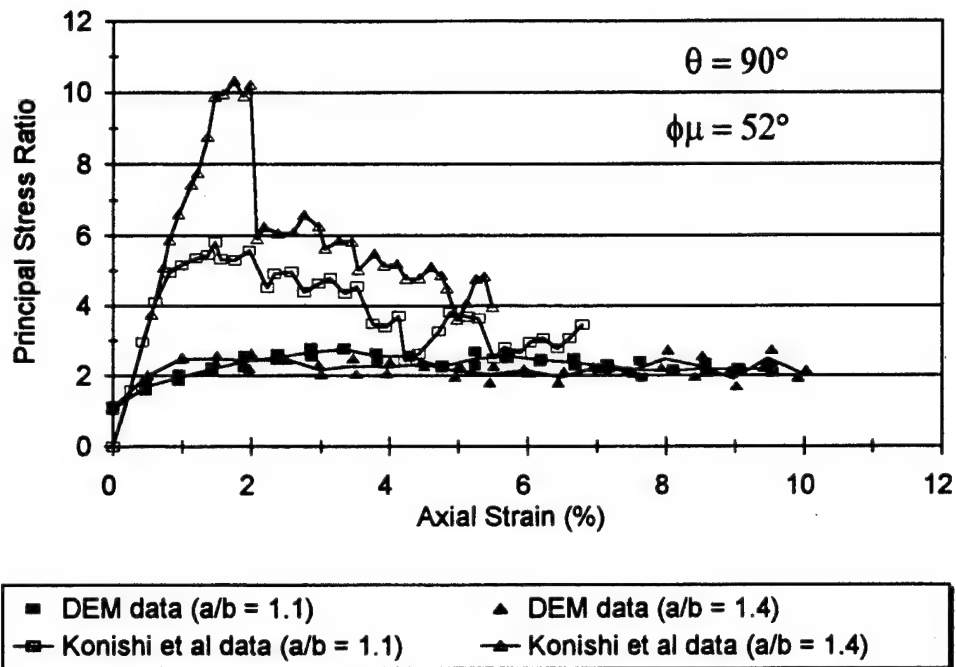
Figure 51. Comparison of DEM and Konishi *et al* physical results for samples with 60° bedding and interparticle sliding friction angle ϕ_μ of 26°.
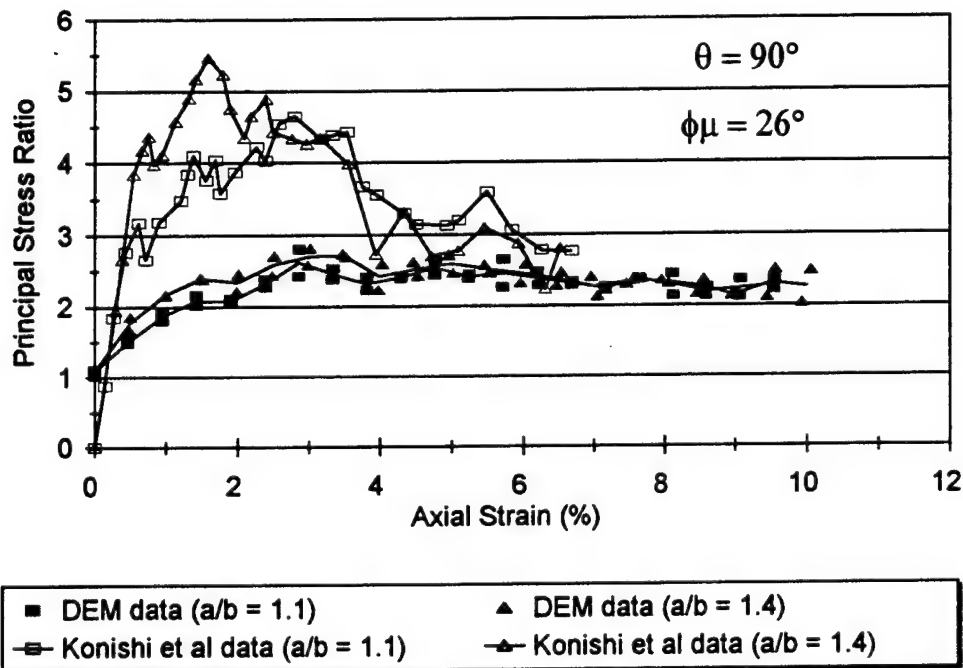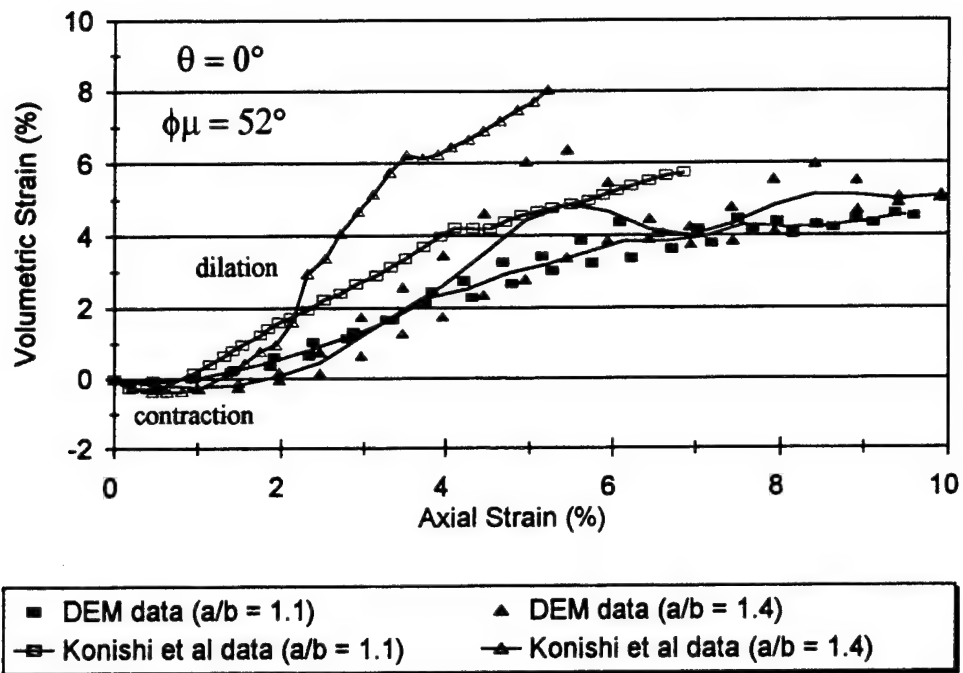

Figure 52. Comparison of DEM and Konishi *et al* physical results for samples with 90° bedding and interparticle sliding friction angle ϕ_μ of 26°.

Figures 53 to 56 plot the physical and DEM volumetric strain $\Delta V/V_o$ data for assemblages with 0, 30, 60 and 90° bedding (with dilation plotted positive). Assemblages with angular particles (a/b = 1.4) and preferred horizontal bedding ($\theta = 0°$) initially contract more and longer than those consisting of more rounded particles (a/b = 1.1), but ultimately dilate more and faster as deformation continues. For assemblages with 60° bedding, however, particle angularity has the opposite effect on $\Delta V/V_o$. Samples consisting of angular particles experience less dilation throughout the course of deformation than those with rounded particles. Though the physical and DEM samples both exhibit volumetric strain behavior similar qualitatively to that of real granular materials, the physical samples are stiffer, dilating significantly more than the numerical samples and reaching their peak values at much lower axial strains. The differences in the Konishi and DEM results for $\Delta V/V_o$ are larger for samples with horizontal bedding, while for samples with 60° bedding, the differences are smaller.
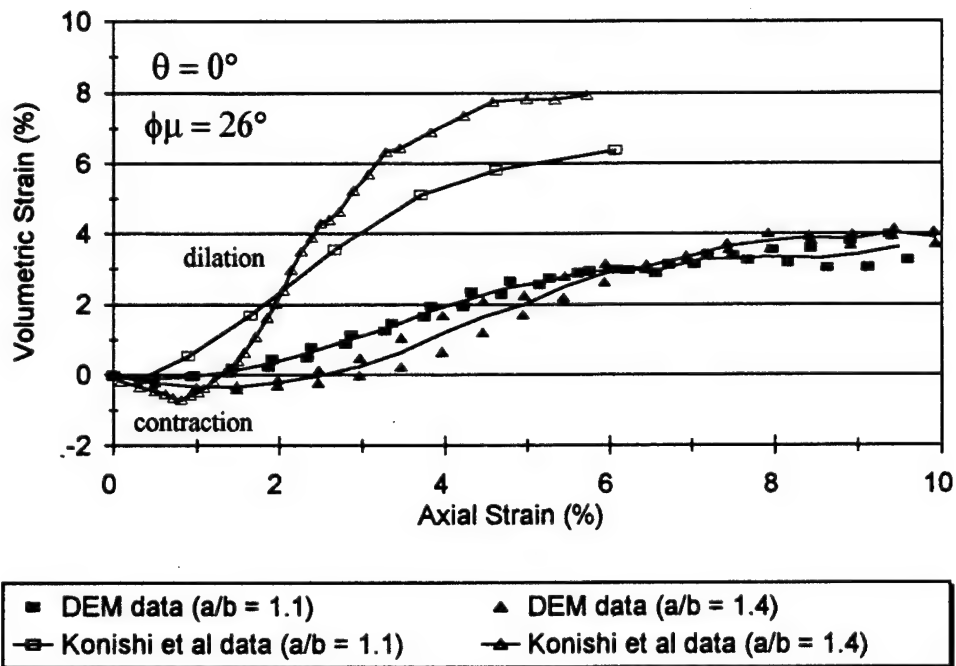
Figure 53. Comparison of DEM and Konishi *et al* physical results for samples with 0° bedding and interparticle sliding friction angle ϕ_μ of 26°.
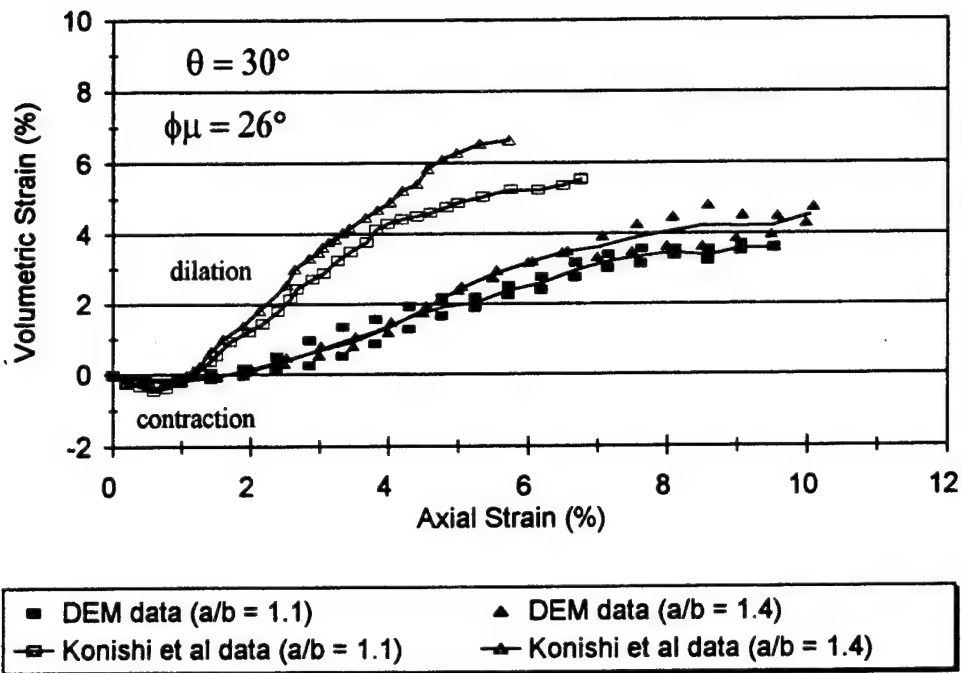
Figure 54. Comparison of DEM and Konishi *et al* physical results for samples with 30° bedding and interparticle sliding friction angle ϕ_μ of 26°.
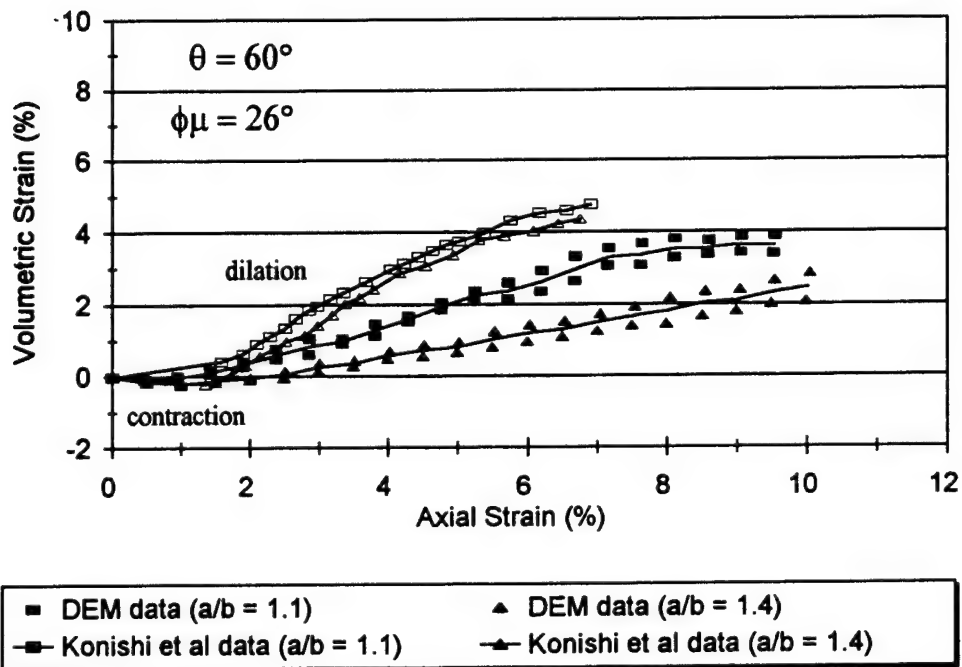
Figure 55. Comparison of DEM and Konishi *et al* physical results for samples with 60° bedding and interparticle sliding friction angle ϕ_μ of 26°.

64
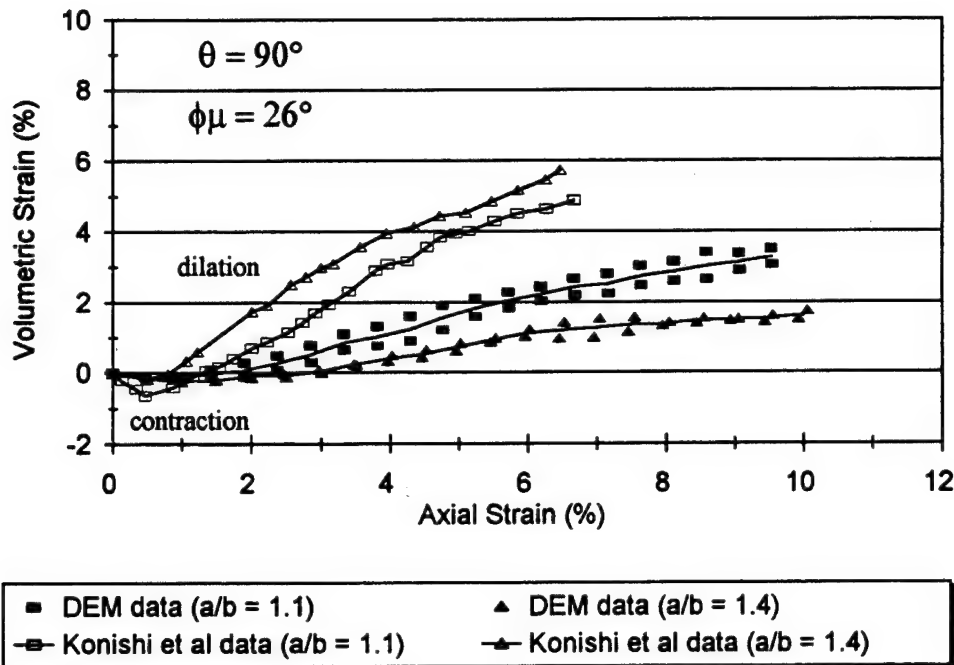
Figure 56. Comparison of DEM and Konishi *et al* physical results for samples with 90° bedding and interparticle sliding friction angle ϕ_μ of 26°

7.2 Data Comparison for Samples with $\phi_\mu = 52°$

Figure 57 plots the influence of particle angularity and preferred particle bedding on the peak internal friction angle ϕ_{max} for the physical and DEM samples with interparticle sliding friction angle ϕ_μ of 52°. Higher values for ϕ_{max} are achieved by samples with preferred horizontal bedding ($\theta = 0°$), while for samples with 60 and 90° bedding, ϕ_{max} is lower. Assemblages with angular particles (a/b = 1.4) yield higher peak internal friction angles than those with more rounded particles (a/b = 1.1). As with the results for $\phi_\mu = 26°$, the physical results are qualitatively similar to the DEM results, but quantitatively much larger in strength.

Table 9 presents the peak friction angle ϕ_{max} and initial void ratio e_o for the physical and numerical samples with $\phi_\mu = 52°$. The DEM results are average values for numerical samples having the same particle aspect ratio a/b, bedding plane θ and confining stress ($\sigma_2 = 0.7$ kPa). Both the Konishi *et al* and DEM assemblages with $\phi_\mu = 52°$ exhibit higher strength than those with ϕ_μ of 26°. As with the results for $\phi_\mu = 26°$, ϕ_{max} increases as particle angularity increases, the exception being the numerical sample with 90° bedding. The differences between the physical and numerical results, however, are still very significant. Though the relative densities of the physical and DEM samples are similar, the test simulations yield significantly lower values for ϕ_{max} than the physical tests.

65
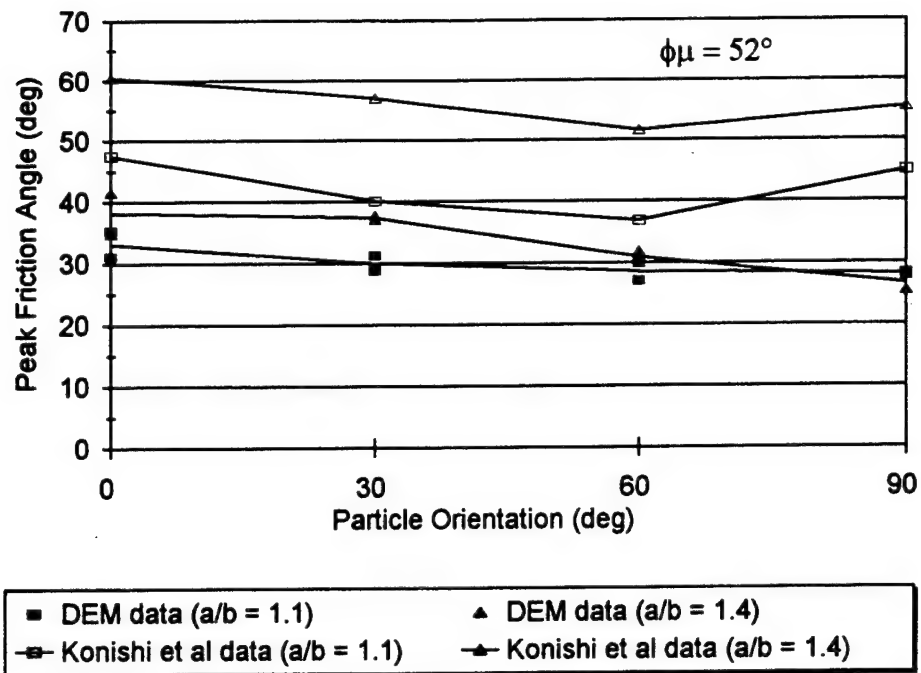
Figure 57. Comparison of DEM and Konishi *et al* physical results for samples with interparticle sliding friction angle ϕ_μ of 52°.

Cross-Section Group	Interparticle Friction Angle ϕ_μ (°)	Bedding Angle θ (°)	Initial Void Ratio e_o		Peak Internal Friction Angle ϕ_{max} (°)	
			DEM data*	Konishi et al data	DEM data*	Konishi et al data
Oval 1	52	0	0.188	0.190	33	49
		30	0.186	0.183	30	40
		60	0.183	0.185	29	37
		90	0.185	0.192	28	45
Oval 2	52	0	0.181	0.177	38	60
		30	0.170	0.154	37	57
		60	0.173	0.159	31	52
		90	0.174	0.155	27	55

* Average values for numerical samples with similar geometries

Table 9. Results of biaxial compression tests performed by Konishi *et al* and DEM test simulations.

Figures 58 to 61 plot the principal stress ratio σ_1/σ_2 vs axial strain for the physical and DEM tests with ϕ_μ of 52° and bedding planes of 0, 30, 60 and 90°, respectively. Though the peak values achieved by the physical and numerical tests do not agree, the residual values compare favorably. Also, the residual values for σ_1/σ_2 are about the same regardless of differences in particle angularity and orientation. As with $\phi_\mu = 26°$, the physical samples with $\phi_\mu = 52°$ exhibit stiffer behavior, yielding higher peak values for σ_1/σ_2 at lower failure strains than the DEM samples.

Figure 58. Comparison of DEM and Konishi *et al* results for samples with 0° bedding and interparticle sliding friction angle ϕ_μ of 52°.

Figure 59. Comparison of DEM and Konishi *et al* results for samples with 30° bedding and interparticle sliding friction angle ϕ_μ of 52°.

Figure 60. Comparison of DEM and Konishi *et al* results for samples with 60° bedding and interparticle sliding friction angle ϕ_μ of 52°.

68

Figure 61. Comparison of DEM and Konishi *et al* results for samples with 90° bedding and interparticle sliding friction angle ϕ_μ of 52°.

Figures 62 to 65 plot the volumetric strain behavior for the physical and numerical tests with an interparticle sliding friction angle ϕ_μ of 52° and 0, 30, 60 and 90° bedding, respectively. Samples consisting of angular particles (a/b = 1.4) with preferred horizontal bedding ($\theta = 0°$) experience more and longer initial contraction than those with more rounded particles (a/b = 1.1). At larger axial strains, however, assemblages with angular particles dilate more. Both the physical and DEM assemblages with a/b = 1.4 and 60° bedding dilate less during the course of deformation than those with a/b = 1.1. Though both the physical and numerical samples exhibit volumetric strain behavior similar qualitatively to that of real granular materials, the physical samples are stiffer, dilating significantly more and faster than the DEM samples.

Figure 62. Comparison of DEM and Konishi *et al* results for samples with 0° bedding and interparticle sliding friction angle ϕ_μ of 52°.
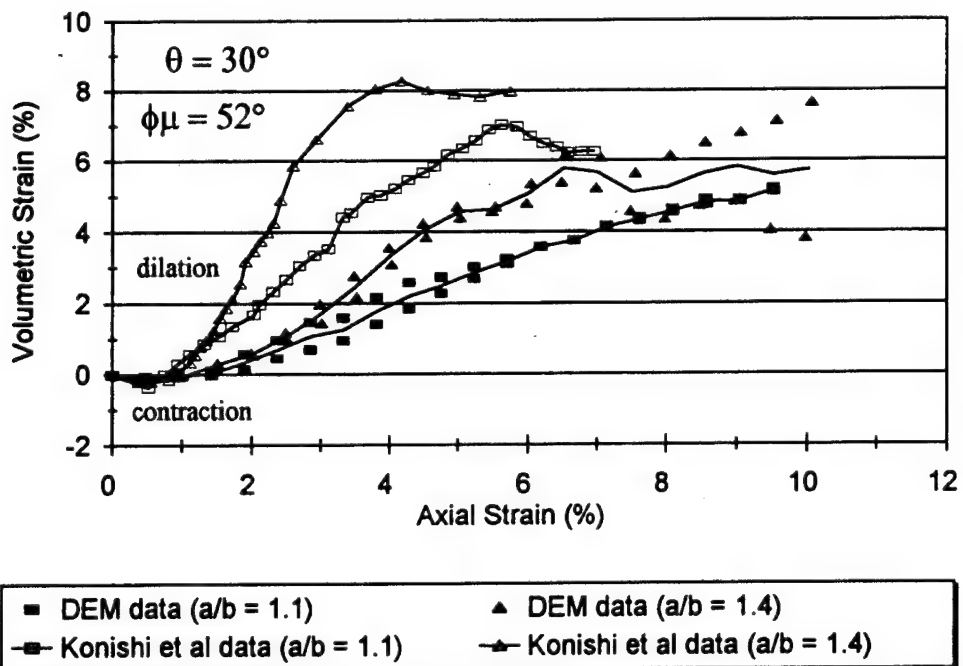
Figure 63. Comparison of DEM and Konishi *et al* results for samples with 30° bedding and interparticle sliding friction angle ϕ_μ of 52°.
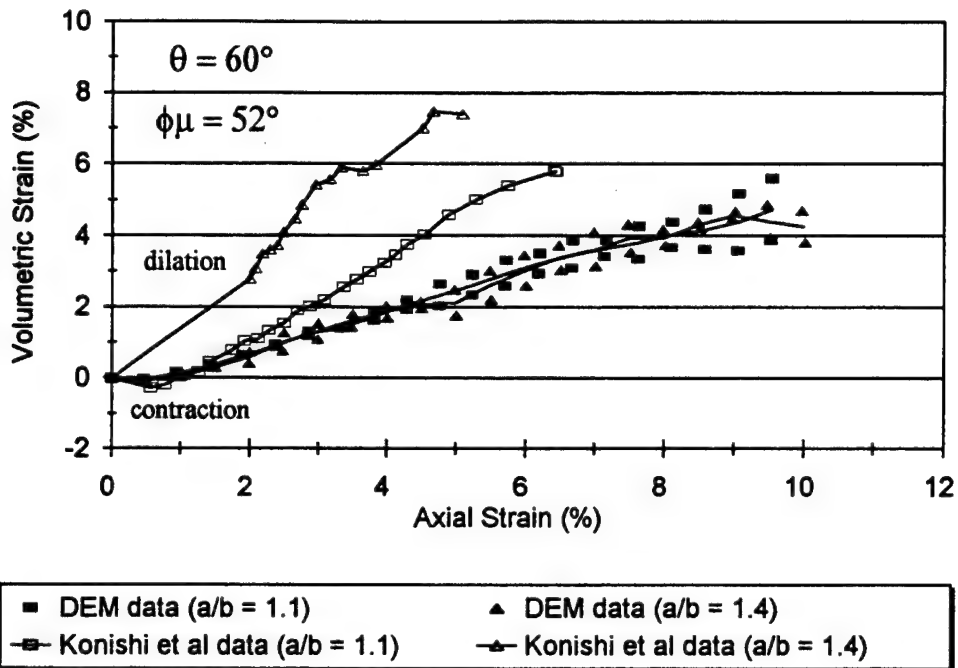
Figure 64. Comparison of DEM and Konishi *et al* results for samples with 60° bedding and interparticle sliding friction angle ϕ_μ of 52°.
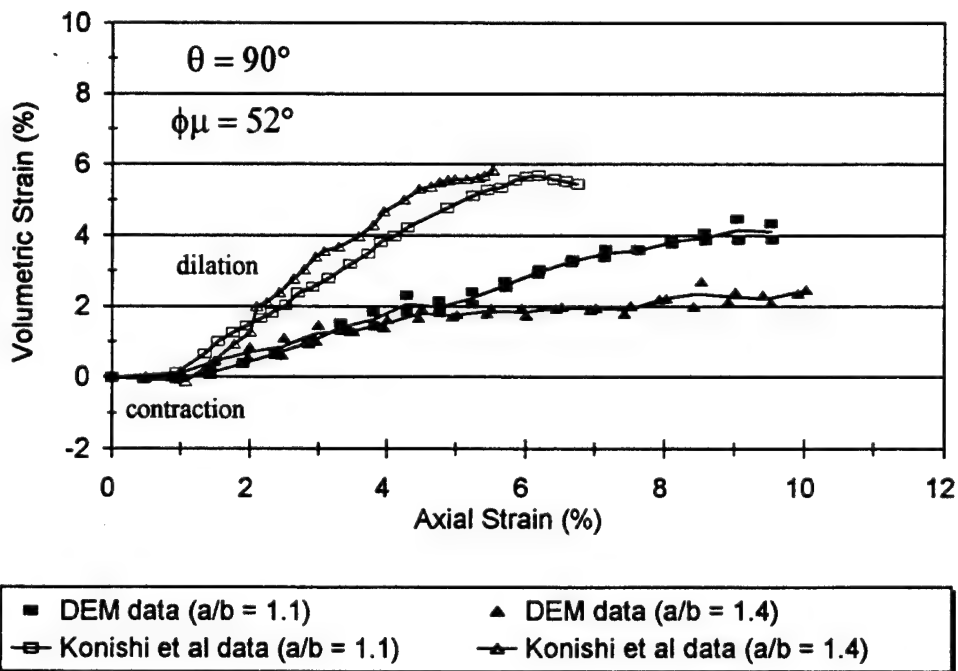
Figure 65. Comparison of DEM and Konishi *et al* results for samples with 90° bedding and interparticle sliding friction angle of 52°.

7.3 Discussion of Data Comparison

As with the validation test on the single digitized sample, comparison of the physical and numerical biaxial shear test results using samples with similar gradation and overall properties demonstrated significant differences in strength and deformation behavior. Higher strength and more dilation are achieved by the physical samples at much lower axial strains. The discrepancies in the physical and DEM data may be caused by a number of reasons. The accuracy of the ellipse-based DEM model, the nature of the contact interaction, the selection of properties and parameters and the differences in the shape of the particles (oval *vs.* ellipse) are considered as possible causes for the discrepancy in results.

Based on extensive testing of the code as outlined in Section 4.4, one presumes that the ellipse-based DEM model is working properly. Based on the results described in Section 5.5, variation of the form and value of the contact properties does not appear to significantly alter the observed macroscopic strength and volume behavior. An alternate explanation for the discrepancy is based on subtle differences in the shape of the physical and numerical particles. This hypothesis was examined for the single digitized test in Section 5.6. In this Section, this hypothesis is further examined for the tests on samples at different bedding angles.

As mentioned earlier, Konishi *et al* used photoelastic rubber rods with oval-shaped cross-sections, while the current study uses ellipse-shaped particles. A close visual examination of the oval-shaped rods in Figures 29 shows that their sides are flattened, while the surface of the ellipse-shaped particles are continuously rounded. Presumably, the flattened sides facilitate a more stable packing when the particles are assembled or "stacked". When subjected to a vertical shear stress, the physical samples form particulate columns that are far more stable and can resist significantly higher shear stresses than the ellipse-based assemblages, especially when the bedding plane is horizontal. For the 1.4:1 aspect ratio test, this is analogous to axial loading of an uncemented brick wall. The particulate columns formed by the ellipse-shaped particles, however, are less stable and hence weaker.

Figures 66 and 67 compare the rose diagrams of the contact normal distribution prior to shear and at peak strength for the numerical and physical samples with a particle aspect ratio a/b of 1.4, preferred horizontal bedding ($\theta = 0°$) and interparticle sliding friction angle ϕ_μ of 26°. The contact statistics are computed assuming two contact normals exist at each contact. The rosettes for the numerical assemblages consider only interparticle contacts and exclude wall-particle contacts. The physical sample yields a more anisotropic distribution prior to shear achieving a maximum frequency of approximately 13%, while the numerical sample is less anisotropic and achieves a maximum frequency of only 9%. This suggests that the physical sample is more stable prior to shear as more contact normals are oriented toward the vertical and are predisposed to provide more resistance to the vertically applied shear stress σ_1. At peak strength, the contact normal distribution for Konishi's assemblage is again more anisotropic than the numerical sample as the flattened sides of the oval-shaped particles produce more contact normals that are coaxial with σ_1.

Discrepancies also exist in the data comparison for samples having preferred bedding planes of 30, 60 and 90°. These differences, however, are not as large as those observed for samples with horizontal bedding. The smallest difference in ϕ_{max} occur in samples with 60° bedding with Konishi *et al* reporting a value of 39° and the DEM yielding an average value of 30°. Presumably, the flattened sides of the rubber particles become less influential on the sample's strength behavior as the orientation of the contact plane and the direction of the applied shear stress becomes skewed.

Figures 68 and 69 compares the contact normal frequency distributions prior to shear and at peak strength for physical and DEM samples with a/b = 1.4, $\theta = 60°$ and $\phi_\mu = 26°$. While the rosettes show that the oval-shaped particles possess a more skewed distribution of contact normals,, the differences are less significant than those observed in samples with preferred horizontal bedding ($\theta = 0°$).
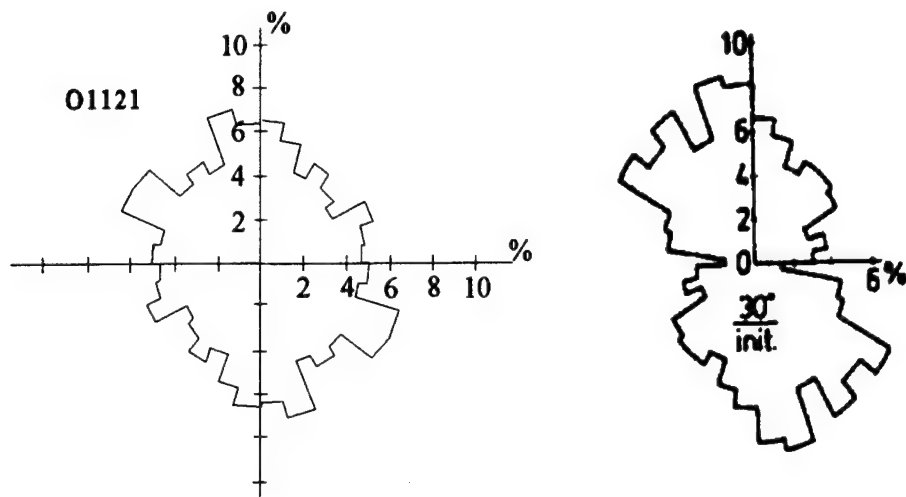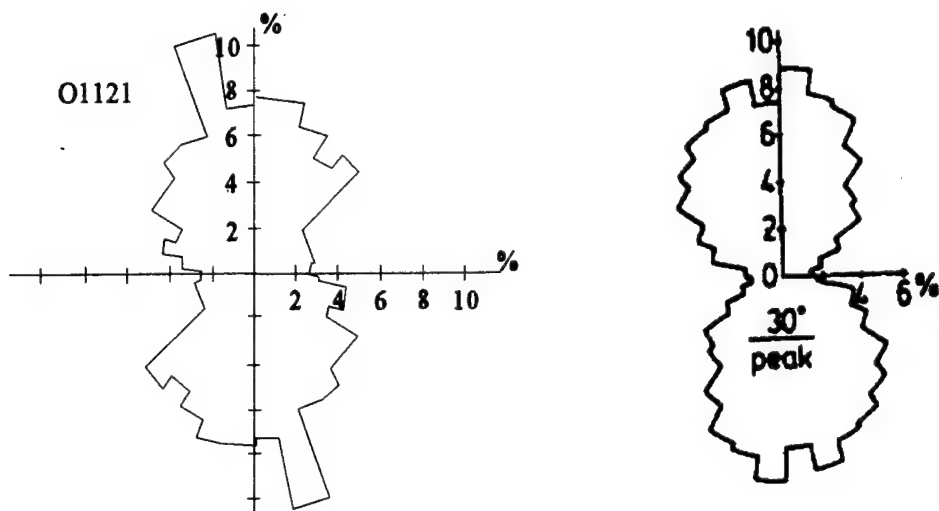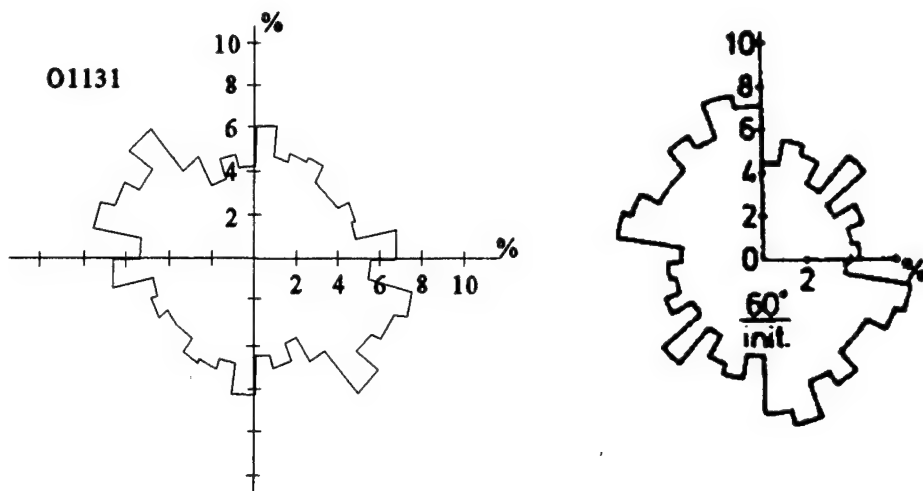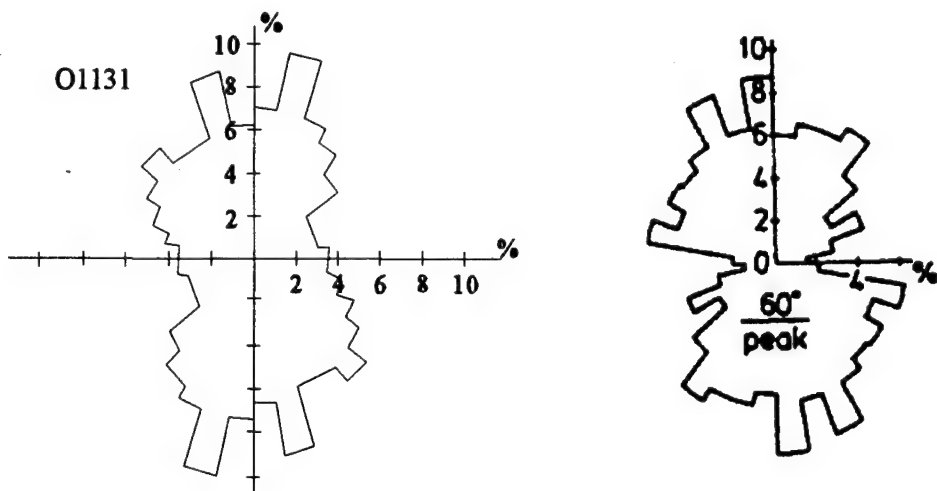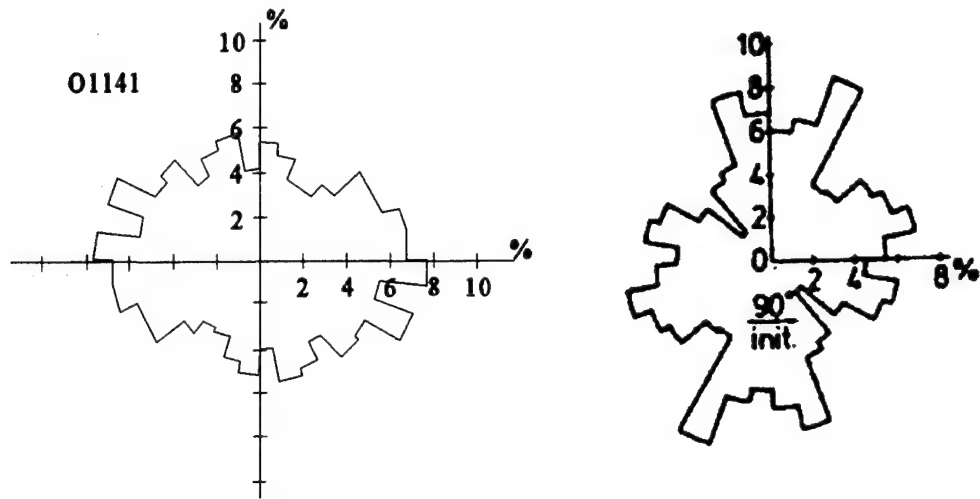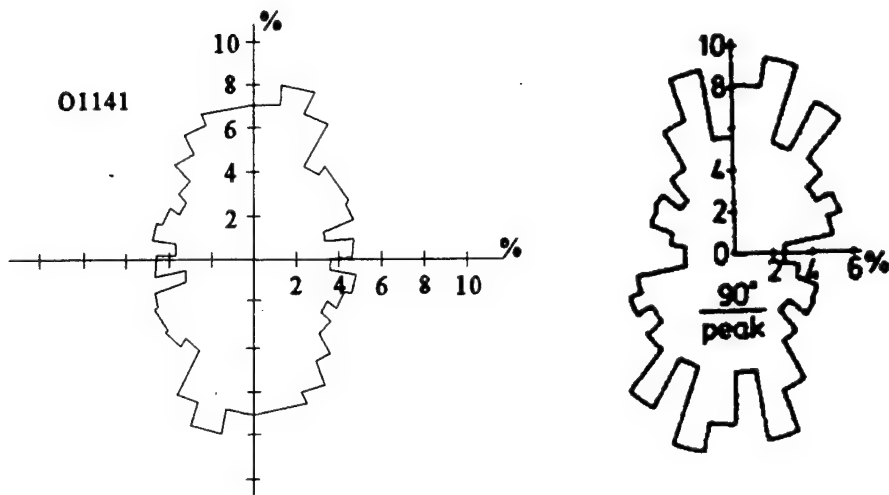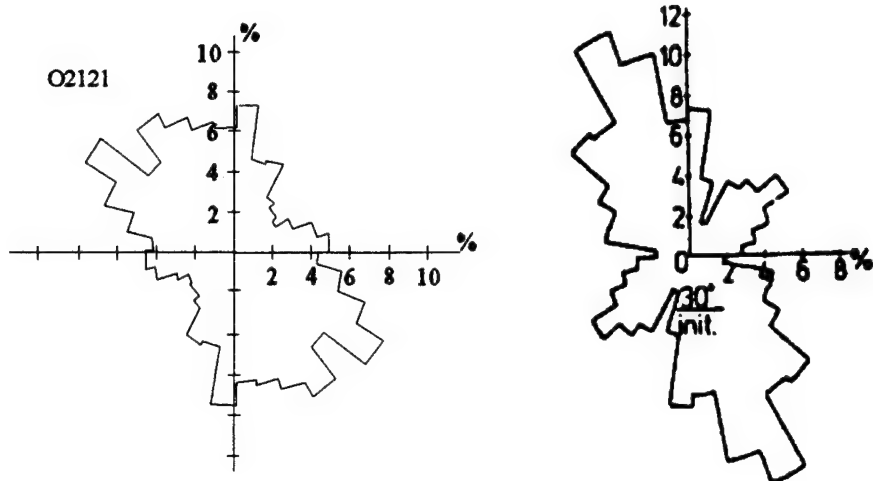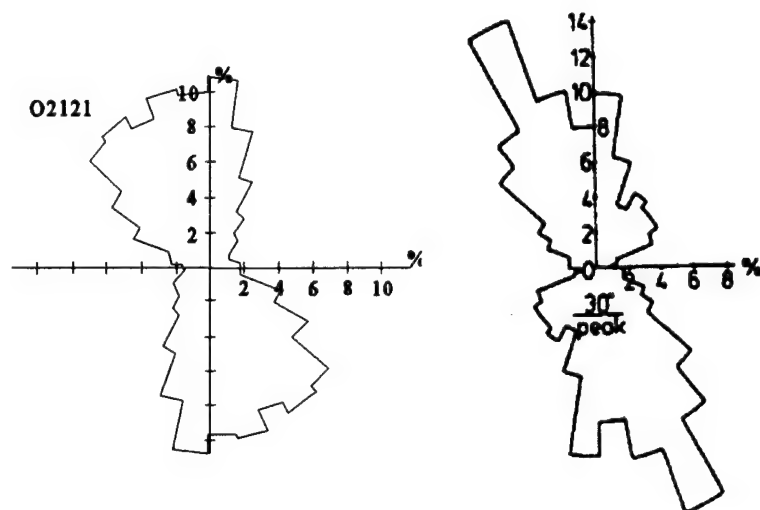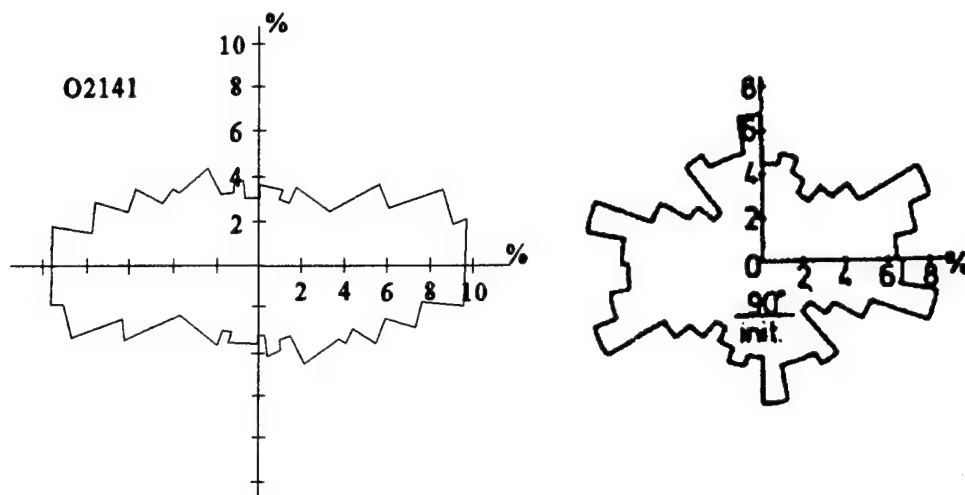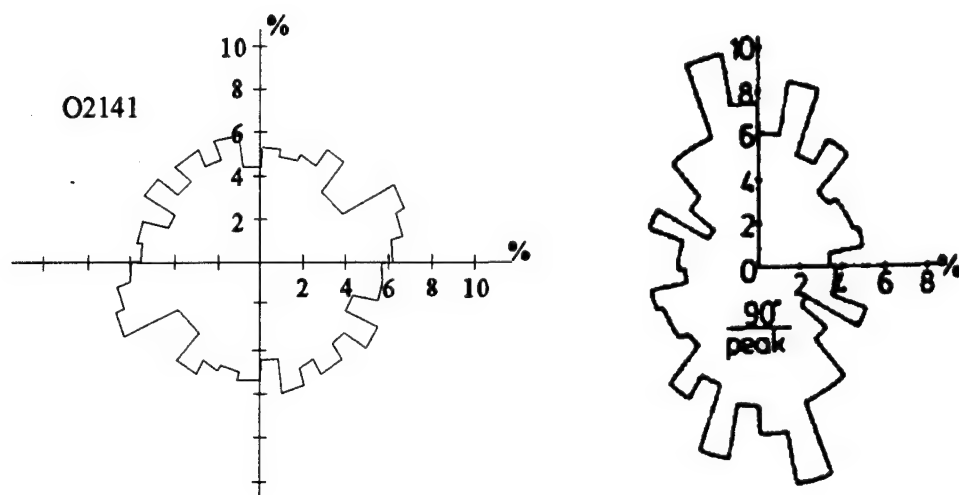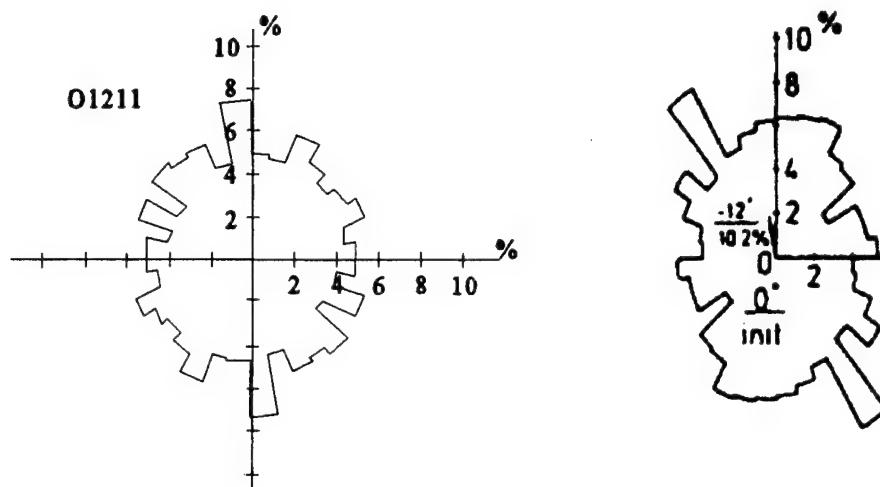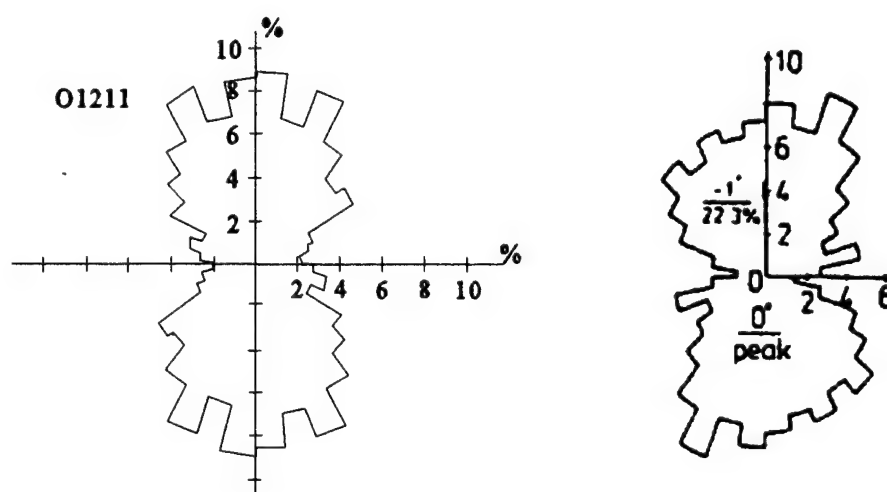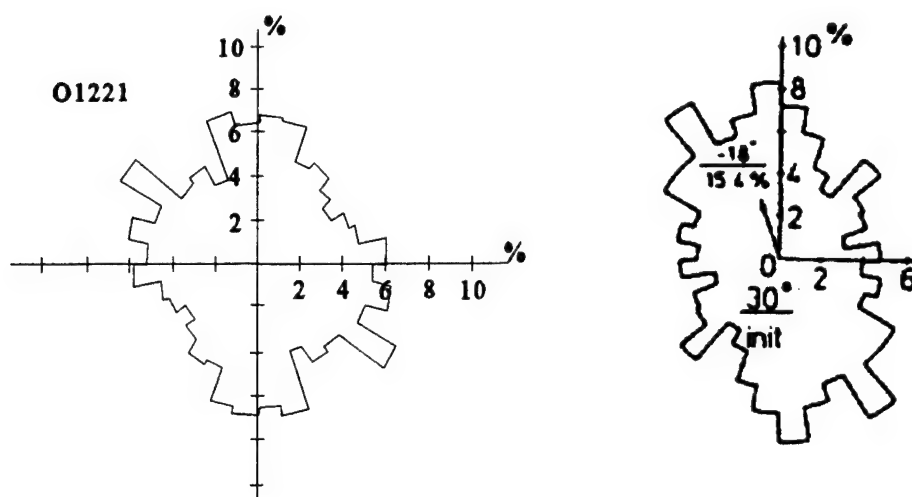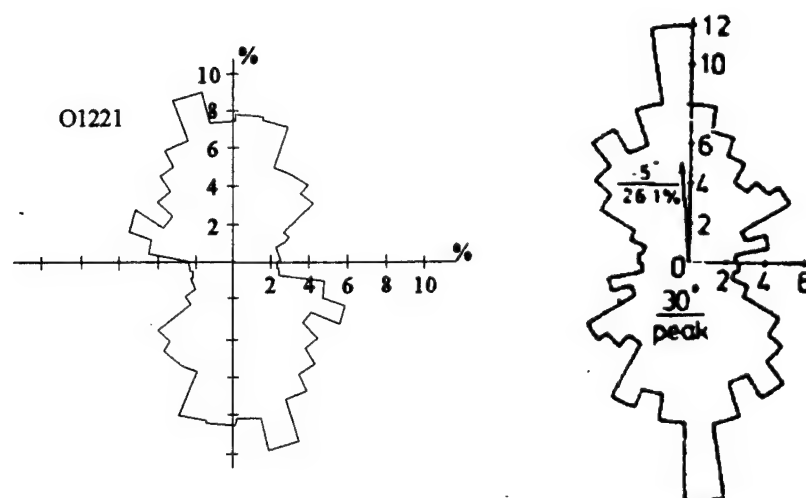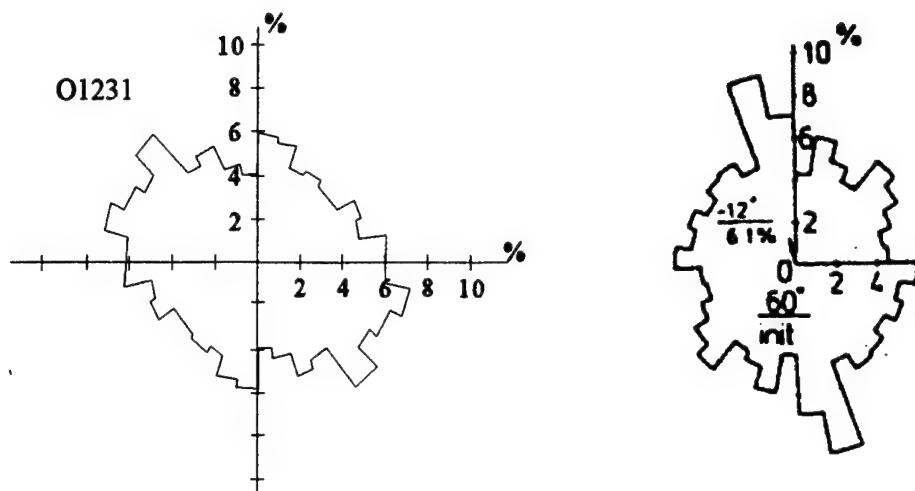
72
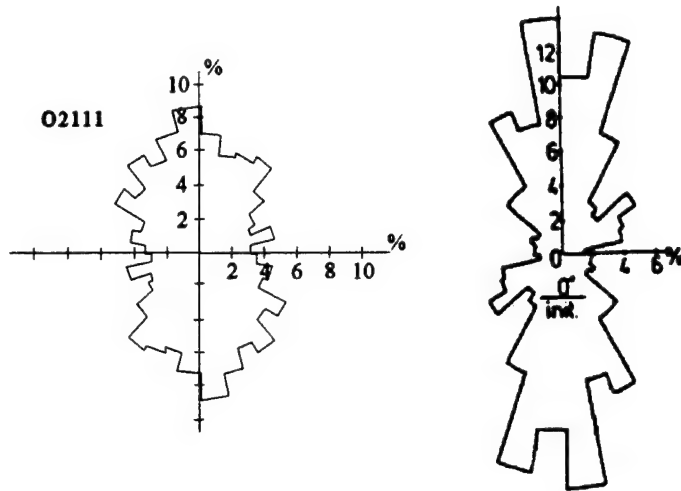
Figure 66. Frequency distribution of contact normals for numerical (left) and physical samples with a/b = 1.4, θ = 0° and ϕ_μ = 26° prior to shear.
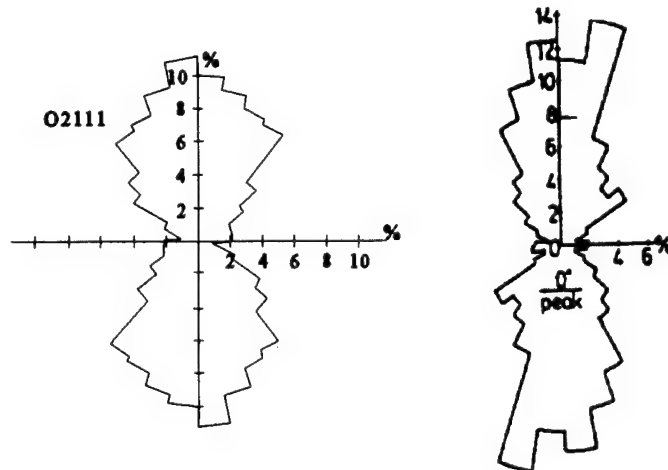
Figure 67. Frequency distribution of contact normals for numerical (left) and physical samples with a/b = 1.4, θ = 0° and ϕ_μ = 26° at peak strength.
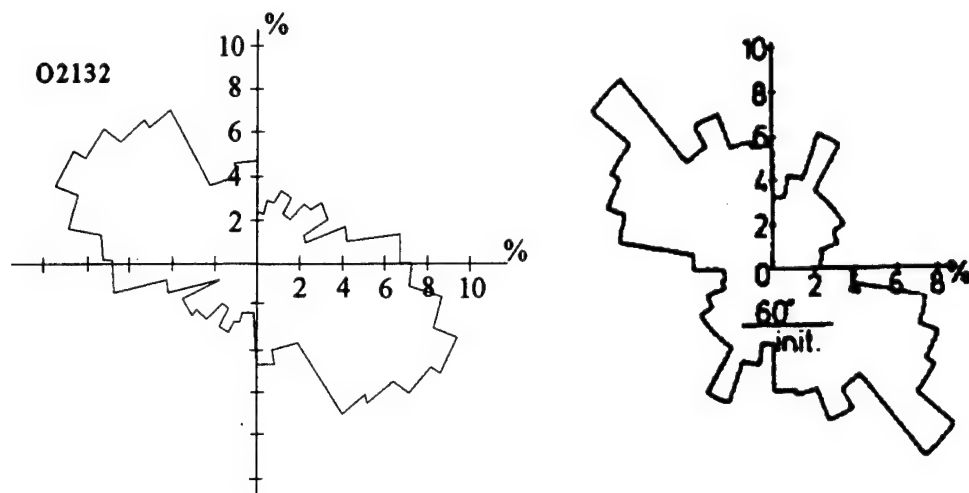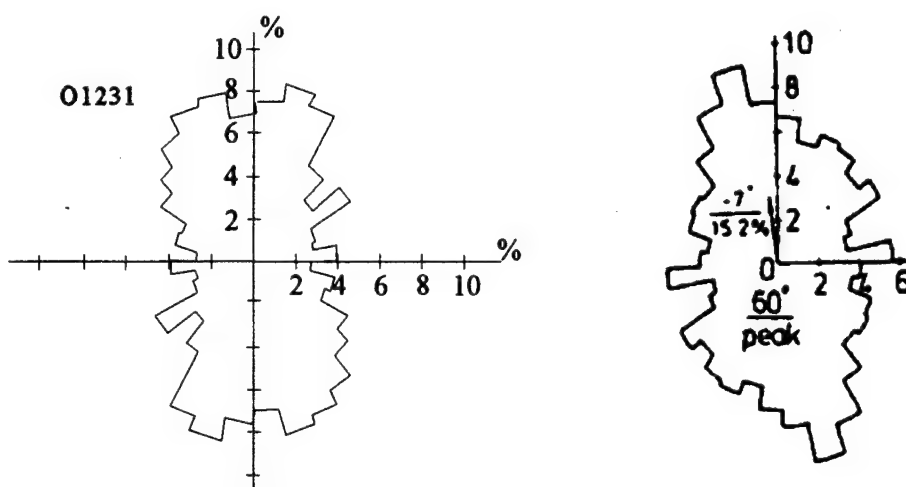
Figure 68. Frequency distribution of contact normals for numerical (left) and physical samples with a/b = 1.4, $\theta = 60°$ and $\phi_\mu = 26°$ prior to shear
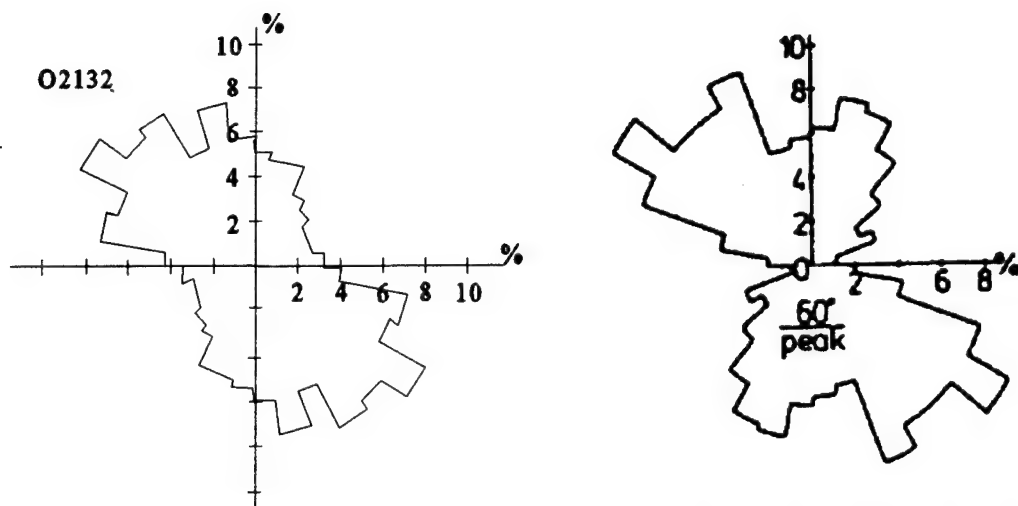
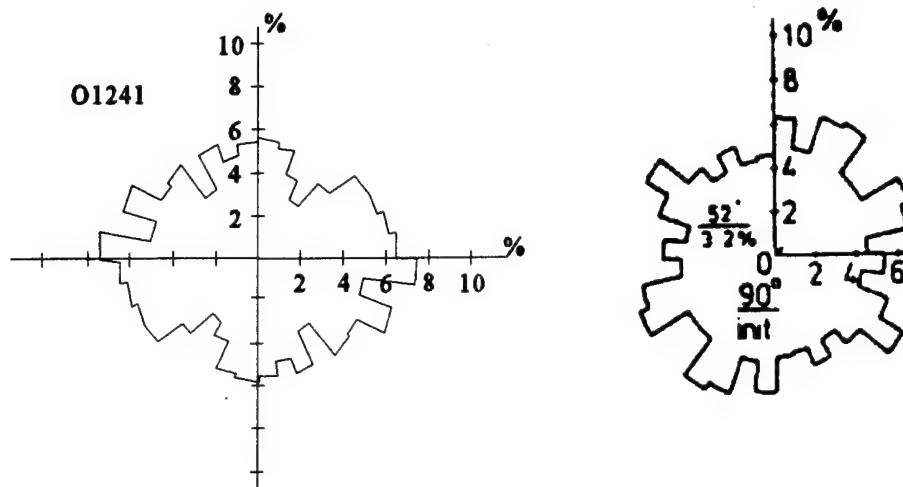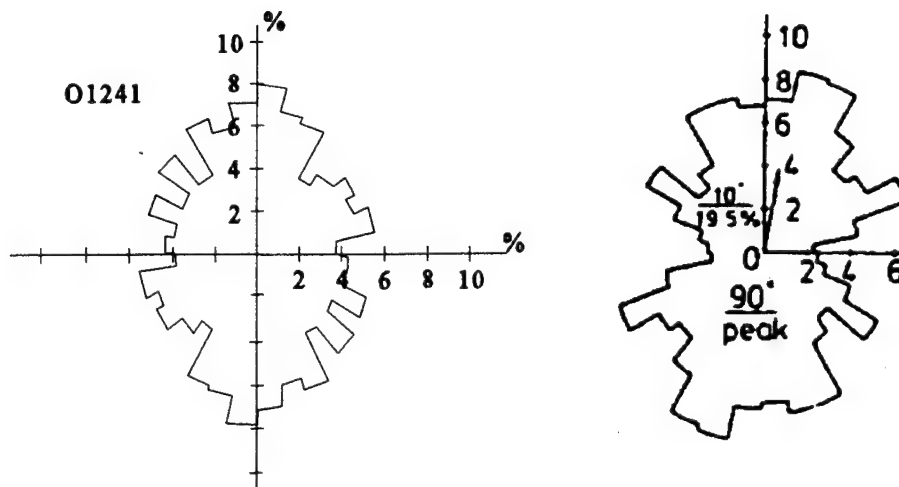**Figure 69.** Frequency distribution of contact normals for numerical (left) and physical samples with a/b = 1.4, $\theta = 60°$ and $\phi_\mu = 26°$ at peak strength

Similar results are observed in comparisons of the contact normal distributions for the remaining Oval 1 and Oval 2 samples. Figures 70 to 77 show comparisons of contact normal distributions for the Oval 1 (a/b = 1.1) samples with preferred bedding planes of 0, 30, 60 and 90°, respectively, and an interparticle sliding friction angle ϕ_μ of 26°. Figures 78 to 81 show the same comparison for the Oval 2 (a/b = 1.4) samples with 30 and 60° bedding, respectively. Comparisons of the contact normal distributions for samples with ϕ_μ of 52° are shown in Figures 82 to 97. Based on the distribution of the contact normals, it is likely that the discrepancies observed in the strength behavior of the physical and numerical samples are due to the dissimilarities in the particle shapes.
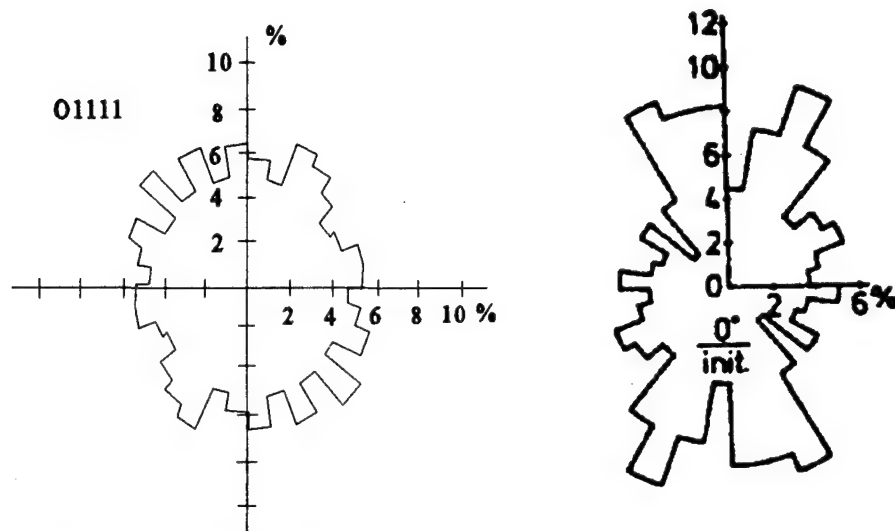
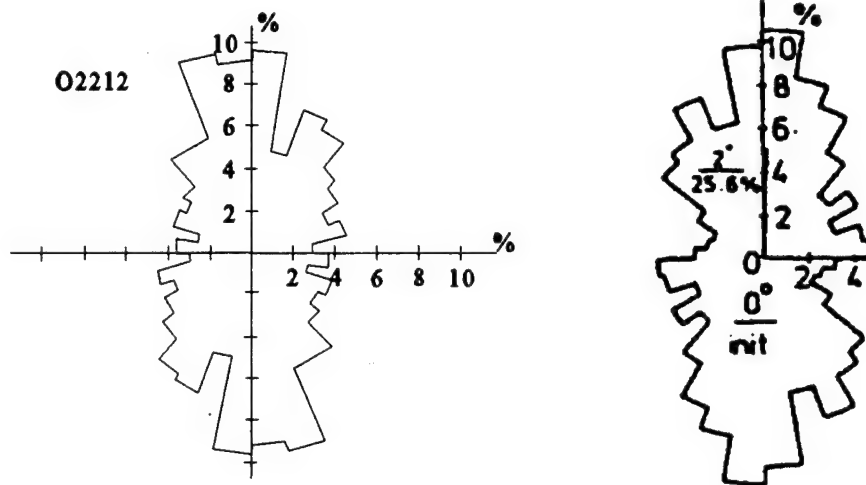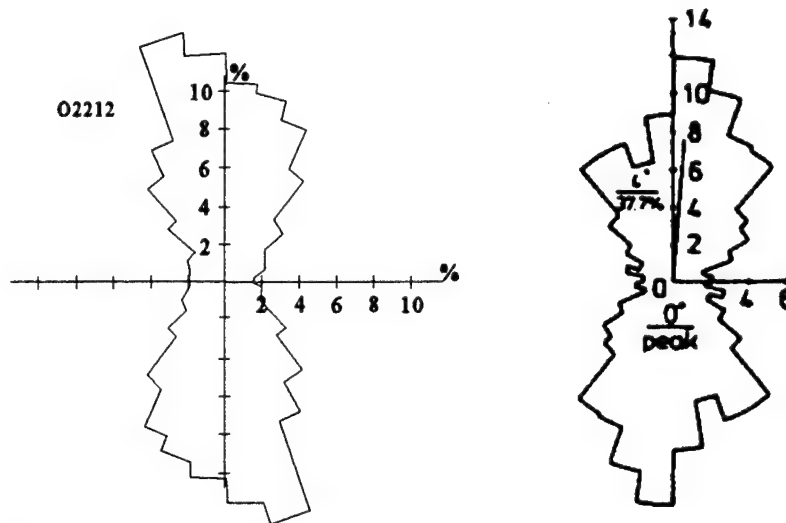**Figure 70.** Frequency distribution of contact normals for numerical (left) and physical samples with a/b = 1.1, $\theta = 0°$ and $\phi_\mu = 26°$ prior to shear.
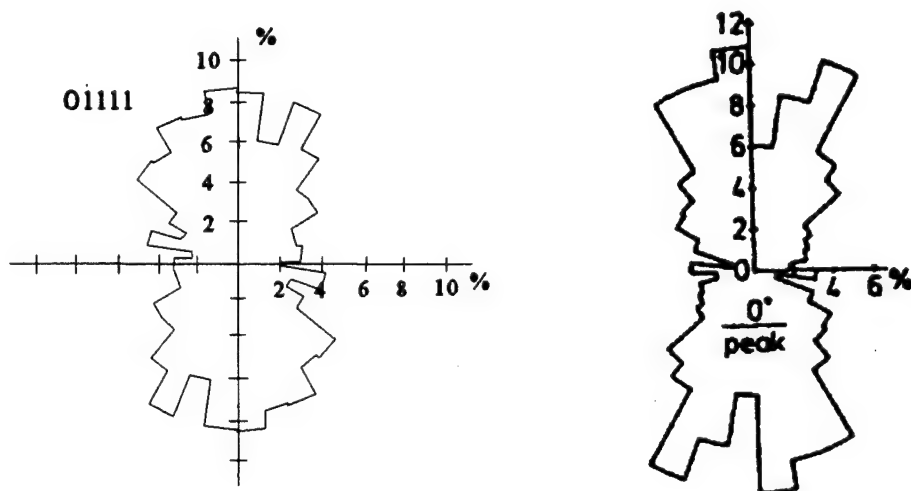
Figure 71. Frequency distribution of contact normals for numerical (left) and physical samples with a/b = 1.1, $\theta = 0°$ and $\phi_\mu = 26°$ near peak strength.
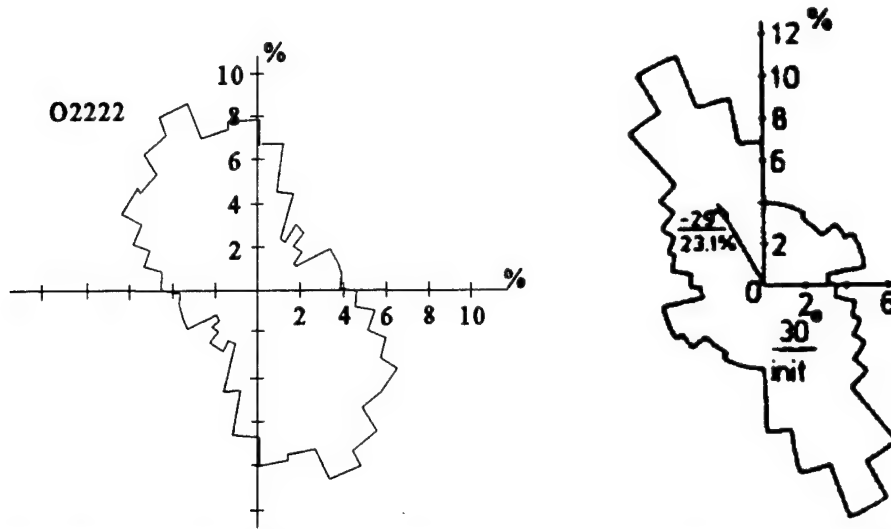
75

Figure 72. Frequency distribution of contact normals for numerical (left) and physical samples with a/b = 1.1, θ = 30° and ϕ_μ = 26° prior to shear.

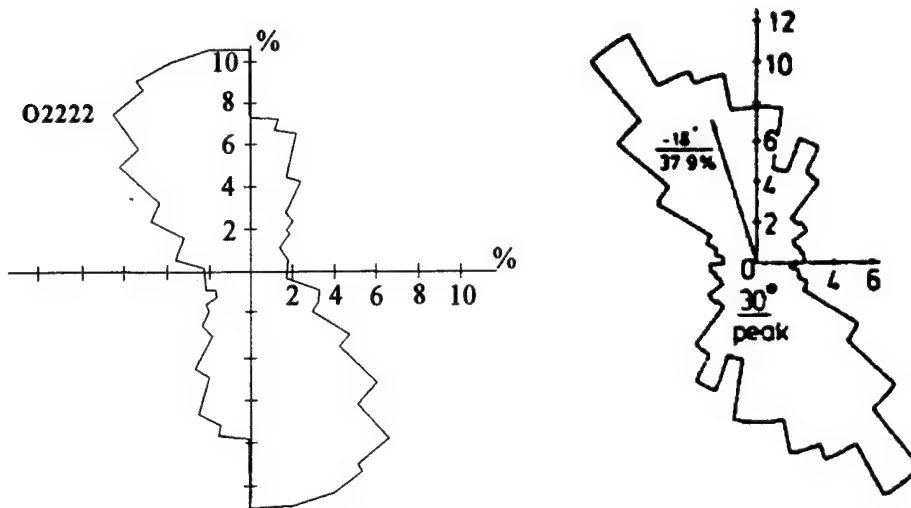**Figure 73.** Frequency distribution of contact normals for numerical (left) and physical samples with a/b = 1.1, θ = 30° and ϕ_μ = 26° near peak strength.

Figure 74. Frequency distribution of contact normals for numerical (left) and physical samples with a/b = 1.1, θ = 60° and ϕ_μ = 26° prior to shear.

Figure 75. Frequency distribution of contact normals for numerical (left) and physical samples with a/b = 1.1, θ = 60° and ϕ_μ = 26° near peak strength.
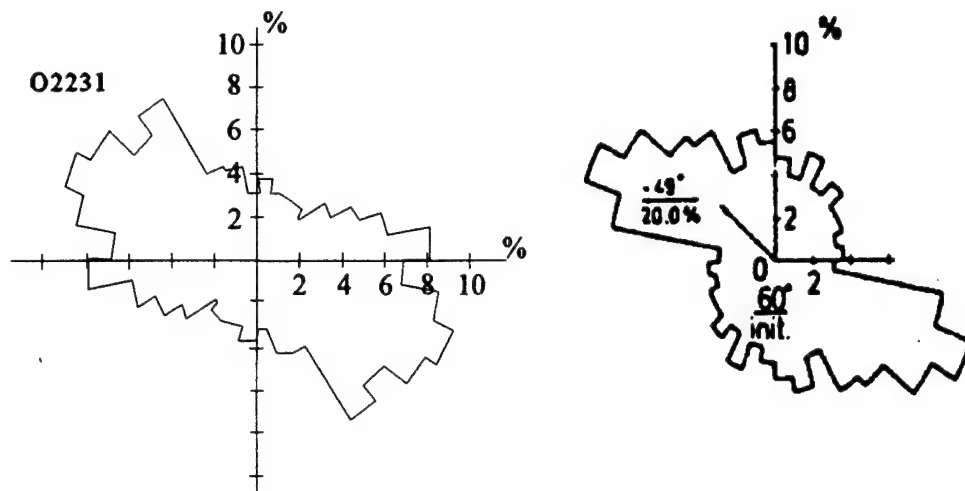
Figure 76. Frequency distribution of contact normals for numerical (left) and physical samples with a/b = 1.1, θ = 90° and ϕ_μ = 26° prior to shear.

Figure 77. Frequency distribution of contact normals for numerical (left) and physical samples with a/b = 1.1, θ = 90° and ϕ_μ = 26° near peak strength.
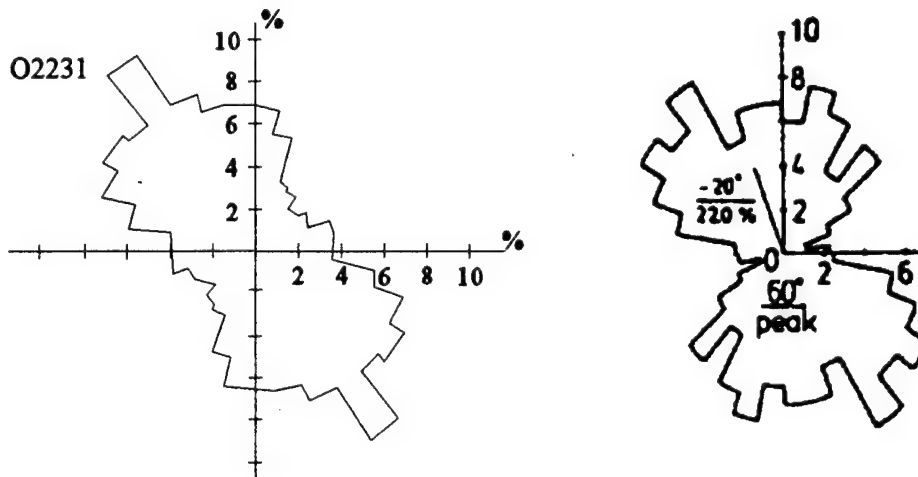
Figure 78. Frequency distribution of contact normals for numerical (left) and physical samples with a/b = 1.4, θ = 30° and ϕ_μ = 26° prior to shear.

Figure 79. Frequency distribution of contact normals for numerical (left) and physical samples with a/b = 1.4, θ = 30° and ϕ_μ = 26° near peak strength.
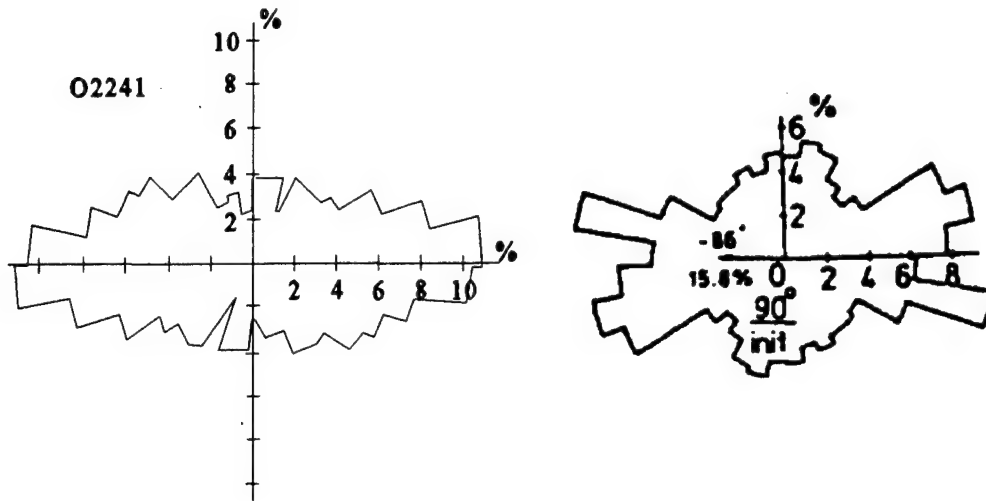
Figure 80. Frequency distribution of contact normals for numerical (left) and physical samples with a/b = 1.4, θ = 90° and ϕ_μ = 26° prior to shear.

Figure 81. Frequency distribution of contact normals for numerical (left) and physical samples with a/b = 1.4, θ = 90° and ϕ_μ = 26° near peak strength.
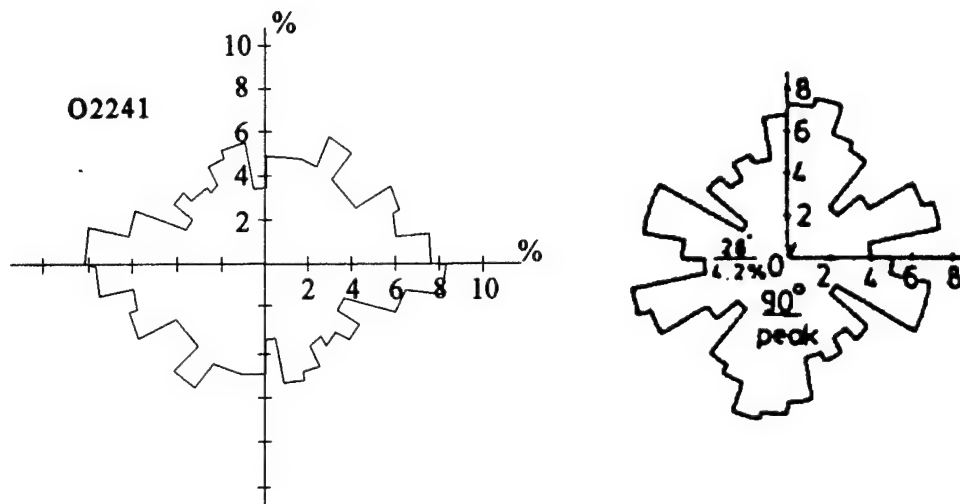
Figure 82. Frequency distribution of contact normals for numerical (left) and physical samples with a/b = 1.1, θ = 0° and ϕ_μ = 52° prior to shear.

Figure 83. Frequency distribution of contact normals for numerical (left) and physical samples with a/b = 1.1, θ = 0° and ϕ_μ = 52° near peak strength.

Figure 84. Frequency distribution of contact normals for numerical (left) and physical samples with a/b = 1.1, θ = 30° and ϕ_μ = 52° prior to shear.

Figure 85. Frequency distribution of contact normals for numerical (left) and physical samples with a/b = 1.1, θ = 30° and ϕ_μ = 52° near peak strength.

Figure 86. Frequency distribution of contact normals for numerical (left) and physical samples with a/b = 1.1, θ = 60° and ϕ_μ = 52° prior to shear.

Figure 87. Frequency distribution of contact normals for numerical (left) and physical samples with a/b = 1.1, θ = 60° and ϕ_μ = 52° at peak strength.

Figure 88. Frequency distribution of contact normals for numerical (left) and physical samples with a/b = 1.1, θ = 90° and ϕ_μ = 52° prior to shear.

Figure 89. Frequency distribution of contact normals for numerical (left) and physical samples with a/b = 1.1, θ = 90° and ϕ_μ = 52° near peak strength.

Figure 90. Frequency distribution of contact normals for numerical (left) and physical samples with a/b = 1.4, θ = 0° and ϕ_μ = 52° prior to shear.

Figure 91. Frequency distribution of contact normals for numerical (left) and physical samples with a/b = 1.4, θ = 0° and ϕ_μ = 52° near peak strength.

Figure 92. Frequency distribution of contact normals for numerical (left) and physical samples with a/b = 1.4, θ = 30° and ϕ_μ = 52° prior to shear.

Figure 93. Frequency distribution of contact normals for numerical (left) and physical samples with a/b = 1.4, θ = 30° and ϕ_μ = 52° at peak strength.

Figure 94. Frequency distribution of contact normals for numerical (left) and physical samples with a/b = 1.4, θ = 60° and ϕ_μ = 52° prior to shear.

Figure 95. Frequency distribution of contact normals for numerical (left) and physical samples with a/b = 1.4, θ = 60° and ϕ_μ = 52° near peak strength.

Figure 96. Frequency distribution of contact normals for numerical (left) and physical samples with a/b = 1.4, θ = 90° and ϕ_μ = 52° prior to shear.

Figure 97. Frequency distribution of contact normals for numerical (left) and physical samples with a/b = 1.4, θ = 90° and ϕ_μ = 52° at peak strength.

8. RESULTS OF DEM ANALYSES

This Section presents the results of the biaxial compression test simulations on numerous cohesionless granular assemblages with various combinations of particle angularity and preferred bedding plane orientation as well as variations in the initial void ratio, packing and confining stress. The interparticle sliding friction angle ϕ_μ for all of the assemblages presented is 26°. Detailed simulation results for each numerical sample are provided in Appendix A of Meachum (1994). The strength and deformation results are discussed in Section 9.

8.1 Influence of Particle Shape on Strength

Particle shape has been shown by numerous experimental and numerical studies to have a strong influence on the overall strength behavior of granular materials. Results show that even slight increases in particle angularity can significantly increase strength. It has been suggested that the increase in strength is due to the fact that angular particles interlock more thereby inhibiting the negative effects due to particle rolling (ting *et al* 1993). Consequently, particles must slide past each other resulting in more frictional shear resistance and higher overall shear strength. Angular particles possess orientation and may form preferred (or aligned) bedding planes producing dense assemblages with extremely anisotropic fabrics. Experimental studies have shown that strength is significantly reduced when the orientations of the contact normal plane and the major principal stress σ_1 are skewed (Ladd *et al* 1977).

The ellipse-based DEM results show good quantitative and qualitative agreement with the results from experimental studies. Strength is shown to increase as particle angularity increases. The strength decreases significantly, however, when the orientation of the bedding plane is aligned toward the predicted Mohr-Coulomb failure plane ($45° + \phi/2$). Looser assemblages are shown to exhibit less strength than the denser assemblages. Finally, assemblages with more isotropic fabrics tend to be looser and exhibit less strength than those with anisotropic fabrics.

8.1.1 Effect of Particle Aspect Ratio

The effect of particle aspect ratio (*a/b*) on the peak internal friction angle ϕ_{max} is shown in Figure 98. Note that the lines are plotted through the averages for two samples with similar geometries. A significant increase in ϕ_{max} is associated with increased particle "angularity". DEM samples consisting of "flat" particles (a/b = 3.0) yield values for ϕ_{max} of approximately 55° while the samples consisting of round particles (a/b = 1.0) yield values of only 25°. Even a slight increase in particle aspect ratio is seen to significantly increase the strength of the assemblage as samples with a/b = 1.1 yield values for ϕ_{max} of approximately 30°. The results of the DEM test simulations shown in Figure 98 are similar qualitatively and quantitatively to results of physical tests performed on real granular materials shown in Figure 1. Physical samples consisting of more angular Olivine sand particles yield significantly higher values for ϕ_{max} than the more rounded glass beads.

8.1.2 Effect of Aspect Ratio and Particle Bedding

The numerical test results shown in Figure 98 are for samples with preferred horizontal bedding ($\theta = 0°$). Figure 99 shows that ϕ_{max} increases as the particles become more flat, but when the bedding plane is inclined toward the vertical, ϕ_{max} decreases significantly. For assemblages consisting of flatter particles (a/b > 2.0), ϕ_{max} is minimum when the bedding plane is oriented 60° from the horizontal (or approximately $45° + \phi/2$). For these samples, ϕ_{max} is approximately the same as the interparticle friction angle ϕ (26°). For all of the numerical samples with variations in particle aspect ratio and bedding, however, the peak internal friction angle is minimum for samples consisting of round particles.
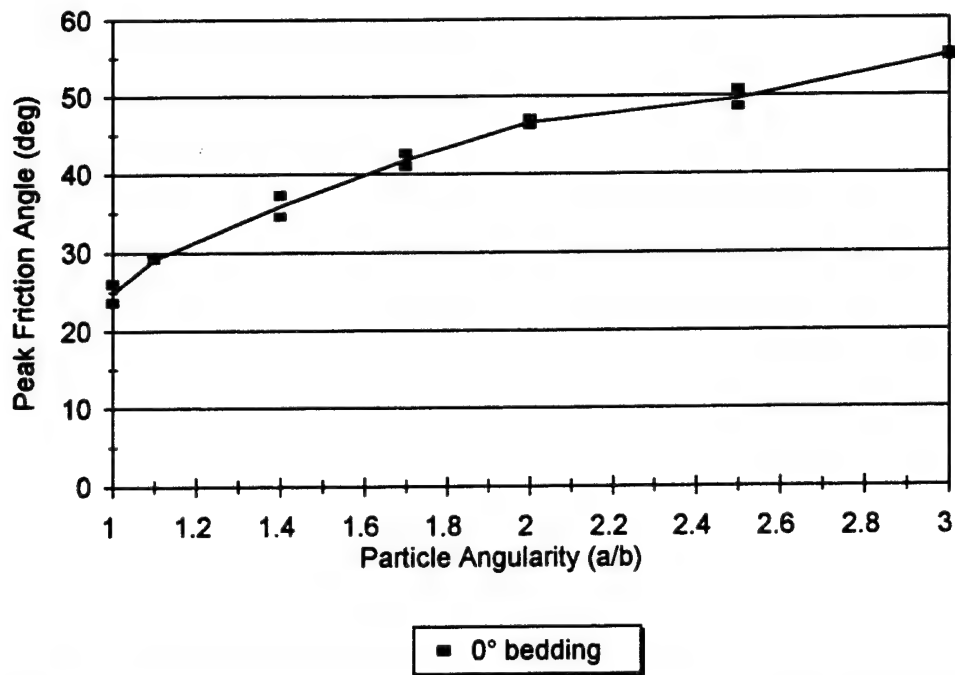
Figure 98. Effect of particle aspect ratio on the peak friction angle ϕ_{max} for DEM samples with preferred horizontal particle bedding ($\theta = 0°$).
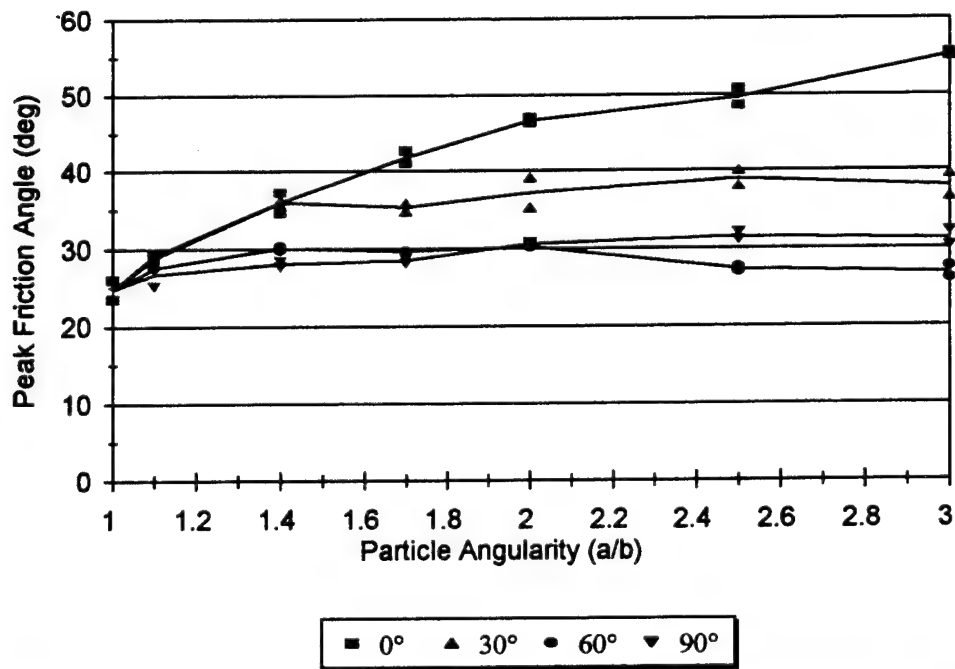

Figure 99. Effect of particle aspect ratio on the peak friction angle ϕ_{max} for DEM samples with preferred particle bedding θ.

The effect of particle aspect ratio and orientation on the peak internal friction angle ϕ_{max} is also shown in Figure 100. Again, note that the lines are plotted through the averages for two samples with similar geometries. The maximum internal friction angle ϕ_{max}, hence the strength, is highest for samples with horizontal bedding (θ = 0°) and lowest for samples with 60 and 90° bedding. The DEM results for ϕ_{max} shown in Figure 100 are qualitatively similar to the results of physical tests performed on different sands shown in Figure 101. ϕ_{max} for the numerical assemblages with 60 and 90° bedding, however, is lower than for the physical samples. Ladd *et al* (1977) defines β as the angle between the contact normal plane and the orientation of the applied principal stress σ_1 which is in effect the same as the angle θ used herein to define the orientation of bedding plane.

Similar peak strength behavior for the numerical samples is illustrated by the shear stress q results shown in Figures 102 and 103 and the principal stress ratio σ_1/σ_2 results shown in Figures 104 and 105. A maximum shear stress q_{max} of approximately 4 kPa is achieved by samples consisting of "flat" particles (a/b = 3.0) with 0° bedding, while those consisting of round particles (a/b = 1.0) yield values for q_{max} of only 0.6 kPa. Similarly, a maximum value for σ_1/σ_2 of approximately 10 is achieved by samples with a/b = 3.0 and θ = 0°, while those with a/b = 1.0 yield values of only 2.5. Values for q_{max} and $(\sigma_1/\sigma_2)_{max}$ are considerably lower, however, when the bedding plane is oriented toward 45° + $\phi/2$. For samples with 30, 60 and 90° bedding, the increase in strength due to particle aspect ratio appears to be less significant when a/b is greater than 1.4.
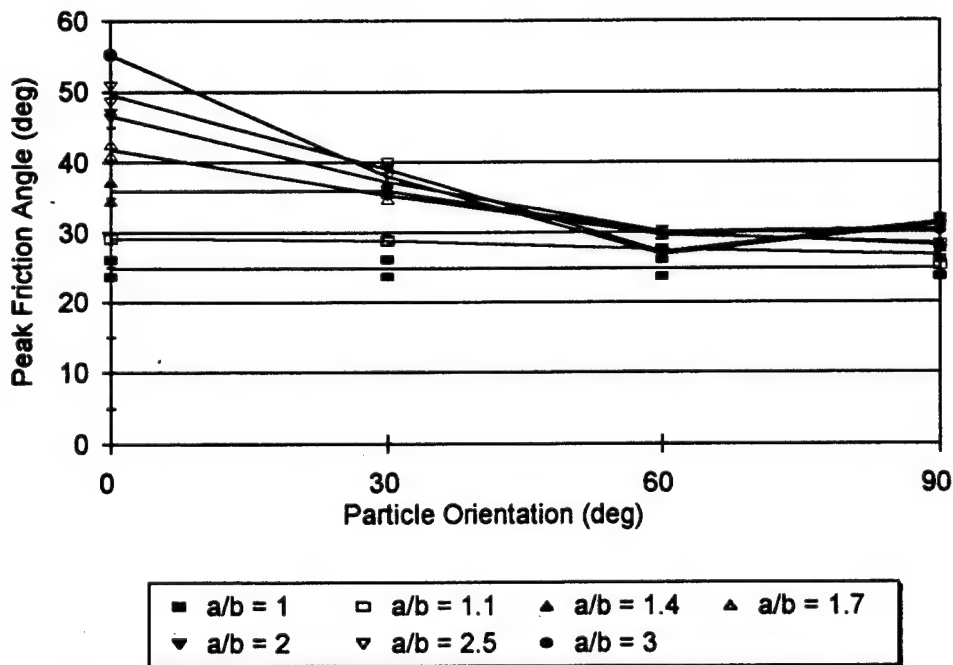
Figure 100. Effect of preferred particle bedding θ on the peak internal friction angle ϕ_{max} for DEM samples with variations in particle aspect ratio *a/b*.

91
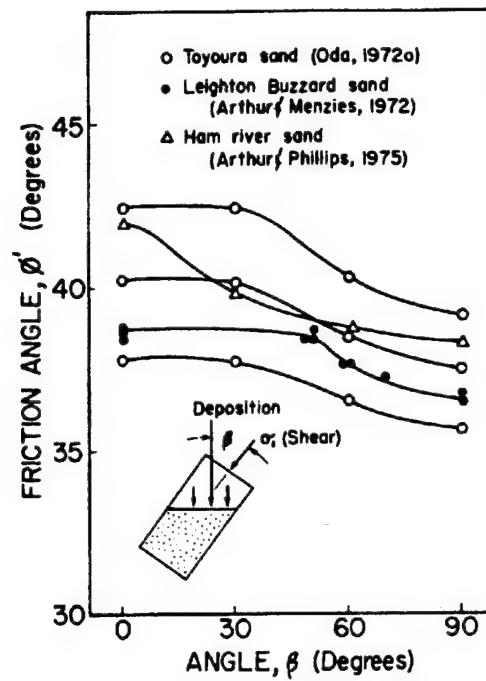
Figure 101. Effect of preferred particle bedding β on the internal friction angle for different sands (from Ladd *et al* 1977).
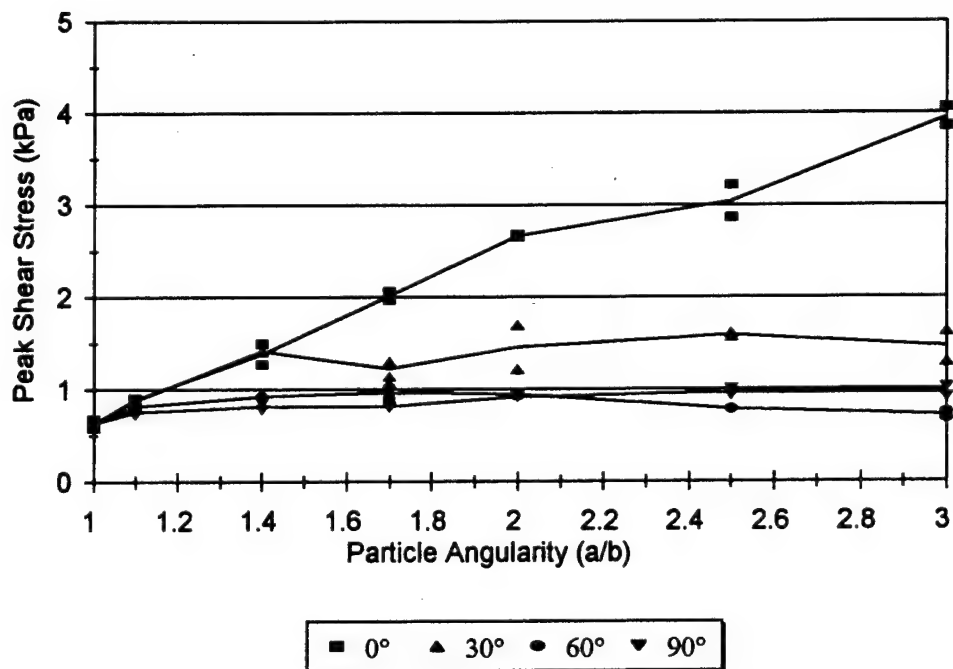
Figure 102. Effect of particle aspect ratio on the peak shear stress q_{max} for DEM samples with preferred particle bedding θ.

92
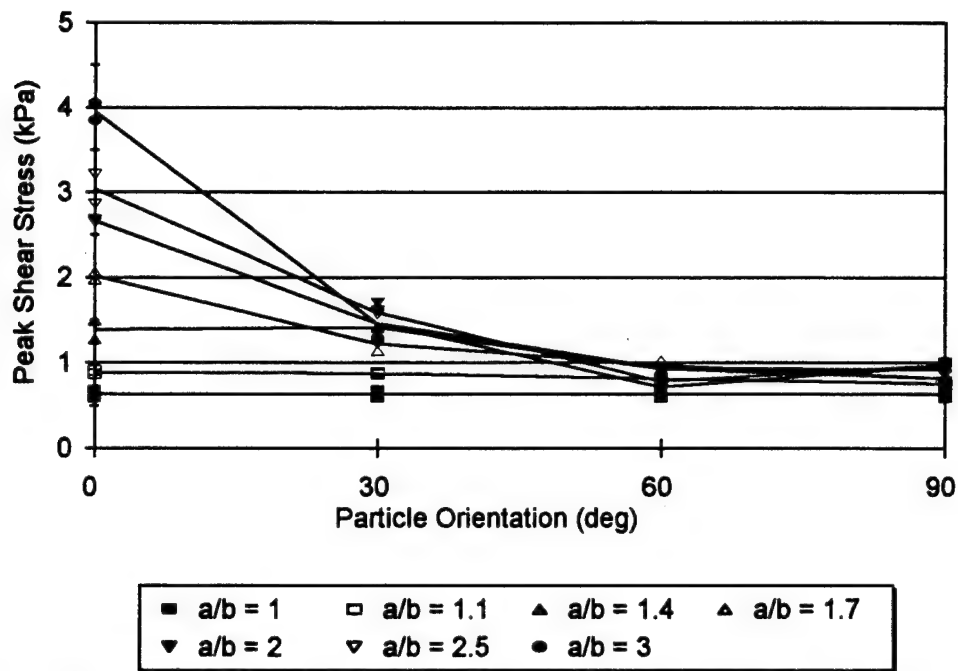
Figure 103. Effect of preferred particle bedding θ on the peak shear stress q_{max} for DEM samples with variations in particle aspect ratio a/b.
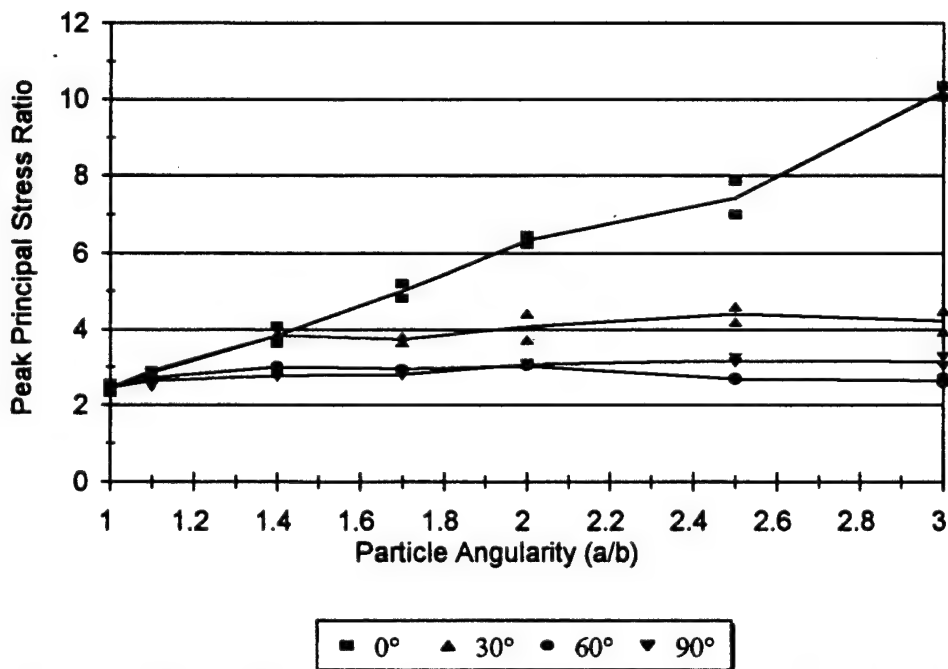
Figure 104. Effect of particle aspect ratio on the peak principal stress ratio $(\sigma_1/\sigma_2)_{max}$ for DEM samples with preferred particle bedding θ.
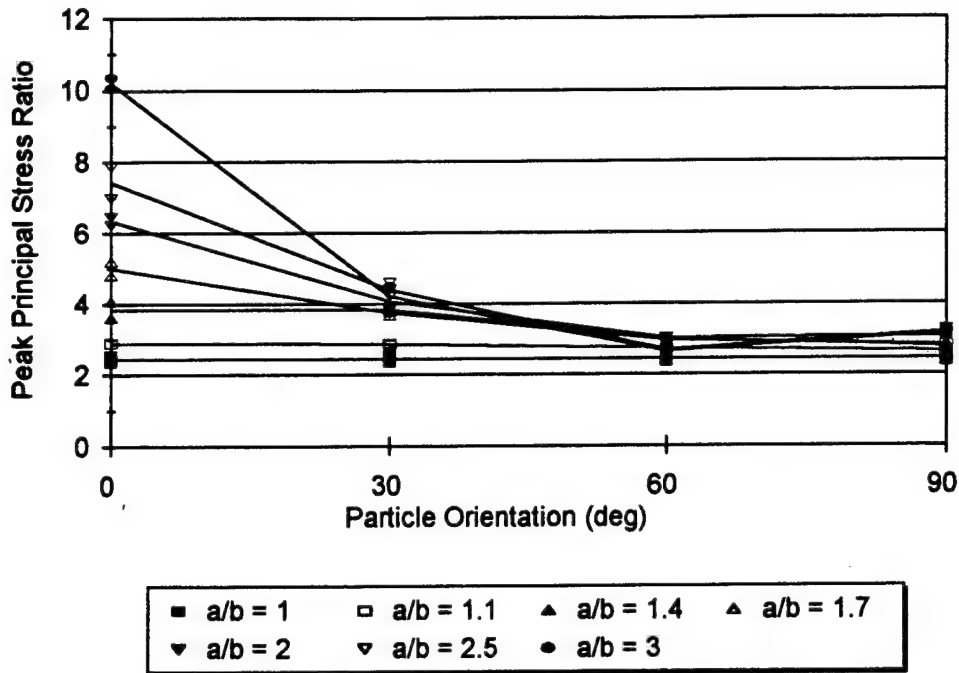
Figure 105. Effect of preferred particle bedding θ on the peak principal stress ratio $(\sigma_1/\sigma_2)_{max}$ for DEM samples with variations in particle aspect ratio *a/b*.

Figures 106 and 107 illustrate the effect of particle aspect ratio on the progression of the mobilized internal friction angle φ during the course of deformation for samples with θ = 0 and 60°, respectively. As shown previously, the ellipse-based DEM model computes mobilized φ at any given instant in time as defined by the user from the shear stress *q* and the mean normal stress *p* using:

$$mobilized \; \phi = \sin^{-1}\left(\frac{q}{p}\right) \tag{57}$$

For samples with preferred horizontal bedding (θ = 0°), mobilized φ achieves higher peak values as particle aspect ratio increases. In addition, these higher values are achieved at higher failure strains. It should be noted that the axial strain is in the direction of σ_1 (or vertical). For samples with 60° bedding, mobilized φ is similar regardless of an increase in particle aspect ratio. No distinct peak is achieved in the samples as their peak strength and their residual strength appear to be about the same value.

Figures 108 and 109 illustrate the effect of particle orientation on the progression of mobilized φ during the course of deformation for samples with a/b = 1.4 and 3.0, respectively. Higher peak values for mobilized φ are achieved by assemblages with preferred horizontal bedding (θ = 0°). As the bedding plane becomes aligned toward 45° + φ/2, ϕ_{max} decreases. For samples consisting of "flat" particles (a/b = 3.0), the difference in the evolution of mobilized φ due to the orientation of the bedding plane is more striking as samples with horizontal bedding yield significantly higher values for mobilized φ than those with 30, 60 or 90° bedding.

Similar trends in the strength of the numerical samples due to particle aspect ratio and bedding are shown by the evolution of the shear stress *q* and stress ratio σ_1/σ_2 during the course of deformation. Figures 110 through 113 present the results of the biaxial compression test simulations for q, while the results for σ_1/σ_2 are presented in Figures 114 through 117.

94
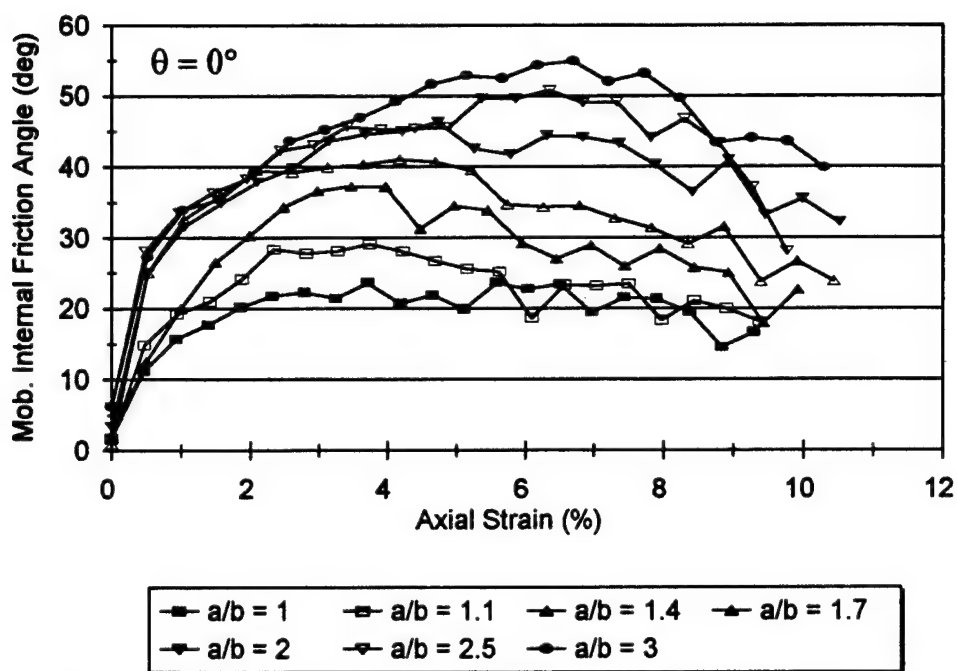
Figure 106. Effect of particle aspect ratio on the mobilized internal friction angle ϕ for DEM samples with preferred horizontal bedding ($\theta = 0°$).
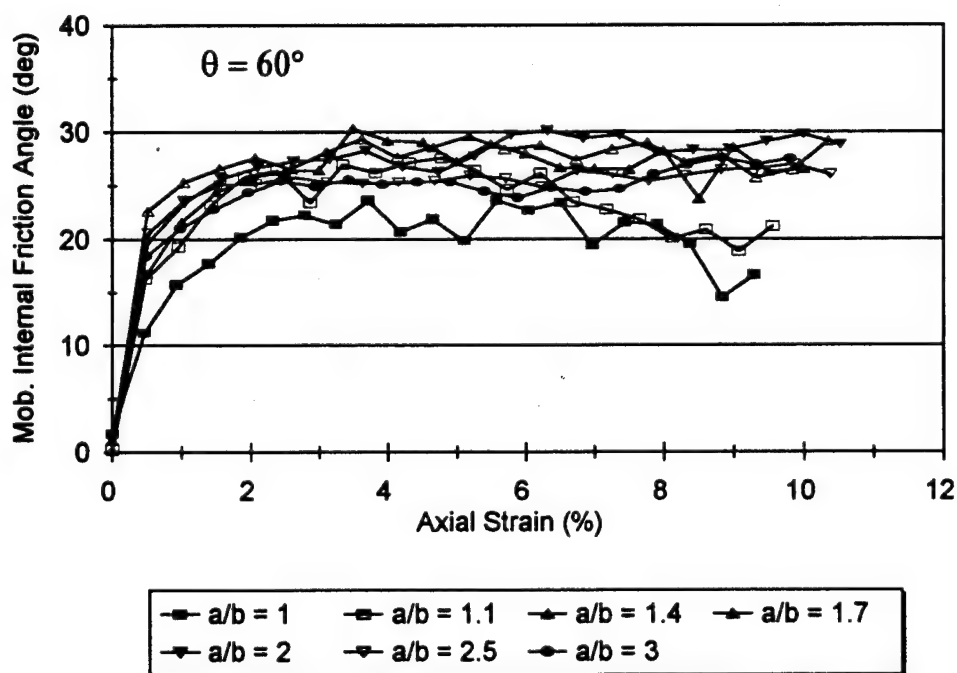

Figure 107. Effect of particle aspect ratio on the internal friction angle ϕ for DEM samples with preferred 60° bedding.
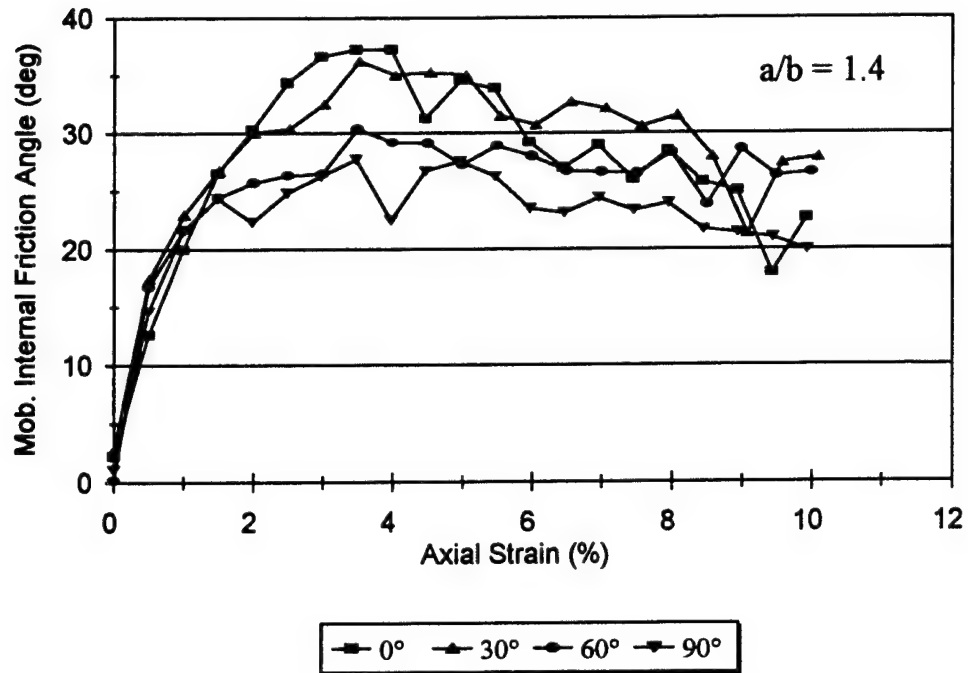
Figure 108. Effect of preferred particle bedding θ on the mobilized internal friction angle φ for DEM samples with a/b = 1.4.
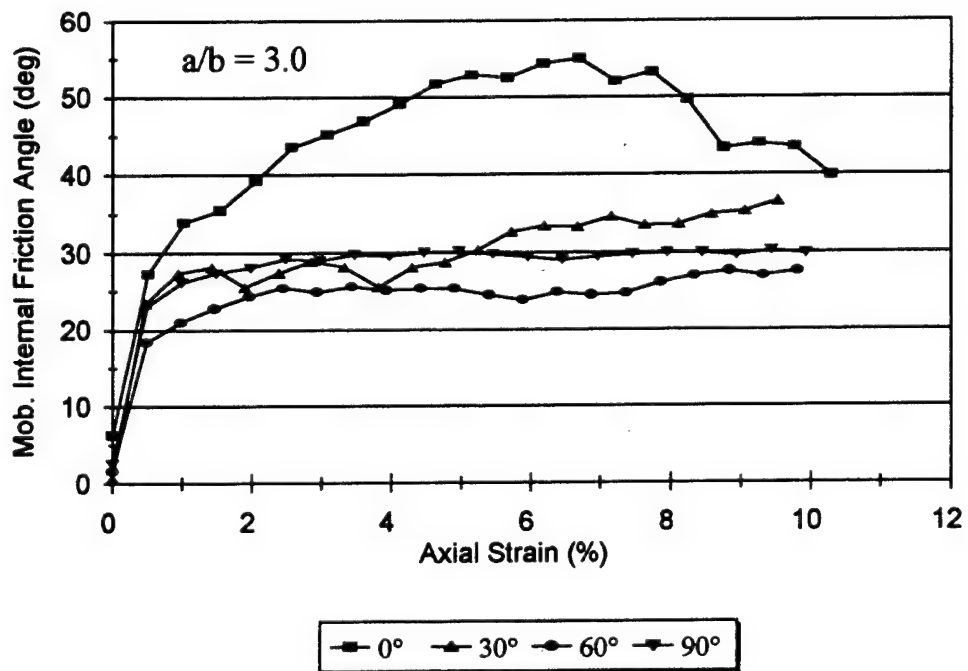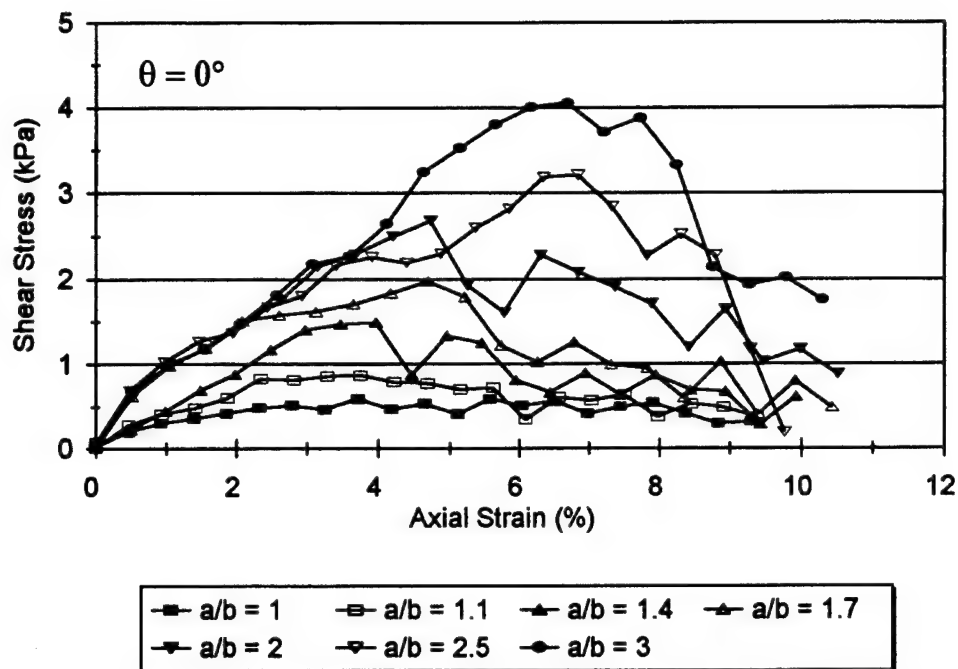

Figure 109. Effect of preferred particle bedding θ on the mobilized internal friction angle φ for DEM samples with a/b = 3.0.

Figure 110. Effect of particle aspect ratio on the maximum shear stress q for DEM samples with preferred horizontal bedding ($\theta = 0°$).
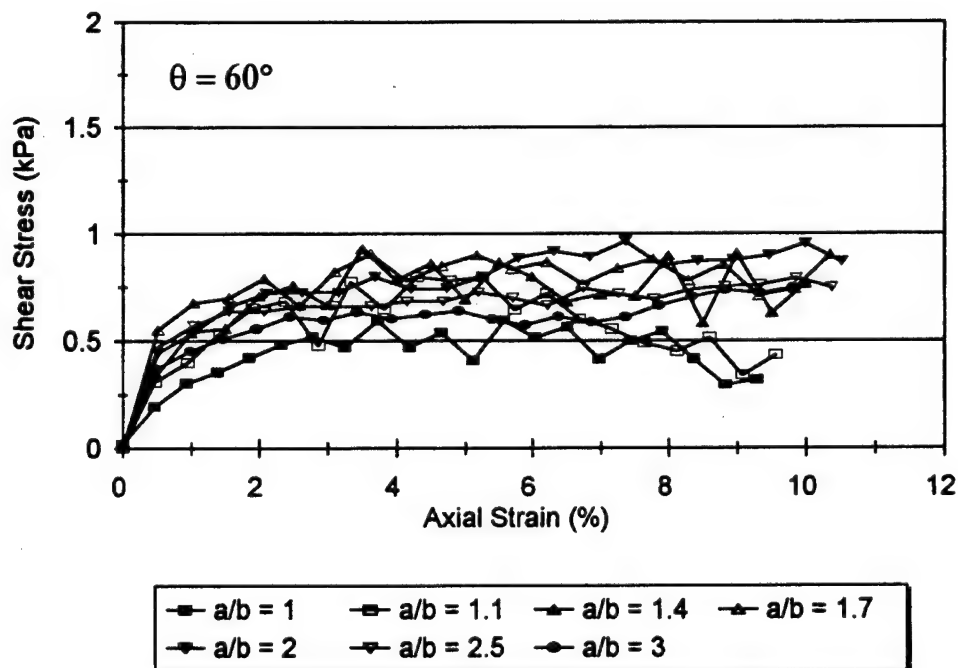
Figure 111. Effect of particle aspect ratio on the maximum shear stress q for DEM samples with preferred 60° bedding.
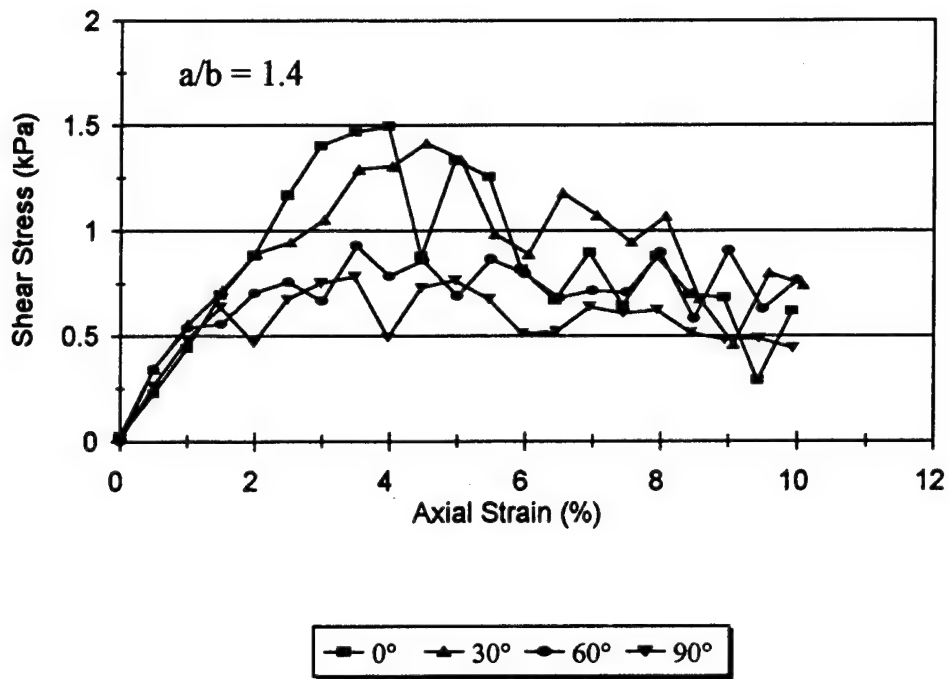
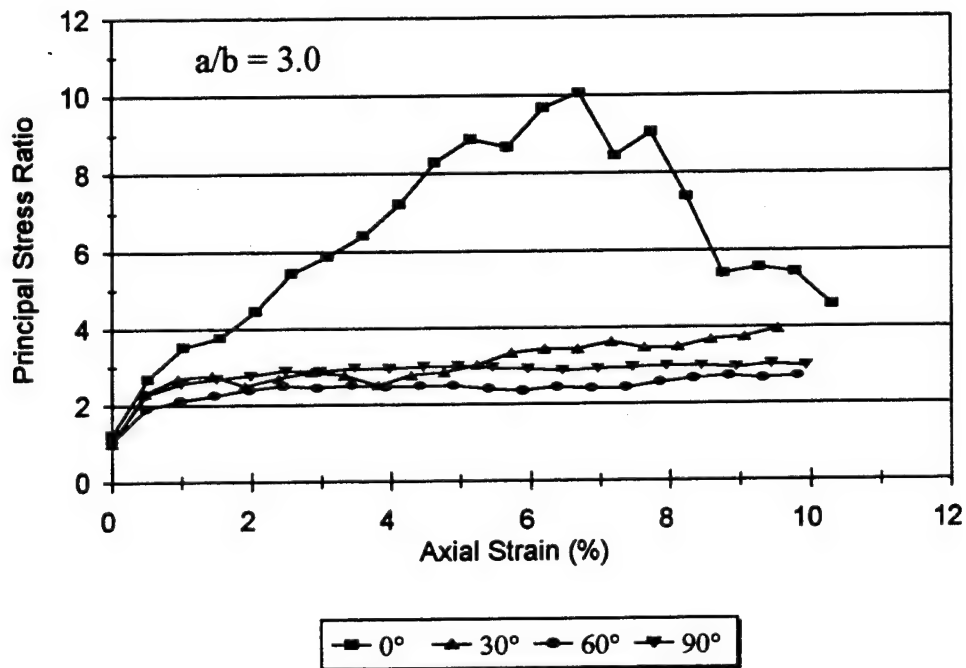**Figure 112.** Effect of preferred particle bedding θ on the maximum shear stress q for DEM samples with a/b = 1.4.
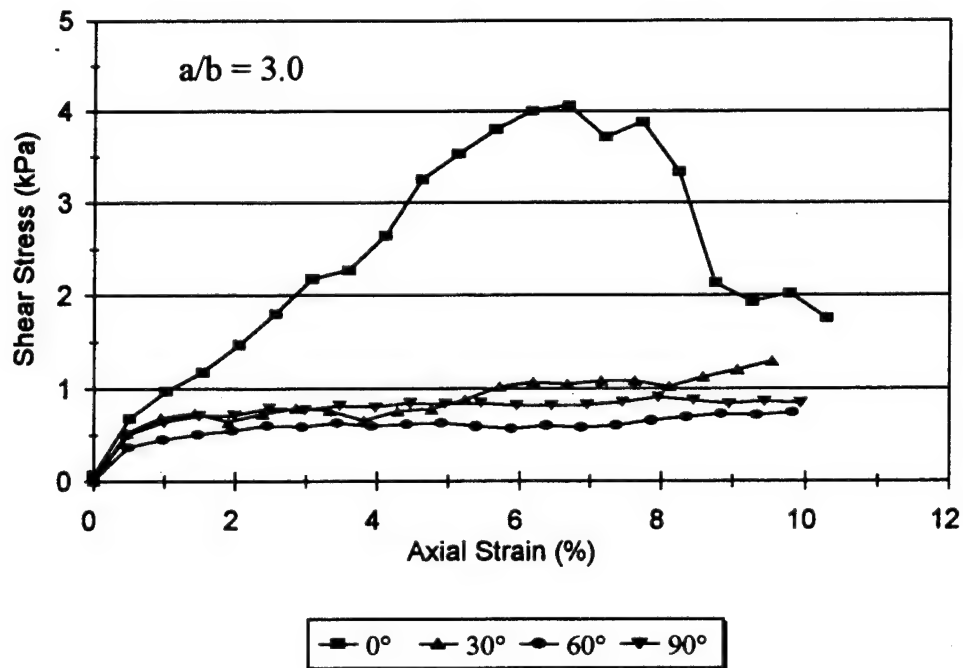
Figure 113. Effect of preferred particle bedding θ on the maximum shear stress q for DEM samples with a/b = 3.0.
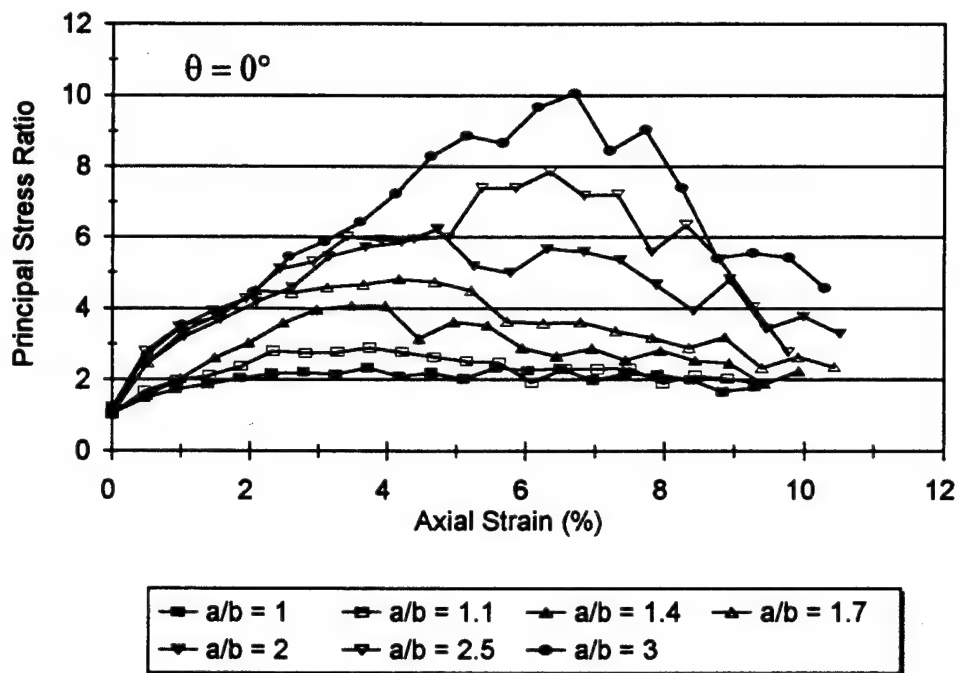
Figure 114 Effect of particle aspect ratio on the principal stress ratio σ_1/σ_2 for DEM samples with preferred horizontal bedding ($\theta = 0°$).
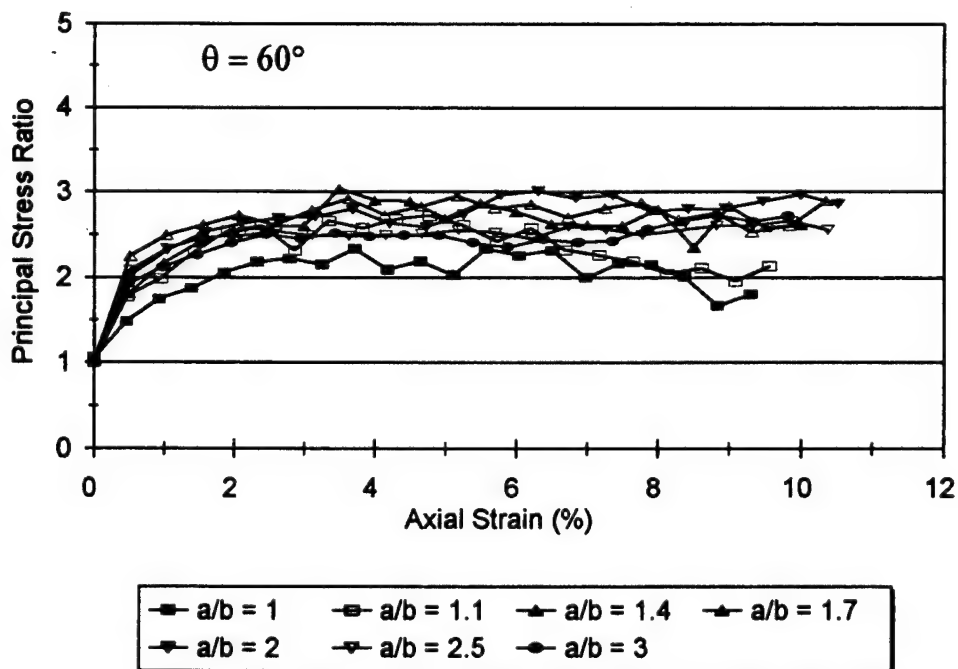
Figure 115. Effect of particle aspect ratio on the principal stress ratio σ_1/σ_2 for DEM samples with preferred 60° bedding.

99
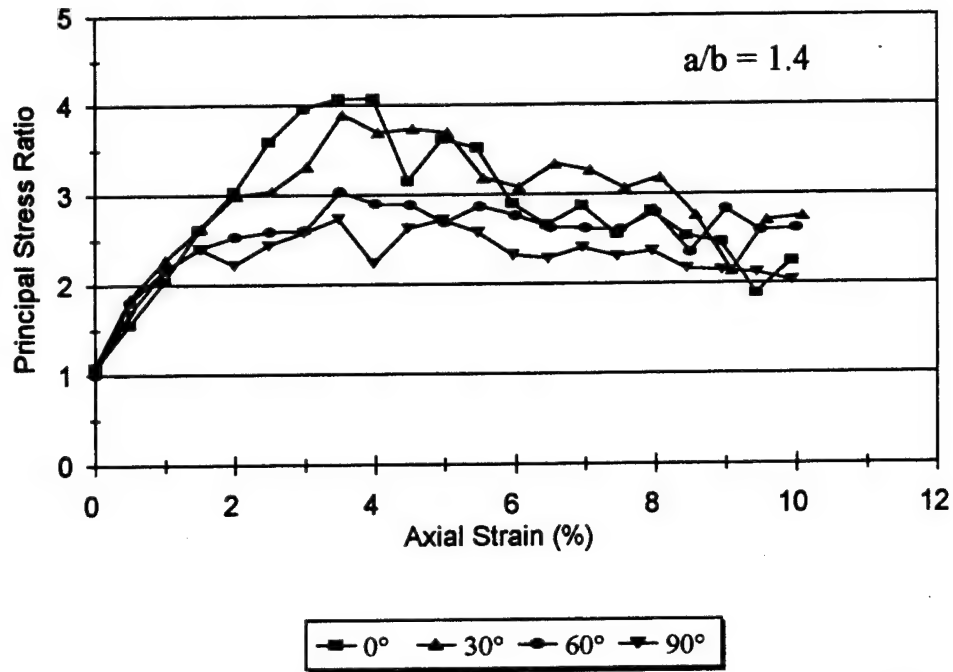
Figure 116. Effect of preferred particle bedding θ on the principal stress ratio σ_1/σ_2 for DEM samples with a/b = 1.4.

Figure 117. Effect of preferred particle bedding θ on the principal stress ratio σ_1/σ_2 for DEM samples with a/b = 3.0.

100

8.1.3 Effect of the Initial Void Ratio on Strength

Because the surface of the ellipse-shaped particles is smooth and continuously curved, it was very difficult to form numerical assemblages with large variations in their initial void ratio e_o while maintaining preferred particle bedding. Even when subjected to low confining stresses, the loose assemblages were extremely unstable and would immediately collapse into a dense packing. Various techniques were used to consolidate the numerical samples to obtain looser packing but most of these packing schemes involved prestressing the systems. These techniques are described in Section 6. The results of the biaxial shear simulations for these prestressed numerical samples are presented later in Section 8.4. Some variation in e_o was achieved for the hand-packed O sample series with a/b = 2.0 and 0° bedding. These samples were not prestressed prior to the isotropic compression simulation.

The effect of the initial void ratio e_o on ϕ_{max} for DEM samples consisting of particles with a/b = 2.0 and preferred 0° bedding is shown in Figure 118. Samples with denser packing exhibit higher strength ($\phi_{max} = 47°$) than those with looser packing ($\phi_{max} = 40°$). The results for the numerical assemblages are similar to the those reported by Holubec and D'Appolonia (1973) for different sands and glass beads shown in Figure 119.

The effect of the initial void ratio e_o is similar on the peak shear stress q and the stress ratio σ_1 /σ_2 as shown in Figures 120 and 121. Higher strength is exhibited by the denser sample ($q_{max} = 2.7$ kPa, $(\sigma_1/\sigma_2)_{max} = 6.3$) than the looser sample ($q_{max} = 1.8$ kPa, $(\sigma_1/\sigma_2)_{max} = 4.7$). The evolution of mobilized ϕ, q and σ_1/σ_2 for the numerical samples with variations in e_o are shown in Figures 122 through 124, respectively.
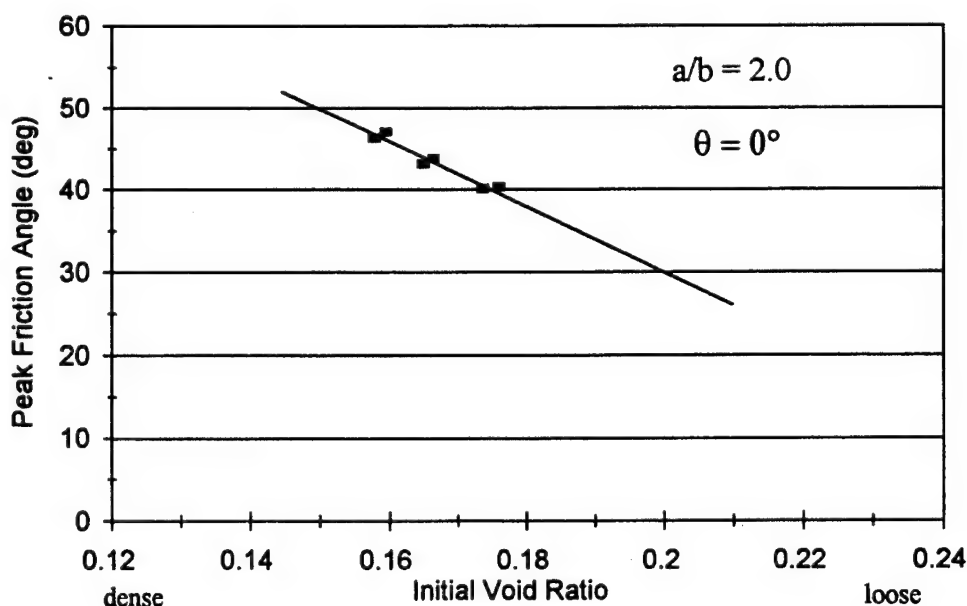

Figure 118 Effect of the initial void ratio e_o on the peak friction angle ϕ_{max} for DEM samples with a/b = 2.0 and $\theta = 0°$.
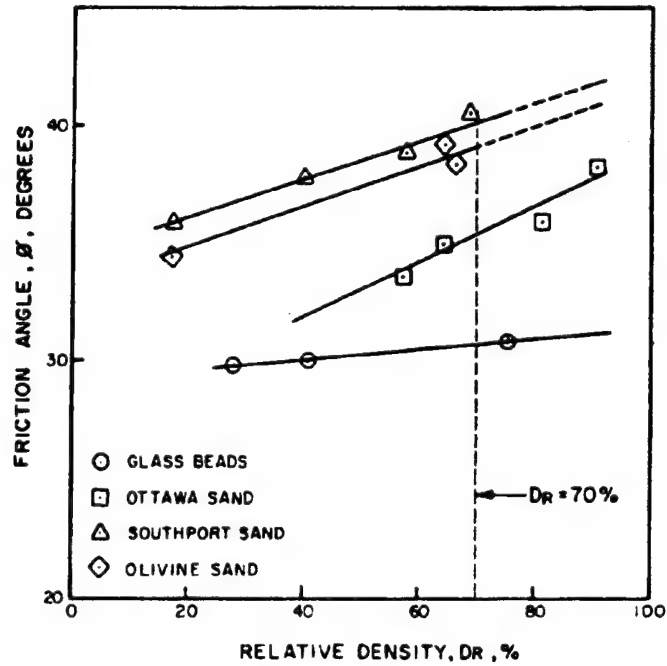
Figure 119. Effect of the relative density on the internal friction angle ϕ for different granular materials (from Holubec and d'Appolonia 1973).
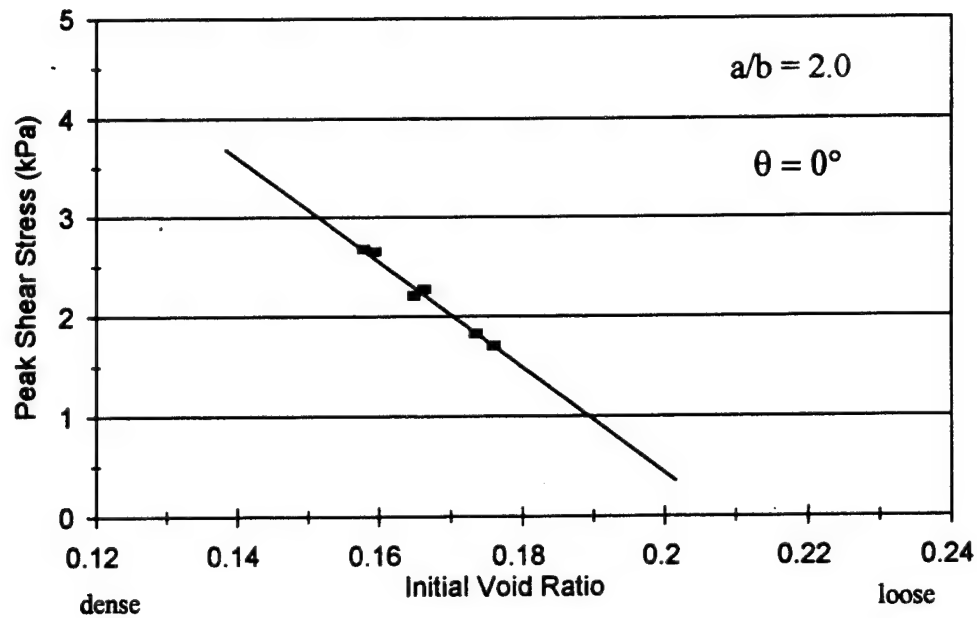

Figure 120. Effect of the initial void ratio e_o on the peak shear stress q_{max} for DEM samples with a/b = 2.0 and $\theta = 0°$.
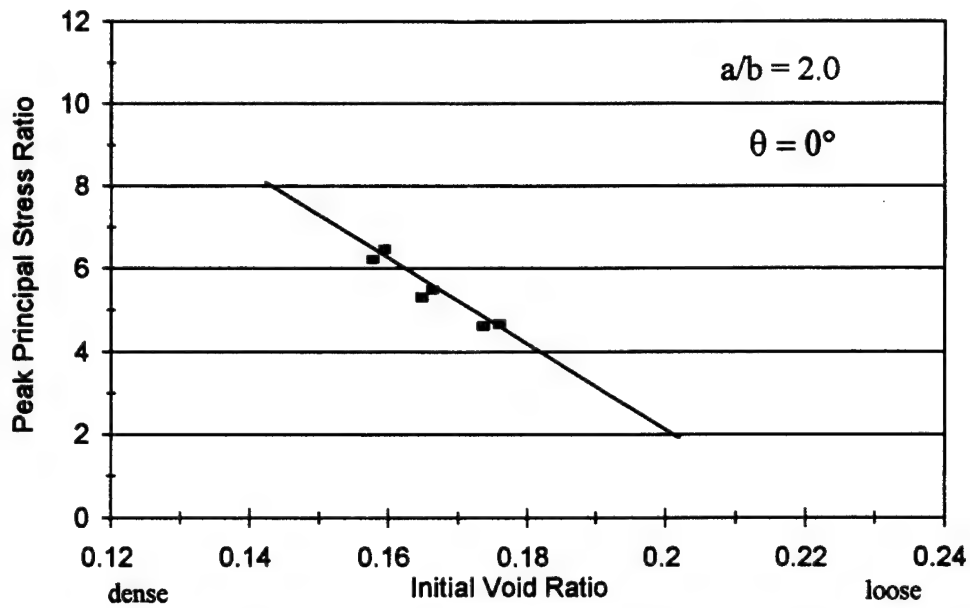
102

Figure 121. Effect of the initial void ratio on the peak principal stress ratio $(\sigma_1/\sigma_2)_{max}$ for DEM samples with $a/b = 2.0$ and $\theta = 0°$.
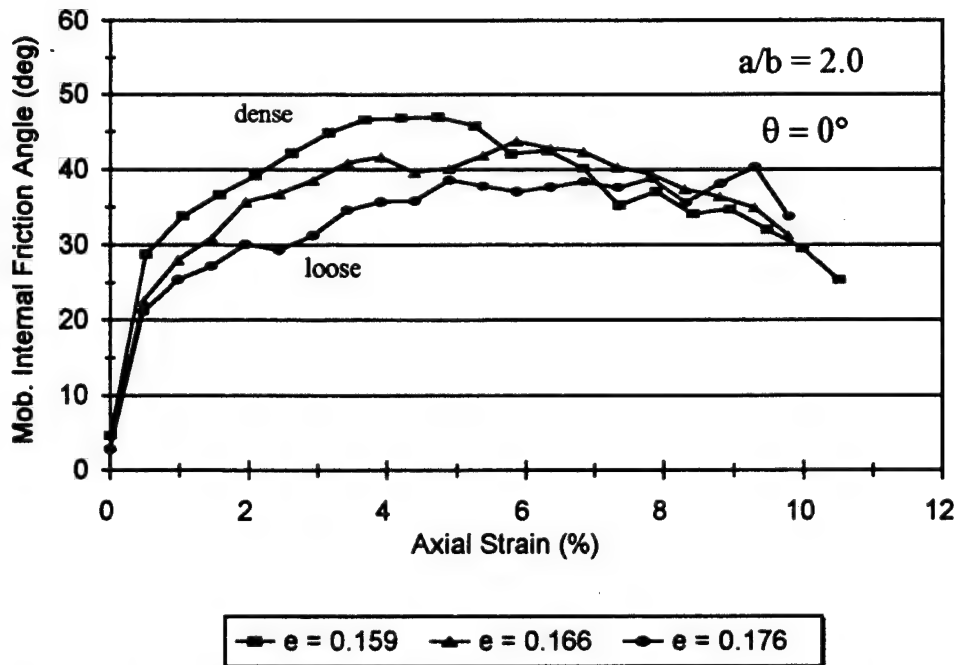

Figure 122. Effect of the initial void ratio e on the mobilized internal friction angle ϕ for DEM samples with $a/b = 2.0$ and $\theta = 0°$.
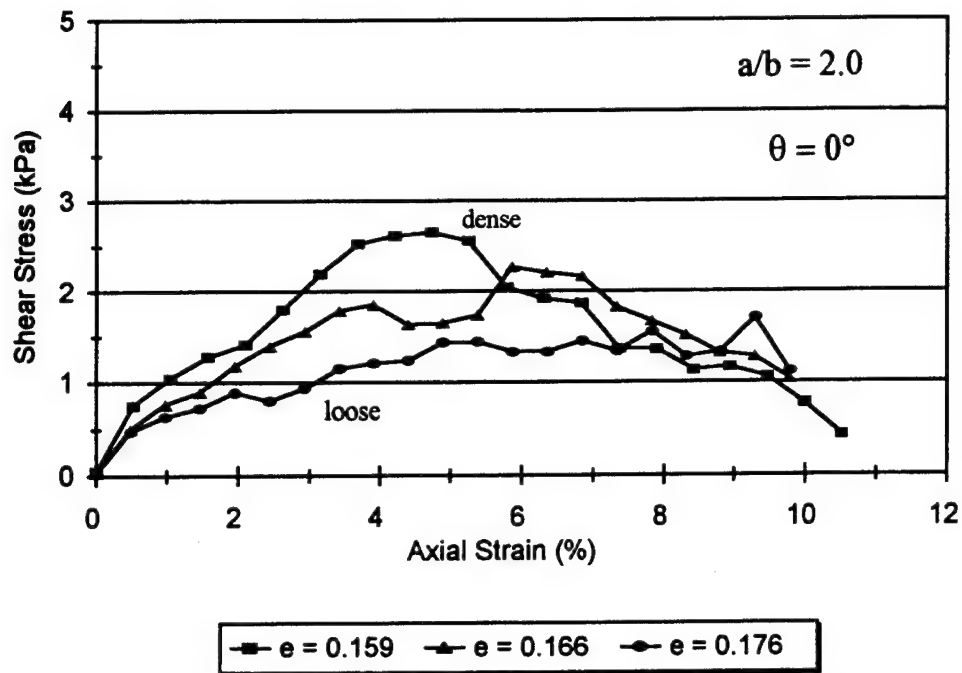
Figure 123. Effect of the initial void ratio e on the maximum shear stress q for DEM samples with a/b = 2.0 and $\theta = 0°$.
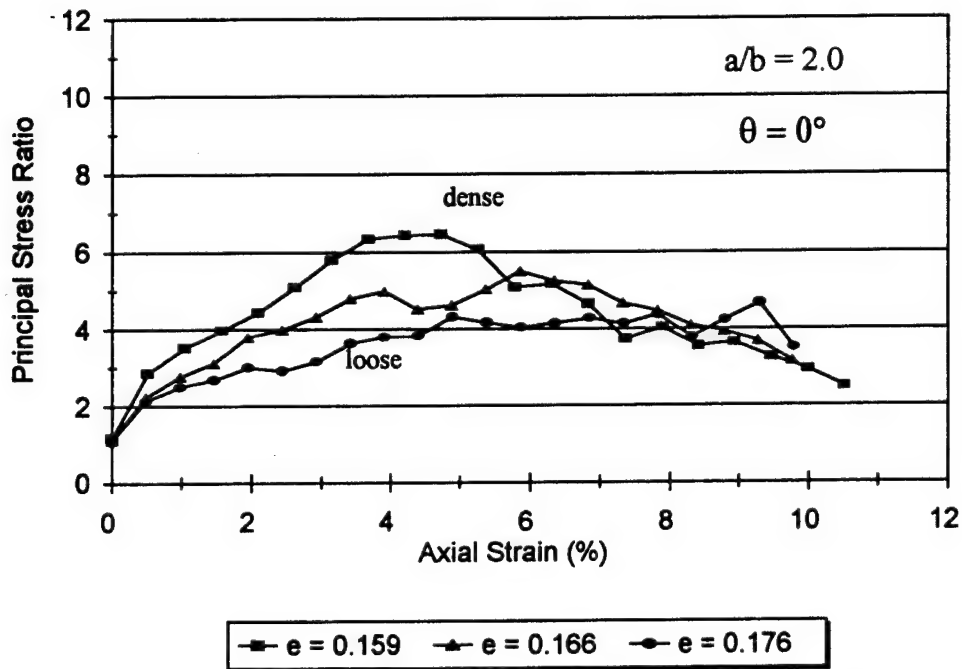
Figure 124. Effect of the initial void ratio e on the principal stress ratio σ_1/σ_2 for DEM samples with a/b = 2.0 and $\theta = 0°$.

8.1.4   Effect of a Random Orientation Fabric

The orientation fabric of the DEM tests presented thus far have been extremely anisotropic. Particles were numerically generated with preferred orientations of 0, 30, 60 and 90° within a standard deviation of 15°. Additional samples were generated with a random distribution of particle orientations creating a nearly isotropic orientation fabric. The samples with random particle bedding were significantly looser than those with aligned particles. For example, the respective initial void ratios for Oval 2 (a/b = 1.4) and Oval 7 (a/b = 3.0) samples with random bedding were 0.204 and 0.236, while those with preferred horizontal bedding ($\theta = 0°$) averaged 0.174 and 0.170. Presumably, the nature of random bedding produces much looser packing as more side to edge contacts exist between the randomly oriented particles. Samples with anisotropic fabrics, on the other hand, tend to be denser as more side to side contacts exist between the aligned particles.

Figures 125 to 127 show the effect of particle aspect ratio on the peak internal friction angle ϕ_{max}, peak shear stress q_{max} and peak stress ratio $(\sigma/\sigma)_{max}$ for samples with preferred horizontal bedding and random bedding. While the overall strength of the assemblages with both preferred and random bedding increases as particle aspect ratio increases, the peak values are significantly lower for samples with random bedding. Oval 2 and Oval 7 samples with random bedding yield respective values for ϕ_{max} of 26 and 31°, while those with preferred horizontal bedding ($\theta = 0°$) yield average values of 36 and 55°. This is due in part to the looser packing in the random samples.
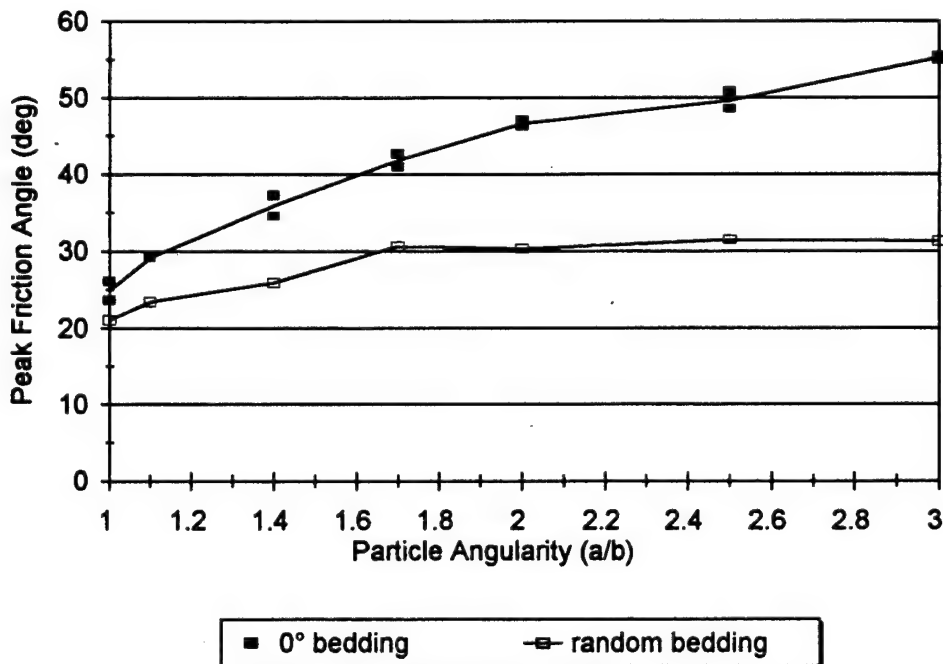

Figure 125.   Effect of particle aspect ratio on the peak friction angle ϕ_{max} for DEM samples with preferred horizontal bedding ($\theta = 0°$) and random bedding.
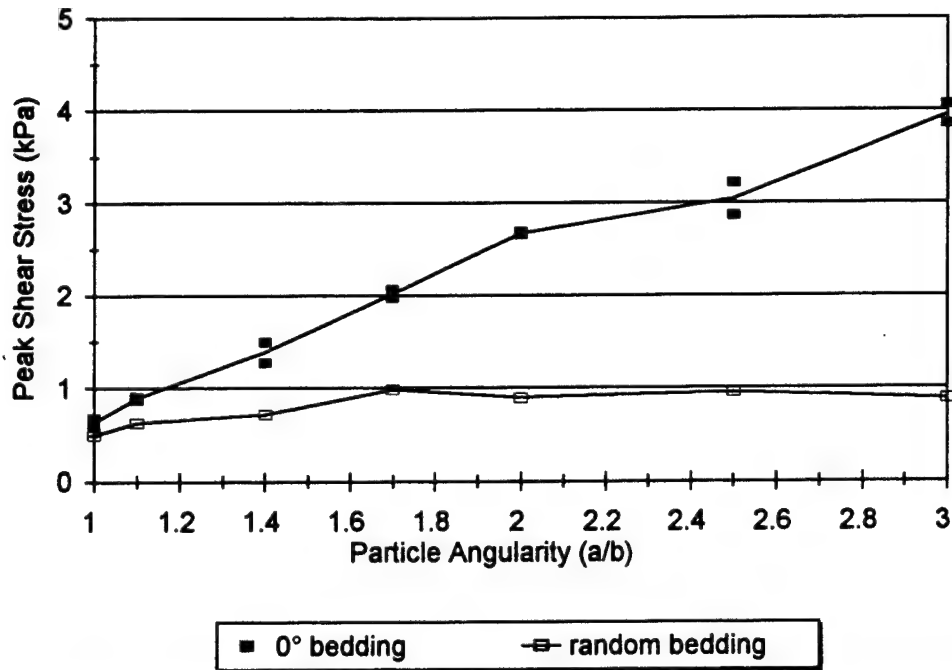
Figure 126. Effect of particle aspect ratio on the peak shear stress q_{max} for DEM samples with preferred horizontal bedding ($\theta = 0°$) and random bedding.
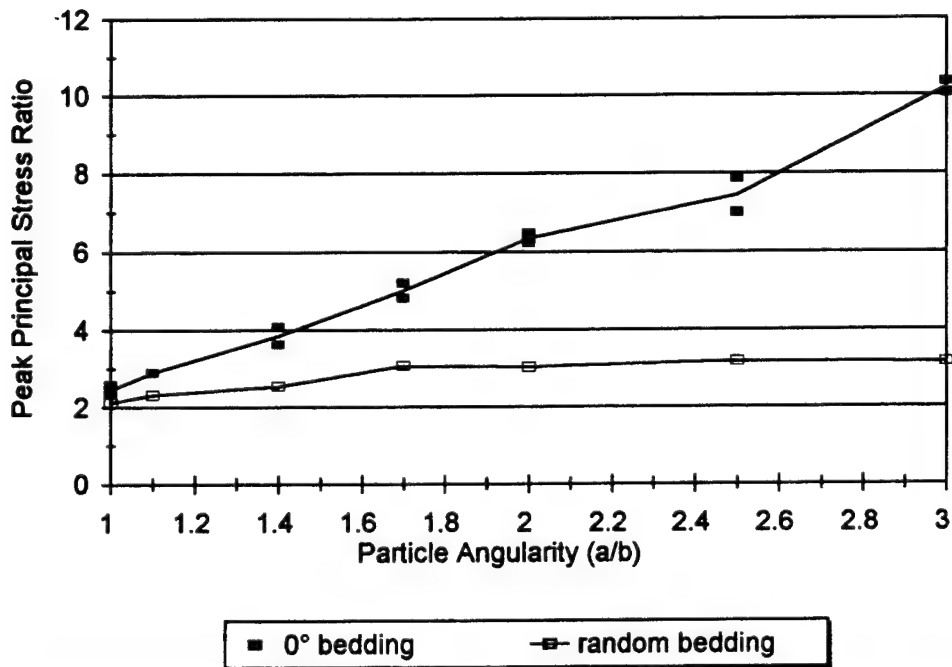

Figure 127. Effect of particle aspect ratio on the peak principal stress ratio $(\sigma_1/\sigma_2)_{max}$ for DEM samples with preferred horizontal ($\theta = 0°$) and random bedding.

8.2 Influence of Particle Shape on Volumetric Behavior

The volumetric behavior of granular materials is also strongly influenced by particle shape. Angular particles interlock more which facilitates more compression during the initial stages of shear. The tendency for assemblages with angular particles to contract more initially was observed in the volumetric strain behavior of both Konishi *et al*'s experimental tests and the ellipse-based DEM simulations presented in Section 7. However, as deformation continues, the angular particles ultimately dilate more than the more rounded particles when the orientation of the preferred bedding plane is normal to the direction of the major principal stress. The data comparison also showed that when the bedding plane is aligned toward the predicted Mohr-Coulomb failure plane ($45° + \phi/2$), the angular particles dilate less than the more rounded particles during biaxial shear. This difference in the dilatant behavior due to particle aspect ratio and bedding is examined further in Section 9.

8.2.1   Effect of Particle Aspect Ratio

The effect of particle aspect ratio on the volumetric strain behavior for DEM samples with preferred horizontal bedding ($\theta = 0°$) is shown in Figure 128. As shown previously, the sign conventions for the volumetric strain plots shown are opposite from those normally associated with contraction and dilation. Though the vertical axial strains shown are positive for compression, the volumetric strains shown are negative for compression and positive for dilation.

As particle aspect ratio increases, the assemblages experience longer periods of initial contraction but ultimately achieve higher dilatant strains over the course of deformation. At larger axial strains, the samples achieve a peak after which a state of constant volume strain exists. This contractant and dilatant behavior is typical for dense soils and other granular materials.
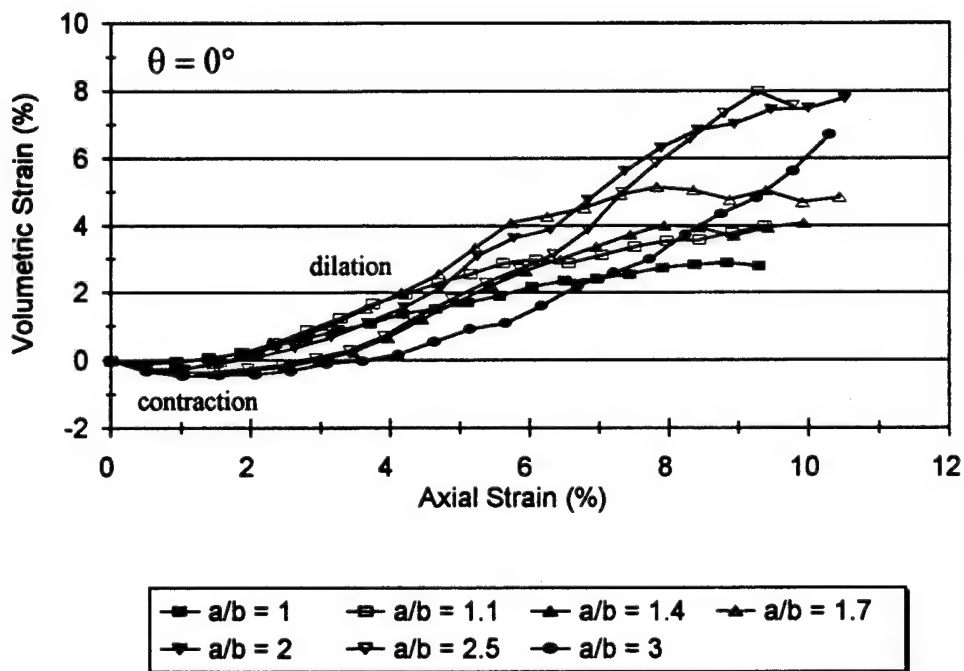

Figure 128.   Effect of particle aspect ratio on the volumetric strain for DEM samples with $\theta = 0°$

107

Similar behavior is observed in the evolution of the void ratio e during the course of stress-induced deformation as illustrated in Figure 129. Prior to shear, the angular particles form denser assemblages than the more rounded particles as they are able to interlock more. During shear, the samples with angular particles and preferred horizontal bedding dilate more. The relative increases in e from its initial value is significantly higher for samples with angular particles. For example, a 15% increase in the voids is yielded by samples with a/b = 1.0 (from e_o = 0.20 to e = 0.23) and 56% in those with a/b = 2.5 (from 0.16 to 0.25). After approximately 10% axial strain, the assemblages with rounded particles approach a state of constant volume strain, while those with more angular particles continue to dilate.
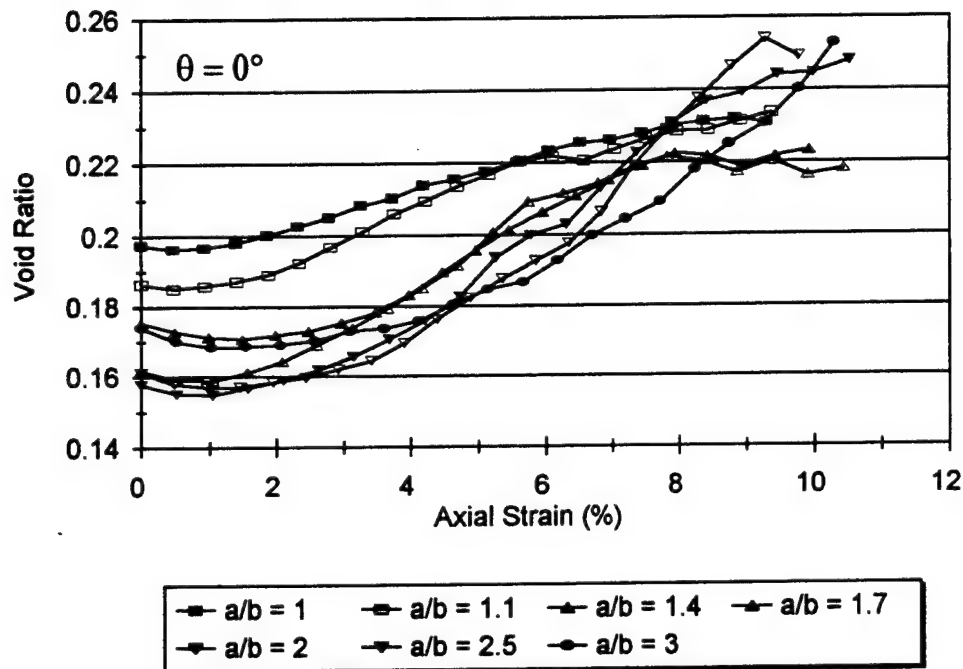

Figure 129. Effect of particle aspect ratio on the void ratio for DEM samples with preferred horizontal bedding during biaxial shear.

8.2.2 Effect of Particle Aspect Ratio and Orientation

The effect of particle aspect ratio on the overall deformation behavior is significantly different for samples with preferred bedding planes of 30, 60 or 90°. As particle aspect ratio increases, the assemblages contract longer and dilate less than the samples with horizontal bedding (θ = 0°). The volumetric strain for DEM samples with 60° bedding is shown in Figure 130. Though the samples have similar initial densities (or void ratios), the volumetric strain behavior exhibited is similar to that typically exhibited by loose materials. As the bedding plane becomes aligned toward the orientation of the Mohr-Coulomb failure plane (45° + ϕ/2), dilation actually decreases with increased particle aspect ratio. This trend is due to the coaxial alignment of the interlocking plane (or bedding plane) with 45° + ϕ/2 [8]. When these planes become coaxial, assemblages with higher degrees of interlocking deform more as a "rigid body" thereby exhibiting significantly less overall volumetric strain. This behavior is explained further in Chapter 9.
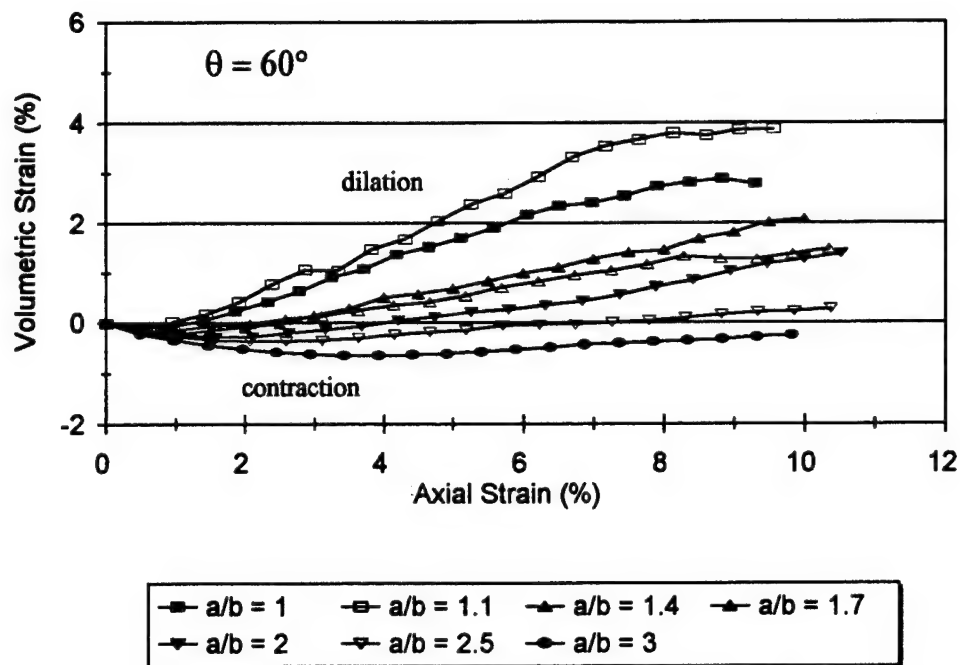
Figure 130.   Effect of particle aspect ratio on the volumetric strain for DEM samples with θ = 60°

Figure 131 shows the effect of preferred particle orientation on the volumetric strain behavior for samples consisting of "flat" particles (a/b = 3.0). Significantly more dilation occurs when the bedding plane is aligned normal to the major principal stress (θ = 0°) than when the bedding plane (or interlocking plane) is 30, 60 or 90°.
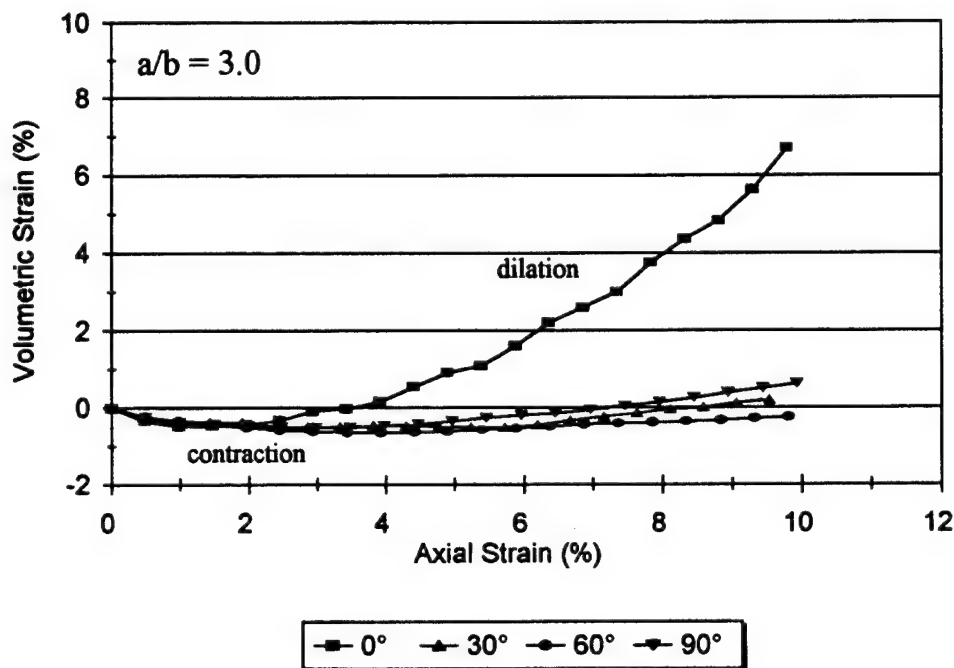

Figure 131.   Effect of particle bedding on the volumetric strain for DEM samples with a/b = 3.0.

While differences in the deformation behavior of granular materials is normally associated with differences in the sample's relative density, the numerical assemblages possess approximately the same initial void ratios (e_o = 0.174, 0.186, 0.178 and 0.178 for 0, 30, 60 and 90° bedding, respectively). Similar trends are observed in the evolution of the void ratio shown in Figures 132 and 133.
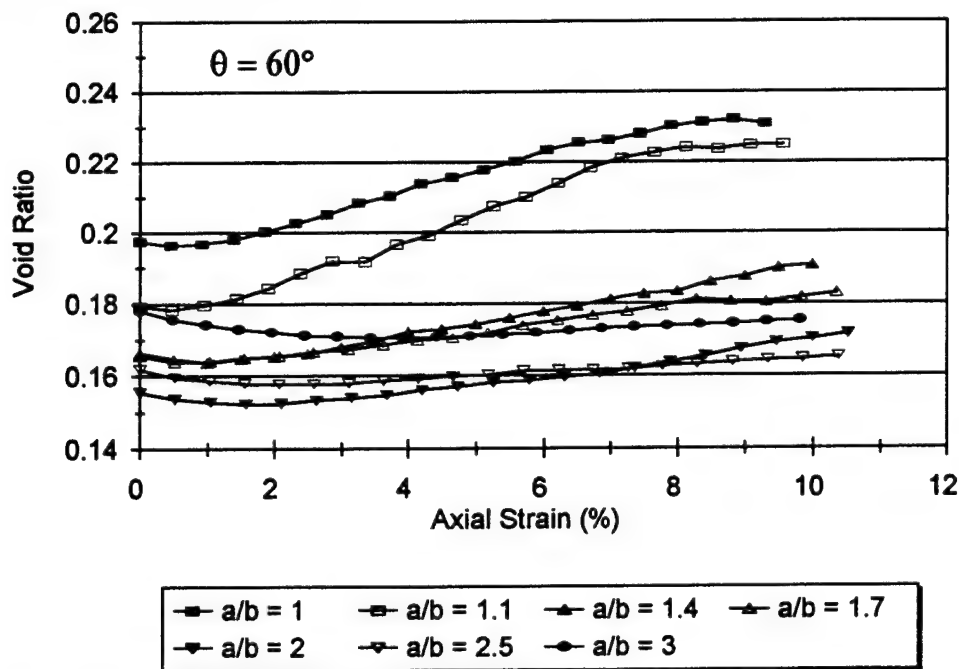

Figure 132. Effect of particle aspect ratio on the void ratio for DEM samples with preferred 60° bedding during biaxial shear.
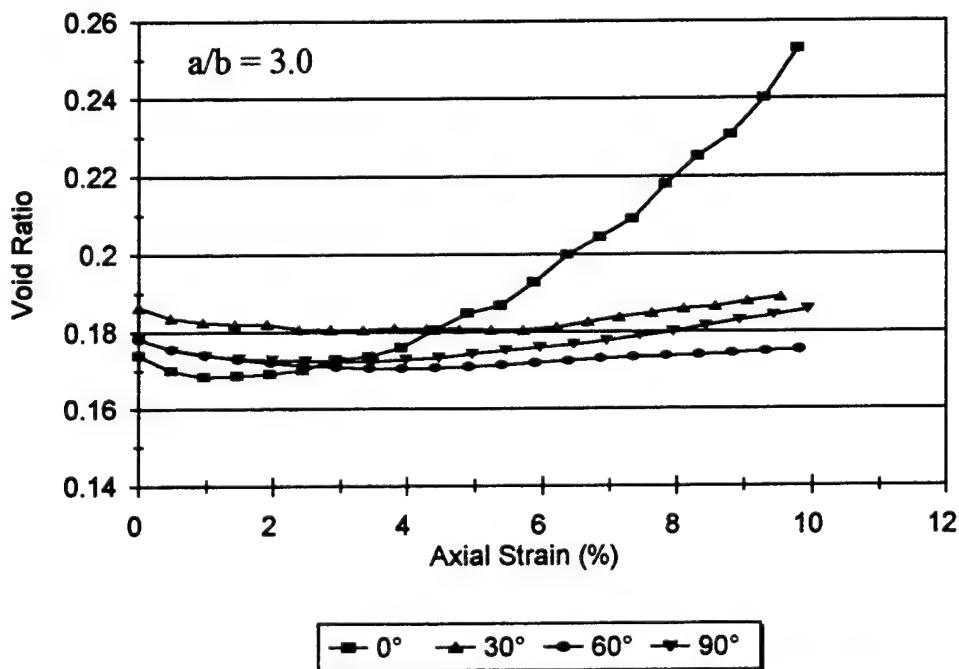

Figure 133. Effect of particle orientation on the void ratio for DEM samples with a/b = 3.0.

The angle of dilatancy δ represents the overall volumetric strain rate for the DEM assemblages from the start of shear ($\varepsilon_1 = 0\%$) to the strain at which $\Delta V \backslash V_o$ is maximum. The following equation is used to compute the dilatancy angle for the rectangular DEM samples under biaxial compression:

$$\sin\delta = \frac{d\varepsilon_v}{d\gamma_{max}} = -[\frac{d\varepsilon_1 + d\varepsilon_2 - d\varepsilon_1 d\varepsilon_2}{d\varepsilon_1 - d\varepsilon_2}] \tag{58}$$

where $d\varepsilon_v$, $d\gamma_{max}$, $d\varepsilon_1$ and $d\varepsilon_2$ are the changes in volumetric strain, shear strain, axial (vertical) strain and lateral (horizontal) strain, respectively. The strain increments are positive for compression and negative for dilation and are taken over the same time increment.

The effects of particle aspect ratio and the orientation of the bedding plane on δ for the DEM samples are shown in Figures 134 and 135. Assemblages consisting of round particles (a/b = 1.0) yield values for δ of 7.5°, while samples with angular particles and horizontal bedding ($\theta = 0°$) yield values for δ of approximately 15°. While δ increases with increased aspect ratio for samples with $\theta = 0°$, it decreases significantly with increased aspect ratio for samples with $\theta = 30, 60$ and $90°$. The difference in δ due to particle orientation is small for samples consisting of rounded particles, but as aspect ratio increases and the orientation fabric becomes more anisotropic, the difference is much greater. The angle of dilatancy is lowest for samples consisting of angular particles with 60° bedding as they approach $\delta = 0°$ indicating almost no dilation behavior.

The deformation of the particulate assemblages with $\theta = 0°$ can be related to the strength as shown in Figure 136. Higher strength is achieved by samples that experience more overall dilation during the deforming process.
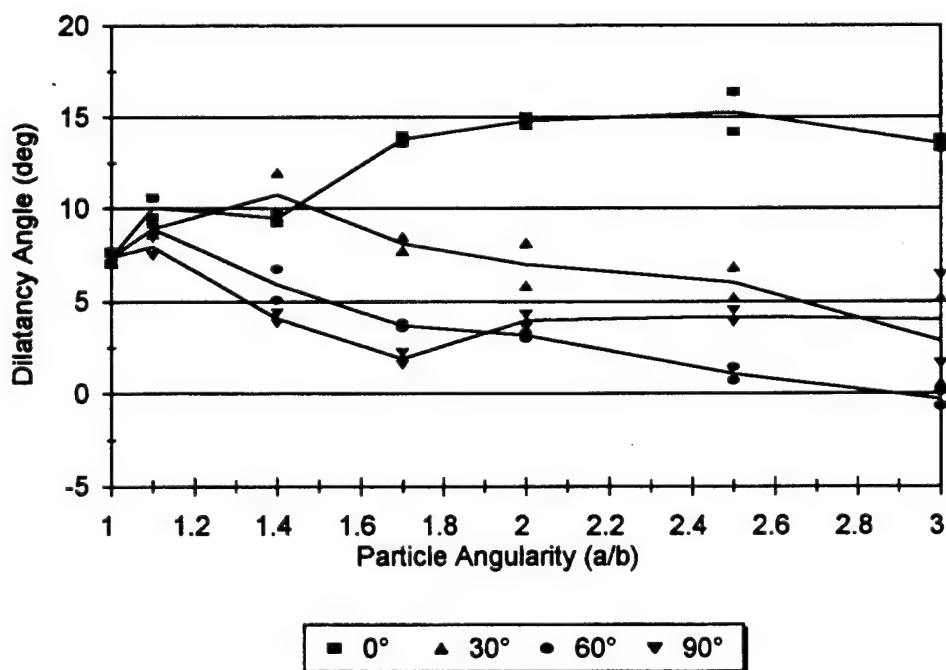

Figure 134. Effect of particle aspect ratio on the dilatancy angle for DEM samples with preferred particle bedding.
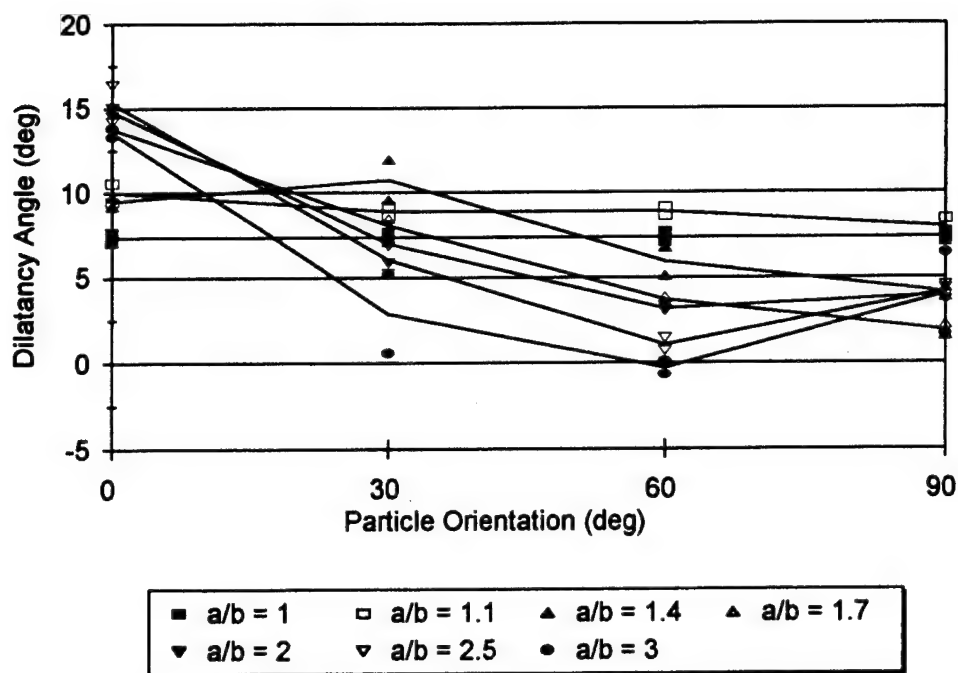
Figure 135. Effect of particle bedding on the dilatancy angle for DEM samples with variations in particle aspect ratio.
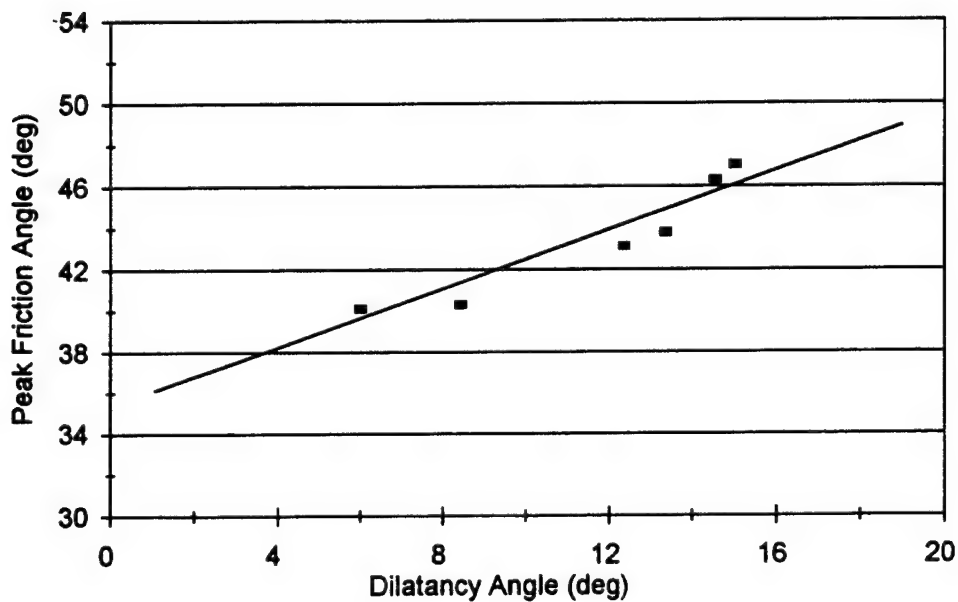

Figure 136. Effect of the dilatancy angle on the peak internal friction angle for DEM samples with a/b = 2.0 and $\theta = 0°$.

112

8.2.3   Effect of Void Ratio

The effect of the initial void ratio e_o on the volumetric strain of DEM samples with a/b = 2.0 and preferred horizontal bedding ($\theta = 0°$) is shown in Figure 137. The sample with looser packing ($e_o = 0.176$) exhibits less dilatant behavior than the denser sample ($e_o = 0.158$). Similarly, Figure 138 shows the evolution of the void ratio during the course of deformation for the same numerical samples. While each sample exhibits "dense" behavior, the denser sample ($e_o = 0.158$) dilates more than the looser sample. This is typical deformation behavior for "real" granular materials with variations in their initial relative density.

The effect of the void ratio on the dilatancy angle δ for DEM samples with a/b = 2.0 and preferred horizontal bedding ($\theta = 0°$) is shown in Figure 139. Again, the tendency for the denser sample to dilate more than the less dense sample is apparent. The assemblage with $e_o = 0.158$ yields a value for δ of 15°, while for $e_o = 0.176$, δ is approximately 7 or 8°.
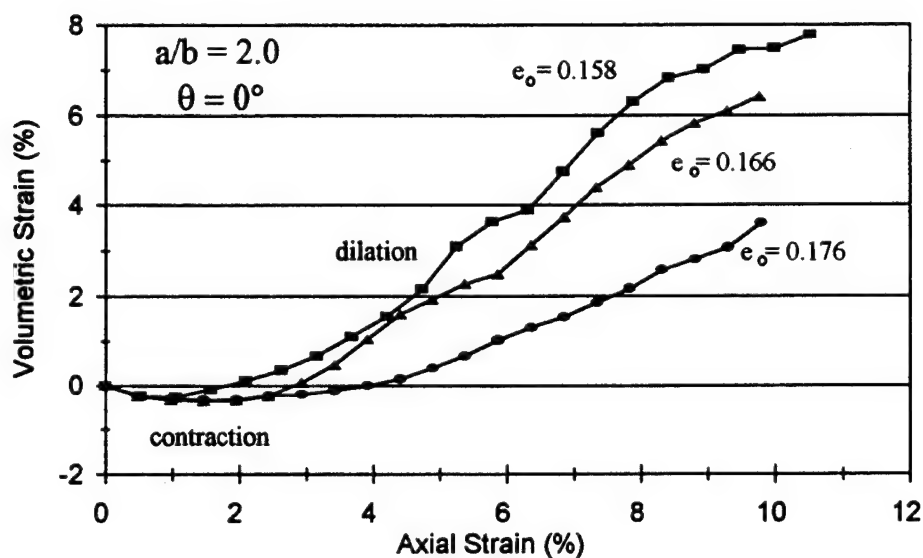

Figure 137.   Effect of void ratio on the volumetric strain for DEM samples with a/b = 2.0 and $\theta = 0°$.
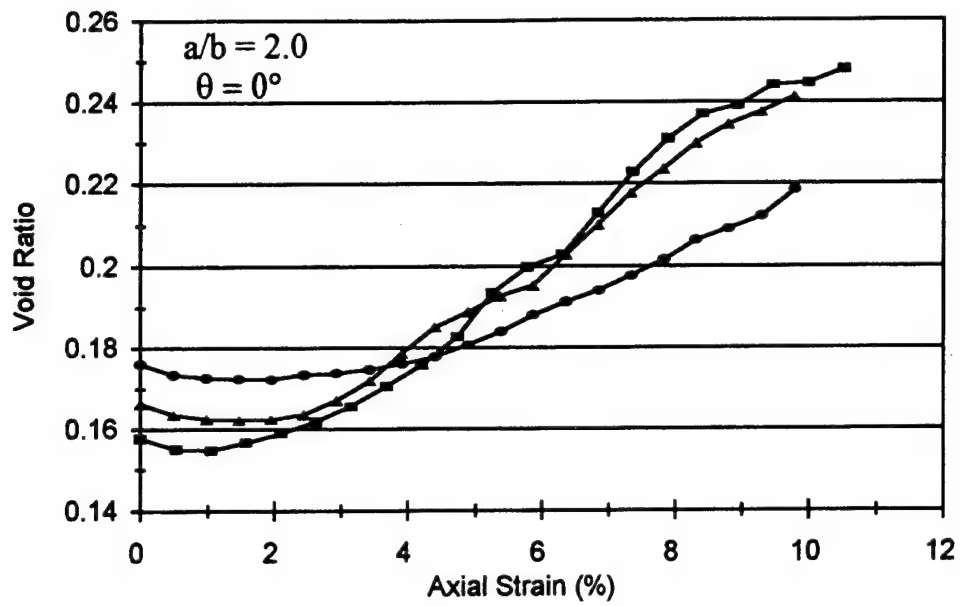
113

Figure 138. Evolution of the void ratio e for DEM samples with a/b = 2.0, θ = 0° and variations in the initial void ratio.
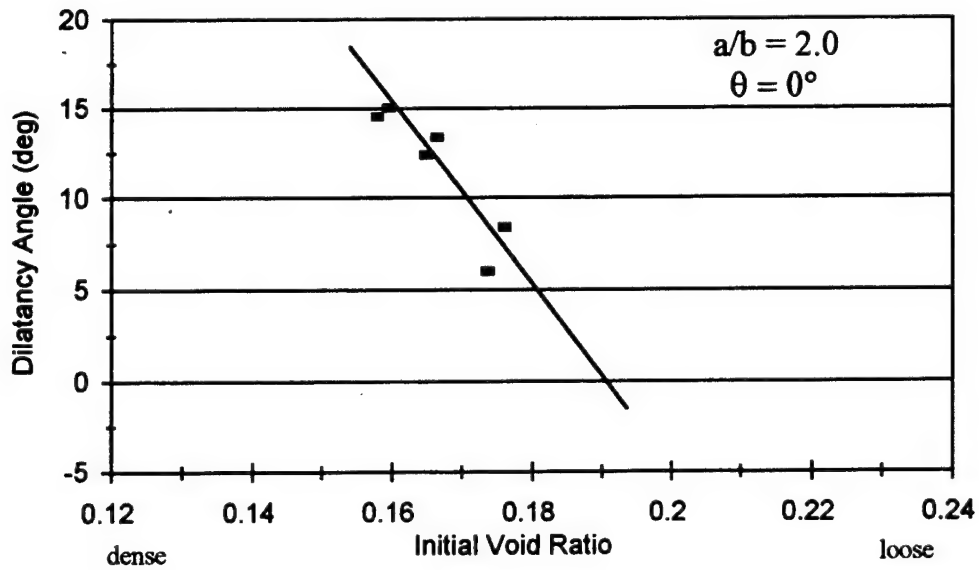

Figure 139. Effect of the initial void ratio on the dilatancy angle for DEM samples with a/b = 2.0 and θ = 0°.

8.2.4   Effect of an Isotropic Orientation Fabric

The progressions of the volumetric strain for numerical assemblages with random bedding are shown in Figure 140.. The random sample consisting of round particles is approximately isotropic and experiences almost no volume change during the course of deformation. As particle aspect ratio increases, however, the assemblages contract and dilate slightly more. Because the fabrics are looser and significantly less anisotropic than the assemblages with preferred bedding, the random samples contract and dilate less. The small increase in the dilatant behavior for the random assemblages consisting of flatter particles is due to an increase in interlocking.

Figure 141 illustrates the effect of particle aspect ratio on the angle of dilatancy δ for DEM samples with preferred horizontal and random bedding. The samples with more isotropic fabrics (random bedding) exhibit significantly less dilatant behavior than the samples with preferred bedding. Though the numerical assemblages with preferred bedding yield values for δ that increase with particle aspect ratio, the samples with random bedding remain at approximately the same value.

The fabric of assemblages consisting of perfectly round particles (a/b = 1.0) are more isotropic since round particles have no orientation. Consequently, the difference in δ for these samples is primarily attributed to the difference in their initial void ratios.
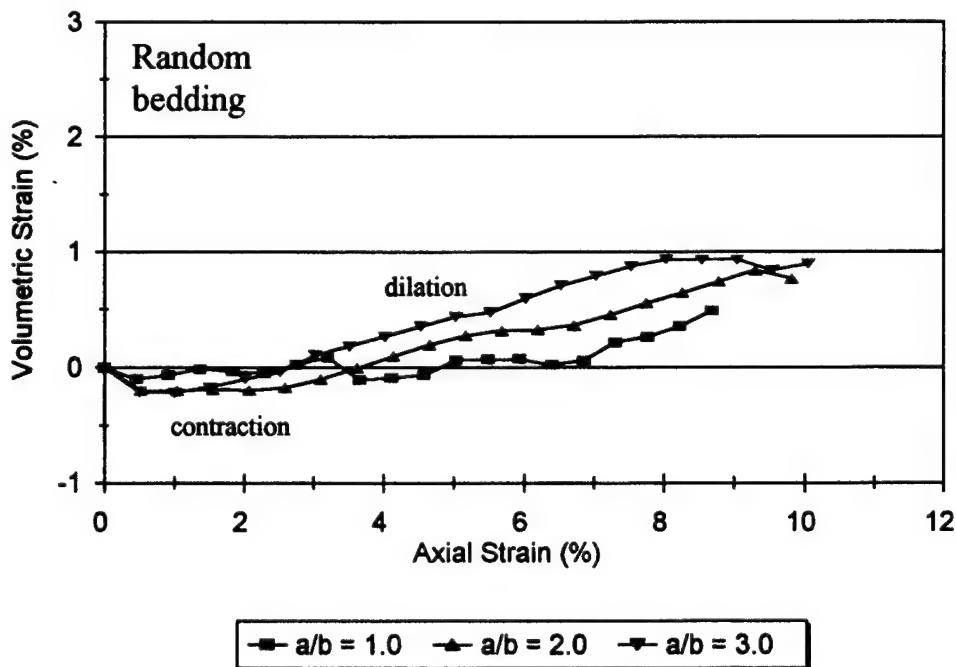

Figure 140.   Effect of particle aspect ratio on the volumetric strain for DEM samples with random bedding.
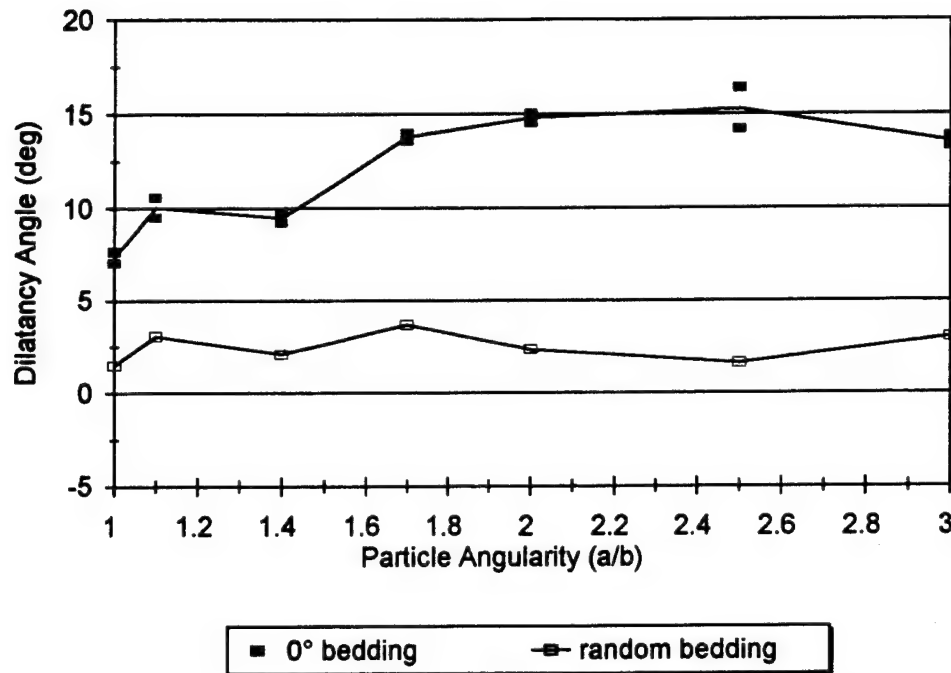
Figure 141. Effect of particle aspect ratio on the dilatancy angle for DEM samples with preferred horizontal bedding ($\theta = 0°$) and random bedding.

8.2.5 Deformation Mechanisms

Previous micromechanical investigations have shown that particle rolling may be the dominant deformation mechanism and primary cause for failure of particulate systems (Oda *et al* 1983, Ting *et al* 1993). Numerical models using circles or spheres for particle shapes have consistently yielded lower overall strength compared with real sands because the round particles tend to roll excessively during the assemblage's deformation. For samples with round particles (a/b = 1.0) in the current study, the peak angle of internal friction ϕ_{max} ranges from a low of 19° in looser assemblages to a high of 26° in those with denser packing. Since ϕ_{max} on average is lower than the interparticle sliding friction angle ϕ_μ of 26°, it is likely that the low strength exhibited by assemblages with round particles is due to particle rolling. The primary advantage to using angular shapes such as the ellipse is that particle interlocking can occur which significantly reduces the negative effects of particle rolling and more accurately simulates the micromechanical behavior of real particulate systems.

The ellipse-based DEM model tracks the motion of each particle during the course of the simulation and decomposes the relative contact velocities between colliding particles into translation and rotation components. The total rotation and translation components of the relative contact velocities are further decomposed into normal and tangential components. These incremental quantities are summed over every contact within the assemblage to assess the overall relative importance of particle motion due to rolling and sliding during the assemblage's deformation. Very little net contact motion occurs in the subdomains within the assemblages where rigid body motion exists. Consequently, net contact deformations are used instead of total contact deformations to effectively exclude the rigid body motion from the contact deformation statistics. Details of how the model decomposes these contact deformations have been presented elsewhere (Ting *et al* 1993).

Figure 142 shows the effect of particle aspect ratio on the relative importance of rotation and translation on the total, normal and tangential particle motion for the DEM samples with preferred bedding of 0°. For the numerical samples consisting of round particles (a/b = 1.0), the net total particle rotation is over 2 times higher than particle translation. No net normal rotation occurs for the round particles since their rotation cannot exert eccentric normal forces on neighboring particles. Instead, contact motion due to rotation between round particles is entirely tangential. As particle aspect ratio increases, however, the relative importance of particle motion due to rotation and translation converges toward unity. This is true for the total, normal and tangential components of particle motion. This suggests that angular particles exert eccentric normal forces on neighboring particles in contact thereby significantly reducing the negative effects of particle rolling.

Similar results are observed in Figure 143 for DEM samples with preferred 30° bedding. The similarities indicate that the relative importance of particle motion due to rotation and translation are independent of the bedding plane's orientation with respect to the orientation of the principal stress σ_1.
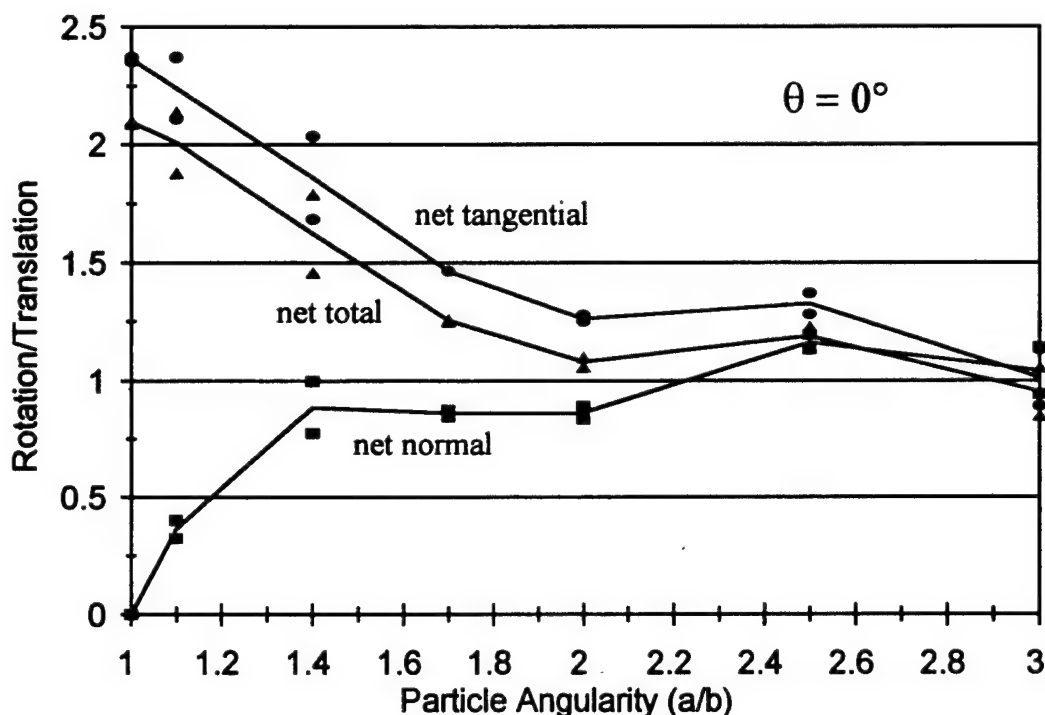

Figure 142. Effect of particle aspect ratio *a/b* on the relative importance of deformation mechanisms for DEM samples with preferred 0° bedding.
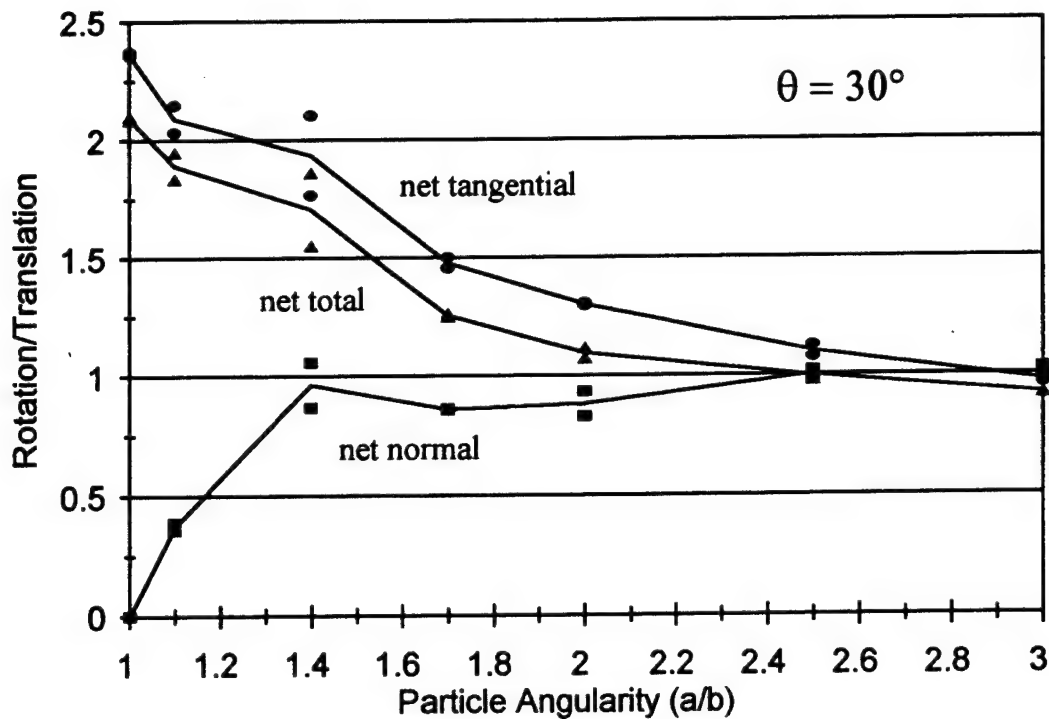
Figure 143. Effect of particle aspect ratio *a/b* on the relative importance of deformation mechanisms for DEM samples with preferred 30° bedding.

8.3 Influence of Particle Shape on the Coordination Number

The coordination number C_n is the average number of contacts per particle and represents the local variability of the assemblage's porosity (or void ratio). Studies have shown that samples with higher coordination numbers tend to exhibit higher strength as more particle contacts produce a denser and more stable sample (Feda 1982). The effect of particle aspect ratio on the initial coordination number for the numerical samples with 0, 30, 60 and 90° bedding is shown in Figure 144. The initial C_n increases with increasing particle aspect ratio and is apparently unaffected by the orientation of the overall preferred bedding plane.

During the course of stress-induced deformation, however, the orientation of the bedding plane as well as particle aspect ratio have a significant effect on the evolution of the coordination number. Figures 145 and 146 illustrate the effect of particle aspect ratio on C_n for samples with 0 and 60° bedding, respectively.
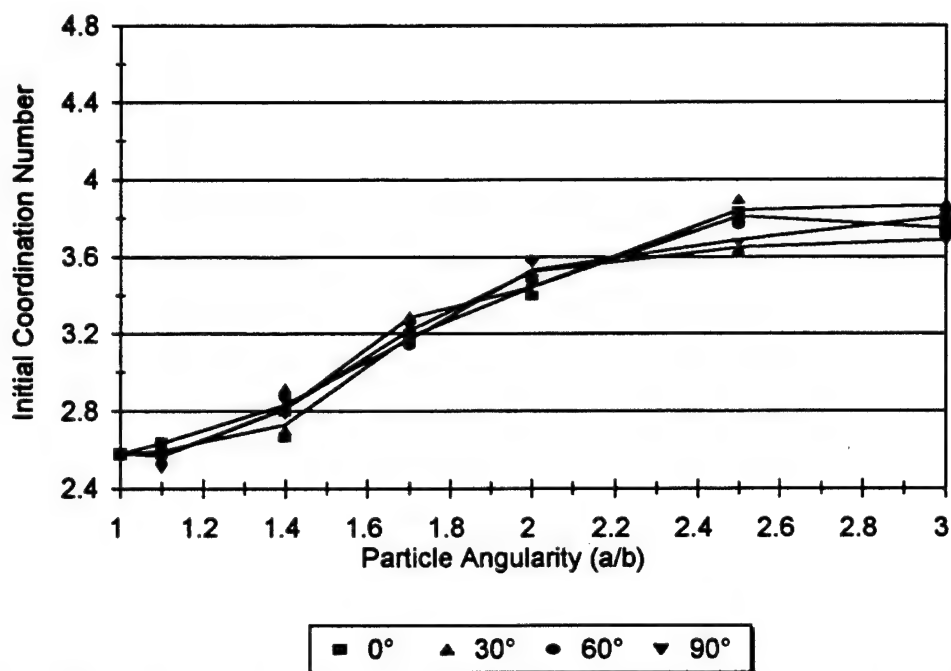
Figure 144. Effect of particle aspect ratio on the initial coordination number for DEM samples with preferred bedding θ.
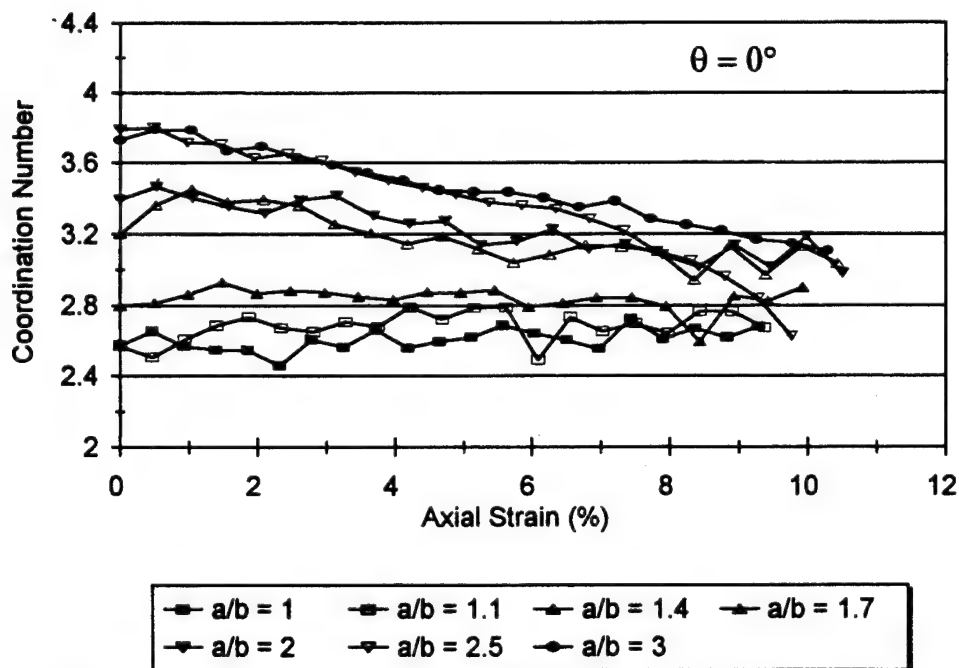

Figure 145. Effect of particle aspect ratio on the coordination number for DEM samples with θ = 0°.

119

As the samples with horizontal bedding ($\theta = 0°$) are sheared, relatively little change in C_n is observed for those samples with a/b of 1.4 or less. For samples consisting of more angular particles (a/b > 1.4) and 0° bedding, however, C_n decreases from its high initial value to a significantly lower value that is similar to that of the samples consisting of more rounded particles. For example, C_n for samples consisting of "flat" particles (a/b = 3.0) decreases from a value of 3.8 prior to shear to a value of approximately 3.1 at 10% axial strain. Collectively, the samples with preferred horizontal bedding appear to be converging to a similar residual C_n value of approximately 2.8 as the particles become fully mobilized. In another DEM study in which randomly oriented and uniform sized ellipse-shaped particles were used, Rothenburg and Bathurst (1991) found that C_n approached a "critical" value of approximately 3.5. The fabric of their numerical samples, however, were more isotropic.

C_n for the samples with 60° bedding, however, does not tend to converge. Instead, for those samples consisting of more angular particles, the coordination number quickly increases from its initial value and then remains relatively constant during the course of deformation. For example, C_n for samples consisting of flatter particles (a/b = 3.0) increases from its initial value of 3.8 to a value of 4.2 at approximately 4% axial strain and thereafter remains about the same.

The effect of particle bedding on the evolution of the coordination number for DEM samples with a/b = 1.1 and 3.0 is shown in Figures 147 and 148, respectively. For samples consisting of rounded particles (a/b = 1.1), the effect of the bedding plane is rather insignificant as similar values for C_n are obtained for the numerical samples with variations in particle bedding. During biaxial shear, C_n remains approximately the same for samples with a/b = 1.1. The evolution of C_n is strongly influenced, however, as the particles become more angular. For samples consisting of flatter particles (a/b = 3.0) with preferred horizontal bedding ($\theta = 0°$), the coordination number decreases significantly during the course of deformation. The decrease in C_n is less for samples with 30° bedding, while for samples with 60 and 90° bedding, C_n actually increases. Similar decreases in the coordination number have been reported by Rothenburg and Bathurst (1991, Chen and Ishibashi (1990).
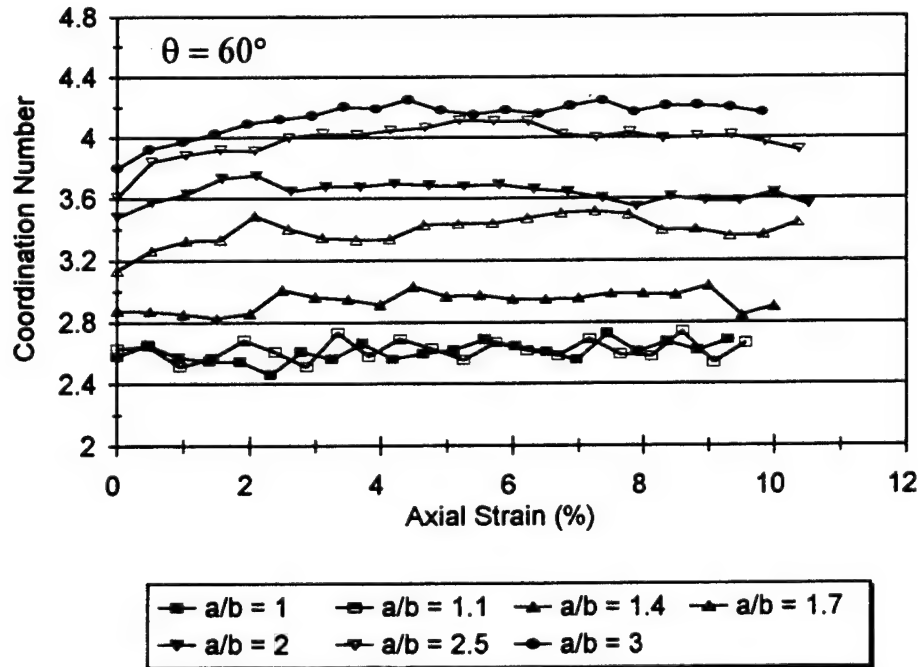

Figure 146.   Effect of particle aspect ratio on the coordination number for DEM samples with $\theta = 60°$.
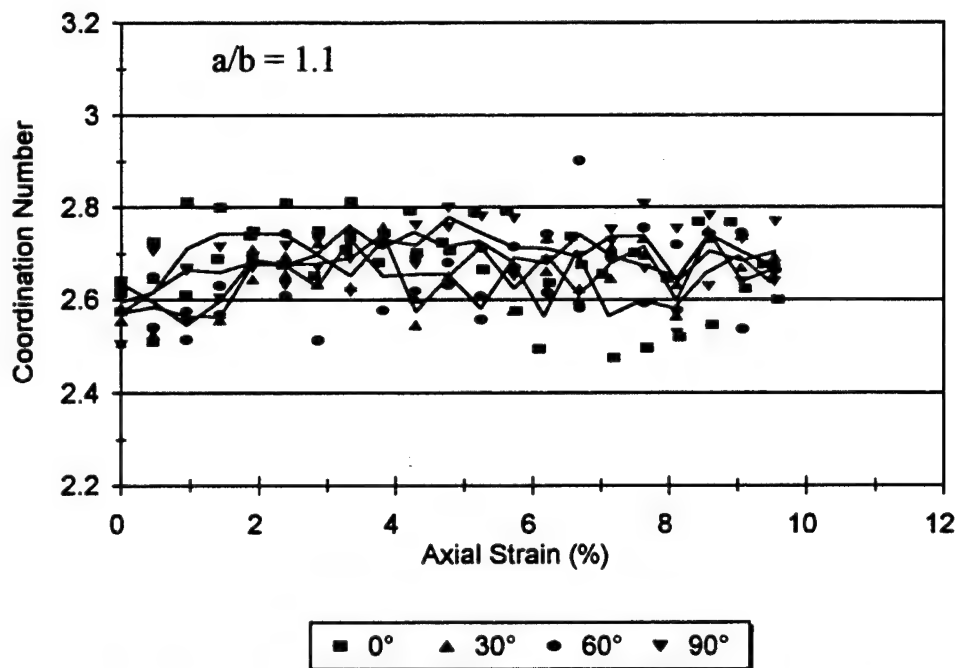
120

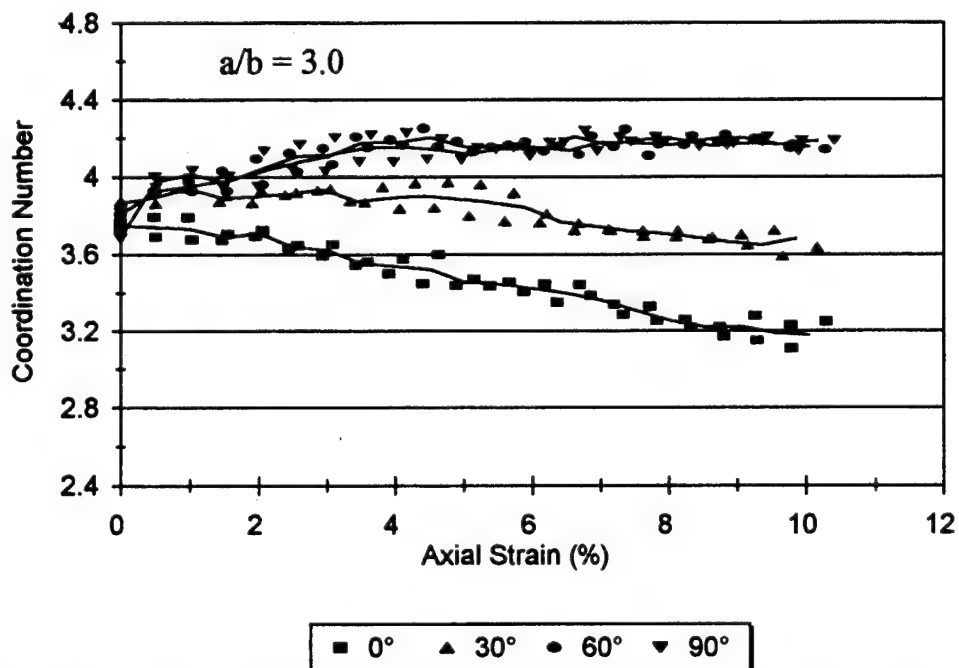**Figure 147.** Effect of particle bedding on the coordination number for DEM samples with a/b = 1.1.

Figure 148. Effect of particle bedding on the coordination number for DEM samples with a/b = 3.0.

This is in agreement with the deformation behavior of the particulate assemblages presented previously. When subjected to biaxial shear, samples consisting of angular particles with preferred horizontal bedding dilate more than those with 30, 60 or 90° bedding. As a result, more contacts are broken between particles as the assemblage dilates, while more contacts are made between particles with 60 and 90° bedding as the assemblage contracts. This trend is not as distinct in samples consisting of rounded particles, however, because less differences exist in the dilatant behavior due to particle bedding.

The effect of particle aspect ratio on the coordination number for numerical samples with preferred horizontal bedding ($\theta = 0°$) and random bedding is shown in Figure 149. Figure 144 showed no significant differences in C_n for samples with preferred particle bedding of 0, 30, 60 and 90°. Similarly, no significant differences in C_n are evident for assemblages with preferred and random bedding. This is unexpected since the relative densities of the assemblages are quite different. Because C_n is generally regarded as being closely associated with the relative density, it is expected that the coordination number for the looser samples with random bedding to be lower than for those with preferred bedding. However, Chen and Ishibashi (1990) suggest in their numerical simulations using spherical particles that isotropic fabrics have the highest coordination number.
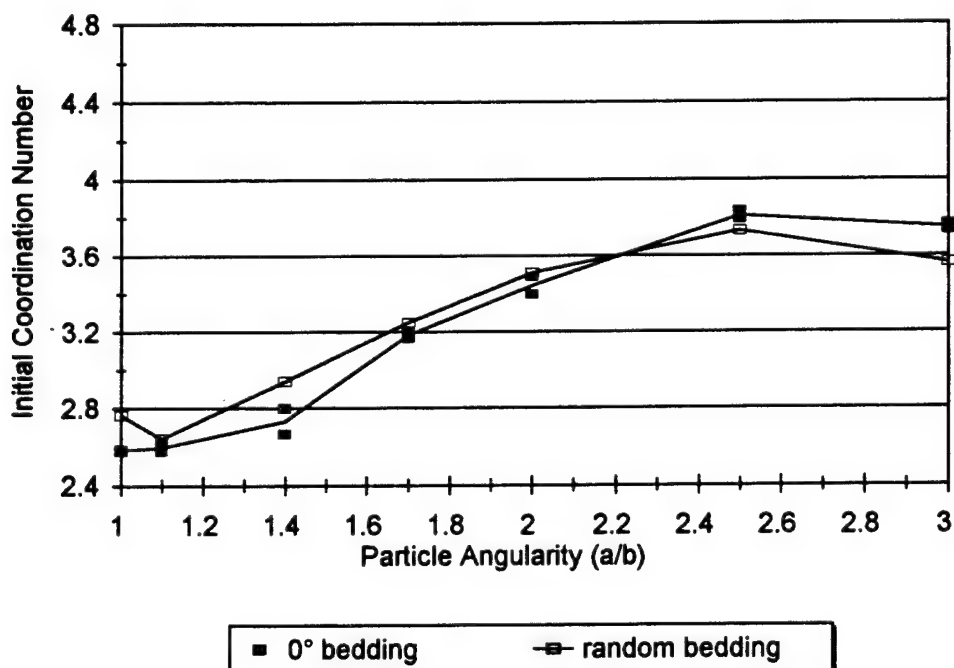

Figure 149. Effect of particle aspect ratio on the initial coordination number for DEM samples with preferred horizontal bedding ($\theta = 0°$) and random bedding.

122

8.4 Effect of Sample Formation

The majority of the numerical assemblages were formed by individually placing the particles in their initial locations forming densely packed samples (O sample series). In an effort to obtain samples with more variations in the initial void ratio e_o while maintaining control of particle bedding, other packing techniques were used to form the L, FD and FL sample series. A wider range for e_o was achieved using the different packing schemes, however the ranges for individual packing methods were still rather narrow. For example, the L sample series yielded values for e_o ranging from 0.185 to 0.211, while for the FD series, e_o ranged from 0.139 to 0.149.

The effect of the initial void ratio e_o and the different packing methods on the peak internal friction angle ϕ_{max} for samples with a/b = 2.0 and $\theta = 0°$ is shown in Figure 150. Though e_o varies significantly for the combination of sample series, the magnitude of ϕ_{max} does not vary accordingly. Instead, the e $_{max}\phi$ relationship for the individual sample series shifts along the e_o axis while ϕ_{max} remains relatively unchanged. These results illustrate the extreme sensitivity of the ellipse-based DEM model to the stress history of the samples during their formation.

The progression of the maximum shear stress q and volumetric strain $\Delta V/V_o$ for individual numerical samples with a/b = 2.0 and 0° bedding is shown in Figures 151 and 152. Assemblages that were prestressed during their consolidation (FD5114 and L5112) generally exhibit stiffer responses to shear, while the hand-packed sample (O5114) which was not prestressed exhibits a softer response. Sample FL5114 exhibits a softer response similar to the hand-packed sample suggesting that its initial stress fabric prior to shear is less anisotropic than samples FD5114 and L5112. Presumably, the more anisotropic stress fabric produces a more stable sample initially and brittle stress-strain behavior, while less stress fabric anisotropy produces a less stable sample and plastic behavior. Similar stiff responses to shear due to prestressing was observed by Ishibashi and Agarwal (1991) in their numerical simulations using spheres.
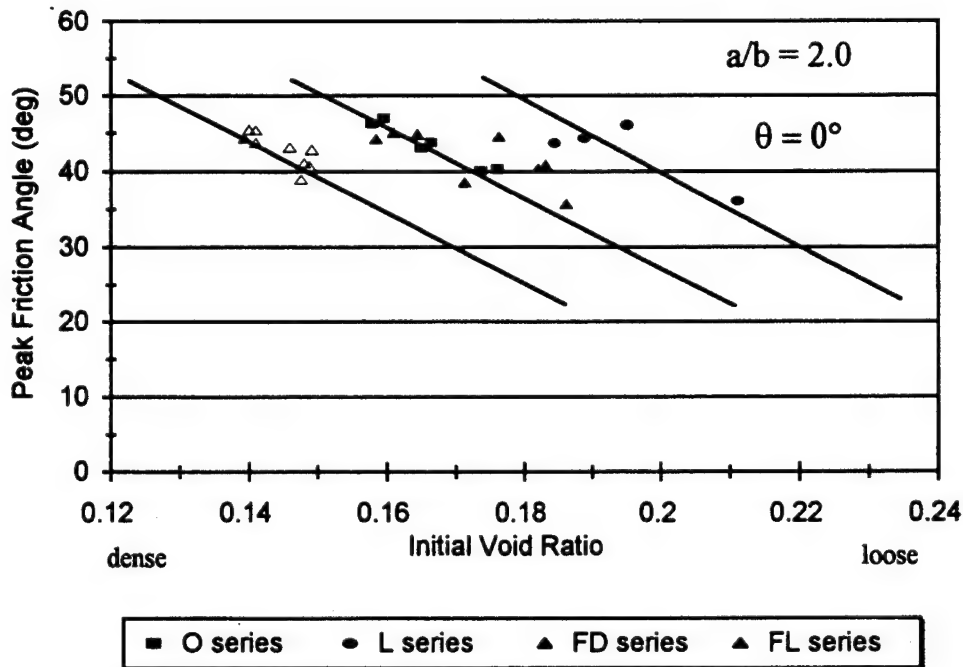

Figure 150. Effect of the initial void ratio e_o on the peak friction angle ϕ_{max} for DEM samples (a/b = 2.0 and $\theta = 0°$) formed differently
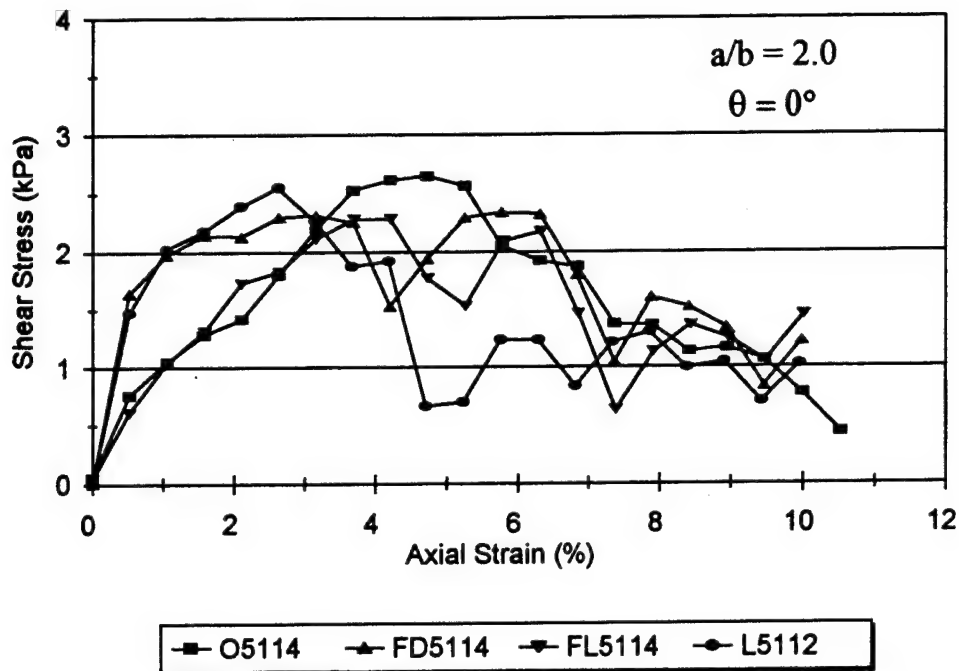
123

Figure 151. Effect of the initial void ratio e_o on the shear stress q_{max} for DEM samples (a/b = 2.0 and θ = 0°) formed differently.
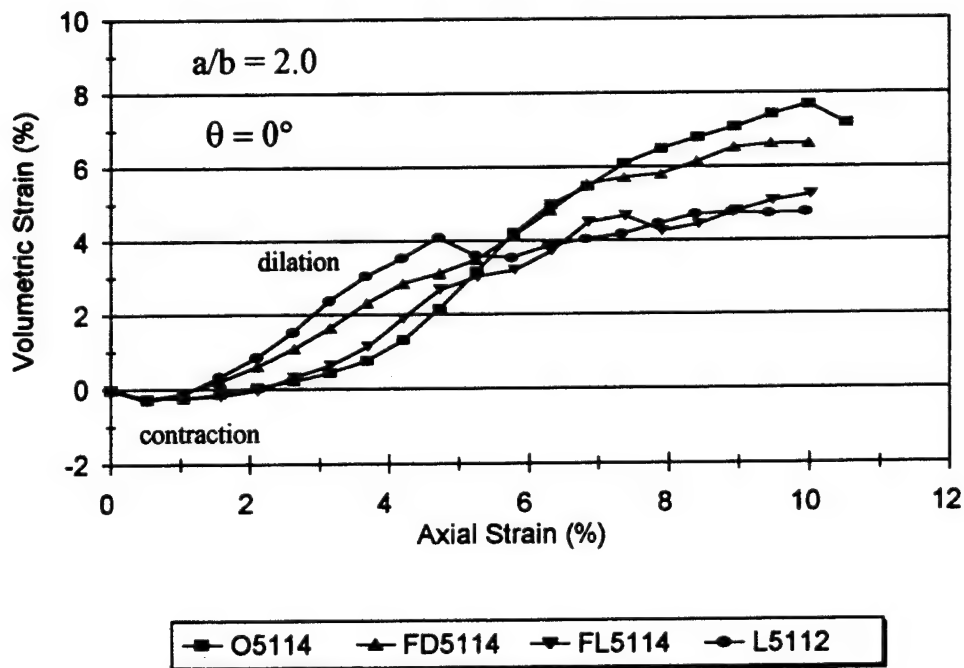

Figure 152. Effect of the initial void ratio e_o on the volumetric strain for DEM samples (a/b = 2.0 and θ = 0°) formed differently.

8.5 Effect of Confining Stress σ_2

The data presented thus far was obtained from samples that were isotropically compressed to a mean stress p of 0.7 kPa and then biaxially sheared while laterally applying a constant confining stress σ_2 of 0.7 kPa. Additional samples with particle aspect ratios a/b of 1.4 and 2.0 and with preferred horizontal bedding ($\theta = 0°$) were isotropically compressed to a p of 1.4 and 2.1 kPa and then sheared with $\sigma_2 = 1.4$ and 2.1 kPa applied laterally. This Section presents the strength and deformation results of these additional test simulations with variations in σ_2.

Figure 153 shows the effect of variations in σ_2 on the shear stress q for the same numerical assemblage with $a/b = 1.4$ and $\theta = 0°$. An increase in the shear resistance, hence the strength, is achieved by the assemblage with increased σ_2. The effect is similar for a DEM sample with $a/b = 2.0$ and $\theta = 0°$ as shown in Figure 154. A comparison of the results shown in Figures 153 and 154 shows the effect of particle angularity on the strength of the assemblages. For each σ_2, the sample consisting of angular particles ($a/b = 2.0$) yields significantly higher peak values for q than that with the more rounded particles ($a/b = 1.4$). For example, assemblages with $a/b = 1.4$ and 2.0 that are confined laterally with $\sigma_2 = 0.7$ kPa yield values for q_{max} of 1.5 and 2.7 kPa, respectively, while those with $\sigma_2 = 2.1$ kPa yield values for q_{max} of 4.0 and 6.5 kPa.

The maximum shear stress q is plotted against the mean stress p in Figure 155 for the numerical sample with $a/b = 1.4$ and in Figure 156 for the sample with $a/b = 2.0$. The stress paths are oriented at 45° from the horizontal as they are for "real" granular materials. The angle of internal friction ϕ is a material property and does not change significantly as the confining stress σ_2 is varied. The Mohr-Coulomb failure envelope defines ϕ as illustrated in Figures 155 and 156. The effect of particle angularity on ϕ is evident as the more angular particles with $a/b = 2.0$ yield a higher average value for ϕ than the more rounded particles with $a/b = 1.4$ ($\phi = 47.0$ and 38.4°, respectively).
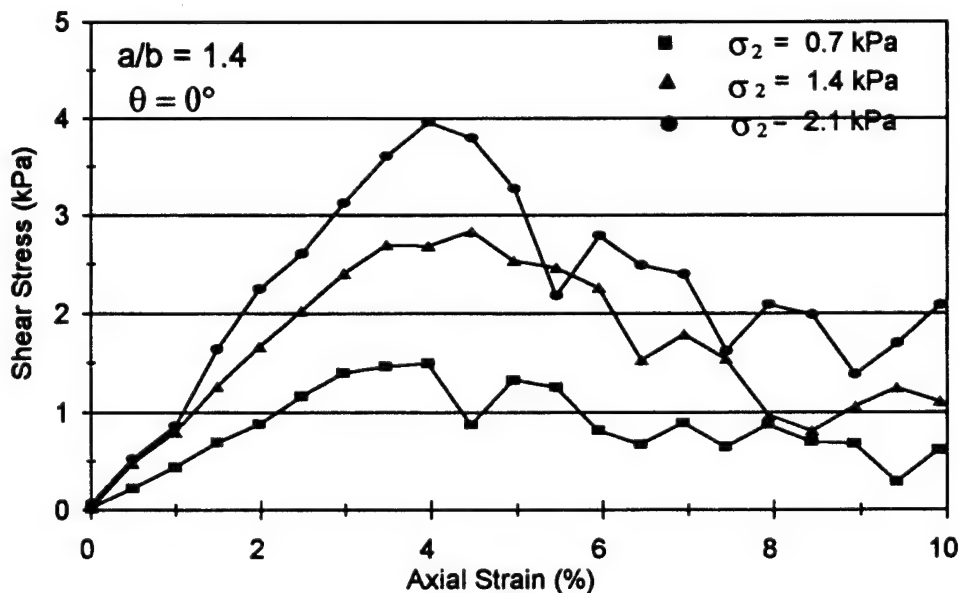

Figure 152. Effect of the confining stress σ_2 on the shear stress q for a DEM sample with $a/b = 1.4$ and 0° bedding.
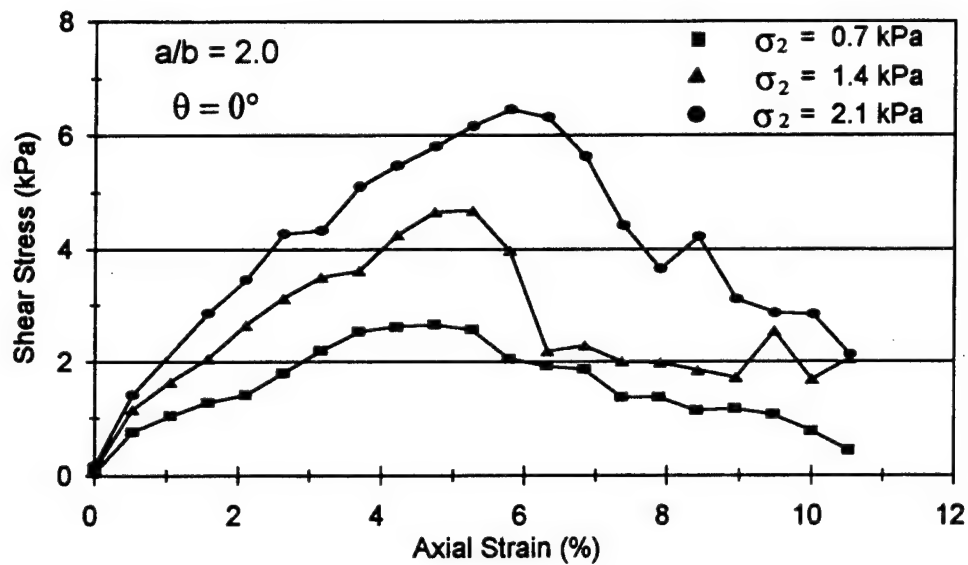
Figure 154. Effect of the confining stress σ_2 on the shear stress q for a DEM sample with a/b = 2.0 and 0° bedding.
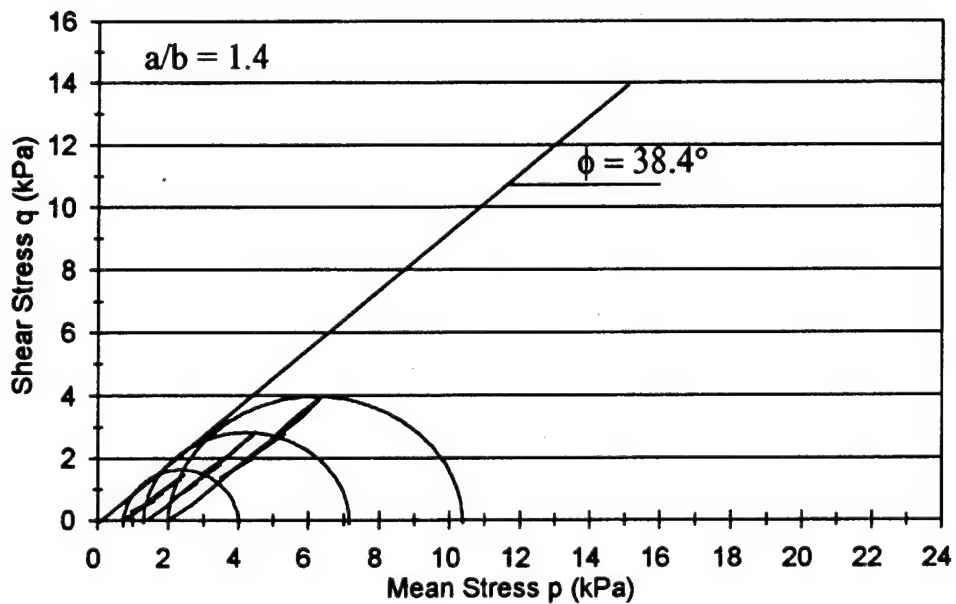

Figure 155. Mohr circles for a DEM sample (a/b = 1.4, θ = 0°) with confining stresses of 0.7, 1.4 and 2.1 kPa and the resulting Mohr-Coulomb failure envelope.
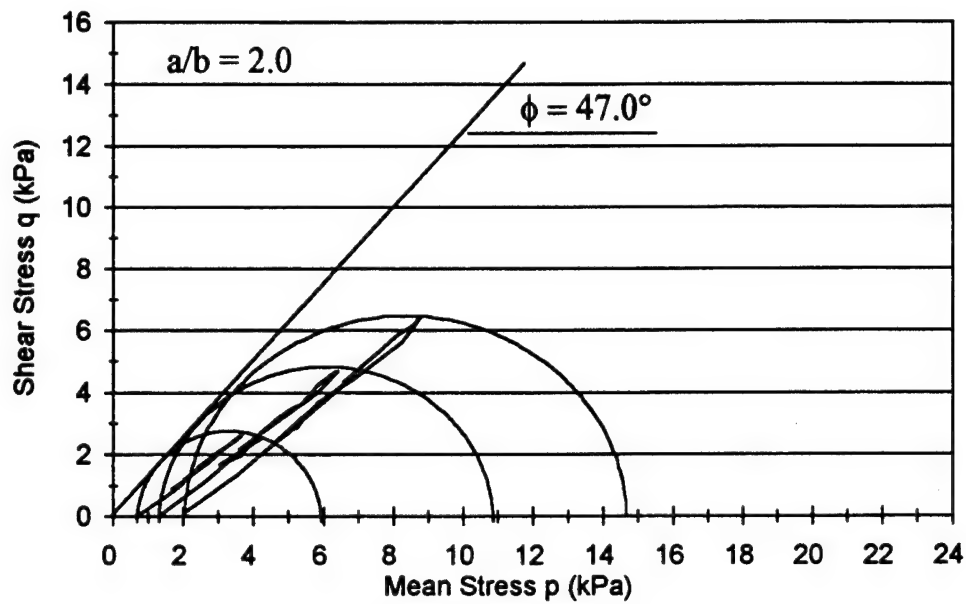
Figure 156. Mohr circles for a DEM sample (a/b = 2.0, θ = 0°) with confining stresses of 0.7, 1.4 and 2.1 kPa and the resulting Mohr-Coulomb failure envelope.

The effect of σ_2 on the volumetric strain $\Delta V/V_o$ is shown in Figures 157 and 158. The DEM results show that the sample with the higher confining stress dilates less throughout the course of deformation. This behavior is typical for soil and other granular materials. A comparison of Figures 157 and 158 illustrate the effect of particle angularity on $\Delta V/V_o$. The assemblage with angular particles (a/b = 2.0) dilates more than that with more rounded particles.

127

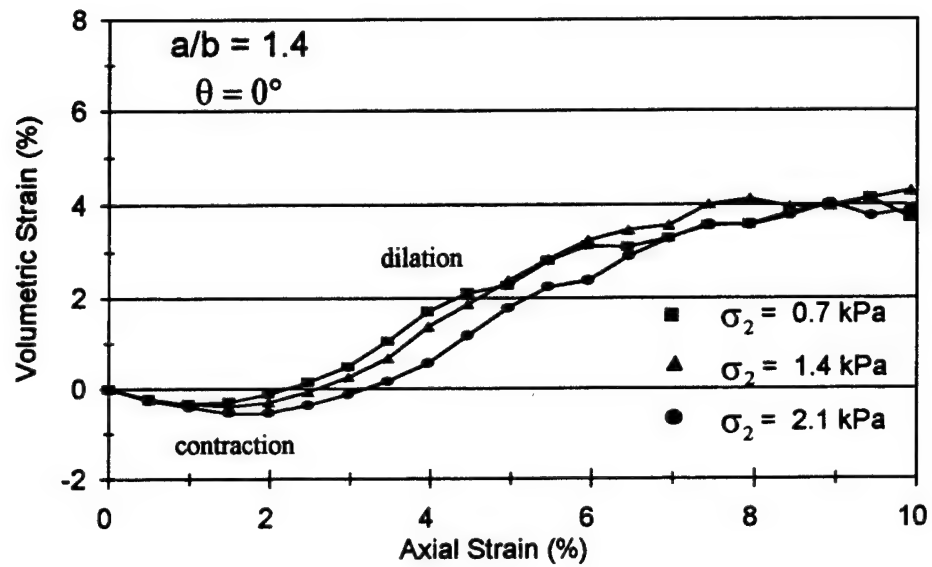**Figure 157.** Effect of the confining stress σ_2 on the volumetric strain for a DEM sample with a/b = 1.4 and 0° bedding.
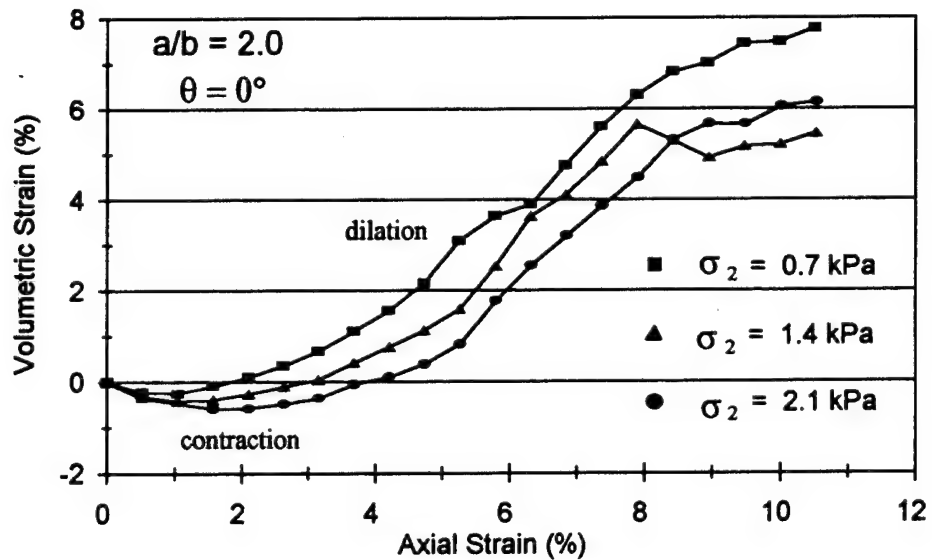

Figure 158. Effect of the confining stress σ_2 on the volumetric strain for a DEM sample with a/b = 2.0 and 0° bedding.

9. DISCUSSION OF DEM RESULTS

The results of the biaxial compression test simulations presented in Section 8 show that the overall mechanical behavior of granular materials is strongly influenced by the shape of the particles. Higher strength and more dilation are exhibited by the numerical assemblages with preferred horizontal bedding and increases as the particles become more angular. When the bedding plane is inclined toward $45° + \phi/2$, however, the strength and dilation are significantly less, particularly when the particles become more angular. Assemblages with more isotropic (or random) bedding exhibit a modest increase in strength and dilation as particle aspect ratio increases. Like soil and other real granular materials, the strength and dilation are lower for looser numerical assemblages.

This Section attempts to explain why particle shape and fabric anisotropy influence the macroscopic behavior using Rowe's stress-dilatancy theory for cohesionless granular materials. This discussion of the ellipse-based DEM results suggest that angular particles interlock more and, as a result, remold and dilate significantly less when the bedding plane is inclined with respect to the major principal plane. Strength and dilatant behavior is minimum for assemblages consisting of angular particles when the preferred bedding plane is coaxial with the slip planes ($45° \pm \phi/2$). As the bedding plane deviates from the slip plane, the numerical assemblages dilate more and exhibit more strength as particle interlocking is more easily deteriorated by the vertical shear stress. Strength and dilatant behavior is highest when the bedding plane is coaxial with the major principal plane.

9.1 Stress-dilatancy

Soil and other discontinuous materials are typically anisotropic in nature and are known to contract and dilate during the course of deformation. Rowe (1962) used basic energy principles with regular and irregular packing of two- and three-dimensional round particles to develop the following relationship between the strength and deformation behavior for cohesionless granular materials subjected to triaxial compression:

$$\tan^2\left(45 + \frac{1}{2}\phi_f\right) = \frac{\sigma_1'/\sigma_3'}{1 + dV/V\varepsilon_1} \tag{59}$$

where ϕ_f is the internal friction angle corrected for the energy due to expansion, σ' and σ' are the effective principal stresses and $dV/V\varepsilon_1$ is the volumetric strain rate. This relationship states simply that the work done on a system by the major principal stress σ_1' is proportional to the work done by the system on the minor principal stress σ_3'.

Rowe's work shows that the strength of granular materials is related to the amount of energy that is spent on dilation, remolding and friction as shown in Figure 159. In order for an assemblage of particles to deform, a minimum amount of work is spent on frictional heat. An additional amount of energy is then required to remold and dilate the assemblage. For loose assemblages, the additional energy is spent on remolding (or particle rearranging) and on dilating for dense assemblages. For intermediate assemblages, the additional energy is spent on a combination of remolding and dilating.

The results of the ellipse-based DEM simulations show that assemblages with angular particles generally exhibit higher strength than those with round particles. The increase in strength due to increased particle aspect ratio, however, is significantly reduced as the preferred bedding plane (or interlocking plane) inclines toward the slip plane ($45° - \phi_f/2$ from the major principal stress σ_1). When the bedding plane and the slip plane become coaxial, an "easy" failure plane is formed and the strength exhibited tends toward the minimum, particularly for assemblages consisting of flatter particles. The DEM results show that strength is maximum when the bedding plane is aligned parallel to the minor principal stress σ_2 and increases with aspect ratio.
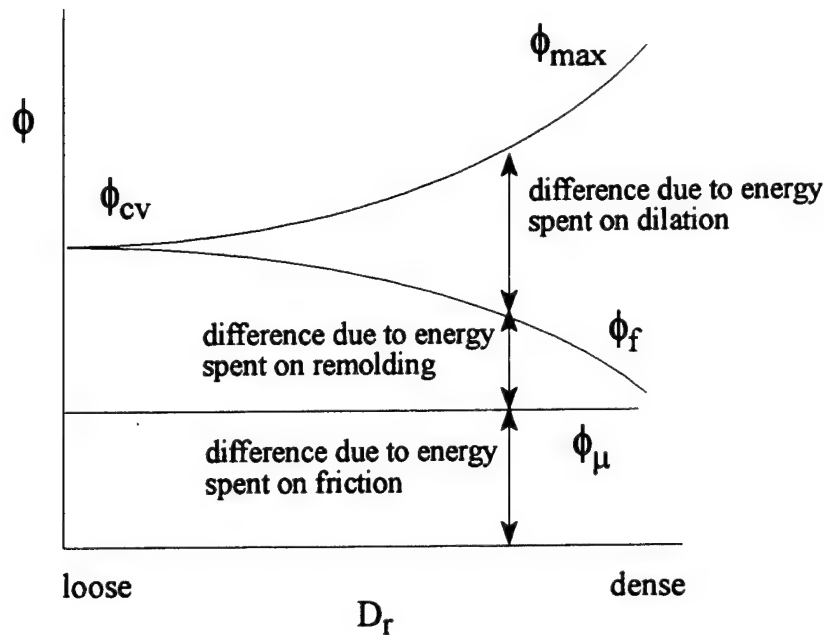
129

Figure 159. Rowe's (1962) stress-dilatancy theory for cohesionless granular materials.

As particle aspect ratio increases, particles tend to interlock more. This suggests that the ϕ_f curve shown in Figure 159 rises as particle aspect ratio increases as more energy is spent on remolding. As deformation continues, assemblages with preferred horizontal bedding ($\theta = 0°$) dilate significantly more and achieve higher values for ϕ_{max} than those with inclined bedding planes.

To determine the effect of increased particle aspect ratio on the energy spent on remolding, ϕ_f was computed for the numerical assemblages using equation (59) with values for σ_1/σ_2 and $\Delta V/V\varepsilon_1$ taken at the peak shear stress q_{max}. It was necessary to use the values at q_{max} because $(\sigma_1/\sigma_2)_{max}$ and $(\Delta V/V\varepsilon_1)_{max}$ did not always occur at the exact moment of shear. However, σ_1/σ_2 and $\Delta V/V\varepsilon_1$ were approximately maximum at q_{max}.

Values obtained for ϕ_f using equation (59) for assemblages with 0 and 60° bedding are shown in Figure 160. The increase in ϕ_f due to particle aspect ratio for assemblages with 0° bedding is significantly higher than for those with 60° bedding. The results indicate that more energy is spent on particle rearranging (or remolding) when the bedding plane is aligned parallel to σ_2 ($\theta = 0°$), and as a result, ϕ_f and ϕ_{max} increase significantly. A comparison of Figures 98 and 160 shows that both ϕ_{max} and ϕ_f increase by approximately 30° due to increased particle aspect ratio for assemblages with horizontal bedding. This suggests that the increase in ϕ_{max} is due almost entirely to the increase in the energy required to rearrange the angular particles and not the amount of energy spent on the assemblage's dilation during the course of deformation.

For assemblages with 60° bedding, however, less remolding and dilating occur as the flatter particles tend to interlock more during the course of deformation and move together as a "rigid body". Since less energy is spent on remolding and dilating in assemblages with 60° bedding, the increase in ϕ_f and ϕ_{max} is much less significant than for those with preferred horizontal bedding.
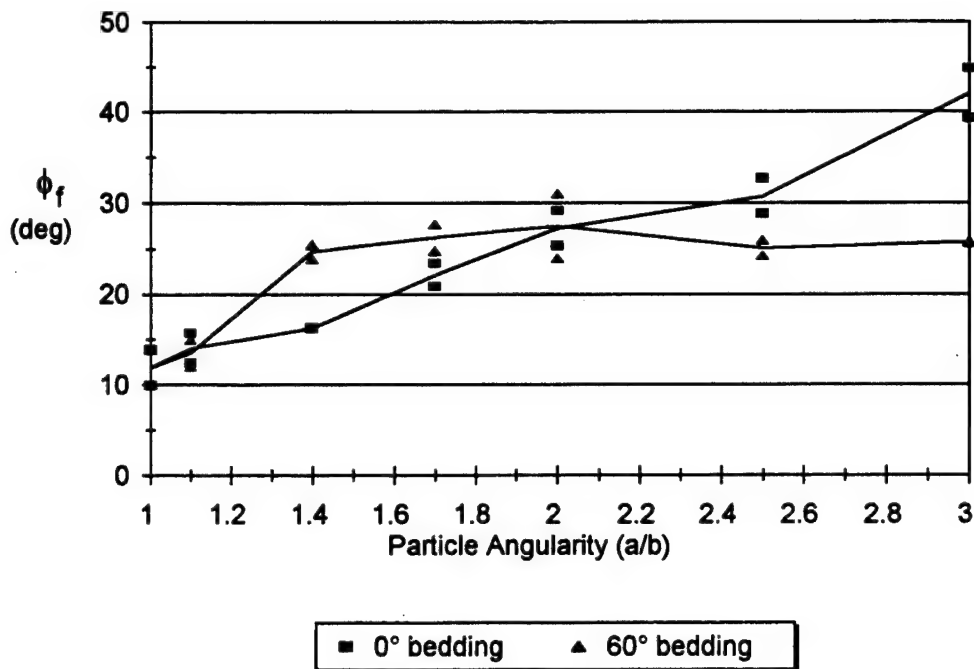
130

Figure 160. Effect of particle aspect ratio on ϕ_f (internal friction angle corrected for energy spent on dilation) for DEM samples with 0 and 60° bedding.

DEM samples with random bedding are more isotropic and deform with very little volume change. Almost no volumetric strain is exhibited by the random sample consisting of round particles. However, as aspect ratio increases, more interlocking occurs resulting in slightly more remolding and dilating behavior. The increase in the contractant and dilatant behavior for assemblages with random bedding is significantly less than for those with preferred bedding. Accordingly, the increase in ϕ_f and ϕ_{max} is also significantly less. Random samples with round particles (a/b = 1.0) yield values for ϕ_f and ϕ_{max} of 19.1 and 21.1°, respectively, while those with flatter particles (a/b = 3.0) yield values of 27.4 and 31.3°. Note that ϕ_{max} for the random sample with round particles is less than the interparticle sliding friction angle ϕ_μ of 26°. This is due to the negative effects of particle rolling on the true frictional resistance.

According to Rowe and Figure 159 looser assemblages dilate less and remold more than denser assemblages resulting in lower values for ϕ_{max} and higher values for ϕ. Results of the ellipse-based DEM simulations agree with Rowe's theory. For numerical assemblages with a/b = 2.0 and 0° bedding, those that are looser yield lower average values for ϕ_{max} and slightly higher average values for ϕ_f ($e_o = 0.175$, $\phi_{max} = 40.2°$, $\phi_f = 30.9°$) than those that are denser ($e_o = 0.158$, $\phi_{max} = 46.7°$, $\phi_f = 27.2°$).

Though Rowe assumes a sliding-type failure, the true friction angle is generally regarded as consisting of both sliding and rolling frictional mechanisms. It has been suggested that particle rolling is the dominant deformation mechanism for assemblages with high interparticle friction (Oda *et al* 1983). The DEM assemblages with round particles (a/b = 1.0) and $\phi_\mu = 26°$ yield values for ϕ_{max} ranging from 19 to 26°. Since ϕ_{max} is lower than ϕ_μ in some cases, the difference is likely due to increased particle rolling. DEM assemblages with $\phi_\mu = 52°$ yield higher values for ϕ_{max} than for those with $\phi = 26°$. However, the results show that ϕ does not increase monotonically with the increase in ϕ_μ, which is in agreement with Skinner (1969). This lends further proof that the negative effects of particle rolling on the frictional resistance and the overall strength of granular materials increases as the interparticle sliding friction increases.

131

As mentioned previously in Section 8.2.5, the ellipse-based DEM model allows the decomposition of contact deformations into rotation and translation components (Ting *et al* 1993). The incremental quantities are summed over every contact to assess the relative importance of rolling and sliding mechanisms within the assemblage. Figure 161 illustrates the effect of increased interparticle friction angle ϕ_μ on the amount of particle rolling that occurs in the numerical assemblages during the course of deformation. Particle sliding is reduced by the increase in frictional resistance. Consequently, particle rolling must increase in order for the assemblage to deform thereby becoming the dominant deformation mechanism, which seems to confirm previous hypotheses.
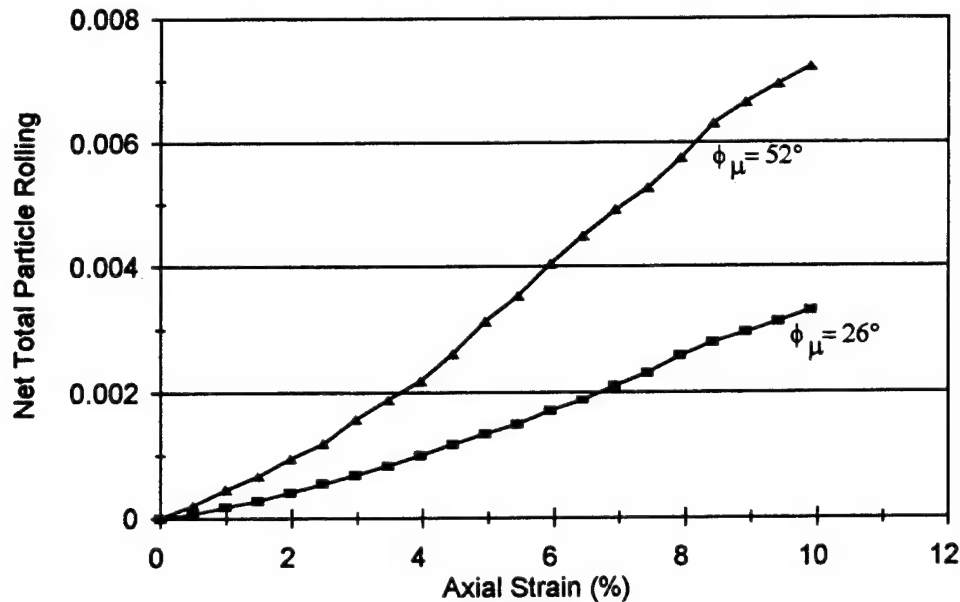

Figure 161. Cumulative particle rolling statistics for DEM samples with a/b = 1.4 and 0° bedding with variations in the interparticle friction angle ϕ_μ.

9.2 The Failure Plane

According to Rowe, failure of discontinuous materials occurs when the α-plane (or the preferred bedding plane θ) corresponds to the average packing geometry of critical particle groups at the instant of collapse. Furthermore, Rowe states that the slip plane is oriented at $45° - \phi_f/2$ with respect to the direction of the major principal stress and is not related to the peak strength of the assemblages. This apparently contradicts the continuum-based Mohr-Coulomb theory prediction of $45° + \phi_{max}/2$.

Figures 162 through 164 plot particle displacement vectors for assemblages with a/b = 1.4 and preferred bedding θ of 0, 30 and 90°, respectively. The displacements of flatter particles (a/b = 3.0) with preferred particle bedding θ of 0, 30, 60 and 90° are shown in Figures 165 through 168. Particle displacements are shown as lines that indicate the initial and final positions of the particle centers. Distinct failure planes are visible, particularly in assemblages with inclined particle bedding. Since angular particles interlock more, they tend to form subdomains that move together as a group. When the preferred bedding plane is horizontal (or coaxial with the major principal plane), the interlocking is rapidly deteriorated under the vertical shear stress as the particles are predisposed to move laterally. As the bedding plane inclines toward the predicted slip plane, however, the interlocking does not deteriorate as easily. Instead, inclined angular particles tend to remain interlocked and, as a result, more rigid body-type deformation occurs.

132

Figure 162. Particle displacements for a DEM sample with a/b = 1.4 and 0° bedding at 10% axial strain.

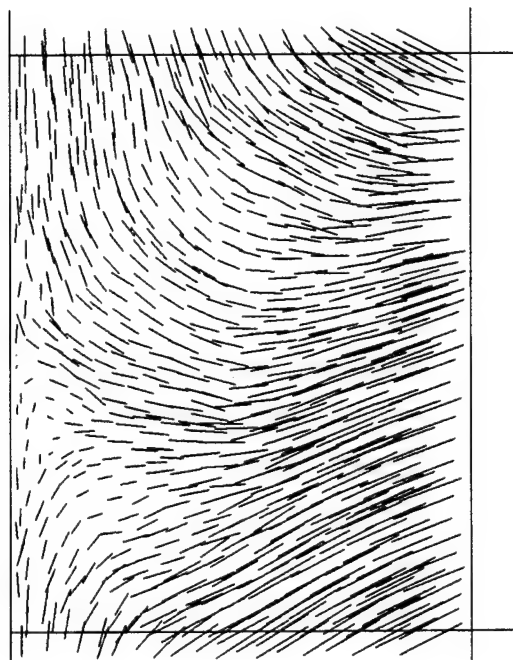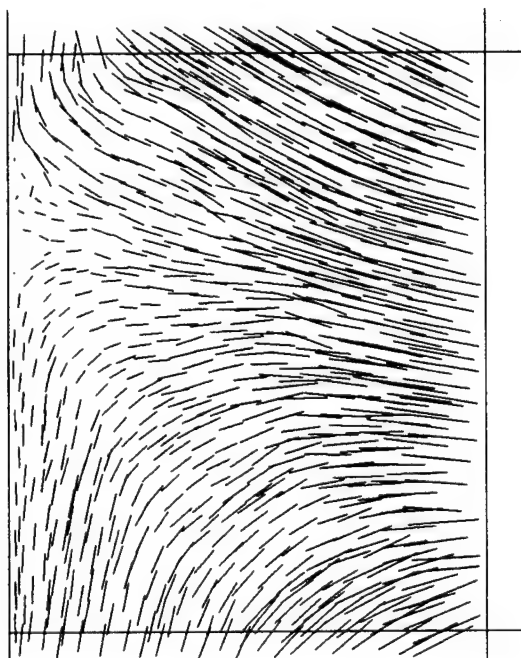**Figure 163.** Particle displacements for a DEM sample with a/b = 1.4 and 30° bedding at 10% axial strain.

133

O2141
a/b = 1.4
θ = 90°

Figure 164. Particle displacements for a DEM sample with a/b = 1.4 and 90° bedding at 10% axial strain.

O7111
a/b = 3.0
θ = 0°

Figure 165. Particle displacements for a DEM sample with a/b = 3.0 and 0° bedding at 10% axial strain.
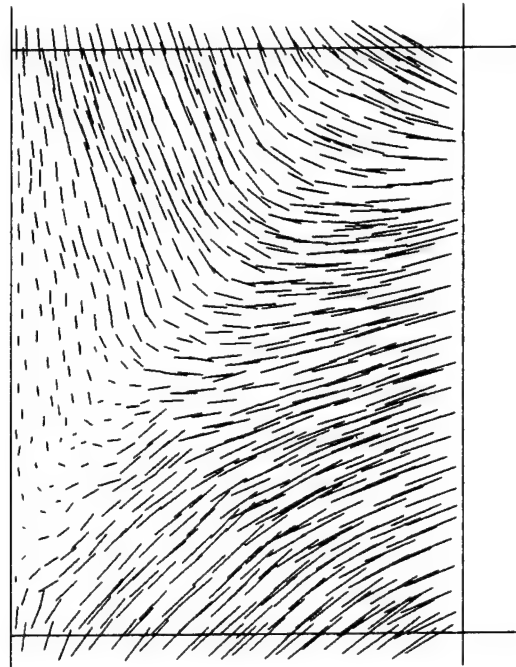
O7121
a/b = 3.0
θ = 30°

Figure 166.   Particle displacements for a DEM sample with a/b = 3.0 and 30° bedding at 10% axial strain.

O7131
a/b = 3.0
θ = 60°

Figure 167.   Particle displacements for a DEM sample with a/b = 3.0 and 60° bedding at 10% axial strain.
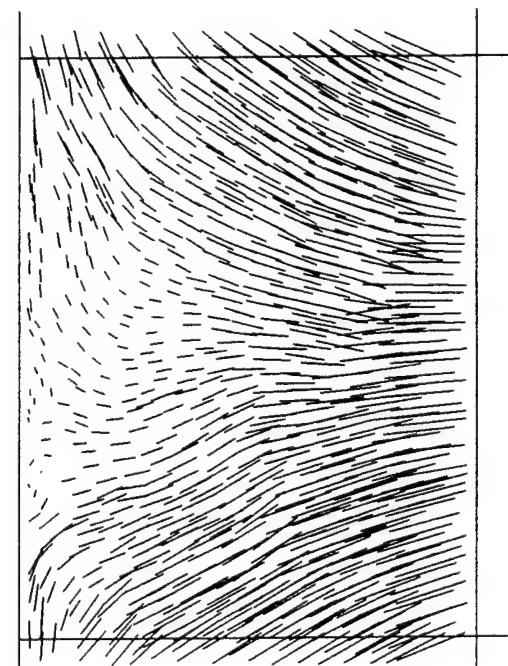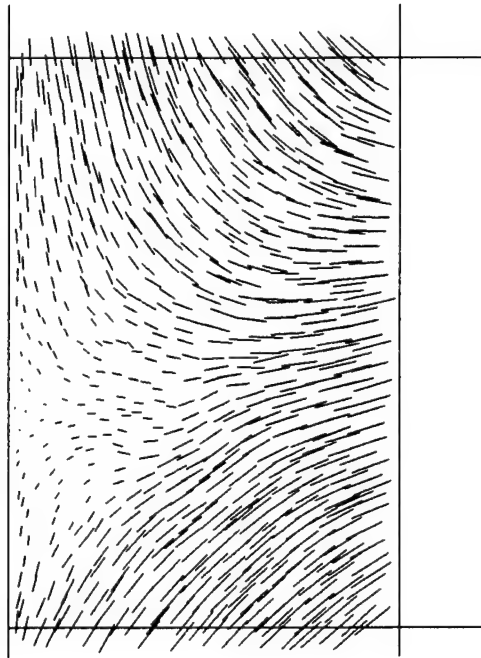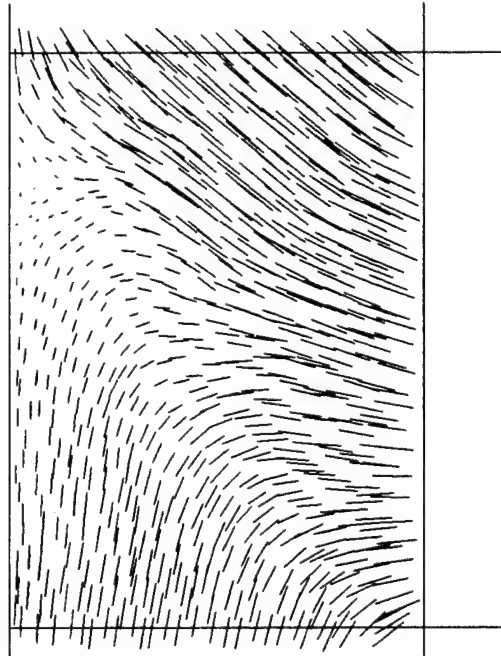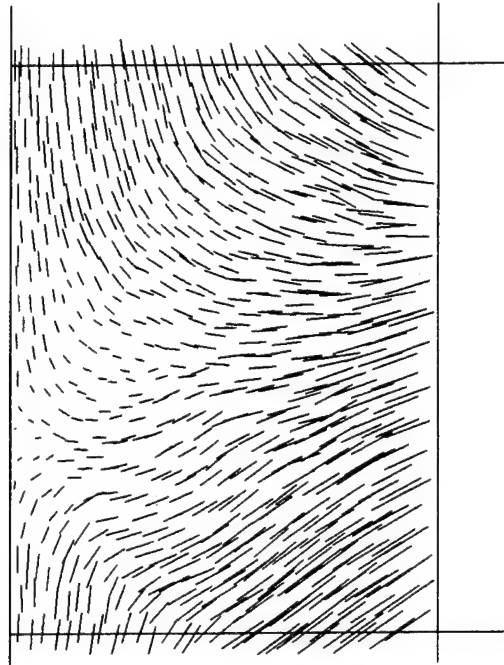
135

O7141
a/b = 3.0
θ = 90°

Figure 168. Particle displacements for a DEM sample with a/b = 3.0 and 90° bedding at 10% axial strain.
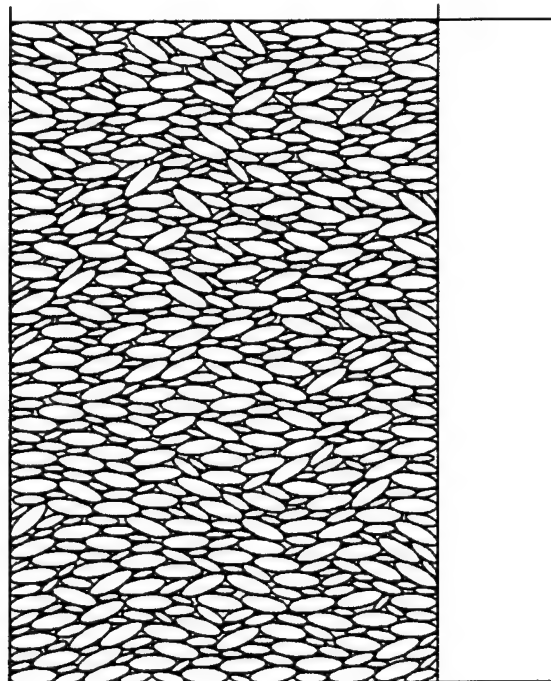

O7112
a/b = 3.0
θ = 0°

Figure 169. System plot of DEM sample with a/b = 3.0 and 0° bedding prior to biaxial shear.
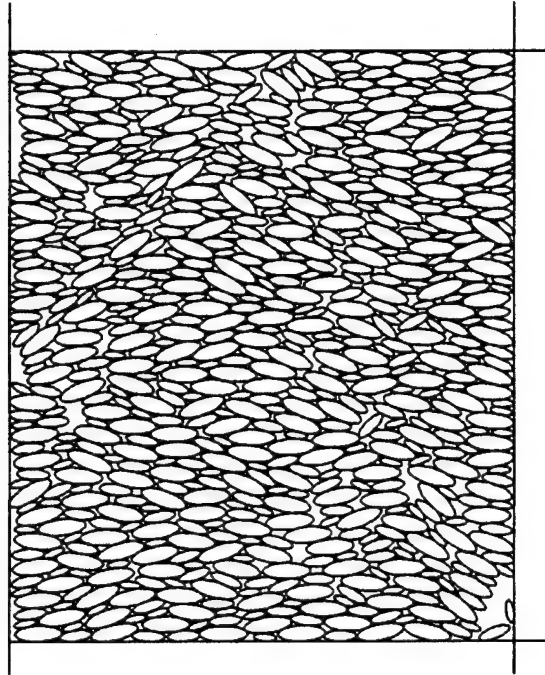
O7112
a/b = 3.0
θ = 0°

Figure 170. System plot of DEM sample with a/b = 3.0 and 0° bedding at 10% axial strain.

Figure 169 shows a DEM sample consisting of flat particles (a/b = 3.0) with preferred horizontal bedding (θ = 0°) prior to shear, while Figure 170 shows the same sample at approximately 10% axial strain. Prior to shear, the angular particles interlock and form an extremely dense assemblage. When the numerical sample is sheared, however, particle interlocking deteriorates rapidly under the applied shear stress σ_1 as the particles are predisposed to move horizontally in the direction of the minor principal stress σ_2. Particulate columns form to resist σ_1 resulting in spalling-type behavior and producing more lateral expansion (or dilation). Failure occurs when the columns become unstable and collapse. Similar spalling-type behavior was observed by Oda *et al* (1983) in biaxial shear tests using photoelastic rubber rods.

At large axial strains, slip planes are clearly visible and possess positive (inclined toward the right) or negative (inclined toward the left) inclination. Particles on the slip planes roll and slide producing large shear strains, while those between the slip planes remain interlocked, moving together as a single particulate body with significantly less shear strain. Figure 171 plots the contours of maximum shear strain γ_{max} for a larger numerical assemblage consisting of 2004 "flat" particles with a/b = 3.0 and 0° bedding at approximately 18% axial strain.

Figure 172 shows a DEM sample consisting of flat particles (a/b = 3.0) with preferred 60° bedding prior to shear, while Figure 173 shows the same sample at approximately 10% axial strain. The spalling-type behavior observed in the DEM sample with 0° bedding is not evident in the sample with θ = 60°. Assemblages with inclined bedding dilate less because more rigid body-type deformation occurs as the inclined particles remain interlocked throughout the assemblage's deformation. The result is the formation of a rather wide single shear band in which the particles are significantly disturbed due to rolling and sliding. On both sides of the shear band, however, very little remolding and dilating occurs in the granular wedges as the particles remain interlocked.

137

O7113
a/b = 3.0
$\theta = 0°$
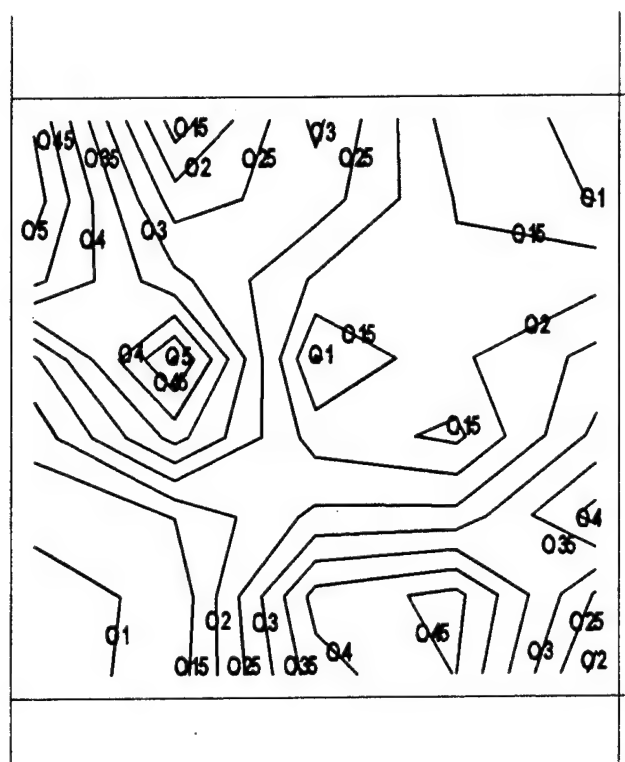
Figure 171. Maximum shear strain contours for DEM sample with a/b = 3.0 and $\theta = 0°$ at 18% axial strain.

O7132
a/b = 3.0
$\theta = 60°$

Figure 172. System plot of DEM sample with a/b = 3.0 and 60° bedding prior to biaxial shear.

138

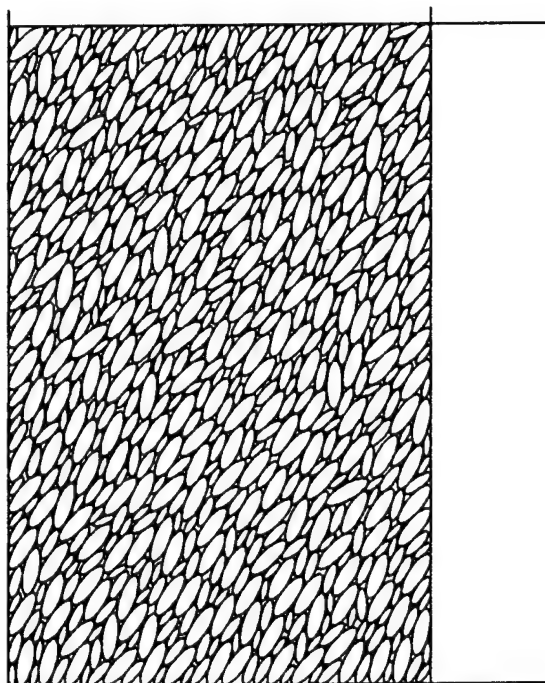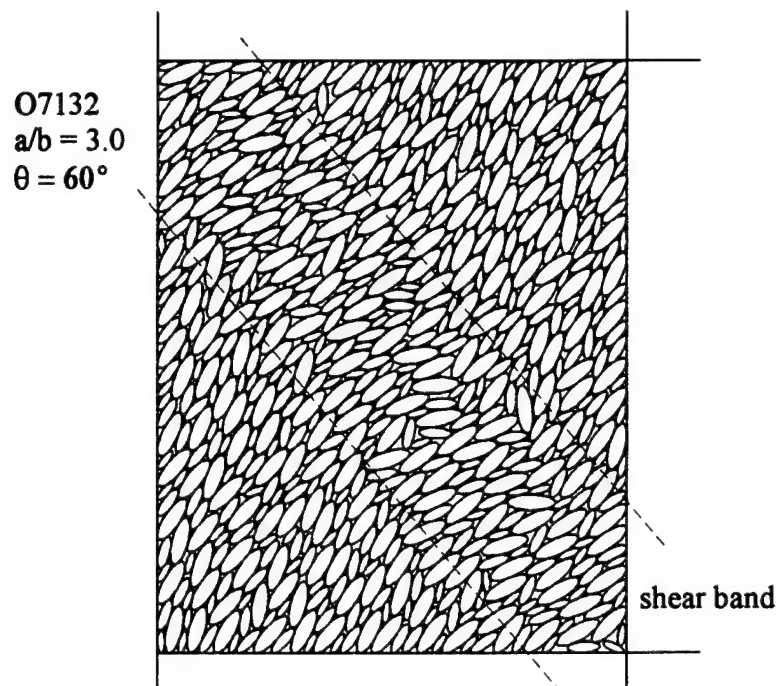**Figure 173.** System plot of DEM sample with a/b = 3.0 and 60° bedding at 10% axial strain.
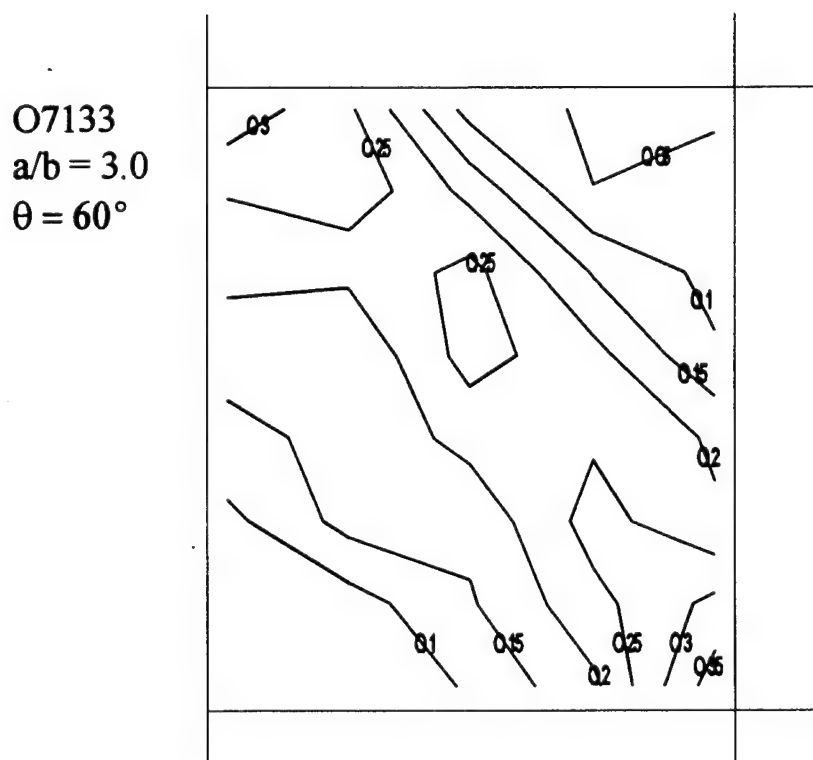

Figure 174. Maximum shear strain contours for DEM sample with a/b = 3.0 and θ = 60° at 15% axial strain.

139

While pockets of large local shear strains occur in the sample with preferred horizontal bedding ($\theta = 0°$), a band of large shear strains develops in the sample with 60° bedding as shown in Figure 174. The maximum shear strains within the shear band, however, are significantly lower in magnitude (25%) than the strains experienced by the sample with $\theta = 0°$. It should be noted, however, that the numerical assemblages are shown at different stages of shear (or axial strains). The shear strains decrease significantly in the opposing wedges along the shear band.

For isotropic granular materials, the inclination of the failure plane may be positive or negative as both are equally likely to occur. The fabric of the numerical samples with preferred bedding, however, were extremely anisotropic. Though positive and negative inclinations did occur for the DEM samples with preferred particle bedding of 0, 30 and 90°, the failure plane inclination was always negative (inclined toward the left) for those with $\theta = 60°$.

Particles in the shear band roll significantly from their initial orientation, while those outside the shear band do not rotate significantly because of more interlocking and "rigid body" motion. For a DEM sample with a/b = 3.0 and 60° bedding, particles in the shear band that rotate ($\Delta\theta$) more than 10° during the course of deformation are shown in Figure 175, while those with $\Delta\theta$ of more than 20° are shown in Figure 176.

O7131
a/b = 3.0
$\theta = 60°$
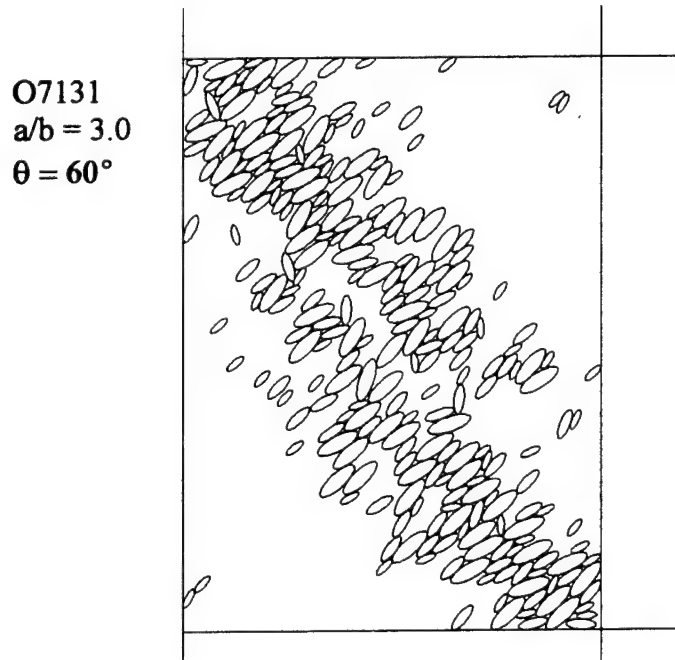
Figure 175. Particles in a DEM sample with a/b = 3.0 and $\theta = 60°$ having a change in rotation ($\Delta\theta$) of greater than 10° at 10% axial strain

A numerical assemblage was biaxially sheared in separate simulations with lower interparticle sliding friction angles ϕ_μ than 26° to determine whether a sliding-type failure could be initiated. The simulations were performed under the same conditions except that ϕ_μ was varied using values of 5, 15 and 23°. For assemblages with ϕ_μ = 5 and 15°, the inclination of the failure plane was positive (with the grain) indicating sliding failure, while the sample with ϕ_μ = 23° initially developed a positive inclination but ultimately failed against the grain. This seems to confirm that particle rolling is the dominant failure mechanism for assemblages with high sliding friction, even causing samples with preferred 60° bedding to fail against the grain of the bedding plane.

O7131
a/b = 3.0
θ = 60°

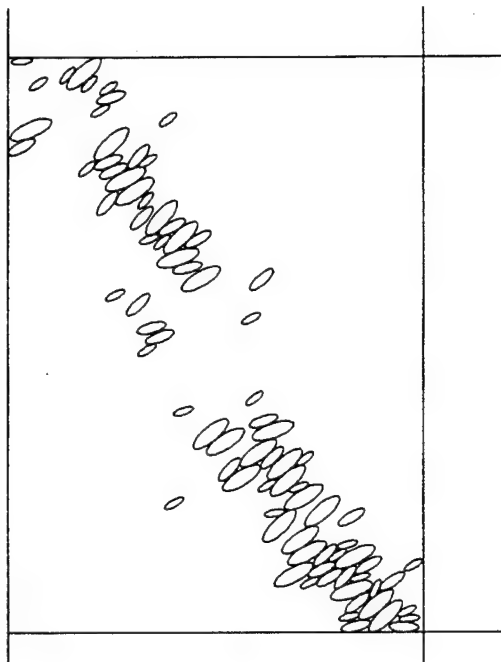**Figure 176.**   Particles in a DEM sample with a/b = 3.0 and θ = 60° having a change in rotation (Δθ) of greater than 20° at 10% axial strain.

9.3 Contact Normal Distribution

Results of the ellipse-based DEM simulations show that higher strength is exhibited by assemblages that have initially anisotropic contact normal distributions parallel to the direction of the vertically applied shear stress σ_1 (or when the bedding plane is horizontal). Less strength is exhibited when the initial distribution anisotropy and σ_1 are skewed. For assemblages with more isotropically distributed contact normals, the strength is also less. During the course of deformation, the contact normals tend to rotate toward the major principal stress axis. Similar fabric evolution has been observed in numerous previous physical and numerical micromechanical studies (Konishi *et al* 1983, Oda *et al* 1980, Rothenburg and Bathurst 1991, Chen and Ishibashi 1990).

Angular particles interlock more and possess more contacts as indicated by the increase in the coordination number. For horizontal bedding ($\theta = 0°$), an increase in the number of vertical contact normals produces a more anisotropic fabric, thereby providing more stability and more resistance to the vertical shear stress. For inclined bedding, however, the increase in the number of contact normals provides significantly less benefit because the alignment of the more anisotropic fabric is skewed with σ_1. For random bedding, an increase in the number of particle contacts provides only slightly more stability and shear resistance because the contact normals are distributed more randomly and only a few more are aligned toward σ_1.

Rose diagrams illustrating the contact normal distribution for a DEM sample consisting of round particles ($a/b = 1.0$) prior to shear and at peak strength are shown in Figure 177. Initially, the contact normals are isotropically distributed as the round particles do not possess preferred orientations. At peak strength, however, the distribution is more anisotropic and oriented toward the vertical (parallel to σ_1). As the assemblage deforms, horizontal contacts are broken while more vertical contacts are made.

Figure 177. Distribution of contact normals for a DEM sample with $a/b = 1.0$ (no orientation) prior to shear (left) and near peak strength (right).

Figures 178 through 180 show the initial and peak strength contact normal distributions for DEM samples with preferred horizontal bedding ($\theta = 0°$) and a/b = 1.1, 1.7 and 3.0, respectively. Though the coordination number for the assemblages consisting of flatter particles decreases during the course of deformation, the majority of the lost contacts are horizontal. The maximum frequency of the contact normals indicate that vertical contact normals are still made even while the coordination number decreases. Higher strength is exhibited by assemblages consisting of flatter particles as the increase in the number of vertical contact normals provide more stability and shear resistance.

Figure 178. Distribution of contact normals for a DEM sample with a/b = 1.1 and 0° bedding prior to shear (left) and near peak strength (right).

Figure 179. Distribution of contact normals for a DEM sample with a/b = 1.7 and 0° bedding prior to shear (left) and near peak strength (right).
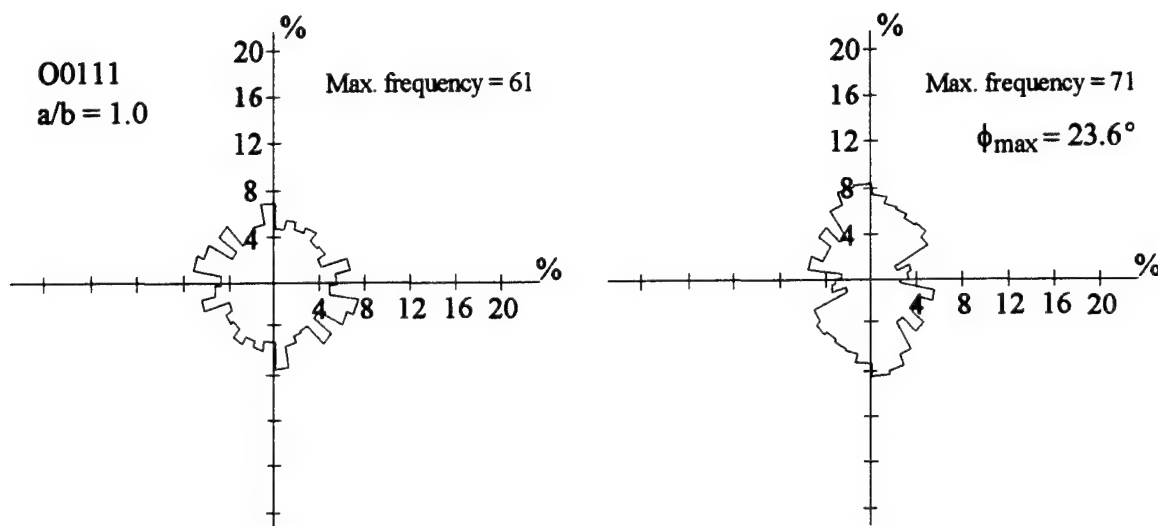
143

Figure 180. Distribution of contact normals for a DEM sample with a/b = 3.0 and 0° bedding prior to shear (left) and near peak strength (right).

For assemblages with preferred 60° bedding, the contact normals are initially oriented 60° from the vertical and, as a result, do not provide as much resistance to a vertical shear stress. Figures 181 through 183 show the orientation and frequency distribution of contact normals for DEM samples with a/b = 1.1, 1.7 and 3.0, respectively. The rose diagrams become more anisotropic as particle angularity increases. As the assemblages are sheared, the skewed rosettes tend to rotate toward the vertical. Though the assemblages consisting of "flat" particles (a/b = 3.0) are more anisotropic and possess a higher number of contact normals than those consisting of rounded particles, no significant increase in the strength is exhibited as the anisotropic distribution is not parallel to σ_1 (or vertical).
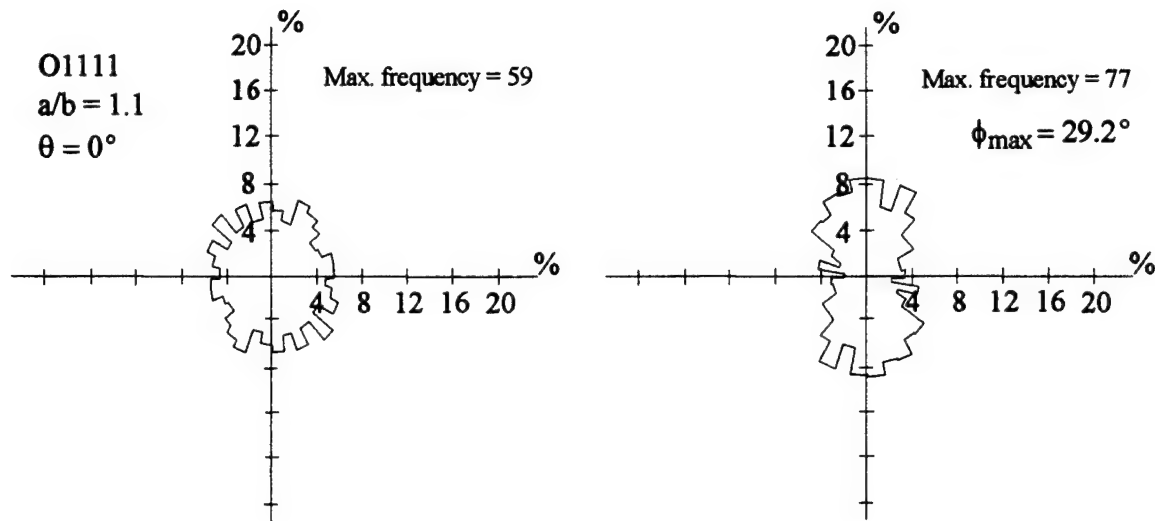

Figure 181. Distribution of contact normals for a DEM sample with a/b = 1.1 and 60° bedding prior to shear (left) and near peak strength (right).

144

Figure 182. Distribution of contact normals for a DEM sample with a/b = 1.7 and 60° bedding prior to shear (left) and near peak strength (right).

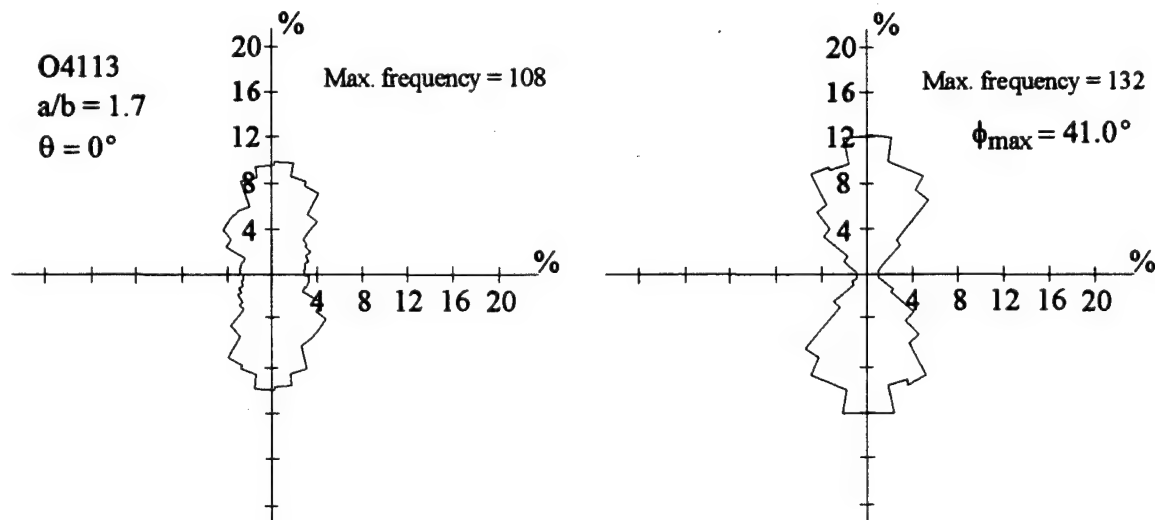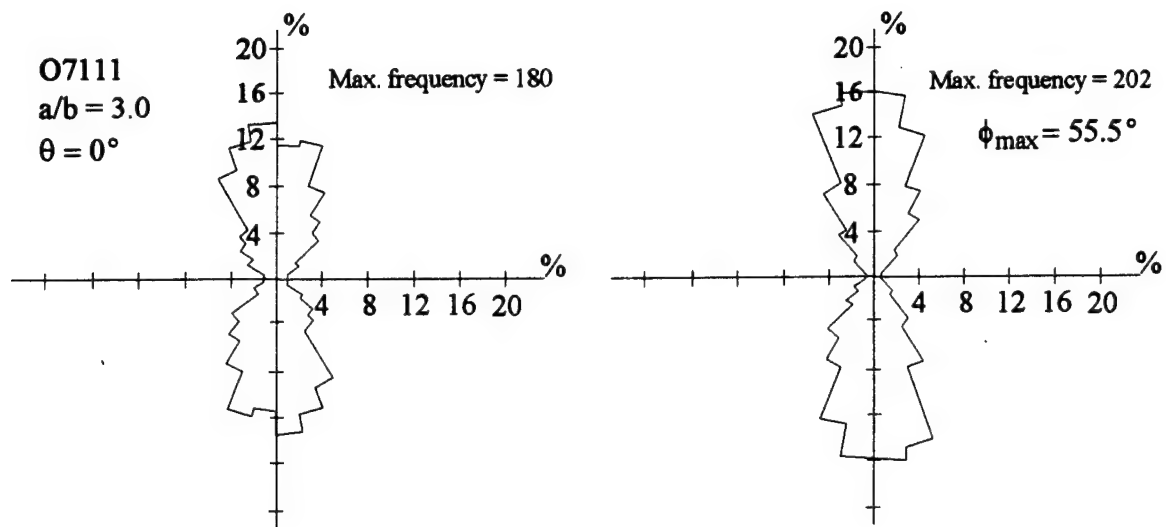**Figure 183.** Distribution of contact normals for a DEM sample with a/b = 3.0 and 60° bedding prior to shear (left) and at peak strength (right).

Figures 184 and 185 show the initial and peak strength contact normal distributions for DEM samples with 30° bedding and particle aspect ratios a/b of 1.4 and 3.0, respectively. Rose diagrams for the numerical assemblages with 90° bedding and a/b = 1.4 and 3.0 are shown in Figures 186 and 187. Assemblages with 30° bedding exhibit less strength than those with 0° bedding due in part to the skewed alignment of the contact

145

normals with respect to σ_1. The strength is even less for samples with 90° bedding as the initial horizontal fabric anisotropy provides fewer vertical contact normals and less resistance to the vertically applied σ_1. As the samples are sheared, the horizontal anisotropy deteriorates and re-orientates toward the vertical as more horizontal contacts are lost while vertical contacts are made. For samples consisting of more angular particles (a/b = 3.0), deterioration and re-orientation is inhibited by the more anisotropic fabric.
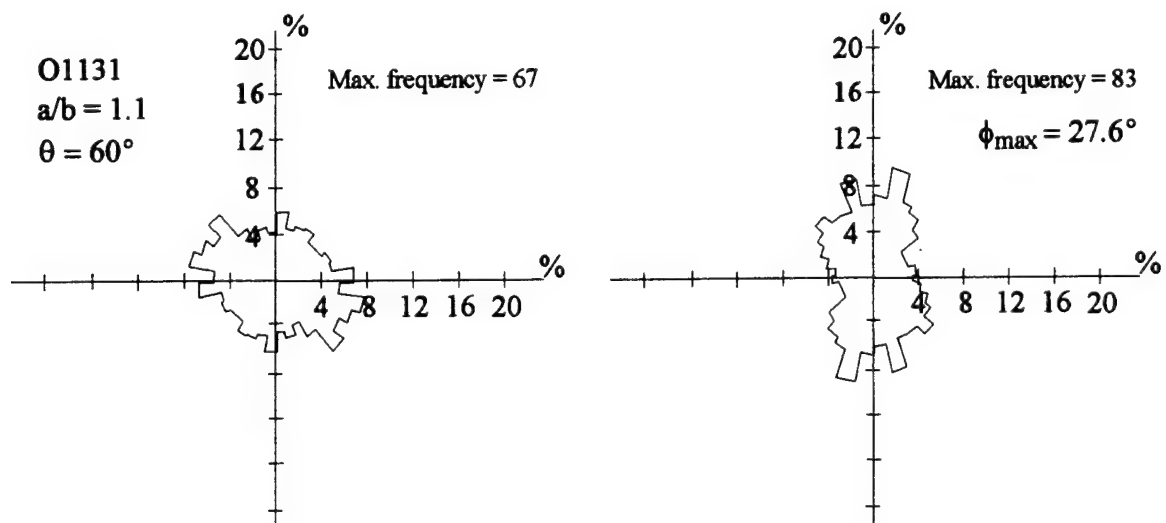

Figure 184. Distribution of contact normals for a DEM sample with a/b = 1.4 and 30° bedding prior to shear (left) and near peak strength (right).

Figure 185. Distribution of contact normals for a DEM sample with a/b = 3.0 and 30° bedding prior to shear (left) and near peak strength (right).
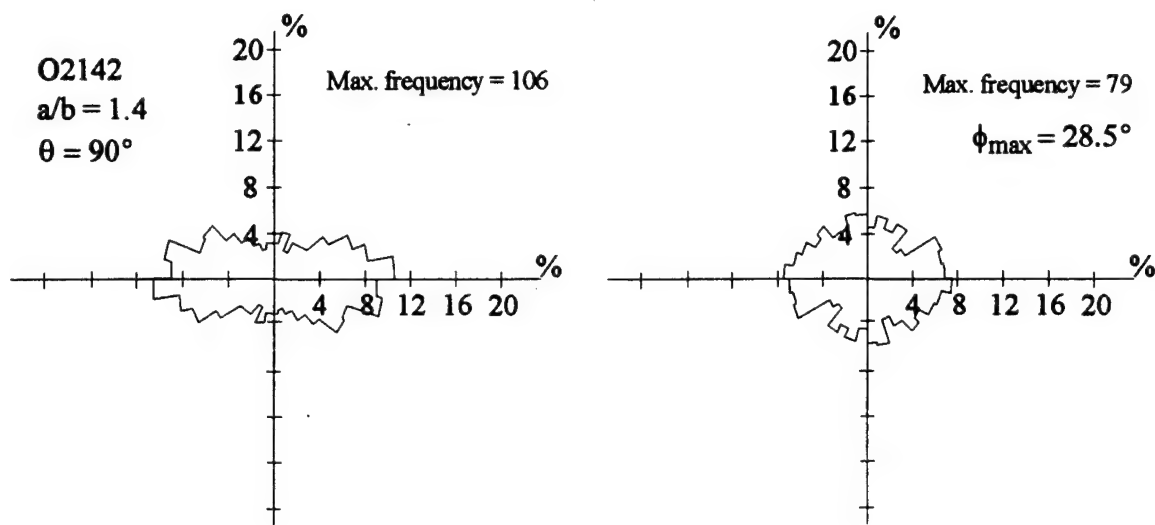
Figure 186. Distribution of contact normals for a DEM sample with a/b = 1.4 and 90° bedding prior to shear (left) and near peak strength (right).
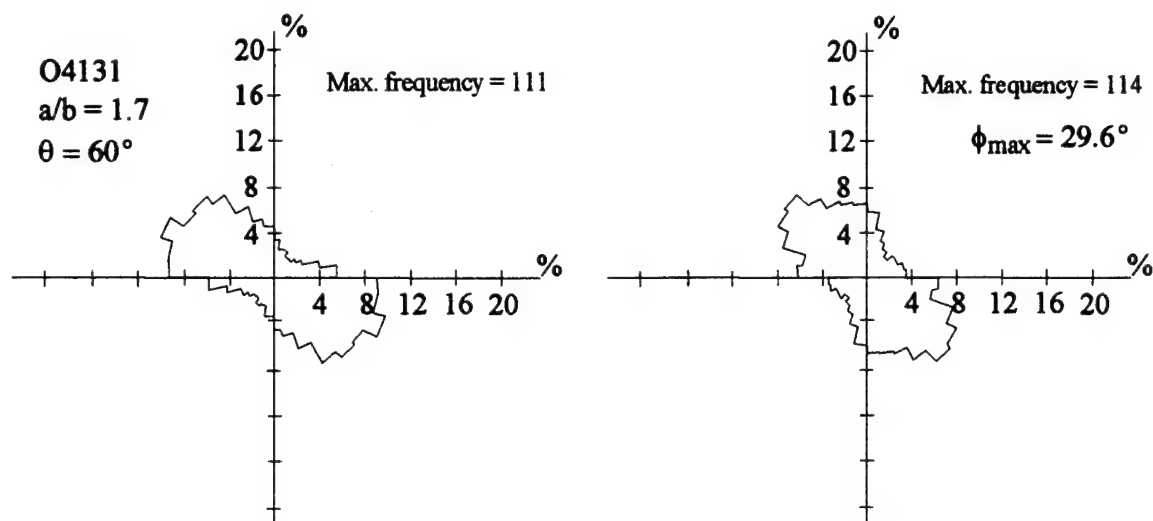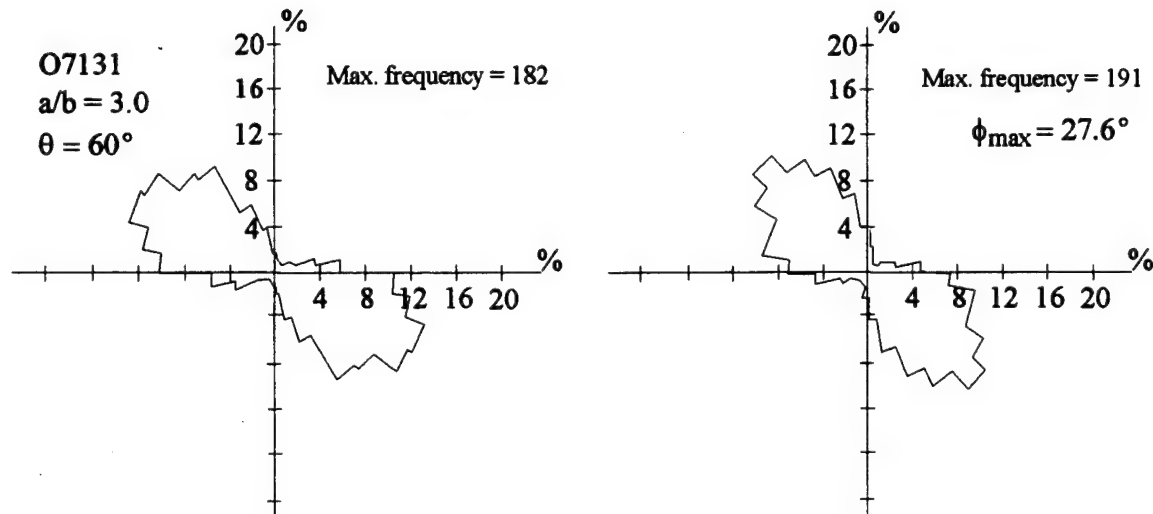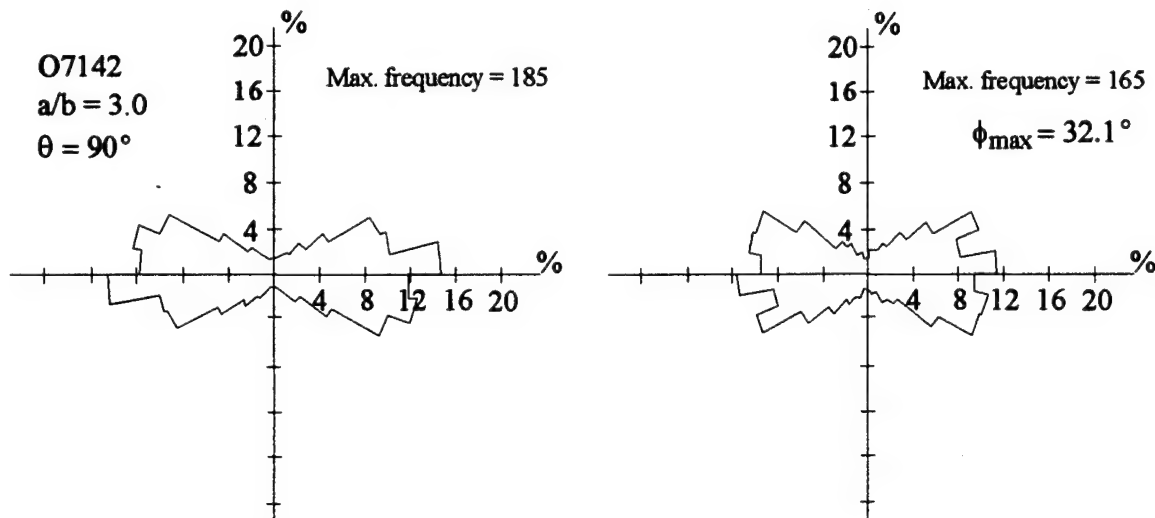

Figure 187. Distribution of contact normals for a DEM sample with a/b = 3.0 and 90° bedding prior to shear (left) and near peak strength (right).

Figures 188 through 191 show the initial (prior to shear) and peak strength contact normal distributions for samples with randomly oriented particles and a/b = 1.0, 1.1, 1.7 and 3.0, respectively. Though the random samples are much looser than the assemblages with preferred bedding, their initial coordination numbers were shown to be very similar. However, because the initial fabrics for the random samples are significantly less anisotropic, their evolution toward the major principal stress axis occurs more easily. The fabric evolution occurs as many of the horizontal contacts are broken while vertical contacts are made. Prior to shear and at peak strength, assemblages consisting of flatter particles possess more vertical and less horizontal contacts than those with rounded particles.

147
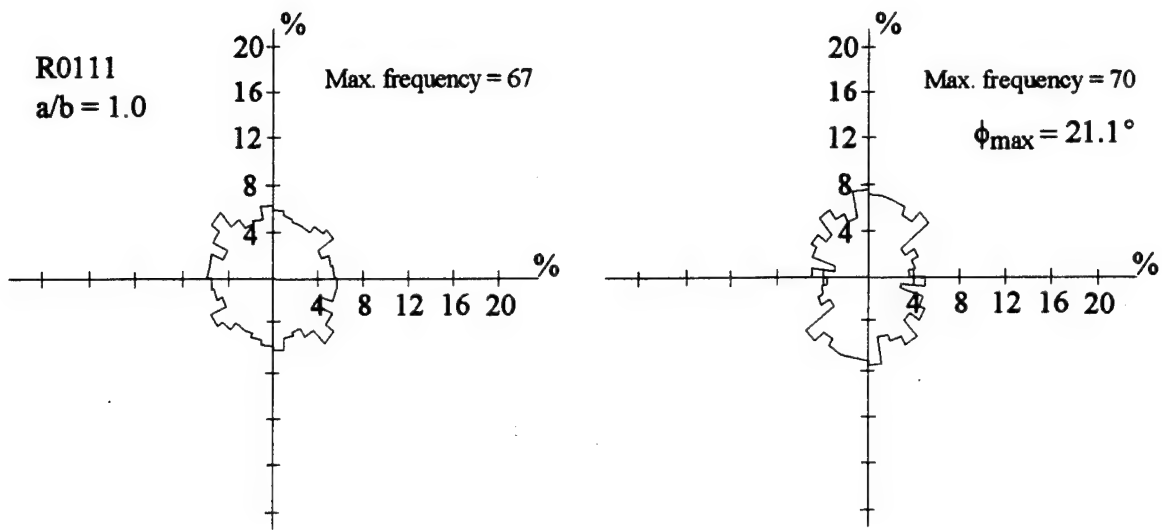
Figure 188. Distribution of contact normals for a DEM sample with a/b = 1.0 (no orientation) prior to shear (left) and at peak strength (right).
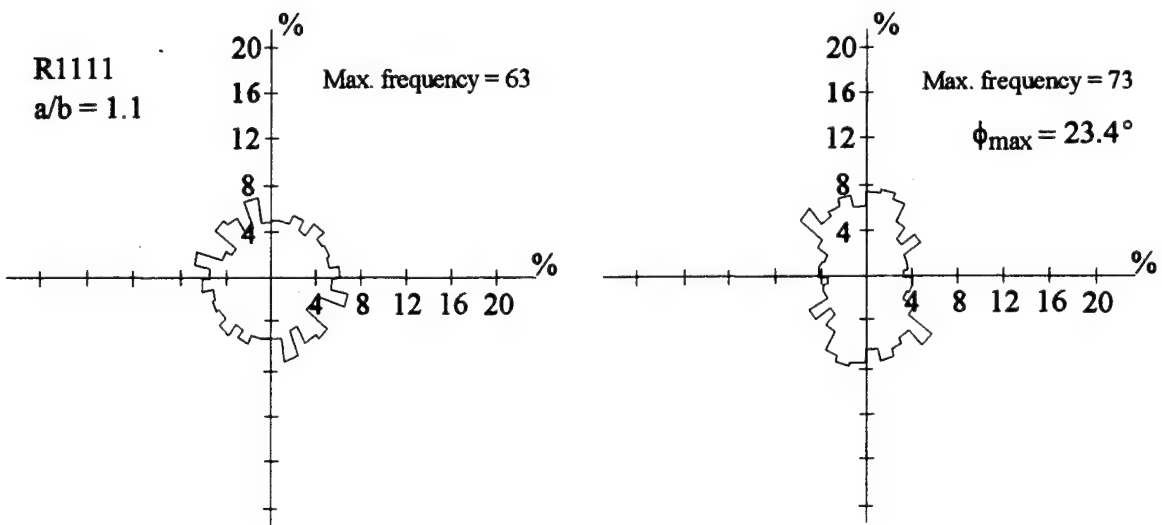
Figure 189. Distribution of contact normals for a DEM sample with a/b = 1.1 and random bedding prior to shear (left) and at peak strength (right).

148
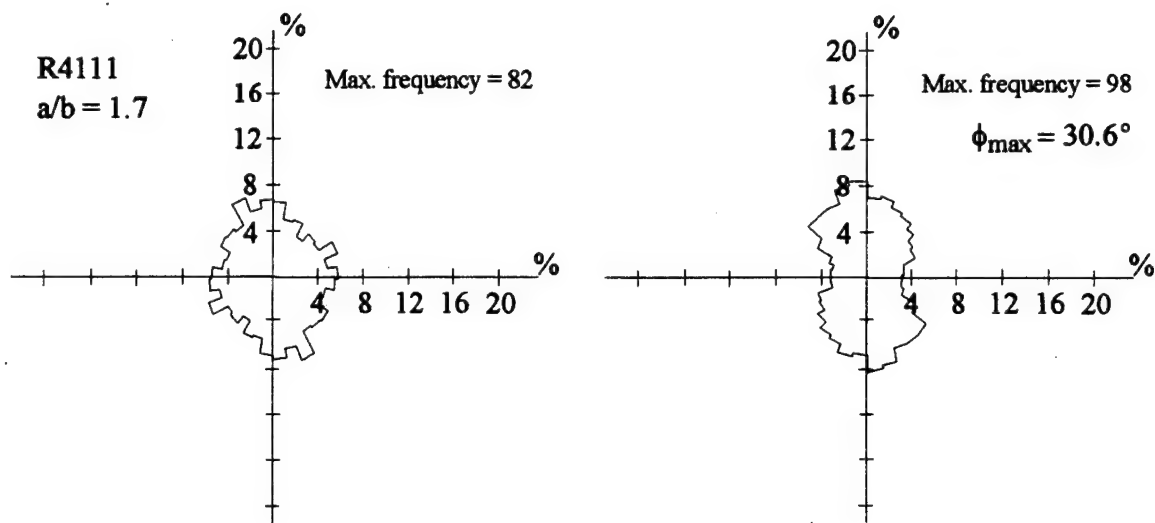
Figure 190. Distribution of contact normals for a DEM sample with a/b = 1.7 and random bedding prior to shear (left) and at peak strength (right).
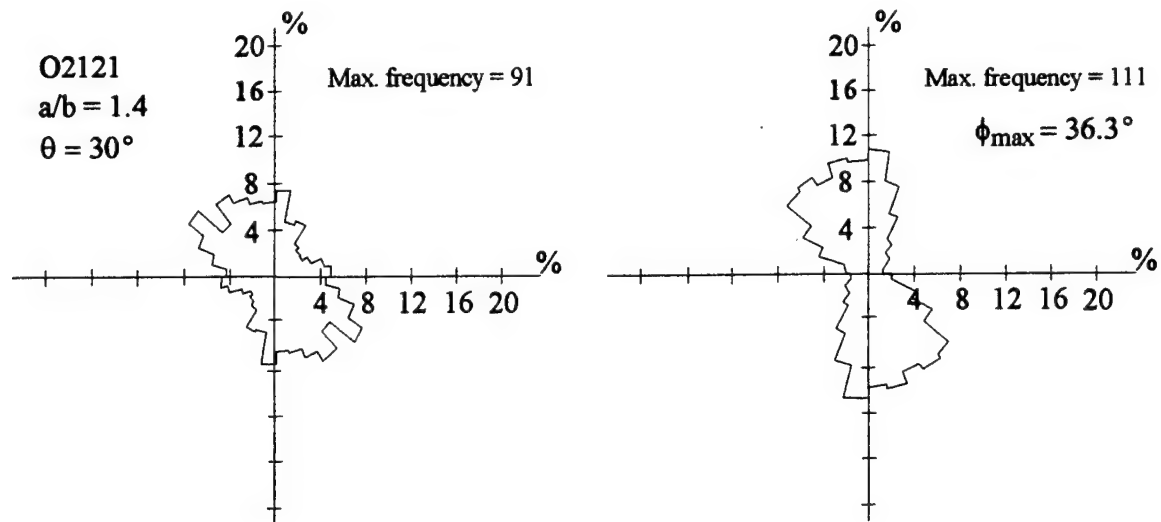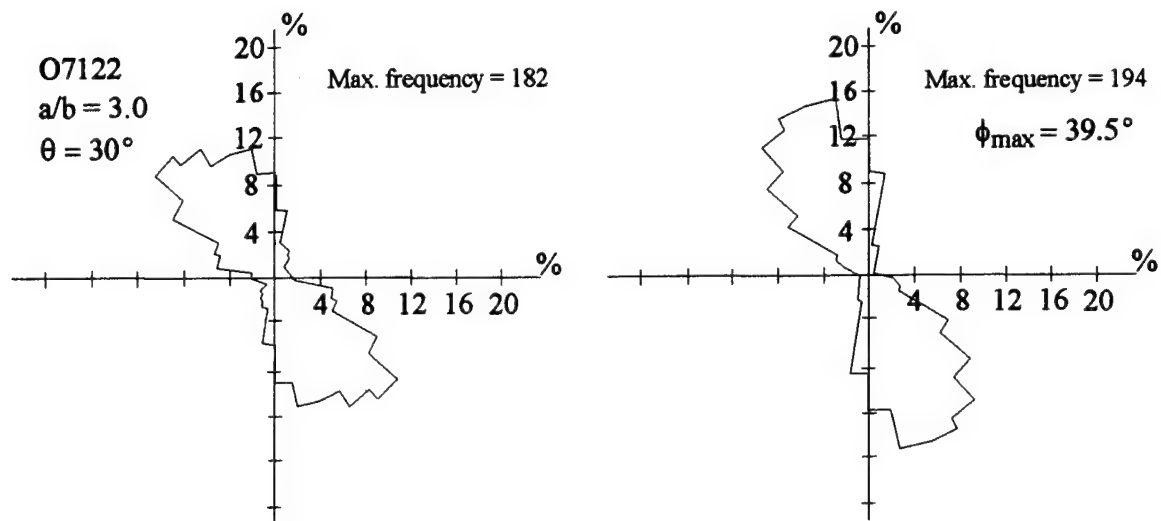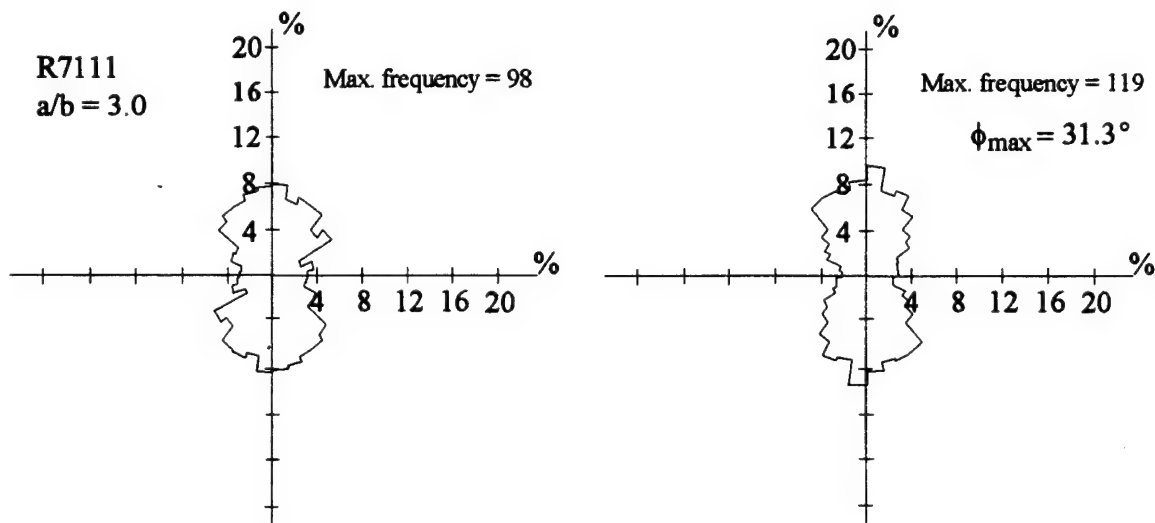

Figure 191. Distribution of contact normals for a DEM sample with a/b = 3.0 and random bedding prior to shear (left) and at peak strength (right).

The evolution of the contact normals during the course of deformation for DEM samples with a/b = 2.0 and preferred 0 and 60° bedding is shown in Figures 192 and 193, respectively. For assemblages with 0° bedding, the orientation of the contact normals distribution remains parallel with the vertical shear stress. For assemblages with 60° bedding, however, the initial contact normals are aligned 60° from σ_1 and as the sample is sheared, their orientation tends to rotate toward the vertical. Though particle angularity is the same for both assemblages, the contact normal distribution for the sample with 0° bedding is significantly more anisotropic than for the assemblage with 60° bedding.

149
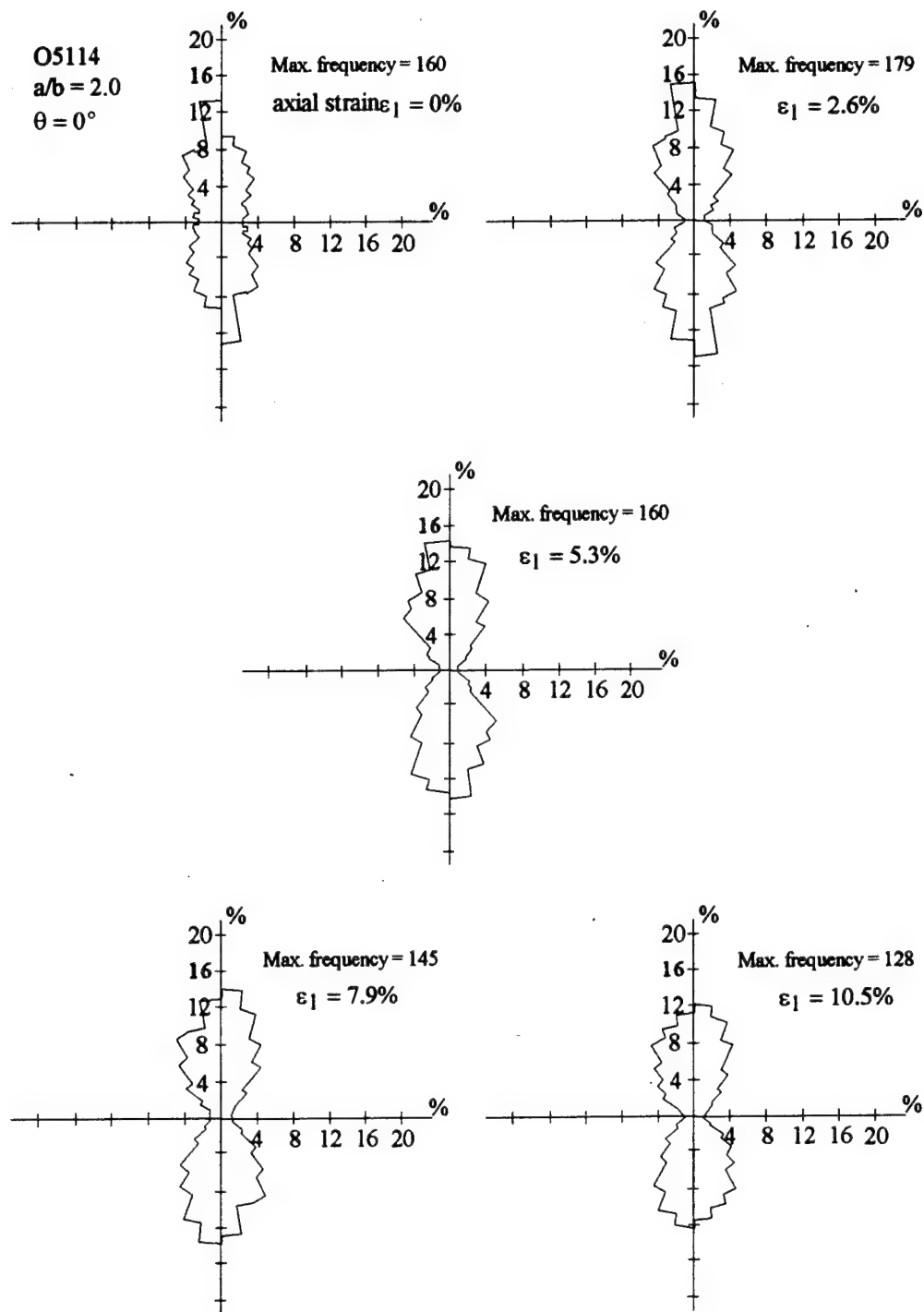
Figure 192. Evolution of contact normal distributions for a DEM sample with a/b = 2.0 and 0° bedding (peak strength at ε_1 = 4.7%).

150
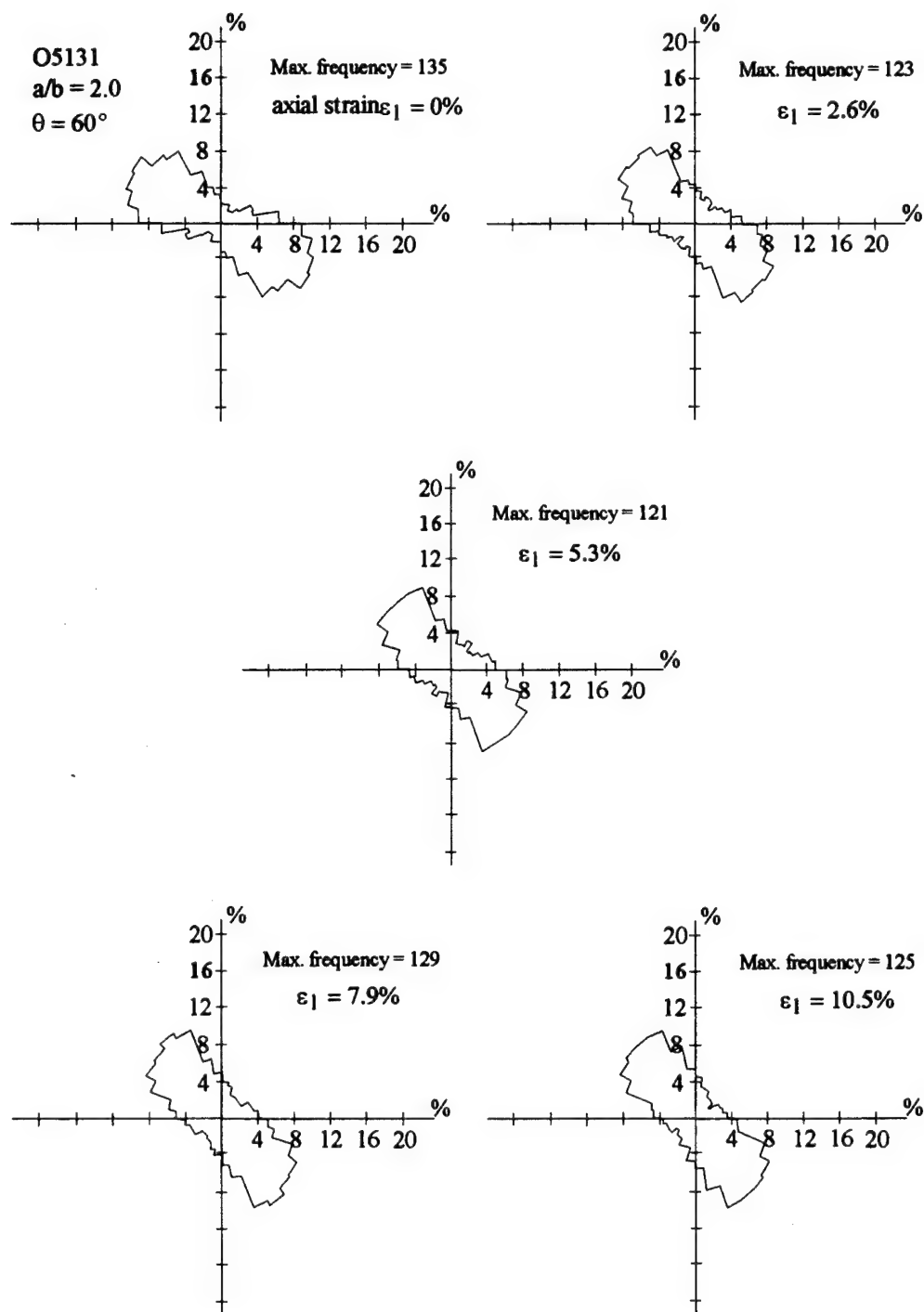
Figure 193. Evolution of contact normal distributions for a DEM sample with a/b = 2.0 and 60° bedding (peak strength at ε_1 = 7.4%).

10. CONCLUSIONS AND RECOMMENDATIONS

This Report has presented results of a multi-year, Air Force Office of Scientific Research-funded study on the mechanical behavior of anisotropic granular systems. A two-dimensional discrete element method (DEM) model using ellipse-shaped particles was used to investigate the influence of particle shape on the overall mechanical behavior of granular materials. Numerous particulate assemblages with variations in particle angularity and bedding were subjected to biaxial shear in numerical simulations under similar initial conditions. Some initial conditions such as the initial void ratio, method of sample formation and the confining stress were varied in other test simulations to examine their effect on the stress-dilatant behavior of granular assemblages. The numerical samples consisted of dry, weightless and cohesionless ellipse-shaped particles that were generated in "space". Because the effects of gravity are neglected, the significance of the orientation of the preferred bedding plane is with respect to the laterally-applied principal (or confining) stresses.

The comparisons of the numerical test results to those from physical tests on sand and other granular materials show that the ellipse-based DEM model can realistically simulate real soil behavior. Good agreement was found with the circular rod data of Chapuis (1976). Though good quantitative agreement between the data reported by Konishi *et al* (1983) and that yielded by the ellipse-based DEM model was not achieved, the differences are attributed to the subtle but significant differences in the shape of the particles used in both micromechanical investigations. The ellipse-based DEM model used in the current numerical study yields stress-dilatant behavior results that are quantitatively closer to real soil and other granular materials than those yielded by other DEM models using round or elliptic particle shapes.

The results of the biaxial shear simulations using the ellipse-based DEM model show that the strength and dilatant behavior of granular materials generally increases as the particulate constituents become more angular. Upon deposition, angular particles may become aligned producing dense assemblages with extremely anisotropic fabrics or they may be randomly distributed producing loose assemblages with more isotropic fabrics. Results yielded by the ellipse-based DEM model's biaxial shear simulations show that fabric anisotropy significantly influences the strength and deformation behavior exhibited by the particulate assemblages. Since round particles do not possess orientation, the fabric tends to be more isotropic. Fabric anisotropy increases as particle aspect ratio increases.

The numerical simulation results show that the strength of granular materials is lowest for assemblages consisting of round particles and increases as particle angularity increases. For assemblages consisting of particles with similar shapes, the strength and dilatant behavior exhibited is highest when particle bedding is normal to the applied shear stress (or horizontal for the current study). The exhibited strength and dilatant behavior decreases as the bedding plane inclines toward the predicted failure plane defined by Rowe's stress-dilatancy theory ($45° - \phi_f/2$ from applied shear stress σ_1). For assemblages consisting of flatter particles, the strength and dilatant behaviors are lowest when the bedding plane and $45° - \phi_f/2$ are coaxial. The results of the numerical simulations show that stress-dilatancy behavior of granular materials increases as the bedding (or interlocking) plane deviates from the predicted slip plane.

As particle angularity increases, more interlocking occurs. Consequently, the numerical granular assemblages experience more remolding and longer periods of initial contraction. After the extended initial contractant behavior, assemblages with preferred horizontal bedding ($\theta = 0°$) ultimately dilate more achieving higher volumetric strains than assemblages consisting of more rounded particles. As a result, assemblages with preferred horizontal bedding exhibit higher strength as more energy is required to deform the assemblage by expansion.

Though the assemblages with preferred 60° bedding are extremely dense, they exhibit behavior typically

associated with loose assemblages. Because the bedding plane of assemblages with preferred 60° bedding are approximately coaxial with the predicted slip plane (45° - $\phi_f/2$), failure is facilitated more easily. Consequently, the assemblages' deformation more closely resembles rigid body motion of opposing particulate wedges along the slip plane that develops as a distinct shear band. Strength and dilatant behaviors for these assemblages decrease with increased particle angularity as less energy is spent on expansion during the course of shear-induced deformation. Results of the numerical simulations show that looser assemblages having isotropic or anisotropic orientation fabrics exhibit less strength and dilatant behavior than denser assemblages as more energy is spent on remolding than on dilation.

Assemblages with preferred horizontal bedding ($\theta = 0°$) that are confined laterally by higher stresses require more energy to expand against the increased confining stress and as a result exhibit higher strength. The increased confining stress, however, provides more resistance to lateral expansion resulting in less dilatant behavior.

For granular assemblages with low interparticle friction, results of the numerical simulations show that particle sliding is the dominant deformation mechanism. However, the numerical simulations show that particle rolling is the dominant deformation mechanism in assemblages with high interparticle friction. Consequently, as the interparticle friction increases, the strength does not increase monotonically. As the interparticle friction increases, assemblages yield peak macroscopic internal friction angles that are lower than their interparticle sliding friction angles.

Because angular particles possess more interlocking, the negative effects of particle rolling on the strength of the assemblage are significantly reduced. For granular assemblages consisting of round particles, particle motion due to rotation is about 2.5 times larger than particle translation. As particle angularity increases, the relative importance of particle motion due to translation and rotation become virtually equal. Rotation and translation statistics are similar for assemblages with both preferred 0 (horizontal) and 30° bedding suggesting that the relative importance of rotation and translation for assemblages with variations in particle angularity is independent of the orientation of the preferred bedding plane.

Results of the biaxial shear simulations yielded by the ellipse-based DEM model show that assemblages with preferred bedding possess more anisotropic distribution of contact normals. As particle angularity increases, interlocking increases producing a more anisotropic fabric. During the course of deformation, the distribution of contact normal orientations tend to rotate toward the vertical (or the direction of the applied shear stress) providing increased shear resistance as horizontal contacts are broken while vertical contacts are made.

Anisotropic fabrics due to increased particle interlocking are deteriorated more rapidly in assemblages with preferred 0° bedding as the particles are predisposed to move laterally since they possess horizontal major axes that are coaxial with the horizontally-applied confining stress. Consequently, more dilatant and spalling-type behavior occurs resulting in an increase in the ability to resist a vertically-applied shear stress. Because of the increased dilatant behavior of assemblages with preferred horizontal particle bedding, the coordination number decreases significantly during the course of deformation.

Shear resistance is significantly less as the preferred bedding plane inclines toward 45° - $\phi_f/2$ (measured from σ_1). Particulate columns that develop to provide shear resistance are considerably less stable than those with preferred 0° bedding. Particle interlocking increases during the course of deformation resulting in less energy required to laterally expand assemblages with inclined bedding. Consequently, the coordination number increases as the granular assemblages deform.

153

The ellipse-based DEM model used for the current study has been shown to be an effective tool for realistically modeling the microstructure and overall mechanical behavior of granular materials. Because discrepancies exist in the comparison of the results reported by Konishi *et al* (1983) and those yielded by the ellipse-based DEM model, it is recommended that the model's validation continue to include data comparisons with physical tests that specifically use ellipse-shaped particles. Such a study is currently underway using the results of interfacial shear tests between a rough interface an assemblage of carefully machined circular and elliptical rods.

Gradation of the numerical assemblages used in the current investigation was limited to an equal number of three different-sized particles having the same shape (or aspect ratio). Though variations in the gradation of particulate materials can be limitless, it is recommended that more variation in the assemblage's gradation be investigated. Variations in gradation should include mixing of particle shapes in addition to finer and coarser distributions of particle sizes.

Additional work is progressing to investigate the effect of boundaries (rigid, flexible, periodic). As well the ellipse-based DEM is being applied to a limited number of soil-structure interaction problems in geotechnical engineering. Other efforts are currently being made to enable the model to simulate particle-fluid interactions and multiphase materials such as frozen soil systems.

APPENDIX I. REFERENCES

Barbosa, R. and Ghaboussi, J. (1987), "Discrete Element Model for Granular Soils," *Proc. Workshop on Constitutive Laws for the Analysis of Fill Retention Structures*, Ottawa, Canada.

Bathurst, R.J. and Rothenburg, L. (1988), "Micromechanical Aspects of Isotropic Granular Assemblies with Linear Contact Interactions," *Journal of Applied Mechanics*, 55:17-23.

Bažant, Z.P., Tabbara, M.R., Kazemi, M.T. and Pijaudier-Cabot, G. (1990), "Random Particle Model for Fracture of Aggregate or Fiber Composites," *ASCE J. Engineering Mechanics* 116(8):1686-1705.

Bhatia, S.K. and Soliman, A.F. (1990), "Frequency Distribution of Void Ratio of Granular Materials Determined by an Image Analyzer," *Soils and Foundations* 30(1):1-16.

Butkovich, T.R., Walton, O.R. and Heuze, F.E. (1988), "Insights in Cratering Phenomenology Provided by Discrete Element Modeling," *Proc. 29th U.S. Symposium on Rock Mechanics*, Minneapolis, Minn.

Campbell, C.S. and Brennen, C.E. (1983), "Computer Simulation of Shear Flows of Granular Material." in *Mechanics of Granular Materials: New models and constitutive relations*. J.T. Jenkins and M. Satake, ed., Elsevier Science Publ., Amsterdam, 313-326.

Chang, C.S. and Misra, A. (1990), "Application of Uniform Strain Theory to Heterogeneous Granular Solids," *ASCE J. Engineering Mechanics*, 116(10):2310-2328.

Chang, C.S. and Liao, C.L. (1990), "Constitutive Relation for a Particulate Medium with the Effect of Particle Rotation," *Int'l J. Solids Structures* 26(4):437-453.

Chang, C.S., Misra, A. and Xue, J.H. (1989). "Incremental Stress-Strain Relationships for Regular Packings Made of Multi-sized Particles," *Int'l J. Solids Structures*, 25(6):665-681.

Chapuis, R.P. (1976), "De la Structure Géométrique des Milieux Granulaires en Relation avec leur Comportement Mécanique," Sc.D. thesis, *Ecole Polytechnique*, Université de Montréal, Montréal, Canada.

Chen, Y.C. and Ishibashi, I (1990). "Dynamic Shear Modulus and Evolution of Fabric of Granular Materials," Soils and Foundations, 30(3):1-10.

Chen, Y.C. (1989), "Inter-particle Friction and Evolution of Fabric," *Proc. 1st U.S. Conf. on Discrete Elements*, Golden, CO.

Corkum, B.T. and Ting, J.M. (1986), "The Discrete Element Method in Geotechnical Engineering," Dept. Civil Engineering Publ. 86-11, *Univ. of Toronto*, Toronto, Canada. ISBN 0-7727-7086-7.

Cundall, P.A. (1988), "Computer Simulations of Dense Sphere Assemblies," in *Micromechanics of Granular Materials*, M. Satake and J.T. Jenkins, ed., Elsevier Science Publ., Amsterdam, 113-123.

Cundall, P.A. and Strack, O.D.L. (1979), "A Discrete Numerical Model for Granular Assemblies." *Géotechnique*, 29(1):47-65.

Cundall. P.A. (1974), "A Computer Model for Rock-mass Behavior Using Interactive Graphics for the Input and Output of Geometric Data," Rep. AD/A-001 *602, U.S. National Technical Information Service.*

Cundall, P.A., "Computer Simulations of Dense Sphere Assemblies," in *Micromechanics of Granular Materials*, M. Satake and J.T. Jenkins, ed., Elsevier Science Publ., Amsterdam, 113-123 (1988).

Dickin, E.A. (1973), "Influence of Grain Shape and Size on the Limiting Porosities of Sands," in Evaluation of Relative Density and Its Role in Geotechnical Projects Involving Cohesionless Soils, *ASTM STP* No. 523:113-120.

Dobry, R. and Ng, T.T. (1989), "Discrete Modeling of Stress-Strain Behavior of Granular Media at Small and Large Strains," *Proc. 1st U.S. Conf. on Discrete Element Methods*, Golden, Colo.

Feda, J. (1982), "Mechanics of Particulate Materials: the Principles," *Developments in Geotechnical Engineering* Vol. 30, Elsevier Science Publ. Co, Amsterdam.

Ghaboussi, J. and Barbosa, R. (1988). "Three-dimensional Discrete Element Method for Granular Materials," *Int'l J. Numerical and Analytical Methods in Geomechanics.*

Goodman, R.E. and Bray, J.W. (1976). "Toppling of rock slopes," in *Rock Engineering for Foundations and Slopes*, ASCE, Boulder, CO.

Hakuno, M., Iwashita, K. and Uchida, Y. (1989), "DEM Simulation of Cliff Collapse and Debris Flow." *Proc.*

1st U.S. Conf. on Discrete Element Methods, Golden, Colo.

Hassan, P.J. (1990), "Three Dimensional Discrete Element Modelling of Soils," M.A.Sc. thesis, Dept. of Civil Eng., *University of Toronto*, Toronto, Canada.

Hockney, R.W. and Eastwood, J.W. (1981). Computer Simulation using Particles. McGraw-Hill Int'l Book Co., New York, N.Y.

Holubec, I. and D'Appolonia, E. (1973), "Effect of Particle Shape on the Engineering Properties of Granular Soils," in Evaluation of Relative Density and Its Role in Geotechnical Projects Involving Cohesionless Soils, *ASTM STP* No. 523:304-318.

Horne, M.R. (1969), "The Behaviour of an Assembly of Rotund, Rigid, Cohesionless Particles, III," *Proc. Royal Society of London* A310:21-34.

Horne, M.R. (1965), "The Behaviour of an Assembly of Rotund, Rigid, Cohesionless Particles, I & II," *Proc. Royal Society of London* A286:62-97.

Ishibashi, I., and Agarwal, T. K. (1991). "Numerical Experiments for Anisotropic Behavior of Granular Materials," *Proc. ASCE Engineering Mechanics Specialty Conf. on Mechanics Computing in 1990's and Beyond*, Columbus OH, Vol. 2, pp 1239-1243.

Ishibashi, I., Agarwal, T. and Ashraf, S.A. (1989), "Anisotropic Behaviors of Glass Spheres by a Discrete Element Model and Laboratory Experiments," *Proc. 1st U.S. Conf. on Discrete Elements*, Golden, CO.

Ishibashi, I., Sherif, M.A. and Cheng, W.L. (1982), "The Effects of Soil Parameters on Pore Pressure Rise and Liquefaction Prediction," *Soils and Foundations* 22(1):39-48.

Issa, J.A. and Nelson, R.B. (1989), "Numerical Analysis of Micromechanical Behavior of Granular Materials," *Proc. 1st U.S. Conf. on Discrete Element Methods*, Golden, Colo.

Khwaja, M. (in press 1995). "Ellipse-based Discrete Element Modeling: Micromechanical and Large-Scale Modelling," M.Sc. Thesis, Dept. Civil Engineering, *University of Massachusetts*, Lowell, MA.

Kishino, Y. (1988), "Disc Model Analysis of Granular Media," in *Micromechanics of Granular Materials*, M. Satake and J.T. Jenkins, ed., Elsevier Science Publ., Amsterdam, 143-152.

Koerner, R.M. (1970), "Effect of Particle Characteristics on Soil Strength," *ASCE J. Soil Mechanics and Foundation Div.* 96(4):1221-1234.

Konishi, J., Oda, M. and Nemat-Nasser, S. (1983), "Induced Anisotropy in Assemblies of Oval Cross-sectional Rods in Biaxial Compression," in *Mechanics of Granular Materials: New Models and Constitutive Relations*, J.T. Jenkins and M. Satake, ed., Elsevier Science Publ., Amsterdam, 31-39.

Konishi, J., Oda, M. and Nemat-Nasser, S. (1982). "Inherent Anisotropy and Shear Strength of Assembly of Oval Cross-sectional Rods," IUTAM Conference on Deformation and Failure of Granular Materials, 403-412.

Kuhn, M. R. and Mitchell, J.R. (1989), "The Modeling of Soil Creep with the Discrete Element Method," *Proc. 1st U.S. Conf. on Discrete Element Methods*, Golden, Colo..

Ladd, C.C., Foott, R., Ishihara, K., Poulos, H.G. and Schlosser, F. (1977), "Stress-Deformation and Strength Characteristics: State-of-the-Art Report," *Proc. 9th Int'l Conf. Soil Mechanics and Foundation Engineering*, Tokyo, Japan.

Lambe, T.W. and Whitman, R.V. (1968), *Soil Mechanics*, J.Wiley & Sons, New York.

Lorig, L.J. and Brady, B.H.G. (1984), "A Hybrid Computational Scheme for Excavation and Support Design in Jointed Rock Media," *Design and Performance of Underground Excavations*, ISRM/British Geotechnical Society, Cambridge, England, 105-112.

Meachum, L.R. (1994). "Influence of Particle Shape on the Mechanical Behavior of Granular Materials," M.Sc. Thesis, Dept. Civil Engineering, *University of Massachusetts*, Lowell, MA.

Mehrabadi, M.M., Nemat-Nasser, S., Shodja, H.M. and Subhash, G. (1988), "Some Basic Theoretical and Experimental Results on Micromechanics of Granular Flow," in *Micromechanics of Granular Materials*, M. Satake and J.T. Jenkins, ed., Elsevier Science Publ., Amsterdam, 253-262.

Ng, T.T. "Numerical Simulations of Granular Soil Using Elliptical Particles," *Proc. ASME Symposium on Microstructural Characterization in Constitutive Modeling of Metals and Soils*, Tempe, Arizona (1992).

Ng, T.T. and Lin, X. (1993). "Numerical Simulations of Naturally Deposited Granular Soil with ellipsoidal

Elements," Proc. Second Int'l Conf. Discrete Elements, M.I.T., Cambridge, Mass. 557-567.

Oda, M., Nemat-Nasser, S. and Konishi, J. 1985). "Stress-Induced Anisotropy in Granular Masses," *Soils and Foundations*, **25**(3):85-97 (1985).

Oda, M., Konishi, J. and Nemat-Nasser, S. (1983), "Experimental Micromechanical Evaluation of the Strength of Granular Materials: Effects of Particle Rolling," in *Mechanics of Granular Materials: New Models and Constitutive Relations*, J.T. Jenkins and M. Satake, ed., Elsevier Science Publ., Amsterdam, 21-30.

Paikowsky, S.G., Ting, J.M., Xi, F. and Mischel, G. (in press). "Comparison of Numerical and Experimental Testing of Interfacial Shear of a Granular Material", submitted for presentation at 1996 ASME Summer Conference, Ft. Lauderdale, FL.

Rothenburg, L. and Bathurst, R.J. (1992). "Micromechanical features of granular assemblies with planar elliptical particles," *Géotechnique*, **29**:79-95.

Rothenburg, L. and Bathurst, R.J. (1991). "Numerical Simulation of Idealized Granular Assemblies with Plane Elliptical Particles," *Computers and Geotechnics*, 11(4):315-329.

Rowe, P.W. (1962), "The Stress Dilatancy Relation for Static Equilibrium of an Assembly of Particles in Contact," *Proc. Royal Society of London* A269:500-527.

Rowell, J.D. (1994). "Validation of Ellipse-based Discrete Element Modeling in Soil Mechanics," M.Sc. Thesis, Dept. Civil Engineering, *University of Massachusetts*, Lowell, MA.

Sadd, M.H., Tai, Q.M. and Shukla, A. (1993). "Contact law effects on wave propagation in particulate materials using distinct element modeling," *Int'l J. Non-linear Mechanics*, **28**(2):251-265.

Scott, R.F. (1987), "Failure," 27th Rankine Lecture, *Géotechnique* 37(4):423-466.

Skinner, A.E. (1969), "A Note on the Influence of Interparticle Friction on the Shearing Strength of a Random Assembly of Spherical Particles," *Géotechnique* 19(150-157).

Taylor, L.M., and Preece, D.S. (1989), "Simulation of Blasting Induced Rock Motion Using Spherical Element Models," *Proc. 1st U.S. Conf. on Discrete Element Methods*, Golden, Colo.

Terzaghi, K. and Peck, R.B. (1967), *Soil Mechanics in Engineering Practice*, J.Wiley & Sons, New York, 2nd ed.

Ting, J.M., Meachum, L.R. and J.D. Rowell (1995). "Effect of Particle Shape on the Strength and Deformation Mechanisms of Ellipse-shaped Assemblages," *Engineering Computations: Int'l Journal of Computer-Aided Engineering and Software*, ed. D.R.J. Owen and K.J. Bathe, **12**(2): 99-108.

Ting, J.M. and Rowell, J.D. (1995). "Ellipse-based Discrete Element Model for Granular Materials: Validation Testing," Proc. 1995 *ASCE Engineering Mechanics Conference on Discontinuous Materials*, Colorado, May 1995.

Ting, J.M. and L.R. Meachum (1995). "Effect of Bedding Plane Orientation on the Behavior of Granular Systems," *Mechanics of Materials with Discontinuities and Heterogeneities*, ed. A. Misra and C.S. Chang, ASME AMD Vol 201: 43-58.

Ting, J.M., Khwaja, M., Meachum, L.R. and Rowell, J.D. (1993). "An Ellipse-based Discrete Element Model for Granular Materials," *Int'l Journal for Numerical and Analytical Methods in Geomechanics*, 17(9):603-623.

Ting, J.M., J.D. Rowell, and Meachum, L. (1993). "Influence of Particle Shape on the Strength of Ellipse-shaped Granular Assemblages," *Proc. Second Int'l Conf. Discrete Element Methods*, M.I.T., Cambridge, Mass., pp 215-225.

Ting, J.M. and Corkum, B.T. (1992). "A Computational Laboratory for Discrete Element Geomechanics," *ASCE J. Computing in Civil Engineering*, 6(2):129-146.

Ting, J.M. (1992). "A Robust Algorithm for Ellipse-based Discrete Element Modelling of Granular Materials," *Computers and Geotechnics*, 13:175-186.

Ting, J.M. (1991), "An Ellipse-based Micromechanical Model for Angular Granular Materials," *Proc. ASCE Engineering Mechanics Specialty Conf. on Mechanics Computing in 1990's and Beyond*, Columbus OH, Vol. 2, pp. 1214-1218..

Ting, J.M., Corkum, B.T., Kauffman, C.R. and Greco, C. (1989), "Discrete Numerical Model for Soil

Mechanics," *ASCE Journal of Geotechnical Engineering*, 115(3):379-398.

Ting, J.M., and Corkum, B.T. (1988a), "Strength Behavior of Granular Materials Using Discrete Numerical Modelling," *Proc. 6th Int'l Conf. Numerical Methods in Geomechanics*, Innsbruck, Austria, 1:305-310.

Ting, J.M. and B.T. Corkum (1988b). "Discrete Element Models in Geotechnical Engineering," Proc. *3rd International Conference on Computing in Civil Engineering*, Vancouver, Canada, Vol. 2, pp. 587-594.

Ting, J.M. and B.T. Corkum (1988c). "Soil-structure Interaction by Discrete Numerical Modelling," Proc. *Canadian Society for Civil Engineering Annual Conference*, Calgary, Canada, Vol. 3, pp. 196-215.

Ting, J.M., Corkum, B.T., Kauffman, C.R. and Greco, C. (1987), "Discrete Numerical Modelling of Soil: Validation and Application," Publ. 87-03, *Dept. Civil Engineering*, Univ. of Toronto, Toronto, Canada, ISBN 0-7727-7090-5.

Tzaferopoulos, M.A. (1995). "On a Quasi-static Discrete Element Model of Granular Materials," *Computers and Geotechnics*.

Vaid, Y.P., Chern, J.C. and Tumi, H. (1985), "Confining Pressure, Grain Angularity and Liquefaction," *ASCE J. Geotechnical Engineering* 111(10):1229-1235.

Walton, O.R. and Braun, R.L. (1993). "Simulation of rotary-drum and repose tests for frictional spheres and rigid sphere clusters," *Proc. Joint DOE/NSF Workshop on Flow of Particulates and Fluids*, Ithaca, NY.

Walton, O.R., Braun, R.L., Mallon, R.G. and Cervelli, D.M. (1988), "Particle-Dynamics Calculations of Gravity Flow of Inelastic, Frictional Spheres," in *Micromechanics of Granular Materials*, M. Satake and J.T. Jenkins, ed., Elsevier Science Publ., Amsterdam, 153-161.

Wei, Q., Cheng X.H., and Liu, G.T. (1991). "The Elliptic Discrete Element Method as a New Approach to Simulating Granular Media," *Proc. Asian Pacific Conference on Computational Mechanics*, Hong Kong.

Williams, J.R. and Pentland, A.P. (1989), "Superquadrics and Modal Dynamics for Discrete Elements in Concurrent Design," *Proc. 1st U.S. Conf. on Discrete Element Methods*, Golden, Colo.

Youd, T.L. (1973), "Factors Controlling Maximum and Minimum Densities of Sands," in Evaluation of Relative Density and Its Role in Geotechnical Projects Involving Cohesionless Soils, *ASTM STP* No. 523:98-112.

Zhang, Y. and Cundall, P.A. (1986), "Numerical Simulation of Slow Deformations," Proc. Symp. on the Mechanics of Particulate Media, *10th National Congress on Applied Mechanics*, Austin, Texas.

APPENDIX II. SYMBOLS

a, b	major and minor axes for ellipse
c_n, c_s	normal and shear contact viscous damping coefficients
A, B, C	coefficients of general ellipse function
dx, dy	center of ellipse in world coordinates
e	coefficient of restitution
$\hat{e}$	unit normal, outward for ellipses, inward for wall
f_i^c	i^{th} component of force for contact c
F_n, F_s	normal and tangential forces at a contact
I	polar moment of inertia of particle
k_n, k_s	normal and tangential contact spring stiffnesses
l_j^c	j^{th} component of contact vector (particle centroid - contact location) for contact c
m	mass of particle
m_l, b_l	slope and y-intercept of wall in homogeneous local coordinates of ellipse i
M_o	moment about point o
N	total number of particles in a region
P, R, Q, S	constants in ellipse-ellipse intersection equation
S_x, S_y	sum of squares of errors
$\hat{t}$	unit tangential vector to ellipse
T_n, T_s	maximum contact normal and shear strengths
u_i, v_i	displacement components of ith particle
V	volume
$\hat{w}$	unit vector along wall from endpoint 1 to endpoint 2
x, y	Cartesian coordinate variables
x_1, y_1, x_2, y_2	endpoints of wall
x_c, y_c	coordinates of contact
X, Y	homogeneous coordinate variables
$\alpha_1, \alpha_2, \alpha_3$	coefficients of displacement field $u = \alpha_1 + \alpha_2 x_i + \alpha_3 y_i$
$\beta_1, \beta_2, \beta_3$	coefficients of displacement field $v = \beta_1 + \beta_2 x_i + \beta_3 y_i$
ϵ_{ij}	average strain tensor
σ_{ij}	average stress tensor
θ	rotation with respect to world coordinate system